# THÈSE POUR OBTENIR LE GRADE DE DOCTEUR DE L'UNIVERSITÉ DE MONTPELLIER

**En Electronique**

**École doctorale Information, Structures et Système (I2S)**

**Unité de recherche IES Montpellier, UMR-CNRS 5214**

# RADIATION EFFECTS AND SYSTEM-LEVEL TESTING: APPLICATION TO WIRELESS COMMUNICATIONS

# EFFETS DES RADIATIONS ET TESTS AU NIVEAU DU SYSTÈME: APPLICATION AUX COMMUNICATIONS SANS FIL


**Présentée par Alessandro ZIMMARO**
**le 23 Janvier 2024**

**Sous la direction de Jérôme BOCH**
**et Frédéric SAIGNE**


**Devant le jury composé de**

| | |
|---|---|
| Luis Alfonso ENTRENA ARRONTES, Professeur, Université Carlos III de Madrid | Rapporteur |
| Paul LEROUX, Professeur, KU Leuven | Rapporteur |
| Philippe COMBETTE, Professeur, Université de Montpellier, IES | Président du jury |
| Jérôme BOCH, Professeur, Université de Montpellier, IES | Directeur de thèse |
| Frédéric SAIGNE, Professeur, Université de Montpellier, IES | Co-directeur de thèse |
| Salvatore DANZECA, Docteur, CERN | Examinateur |
| Rudy FERRARO, Docteur, CERN | Examinateur |

UNIVERSITÉ DE MONTPELLIER

# Abstract

CERN's electronics systems, both in the accelerator and in experiments, are exposed to the peculiar harsh radiation environments induced by the different particle accelerators. As such, the ability of these systems to withstand the effects of radiation on electronics is crucial to maintaining the smooth operation of the accelerators and achieving the organization's ambitious objectives. To ensure the required reliability, the electronic equipment must pass a series of qualification steps that make up the Radiation Hardness Assurance (RHA) procedure. The scheduled Large Hadron Collider (LHC) upgrade in 2029 (High Luminosity LHC (HL-LHC)) will significantly increase radiation levels that the accelerator's systems must withstand. In these circumstances, achieving successful completion of the RHA procedure while maintaining the currently used LHC radiation design margins and using commercial off-the-shelf (COTS) components may prove to be a complex task.

The objective of this research is to enhance the existing RHA procedure to address these new challenges. The different stages of the process are examined and the 'Radiation Environment Analysis' and 'System-Level Testing' phases are identified as having room for improvement. For this purpose, a new wireless radiation monitoring system for electronics is being developed and presented within this work. Thanks to its faster and more efficient deployment capabilities within the accelerator, this cutting-edge project aims to decrease the uncertainty of the estimation offered by the 'Radiation Environment Analysis' phase. On the other hand, its qualification offers the opportunity to improve the 'System-Level Testing' phase through the development of new system-level testing guidelines and methodologies. These novel approaches will enhance the current RHA process and obtain higher confidence

results during the execution of the 'System-Level Testing' phase.

## Keywords

Radiation Hardness Assurance, Radiation to Electronics effects, Radiation Monitoring, System-Level Testing, Internet of Things, Wireless System

# Résumé

The Organisation Européenne pour la Recherche Nucléaire (CERN) explore les plus petits éléments constitutifs de l'univers, les particules fondamentales, afin de repousser les frontières de la connaissance humaine. Pour explorer l'origine de l'univers, deux faisceaux de particules voient leur énergie augmenter à travers une chaîne complexe d'accélérateurs, également appelée "chaîne d'injecteurs". Le Large Hadron Collider (LHC) est la machine finale et la plus avancée de cette chaîne, où les deux faisceaux sont accélérés jusqu'à 7 $TeV$. Lorsqu'ils ont atteint l'énergie souhaitée, ils sont portés à la collision à une vitesse proche de celle de la lumière dans l'un des quatre détecteurs construits à cet effet le long de l'accélérateur (ATLAS, ALICE, CMS et LHCb). La pluie de particules produite par cette interaction permet aux physiciens des particules d'étudier les particules fondamentales.

En physique des particules, les particules intéressantes dans les interactions sont exceptionnellement rares et nécessitent un grand nombre d'interactions pour les générer. Pour améliorer le fonctionnement du LHC, il existe deux possibilités: augmenter la luminosité instantanée (intensité plus élevée du faisceau) ou améliorer la disponibilité de l'accélérateur. Si la première solution peut être obtenue par une mise à niveau de la machine, comme ce sera le cas pour le High-Luminosity Large Hadron Collider (HL-LHC), la seconde dépend des différents équipements de contrôle de la chaîne de l'accélérateur.

Dans ce contexte, les systèmes électroniques utilisés pour le contrôle des accélérateurs (ATS) doivent avoir une grande disponibilité pendant les opérations afin de permettre à l'organisation d'atteindre ses objectifs. Cependant, il peut être difficile d'atteindre des niveaux élevés de disponibilité dans une machine aussi complexe en raison de

l'environnement de rayonnement généré par son fonctionnement. Cette complexité est d'autant plus grande que les contraintes de coût imposent l'utilisation de composants commerciaux (COTS) dans le secteur des accélérateurs. Ces systèmes, qui ne sont pas prévus pour fonctionner dans un environnement de rayonnement, peuvent être plus sensibles aux effets électroniques du rayonnement et peuvent cesser de fonctionner en raison d'une erreur induite par le rayonnement.

Augmenter la disponibilité de l'accélérateur et la luminosité délivrée, en réduisant le nombre de dysfonctionnements induits par les rayonnements a été le principal mandat du projet Radiation to Electronics (R2E) groupe. Commencé au CERN en 2012, son principal objectif consistait à quantifier le danger des défaillances dues aux rayonnements et à introduire des mesures d'atténuation pour réduire le risque de défaillance à moins d'une par semaine, non seulement pour les faisceaux nominaux, mais aussi pour tous les scénarios à venir qui pourraient se présenter. Ces mesures comprennent le transfert des systèmes dans des zones plus sûres, l'augmentation de les protections et le remplacement des systèmes défectueux par des systèmes plus robustes.

La prochaine mise à niveau du LHC en 2029, connue sous le nom de HL-LHC, permettra d'obtenir une luminosité annuelle cinq fois supérieure à celle du LHC actuel. Il en résultera une augmentation substantielle des radiations générées par le fonctionnement de la machine. La relocalisation et le blindage des équipements peuvent s'avérer insuffisants et, pour certains équipements comme les systèmes de protections contre la perte de supraconductivité des aimants, ils sont impossibles à mettre en place. Afin de répondre aux exigences de fiabilité et de disponibilité du HL-LHC et de se préparer à tous les scénarios possibles, le CERN ATS a créé ses propres procédures d'assurance qualité pour la tenue aux radiations, dite Radiation Hardness Assurance (RHA) pour les systèmes éléctroniques faits sur mesure, qui sont basées sur des composants commerciaux non conçus pour résister aux radiations, afin de garantir des performances efficaces au sein de l'accélérateur. Pour tenir compte de l'environnement unique du spectre des particules au LHC, cette procédure a fait l'objet d'améliorations et d'extensions continues au cours des années, avec des méthodologies d'essai permettant d'obtenir les résultats les plus réalistes possibles. La procédure comprend plusieurs phases qui sont maintenant obligatoires pour tous les systèmes destinés au secteur des accélérateurs. La réussite de chacune des phases est nécessaire pour obtenir l'autorisation d'installer le nouveau système dans le LHC.

L'objectif principal de cette thèse de doctorat est d'étudier comment améliorer la procé-

dure d'assurance qualité à la tenue aux radiations actuelle du CERN pour répondre aux exigences de disponibilité et de fiabilité du HL-LHC. Pour atteindre cet objectif, plusieurs activités ont été conduites: a) étudier l'état actuel de la procédure du CERN et identifier les différents points vulnérables de l'approche actuelle ; b) développer des méthodologies de test au niveau du système adaptées aux besoins du CERN ; et c) démontrer la validité de ces nouvelles approches.

La dernière de ces activités repose sur utilisation d'un cas d'étude pour sa démonstration. Pour cela, un nouveau système de mesure des radiations pour l'éléctronique, basé sur le principe de l'internet des objets (en anglais (the) Internet of Things ou IoT) est utilisé. Premier exemple d'application IoT au CERN, les résultats expérimentaux obtenus pendant la qualification de cette application, nous ont permis d'étudier les avantages (par exemple, la réduction des coûts d'infrastructure dans les accélérateurs plus longs tels que le Future Circular Collider (FCC)) et les défis associés à l'intégration d'un réseau IoT dans un accélérateur de particules.

Cette application représente le premier exemple système de mesure des radiations sans fil pour l'électronique et son développement permettra de faire bénéficier de nombreux avantages dans son contexte d'application, en améliorant implicitement une partie de la procédure de qualfication du CERN. En fait, la mesure des radiations est un des piliers fondamentaux de tout la procédure de qualfication du CERN et influe sur toutes les étapes ultérieures de la procédure. Ces estimations sont utilisées pour définir les spécifications du système en matière de radiations. De plus, des marges supplémentaires dans la tolérance aux radiations sont appliqués lors de la conception pour tenir compte de leur incertitude, augmentant les conditions à satisfaire. Dans un contexte d'augmentation des niveaux de radiations due à la mise à jour du LHC, qui induiront des contraintes encore plus élevé en matière de tenue aux radiation, la généralisation seule des essais au niveau système ne suffiront pas à garantir la fiabilité des équipements. L'incertitude de l'estimation des rayonnements dans les différents secteurs doit également être réduite afin de réduire les marges de conception pour que la procédure soit réalisable. Ensuite, en plus de présenter cette application et sa qualification, un autre objectif de ce travail doctoral est de démontrer ses avantages opérationnels appliqués dans le contexte de la mesure des radiations à travers des exemples réels de son fonctionnement dans le LHC. La structure du manuscrit est présentée ci-dessous afin de donner un résumé complet de l'ensemble du travail.

Le Chapitre 1 présente une description des différents effets des radiations sur

l'électronique. Pour mieux comprendre et définir ces effets, les mécanismes par lesquelles les particules interagissent avec la matière sont étudiés. La deuxième partie du chapitre présente les trois effets des radiations sur l'électronique.

Le chapitre 2 présente le complexe d'accélérateurs du CERN, son principe de fonctionnement et l'environnement radioactif prévu dans les plus importantes régions. Ce chapitre présente le concept de disponibilité de l'accélérateur et l'impact des défaillances induites par les rayonnements dans le système électronique sur les performances de l'accélérateur. La procédure de qualfication du CERN est présenté par une vue d'ensemble de sa structure et une analyse approfondie de ses phases les plus importantes pour cette étude. Une attention particulière est accordée aux phases "Analyse de l'environnement de rayonnement" et "Test au niveau du système", qui sont identifiés comme les parties pouvant bénéficier d'une amélioration. L'analyse approfondie de ces deux phases met en évidence leurs limites mais permet aussi d'identifier des axes d'améliorations du processus. La phase de test au niveau du système, contrairement à son pendant au niveau des composants, manque de standardisation et ne garantit pas les mêmes niveaux de fiabilité. L'ajout de méthodologies et de lignes directrices pourrait permettre d'améliorer cette phase et d'accroître la fiabilité de l'application de la procédure. Parallèlement, l'amélioration des instruments utilisés pour la mesure des niveaux de radiations à l'intérieur de l'accélérateur, en augmentant leur capacité de déploiement, est cruciale pour réduire l'incertitude de l'estimation fournie par la phase "Analyse de l'environnement de rayonnement". Ceci, à son tour, est essentiel pour réduire les exigences de résistance aux rayonnements pour les projets et les rendre plus réalistes et réalisables. Comme cela a été souligné dans ce chapitre, il pourrait s'agir de la seule solution possible pour répondre aux exigences environnementales plus strictes du HL-LHC, ce qui pourrait être difficile à réaliser avec un système COTS auquel sont appliqués les mêmes facteurs de sécurité importants que ceux utilisés pour le LHC. La définition d'une solution électronique pour améliorer ces étapes et les défis d'un tel développement sont examinés dans la dernière partie du chapitre et motivent le travail présenté dans la chapitres suivante.

Le chapitre 3 présente l'instrument utilisé dans cette thèse comme cas d'étude pour améliorer la phase de test au niveau du système, c'est-à-dire le système IoT de mesure des radiations sans fil pour l'électronique, également connu sous le nom de BatMon. Cet instrument est destiné à améliorer la phase "Analyse de l'environnement radiologique". Les limitations opérationnelles et électriques rencontrées avec son prédécesseur, le RadMon, sont rapportées dans ce chapitre. Le concept d'IoT est également introduit ici en définissant ses

avantages et ses inconvénients liés à son intégration dans un accélérateur de particules. Les besoins d'un réseau IoT et les limites de RadMon ont adapté le choix de conception du nouveau système qui, à son tour, a introduit plusieurs implications dédiées à la procédure de qualification qui sont discutées dans ce chapitre. La deuxième partie du chapitre présente la qualification et la validation de la nouvelle plateforme au niveau du système. De nouvelles étapes de validation exécutables sans rayonnement, qui enrichissent la procédure de qualfication du CERN existante, sont introduites et peuvent aider le développeur de l'équipement à définir certaines conditions d'essai pour la partie qualification avec rayonnement. Une méthodologie alternative de test du système sous rayonnement est alors proposée pour être utilisée lorsque le centre d'irradiation en champs mixte du CERN (CERN High energy Accelerator Mixed field (CHARM) en anglais), installation utilisée pour cette phase, n'est pas disponible. Cette solution permet d'éviter de retarder le déploiement. Sa validité est démontrée par son application directe à la plateforme IoT sans fil. Les résultats de l'application de la méthodologie et des exemples pratiques d'essais au niveau du système sont fournis. Enfin, le processus de qualification décrit démontre également la nature non problématique de deux des trois contraintes pour un réseau IoT appliqué au contexte de l'accélérateur.

Dans le chapitre 4, une étude sur la sélection des flux de particules pour les tests et son impact sur l'observabilité des défaillances à faible probabilité d'occurence est présentée à travers le processus de qualification que le BatMon a suivi. Des techniques logicielles pour identifier et réduire ou prévenir l'effet de défaillances (Software Mitigation Schemes ou SMSs en anglais) sur des systèmes IoT sont discutés. Leur efficacité est démontrée à travers des données expérimentales obtenues par application au BatMon. Les résultats obtenus démontrent que les dispositifs IoT peuvent être une solution envisageable pour les systèmes critiques hautement distribuées et le controle à distance dans les futurs accélérateur. La quantification de la probabilité d'occurrence de ces défaillances à travers les SMS développés nous permet de quantifier le lien entre le flux sélectionné et l'observabilité des défaillances à travers les métriques définies dans ce chapitre. Les résultats ont conduit au développement d'un processus de sélection des flux permettant de détecter ce type de défaillance. Ce processus permet d'accroître la confiance dans les résultats, mais il entraîne également des coûts de qualification globaux plus élevés. Dans ce chapitre, son intégration potentielle dans la procédure de qualfication du CERN est proposée et analysée

Le chapitre 5 présente la dernière partie du processus de validation de la plateforme avant sa mise en opération. Une étude de la solution matérielle permettant de préserver

les mesures de la plateforme avec une plus grande fiabilité est réalisée. Les capteurs sélectionnés et donc les performances de la plateforme en matière de mesure des radiations sont ensuite validés par une comparaison des résultats expérimentaux obtenus à l'aide du RadMon en qualité d'instrument de mesure référence. En particulier, une analyse du nouveau capteur SRAM utilisé, de son impact sur les neutrons intermédiaires (0,1 - 10 $MeV$), et de la variabilité intra-lot sur les mesures finales accompagnent le processus de validation. Ensuite, l'infrastructure du réseau du CERN pour les systèmes IoT est présenté et l'intégration de la plateforme dans ce réseau est décrite. Des exemples opérationnels dans le LHC sont fournis démontrant les améliorations dans le contexte de la mesure des radiations introduites par la nouvelle plateforme sans fil. Enfin, la dernière partie du chapitre est dédiée à l'utilisation de la base de la plateforme sans fil pour la mesure d'autres grandeurs que les niveaux de radiations en opération (telle que l'humidité et la température).

# Contents

# Acronyms List

**ADC** Analog-to-Digital Converter

**ALU** Arithmetic Logic Unit

**ATS** AcceleraTor Sector

**B4C** Boron Carbide

**BJT** Bipolar Junction Transistor

**BLM** Beam Loss Monitor

**CERN** European Organization for Nuclear Research

**CHARM** CERN High energy Accelerator Mixed field

**CMOS** Complementary Metal-Oxide Semiconductor

**CNT** Counter

**COTS** Commercial Off The Shelf

**CRAM** Configuration RAM

**CTR** Current Transfer Ratio

**CU** LoRa Confirmed Uplink

**DAC** Digital-to-Analog Converter

**DC** Duty Cycle

**DDD** Displacement Damage Dose

**DDEF** Displacement Damage Enhancement Factor

**DD** Displacement Damage

**DM** Design Margin

**DOFRS** Distributed Optical Fibre for Radiation Sensing

**DS** Dispersion Suppressor

**DUT** Device Under Test

**DWC** Duplication With Comparison

**ECC** Error Correcting Code

**EDAC** Error Detection and Correction

**ELDRS** Enhanced Low Dose Rate Sensitivity

**ESA** European Space Agency

**Ext WTD** External Watchdog

**FCC** Future Circular Collider

**FCNT** LoRa Frame Counter

**FEC** Front-End Computer

**FF** Flip-Flop

**FGDOS** Floating Gate Dosimeters

**FPGA** Field Programmable Gate Array

**FSM** Finite State Machine

**FWCT** Full Working Cycle Time

**FWC** Full Working Cycle

**GPIO** General Purpose Input/Output

**HEH** High Energy Hadron

**HL-LHC** High-Luminosity Large Hadron Collider

**HPP** Homogeneous Poisson Process

**IEL** Ionizing Energy Loss

**IO** Inputs and Outputs

**IP** Interaction Point

**IR** Insertion Region

**IT** Inner Triplet

**IoT** Internet of Things

**JPL** Jet Propulsion Laboratory

**LDO** Low-Dropout Regulator

**LET** Linear Energy Transfer

**LHC** Large Hadron Collider

**LPWAN** Low Power Wide Area Network

**LSS** Long Straight Sections

**LS** Long Shutdown

**MAC** Media Access Control

**MCU** Microcontroller

**MF** Main Failure

**MIEP** Most Important Electrical Parameter

**MOS** Metal-Oxide-Semiconductor

**MOTS** Modified off-the-shelf

**MQTT** Message Queuing Telemetry Transport

**MSF** Minimum SF of Interest

**MTBFO** Mean Time Before the First Observation

**NIEL** Non-Ionizing Energy Loss

**NS** Network Server

**OMERE** Outil de Modélisation de l'Environnement Radiatif Externe

**PC** Power Converter

**PF** Potential Failure

**PIF** Proton Irradiation Facility

**PKA** Primary Knock-on Atom

**PLC** Programmable Logic Controller

**PSB** Proton Synchrotron Booster

**PSI** Paul Scherrer Institute

**PS** Proton Synchrotron

**PTB** Physikalisch-Technische Bundesanstalt

**QPS** Quench Protection System

**R2E** Radiation to Electronics

**RDM** Radiation Design Margin

**RDP** Read Pointer

**RDR** Radiation Design Requirement

**RF** Radio Frequency

**RHA** Radiation Hardness Assurance

**RPL** Radio-Photo-Luminescence

**RSSI** Received Signal Strength Indicator

**RTC** Real Time Clock

**SBU** Single Bit Upset

**SEB** Single Event Burnout

**SECDED** Single-Error Correct and Double Error Detect

**SEE** Single Event Effects

**SEFI** Single Event Functional Interrupt

**SEGR** Single-Event Gate Rupture

**SEL** Single Event Latchup

**SEM** Soft Error Mitigation

**SET** Single Event Transient

**SEU** Single Event Upset

**SF** Subfailure

**SMS** Software Mitigation Scheme

**SND@LHC** Scattering and Neutrino Detector at the LHC

**SNR** Signal to Noise Ratio

**SPI** Serial Peripheral Interface

**SRAM** Static Random-Access Memory

**STMR** Selective Triple Modular Redundancy

**SW WTD** Internal Software Watchdog

**SoC** System-on-Chip

**TCL** Target Collimators Long

**TC** Timer Control

**TEF** Total Expected Fluence

**TENIS** Thermal and Epi-Thermal Neutron Irradiation Station

**TH** Temperature and Humidity

**TID** Total Ionizing Dose

**TMR** Triple Modular Redundancy

**TM** Test Method

**TRIGA** Training Research Isotopes General Atomics

**TS** Technical Stops

**Th** Thermal Neutron

**UJ** Underground Junction chamber

**UL** Underground Liaison gallerie

**UPS** Uninterruptible Power Supply

**USART** Universal Synchronous and Asynchronous Receiver-Transmitter

**WCA** Worst Case Analysis

**WRP** Write Pointer

**YETS** Year-End Technical Stop

# Introduction

The European Organization for Nuclear Research (CERN) explores the smallest building blocks of the universe, the fundamental particles, in pursuit of pushing the frontiers of human knowledge. To explore the universe's origin, two particle beams are boosted in energy through a complex chain of accelerators, also known as "injector chains". The Large Hadron Collider (LHC) is the final and most advanced machine in this chain, where the two beams are accelerated up to 6.8 $TeV$. When achieved the desired energy, they are brought to the collision at close to the speed of light in one of four purpose-built detectors along the accelerator (ATLAS, ALICE, CMS, and LHCb). The particle shower produced by this interaction enables particle physicists to investigate the fundamental particles.

In particle physics, the particles of interest in interactions are exceptionally rare, requiring a high number of interactions to generate them. To improve the LHC operation there are two possible ways: by increasing the instantaneous luminosity (Higher beam intensity) or by improving the availability of the accelerator. While the first can be obtained through an upgrade of the machine, as it will be for the High-Luminosity Large Hadron Collider (HL-LHC), the second depends on the different control equipment of the accelerator chain.

Among these systems, the electronic ones used for control in the AcceleraTor Sector (ATS) must have high availability during operations in order to allow the organization to achieve its goals. However, achieving high levels of availability within such a complex machine can be difficult due to the radiation environment generated by its operation. This complexity is further compounded when cost constraints necessitate the use of Commercial off-the-shelf (COTS) systems within the accelerator sector. Such systems, which are not designed to

operate in a radiation environment, may be more sensitive to radiation to electronic effects and may stop operating due to a radiation-induced failure.

Increasing the accelerator availability and the delivered luminosity reducing the number of radiation-induced failures, has been the main mandate of the Radiation to Electronics (R2E) group. Starting at CERN in 2012, its main objective consisted of quantifying the danger of radiation-induced failures and introducing mitigation to minimize the risk of failures to less than one per week, not only for nominal beams but also for any future scenarios that may arise. These measures consisted of moving the systems to safer areas, increasing the protective shielding, and, replacing the malfunctioning systems with more robust ones. The upcoming upgrade of the LHC in 2029, known as HL-LHC, will deliver an annual luminosity that is five times greater than that of the current LHC. This will result in a substantial increase in radiation levels generated through machine operation. The relocation and shielding of equipment may not be enough and for some equipment as the Quench Protection Systems, it would not be possible. To ensure the reliability and availability requirements for HL-LHC and be prepared for any potential scenarios, CERN ATS has created its own Radiation Hardness Assurance (RHA) procedures for the custom boards, which are based on COTS components, to guarantee effective performance within the accelerator. To account for the unique particle spectrum environment at LHC, this procedure has undergone continuous improvement and extension over the years with testing methodologies to attain the most realistic results achievable. The procedure comprises multiple phases that are now mandatory for all systems designed for the accelerator sector. The successful completion of each phase is necessary to gain approval for installing the new system at the LHC. The main aim of this doctoral work is to investigate how to improve CERN's current RHA procedure to meet the demanding availability and reliability requirements of HL-LHC. To achieve this goal, several activities need to be carried out: a) study the current state of the art of CERN RHA and detect the different weak points of the current approach b) development of test methodologies at the system-level adapted to CERN's needs and c) demonstrate the validity of such new approaches.

The last of these activities requires a case study for its implementation. An innovative Wireless Internet of Things (IoT) Radiation Monitoring system for electronics, developed during this thesis work, is used for this purpose. As the first example of an IoT application at CERN, the experimental results obtained during the qualification of this application allowed us to investigate the advantages (e.g. infrastructure cost reduction in longer accelerators

such as the Future Circular Collider (FCC)) and challenges associated with the integration of an IoT network within a particle accelerator.

This application represents the first instance of wireless radiation monitoring for electronics and its development will also bring numerous advantages in its application context, implicitly improving part of the RHA procedure. In fact, radiation monitoring is a fundamental pillar of the entire RHA process and influences all subsequent steps of the procedure. These estimates are used to define the radiation requirements of the system. In addition, radiation design margins are applied to account for their uncertainty, increasing the requirements to be met. In the context of a more demanding environment than the LHC, i.e. HL-LHC, where the radiation requirements will be even higher, standardizing the test procedure at the system level is not sufficient to increase the reliability of the equipment and have a feasible RHA procedure. The uncertainty of the radiation estimation provided in the different areas must be reduced too in order to be successful. This will directly impact the following stages of the process, enabling the radiation requirements that drive the design margins to be less stringent, but more realistic and achievable. In addition to presenting this cutting-edge application and its qualification, a further objective of this doctoral work is to demonstrate its operational benefits applied in the context of radiation monitoring through real examples of its operation in the LHC. The structure of the manuscript is given below to provide a complete overview of the entire work.

Chapter 1 provides an overview of the different effects of radiation on electronics. To better understand and define these effects, the mechanisms by which particles interact with matter are investigated. In the second part of the chapter, the three effects of Radiation on Electronics are introduced.

The CERN accelerator complex, working principle, and the expected environment in the most significant areas are given in Chapter 2. This chapter introduces the concept of accelerator availability and the impact of radiation-induced failures in the electronic system on accelerator performances. The RHA is introduced by a comprehensive overview of its structure and an in-depth analysis of its most important phases as regards manuscript development. Particular attention is given to the 'Radiation Environment Analysis' and 'System-Level Testing' phases, which are identified as the weakest part of the process. The in-depth analysis of the two phases highlights their weaknesses but also makes it possible to identify margins for improvement in the process. The system-level testing phase, unlike its component-level counterpart, lacks standardization in the CERN RHA process and does

not ensure the same reliable results. The introduction of methodologies and guidelines has the potential to improve this phase and increase the reliability provided by the application of the RHA procedure. In parallel, improving the instruments used for radiation monitoring inside the accelerator by increasing their deployability, is crucial in reducing the uncertainty of the estimation provided by the 'Radiation Environment Analysis' phase. This, in turn, is essential to reduce the radiation requirements for the designs and make them more realistic and achievable. As highlighted in this chapter, this may be the only feasible solution to meet the more demanding environmental requirements of the HL-LHC, which may be difficult to achieve with a COTS system to which the same significant safety factors employed for the LHC are applied. The definition of an electronic solution to improve these stages and the challenges of such development, are examined in the last part of the chapter and motivates the work presented in the following chapters.

Chapter 3 introduces the case study instrument used in this thesis, aimed at enhancing the 'Radiation Environment Analysis' phase, i.e. the Wireless IoT Radiation Monitoring System for Electronics, also known as BatMon. The operational and electrical limitations experienced with its predecessor, the RadMon instrument, are reported in this chapter. The concept of IoT is also introduced here by defining its advantages and criticalities related to its integration within a particle accelerator. The requirements for an IoT network and limitations of RadMon tailored the design choice of the new system which in turn introduced several dedicated RHA implications that are discussed in this Chapter. In its second part, the system-level qualification and validation of the new platform are presented. New validation steps executable without radiation, that enrich the existing RHA procedure, are introduced that may help the equipment developer to define some testing conditions for the qualification part with radiation. An alternative system-level test methodology under radiation is then provided for use when the CERN High energy Accelerator Mixed field (CHARM), facility used to address this phase, is not available. This solution avoids the need to delay deployment. Its validity is demonstrated through its direct application to the wireless IoT platform. Results from the application of the methodology and practical examples of system-level testing are provided. Finally, the described qualification process also demonstrates the non-problematic nature of two of the three constraints for an IoT network applied to the accelerator context.

In Chapter 4, an investigation on testing flux selection and failure observability is provided through the process that the Wireless IoT went through to identify failure with a low

probability of occurrence. Software Mitigation Schemes (SMSs) for IoT devices designed to identify these failures and mitigate them are provided. Their effectiveness is demonstrated through experimental data obtained by their direct application on the Wireless IoT. The enhanced results in terms of application availability prove that IoT devices may be a feasible solution for critical high-distribution systems and remote controlling in the future HL-LHC or even in longer accelerator designs such as FCC. The quantification of the probability of the occurrence of these failures through the SMSs developed allows to quantify the link between flux selected and failure observability through metrics defined within this chapter. The findings have led to the development of a flux selection process that detects this type of failure. Although it increases confidence in the results, it also leads to higher overall qualification costs. Within this chapter, its potential integration within the CERN RHA procedure is proposed and analyzed

Chapter 5 presents the last part of the validation process the cutting-edge platform went through before becoming operational. An investigation of the hardware solution to store the platform's measurements with higher reliability is carried out. The selected sensors and thus platform's radiation monitoring performance are then validated through a comparison of experimental data obtained using the RadMon instrument as a reference. In particular, an analysis of the new SRAM sensor used, the impact of intermediate neutrons (0.1 - 10 $MeV$), and intra-batch variability on final measurements accompany the validation process. Next, the CERN Network for IoT systems is presented and the integration of the platform within it, is described. Operational examples in the LHC are provided through which the improvements in the context of radiation monitoring introduced by the new wireless platform are demonstrated. Finally, the last part of the chapter is dedicated to a discussion of the possible operational extension of the Wireless IoT Main-board for applications different from radiation monitoring. Their feasibility is demonstrated through system-level tests under radiation.

# CHAPTER 1

# Basic Radiation Effects on Electronic Components

To gain insights into the behaviour of electronic systems exposed to radiation and to improve qualification and characterization procedures, it is essential to understand the basic effects that govern their response.

Depending on their type, particles may interact with matter in various ways, as outlined in Section 1.1. The impinging particles release energy at the interaction until they are completely stopped or exit the material. Two types of energy loss contribution can be identified that lead the particle to stop: ionizing loss and non-ionizing loss. Ionizing loss occurs when the particles interact with the target material and ionize the atoms by releasing electrons from them. Non-ionizing loss, on the other hand, results from particles displacing the nucleus from its original position within the lattice, creating defects. In electronic components, both energy loss contributions are associated with radiation to electronic effects.

Understanding these effects is critical not only to understand the degradation of complex systems under radiation but also to develop test methodologies that encompass each effect, ensuring that none is neglected. Therefore, this section of the manuscript focuses on defining these effects and the particles responsible for their occurrence. Furthermore, for each effect, the metrics used to quantify the damage to electronic components will be defined.

## 1.1 Particles Interactions with Matters

When particles interact with materials, two possible interactions can occur. The first effect is called ionizing radiation which occurs when particles interact with the target material and ionize atoms by detaching electrons from them. The second is called non-ionizing radiation, which occurs when particles interacting with the lattice of the target material displace the nucleus from its original lattice position and create defects in the material. To understand those effects, it is crucial to understand how particles can interact with matter. Photons, neutrons, and charged particles will have different behavior when passing within the matter. In Fig. 1.1, the different interactions for the different particle types are depicted.

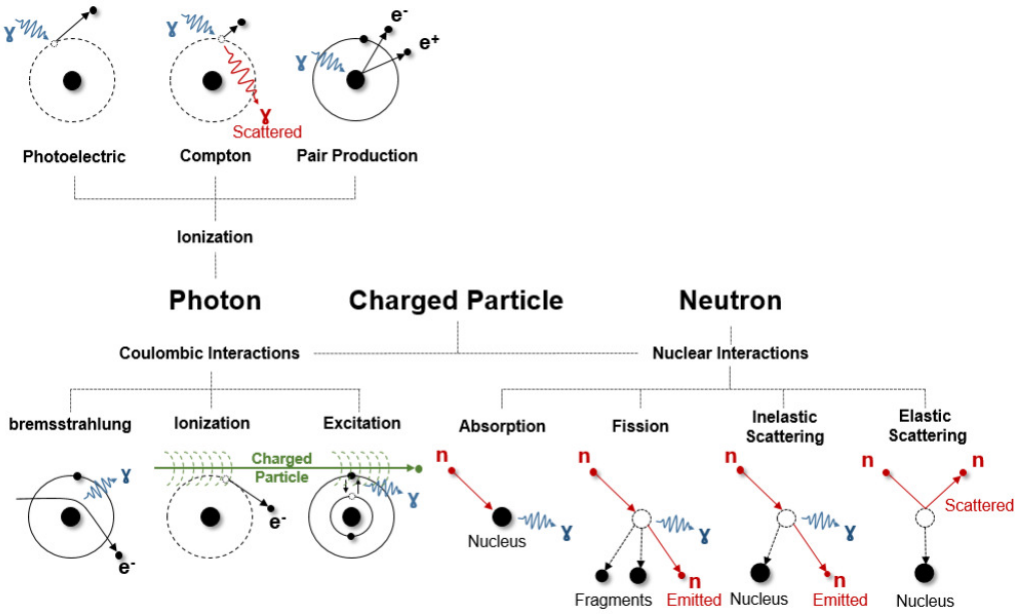


Figure 1.1: Particle Interactions Summary [1].

The absence of electrical charge makes elastic collision not possible for photons. However, they can ionize atoms through the photoelectric (In Si Photons with energy below 0.1 $MeV$), Compton (In Si with energy above 0.1 $MeV$), and pair production effect (In Si with energy higher than 10 $MeV$) as it is visible in Fig. 1.2.

As visible in Fig. 1.1, the photoelectric effect is the process through which the photon interacting with an orbital electron whose binding energy is close to that of the incident photon can release the electron yielding all its energy. The electron released will have an energy equal to the difference between the photon's energy and its binding energy. In the case of ionization due to Compton interaction, the photon has an energy greater than the one of binding and gets scattered after the interaction while an electron is released. Finally,

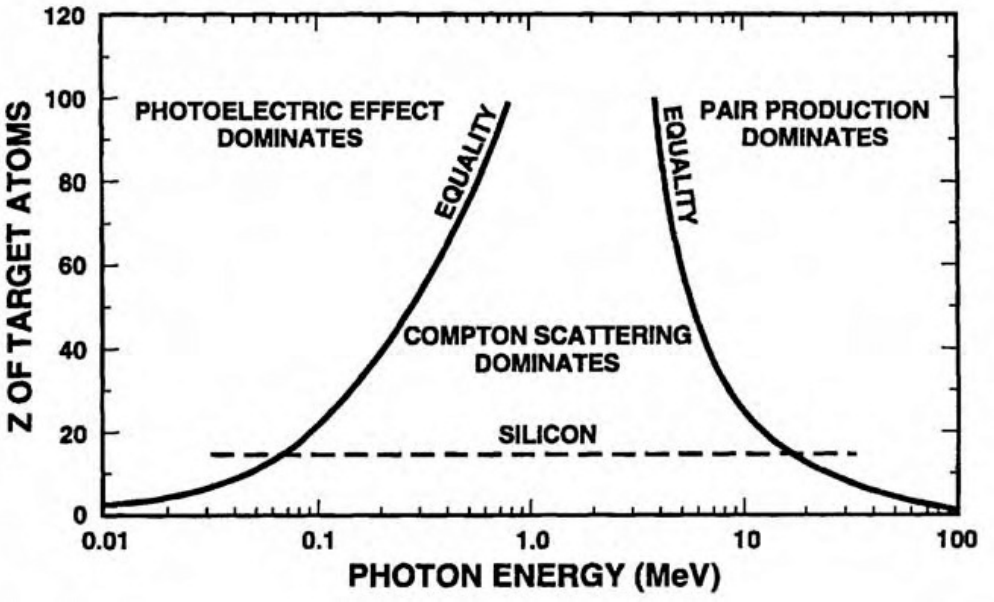


Figure 1.2: The graph illustrates the dominant regions in which the three primary forms of interaction of photons with matter prevail. The curves indicate the points at which the cross-sections of the two primary processes involved (photoelectric effect and Compton scattering on the left curve, and Compton scattering and pair production on the right curve) become equal [2, 3].

if the photon passes very close to the nucleus of the atom and its energy is high enough to create an electron-positron pair which will ionize the matter, we talk about Pair production.

Charged particles (Pions ($\pi\mp$), Protons ($p\mp$), Kaons ($K\mp$), Muons ($\mu\mp$), electrons ($e\mp$), etc.) have two ways of interacting with matter: through Coulombic interaction and nuclear interaction. Neutrons, on the other hand, can only interact with matter through nuclear interaction. However, Coulombic interactions are predominant for charged particles and only a small fraction of their energy is used for nuclear interaction [4].

Three types of Coulombic interactions are known: Bremsstrahlung, Ionization, and Excitation. The Bremsstrahlung effect is generated when the charged particle is deflected by the strong electrical force exerted by the nucleus, and the kinetic energy loss is released in a Photon emission. During Ionization the charged particles passing close to an orbital electron have enough energy to release it due to the strong electrical force exerted on it. In this case, the excited electrons have enough kinetic energy to travel into the matter and ionize other atoms. This mechanism occurs in two steps, primary electron excitation, and secondary ionization, and is called indirect ionization. The excited electrons are called delta-rays or primary knock-on electrons. On the other hand, if the hitting particles do not have enough energy to release the electron but can still allow the electron to move from a lower energetic

orbit to a higher one when the electron goes back to its initial state, a photon is released. This ionization process is called Excitation. The last two mentioned interactions are typical of Heavily charged particles (i.e. $\pi\mp$, $p^+$, $K\mp$, $\mu\mp$) while the Bremsstrahlung effect is mainly due to Light Charged particles (Electrons).

As mentioned above, charged particle interactions are not only Coulombic but can also be nuclear. It is possible to distinguish four types of nuclear interaction: neutron absorption (Neutrons with an energy of about 25 $meV$), elastic scattering (Particles with energy below 1 $MeV$), inelastic scattering (Particles with energy between few to tens $MeV$), fission (Particles with energy above 20 $MeV$). In Neutron Absorption, the incident neutron hits the nucleus leaving it in an excited state. To leave this excited state, a photon is released. In Elastic scattering, the particle when hitting a nucleus is scattered and the energy lost in the collision is transferred to the nucleus. The latter gets in motion or is scattered too if it was already in motion. Differently from the previous type of interaction, in inelastic scattering the incident particle is absorbed by the stricken nucleus. The latter releases a lower-energy neutron which leaves the nucleus in an excited state. To leave this state, one or more photons are emitted. Finally, there is fission when after absorbing a particle, the nucleus splits into fission fragments (smaller fragments). In this reaction, one or more neutrons and photons are released.

These interactions can not only be triggered by the incident particles but also by the secondary particles generated by previous interactions. A photon emitted in the process of excitation produced by the incident charged particles can trigger a photoelectric effect releasing new charged particles (Electrons). However, primary interactions are predominant since incident particles have higher energy concerning secondary particles. These incident particles release energy at the interaction until they are completely stopped. The stopping power can be defined for any particle as a function of the ionizing and non-ionizing loss normalized to the material density, as it is defined in equation (1.1).

$$S = \frac{1}{\rho} \cdot \left( \frac{dE}{dx}\Big|_{IEL} + \frac{dE}{dx}\Big|_{NIEL} \right) \tag{1.1}$$

With:

- $S$: stopping Power $[MeV \cdot cm^2 \cdot mg^{-1}]$
- $\rho$: mass density $[kg \cdot cm^{-3}]$
- $NIEL$: non-Ionizing Energy Loss $[MeV \cdot cm^{-1}]$
- $IEL$: ionizing Energy Loss $[MeV \cdot cm^{-1}]$

While charged particles mainly stop due to IEL and thus, are the main ones responsible for Ionizing effects, nuclear interactions are predominant for neutrons which are the principal responsible for non-ionizing effects. In the electronic component, IEL and NIEL are associated with three different radiation-to-electronic effects: Total Ionizing Dose (TID), Single Event Effects (SEE), and Displacement Damage (DD). While IEL is responsible for TID and SEE, the DD is associated with the NIEL which is the quantity that describes the rate of energy loss due to atomic displacements as a particle traverses a material. The following paragraphs will elaborate on these concepts.

## 1.2 Total Ionizing Dose Effect

As described in the previous section, while photons may be absorbed in a single process (except in Compton interaction), charged particles lose energy gradually within the material until they completely stop. The rate of energy loss is not constant along the particle's path: in fact, 2 mechanisms feed off each other until the particle stops. The probability of interaction between a penetrating particle and electrons in a medium depends on the speed of the particle: slower particles have a higher probability of interaction. Furthermore, as the particle loses energy during its journey through the material, its speed decreases. Consequently, the rate of energy loss increases along the particle's trajectory until it reaches a peak and immediately goes to zero. This peak is called the Bragg Peak. Linear Energy Transfer (LET) described in equation (1.2), is a parameter used to describe the amount of energy deposited by a charged particle in a material, per unit distance traveled. It is typically measured in units of $MeV \cdot cm^2 \cdot mg^{-1}$, but the appropriate SI unit is $J \cdot m^2 \cdot kg^{-1}$.

$$LET = \frac{dE}{dx}\Big|_{IEL} \tag{1.2}$$

The Berthe-Bloch formula [5], defined in (1.3), makes it possible to calculate the LET of heavy charged particles in silicon where, due to the thickness used in microelectronics, it is almost constant.

$$-\frac{dE}{dx} = \rho \frac{2\pi N_A r_e^2 m_e c^2 Z}{A} \frac{z^2}{\beta^2} \left[ \ln \left( \frac{2m_e v^2 \gamma^2 W_{max}}{I^2} \right) - 2\beta^2 - \delta - \frac{2C}{Z} \right] + \Delta \frac{dE}{dx} \tag{1.3}$$

With:

- $\rho$: density of the material $[kg \cdot m^{-3}]$
- $2\pi N_A r_e^2 m_e c^2$: 0.1535 $[MeV \cdot cm^2 \cdot g^{-1}]$
- $N_A$: Avogadro's number, in units of $mol^{-1}$.
- $r_e$: electron radius ($2.817 \cdot 10^{13}\ cm$]
- $m_e$: mass of the electron (511 $keV$).
- $Z$: atomic number of the material.
- $A$: atomic weight of the material.
- $z$: charge of the incident particle.
- $\beta$: velocity of the incident charged particle in units of the speed of light.
- $\gamma$: $\frac{1}{\sqrt{1-\beta^2}}$ Lorentz Factor
- $\delta$: density correction
- $C$: shell correction
- $I$: mean excitation energy of the material, in units of $eV$.
- $W_{max}$: maximum transferable energy
- $\Delta \frac{dE}{dx}$: Bremsstrahlung from atomic electrons

Where:

$$W_{max} = \frac{2m_e (c\beta\gamma)^2}{1 + \frac{2m_e}{M}\sqrt{1 + (\beta\gamma)^2} + \left(\frac{m_e}{M}\right)^2} \tag{1.4}$$

With M the mass of the incident particle. This equation is slightly different for positrons and electrons, to account for possible large deviations due to a collision.

The IEL contribution for the stopping power is depicted in Fig. 1.3. As it is visible, the proton IEL stopping power contribution is always higher than the one of electrons, except at high energy. In fact, at about $10^2\ MeV$, electrons have a higher LET than protons, due to the Bremsstrahlung effect. Heavy charged particles at higher energy respect to the one depicted, begin to exhibit an increase in stopping power due to radiative effects.

As described in Section 1.1, since photons are mainly absorbed in a single process, they cannot be described through the LET. The mass energy transfer coefficient, called $\frac{\mu_{en}}{\rho}$, is used to describe the interactions of photons with matter. It represents the fraction of the energy lost by a photon per unit path length in the material due to elastic (Compton) scattering and inelastic (photoelectric) absorption processes. It is defined in equation (1.5).

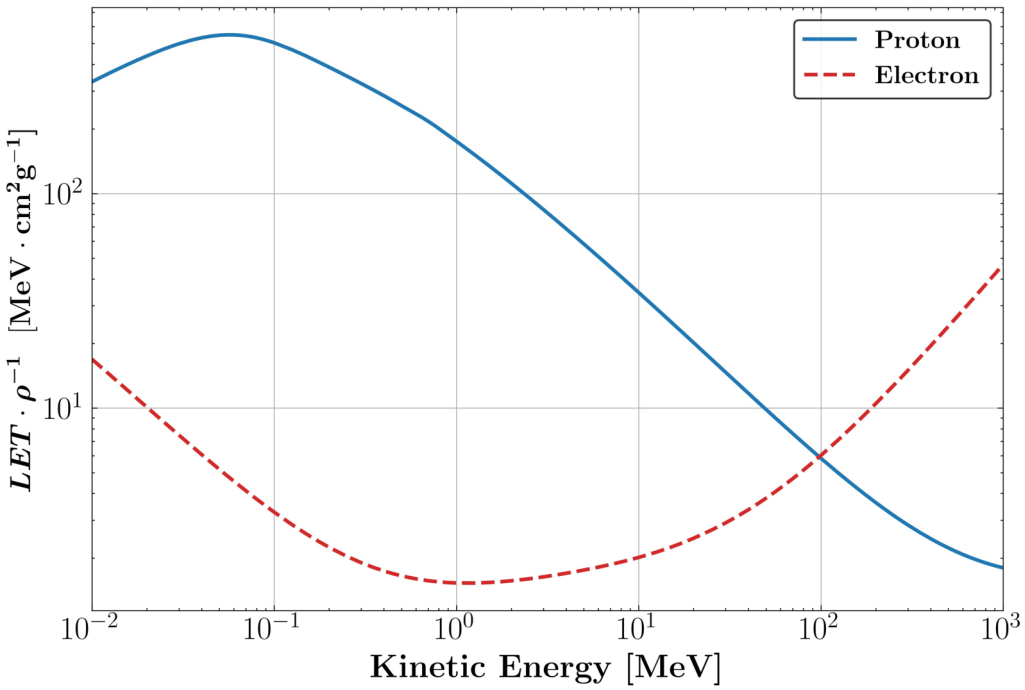


Figure 1.3: Stopping Power (IEL Contribution) for Protons and Electrons with energy from 10 $keV$ to 1 $GeV$ in Silicon. Data from [6, 7].

$$\frac{\mu_{en}}{\rho} = \frac{\mu}{\rho}(1 - R(E)) \tag{1.5}$$

With:

- $\frac{\mu_{en}}{\rho}$: mass-energy transfer coefficient [$cm^{-2} \cdot g^{-1}$]
- $\frac{\mu}{\rho}$: mass interaction coefficient [$cm^{-2} \cdot g^{-1}$]
- 1 - R(E): fraction of the energy transferred from the photons to the matters considering the three possible interactions

It is possible, to obtain the energy deposition per mass unit by multiplying the mass energy transfer coefficient with the respective photon energies which is depicted in Fig. 1.4.

Once defined the LET and the mass energy transfer coefficient, it is possible to define the TID deposited by charged particles and photons. The TID is the magnitude used in electronics to quantify the cumulative damage induced by ionizing radiation. The unit of measurement defined by the International System of Units (SI) is the Gray ($Gy$), which corresponds to one joule of energy absorbed by a kilogram of matter. However, the TID can be also measured in rad which is mainly used by the space community. One $Gy$ corresponds to 100 $rad$. For a charged particle, the TID deposited by a certain particle fluence can be computed as defined in equation (1.6).

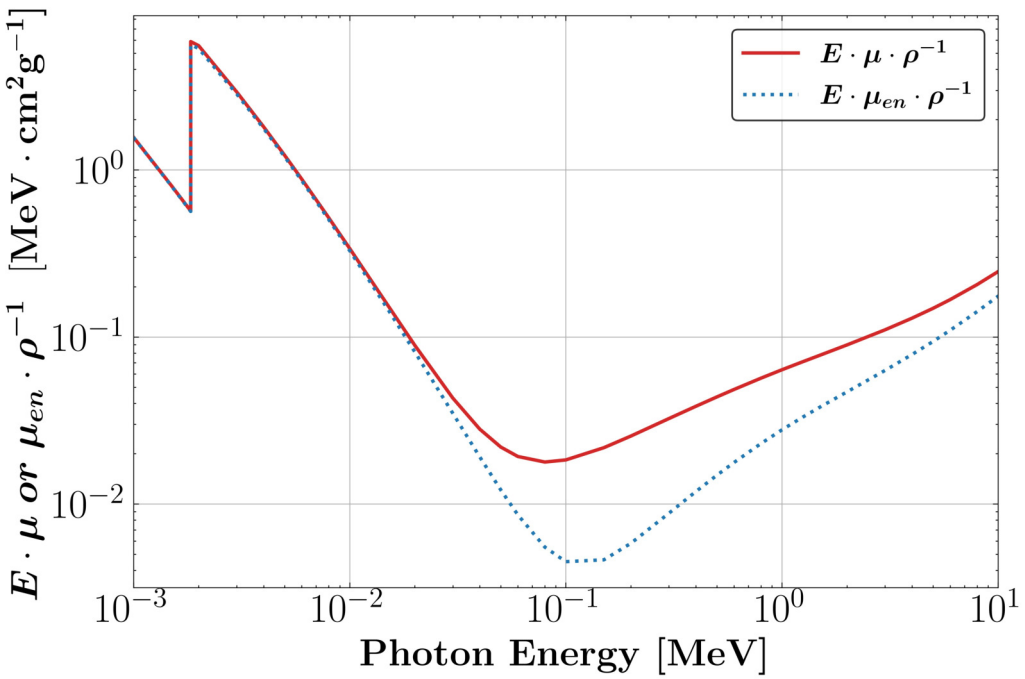


Figure 1.4: Energy deposited by a photon in Silicon material (Z = 14) as function of its energy. Data from [8].

$$TID = K_{Gy} \frac{LET(E)}{\rho} \Phi(E) \tag{1.6}$$

With:

- $K_{Gy}$: unit conversion parameter 1.6 $\cdot 10^{-10}$ $Gy \cdot g \cdot MeV^{-1}$
- $\Phi(E)$: the particle fluence $[cm^2]$

Using this formula, it is possible to evaluate the TID deposited by a proton or an electron in the material as a function of the energy. In Fig. 1.5 the TID deposited by these 2 particles is depicted. Based on the information provided regarding the LET of protons and electrons in silicon, it can be observed that the TID resulting from electron interactions is higher compared to that of protons when the energy of the particle is approximately in the order of $10^2$ $MeV$.

Considering a mixed-field environment such as the LHC or Space one, made of a variety of charged particles with different energies and fluence, the TID deposited on the material is the sum of the different contributions produced by each particle according to their LET and Fluence as shown in equation (1.7).

$$TID = \sum_p \int_0^{E_{max}} K_{Gy} \cdot \frac{LET(E,p)}{\rho} \cdot \Phi(E,p) \cdot dE \tag{1.7}$$

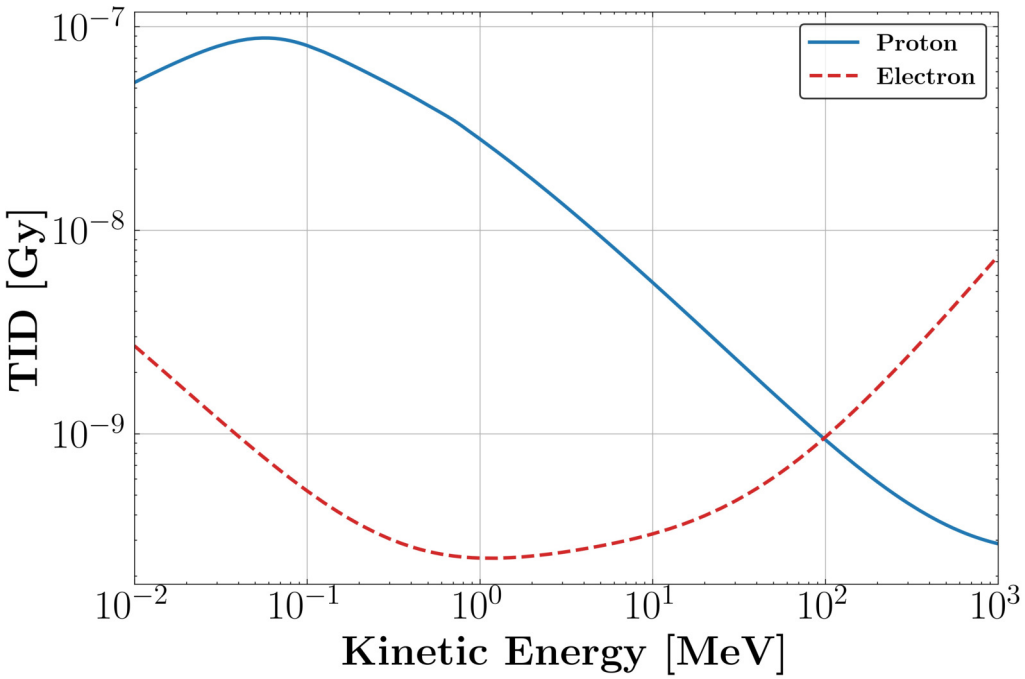


Figure 1.5: TID deposited by a single proton or an electron with energy from 10 *keV* to 1 *GeV* in Silicon.

On the other hand, the TID deposited by a photon can be computed by multiplying the mass energy transfer coefficient by its Energy, fluence, and the $K_{Gy}$ as defined in equation (1.8). The TID deposited by a photon is depicted as a function of the energies from 1 *keV* to 3 *MeV* in Fig. 1.6. As it is visible, the different interaction processes have different impacts on the TID deposited depending on the energy of the particle. For instance, at low energies, photoelectric effects are the main cause of TID.

$$TID = K_{Gy} \cdot \frac{\mu_{en}}{\rho} \cdot E \cdot \Phi(E)\Big|_{\Phi(E)=1} \tag{1.8}$$

As in the case of charged particles, by summing the different contributions it is possible to obtain the TID deposited by all photons belonging to the spectra of the radioactive environment of interest, as defined in equation (1.9).

$$TID = \int_0^{E_{max}} K_{Gy} \cdot \frac{\mu_{en}}{\rho} \cdot E \cdot \Phi(E) \cdot dE \tag{1.9}$$

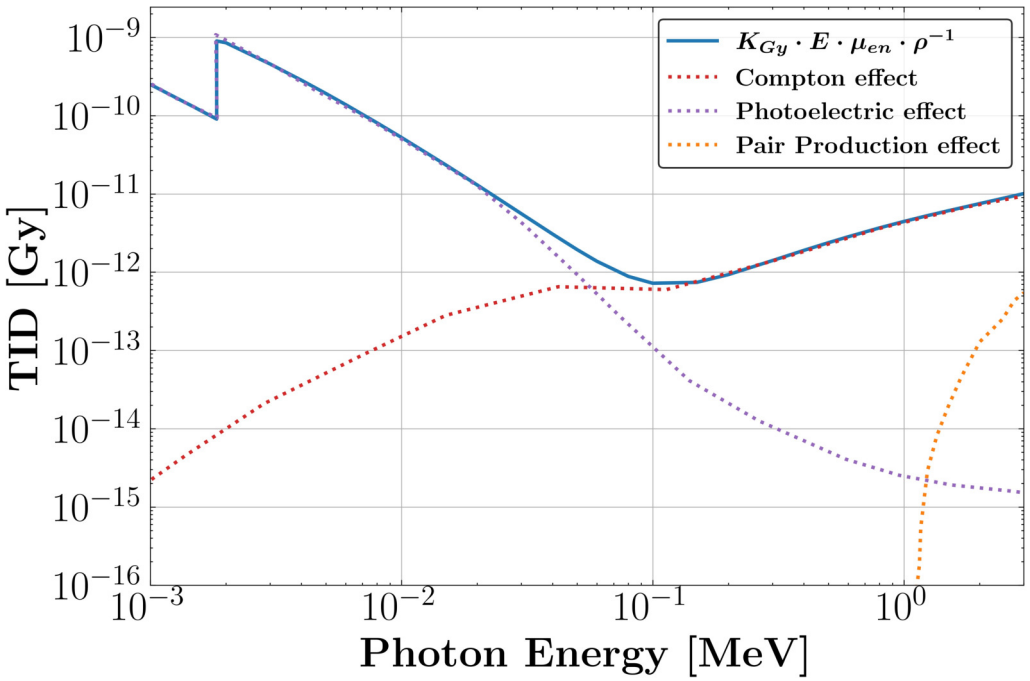


Figure 1.6: TID deposited by a single photon with different interaction process contributions in Silicon. Data of the different contributions obtained from [9].

#### Basic TID effects on semiconductors

Ionizing radiation induces long-term effects only in the oxides of integrated circuits, and the main players in this phenomenon are the charges trapped in $SiO_2$ and at $Si/SiO_2$ interface. The process that leads to the trapping of charges in semiconductor devices based on a Metal-Oxide-Semiconductor (MOS) structure can be divided into four processes. In Fig. 1.7 [10], they are represented in chronological order from left to right in the band diagram of a MOS capacitor. In this example, the gate of the structure is biased to a positive voltage, while the bulk is grounded.

The first mechanism (1) is generated by the incident particle ionizing the atoms along its path. Electron-hole pairs are generated and some of these recombine. In $SiO_2$, the energy required to create an electron-hole pair has been the subject of several studies [11] [12] [13], The energy required to create an e-h pair and the generation rate is defined in Table 1.1 [14].

Table 1.1: Ionization Energy and e-h generation rate for Si and $SiO_2$.

| **Material** | **Ionizing Energy [eV]** | **Pair Generation Rate [e-h pairs · Gy$^{-1}$ · cm$^{-3}$]** |
|---|---|---|
| Silicon (Si) | 3.6 | $4 \cdot 10^{15}$ |
| Silicon Oxide ($SiO_2$) | 18 | $8.2 \cdot 10^{14}$ |

The charges that do not recombine depend on the electric field strength along the oxide

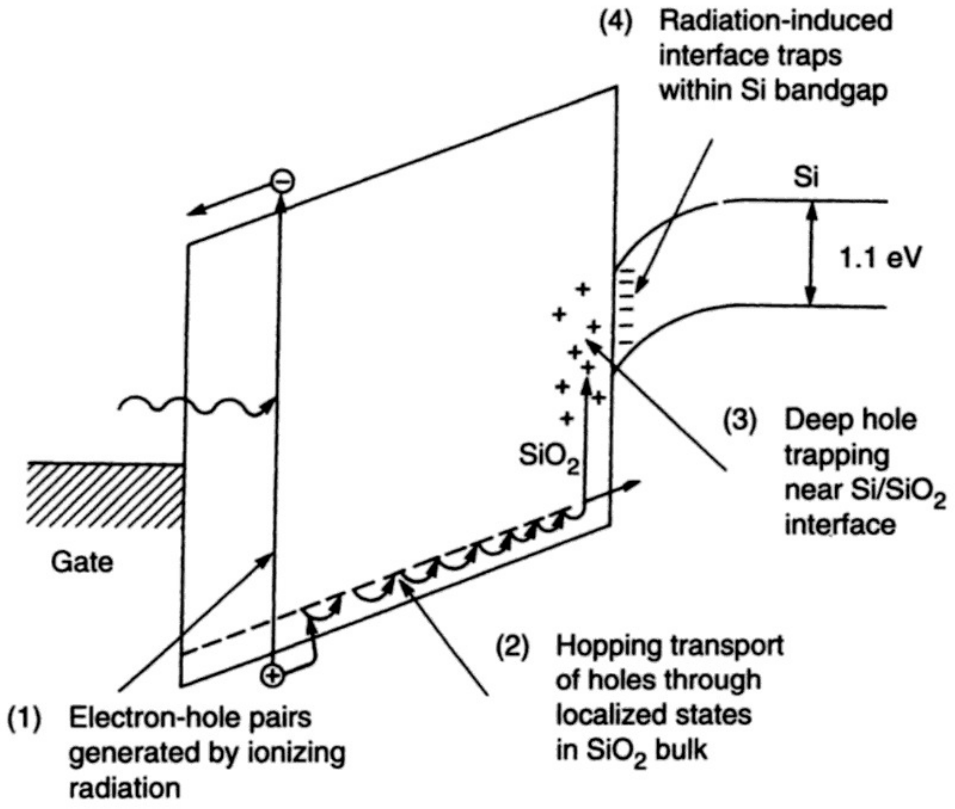


Figure 1.7: Mechanism developing in the MOS insulation layer due to ionization [10].

and the LET of the particle, as can be seen in Fig. 1.8. The non-recombined electron-hole pairs are split by the electric field: in this specific case, the electrons are pushed towards the gate while the holes move in the opposite direction. While the electrons reach the Gate quickly (mobility of 20 $cm^2 \cdot V^{-1} \cdot s^{-1}$ [15]) the holes are slower and move through a particular mechanism called hopping transport. On their way, the holes can be trapped by falling into energy wells (3). Some holes can escape the traps and reach the substrate, where the mobility of the holes is higher and they can be neutralized. Traps are divided into three types according to their position in the MOS structure: oxide traps, border traps, and interface traps. This distinction is important because, although they have an impact on MOS performance by shifting the voltage threshold, they are responsible for non-negligible side effects. For example, in addition to being responsible for the threshold shift, border traps have been shown to cause an increase in the flicker noise of MOS transistors [16]. Finally, with the increase in TID taken, another mechanism (4) to consider is the increase in interface trap density, which leads to an increase in the probability for a carrier to be trapped. The effect of TID on electrical parameters is different from one technology to another. Thresh-

old voltage shift, decrease of the carrier mobility and transconductance, noise and matching performance degradation, and leakage currents are the typical effects of CMOS degradation due to this effect while. In bipolar transistors, typical effects are leakage currents and a decrease of the current gain [17][18]. Traps will have an impact on the behavior of the component subjected to irradiation and, consequently, also on the system in which it is used. Their impact will also depend on the system or component working principle. Component and system-level qualification would allow for assessing the impact of TID degradation on its functionalities [19].

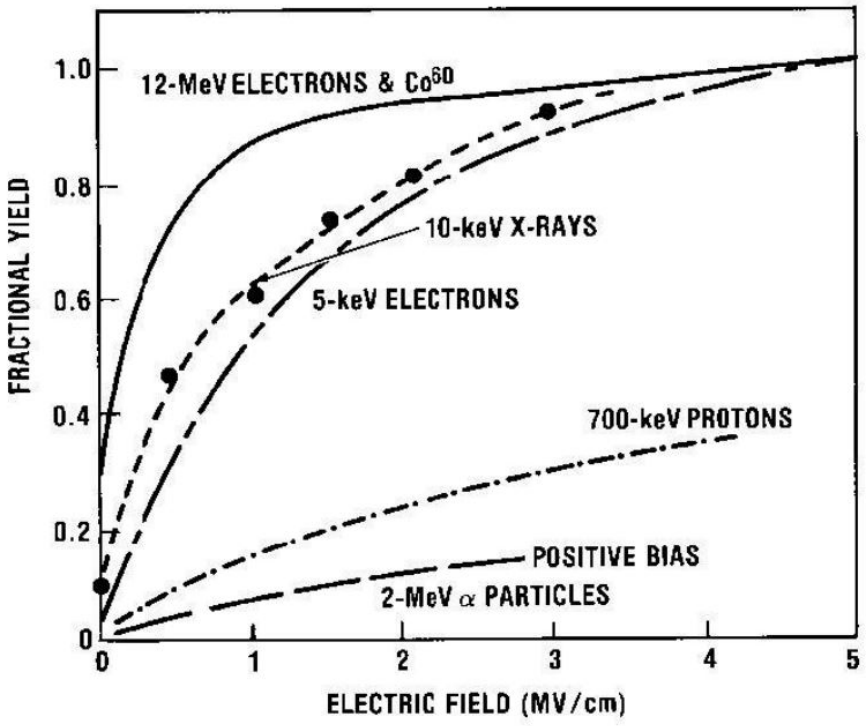


Figure 1.8: Fraction of charges not recombining as a function of the Electric field for different LET [10].

## 1.3 Single Event Effect

A Single Event Effect (SEE) can occur when ionization generated by a single particle takes place in the sensitive volume of an electronic component, resulting in a macroscopically observable effect. The type of effect produced on the device can vary depending on the semiconductor technology, topology, and function, leading to the occurrence of different types of SEEs. The first categorization of SEE can be done on their criticality: non-destructive (Soft) and destructive (Hard). [20]

- Non-Destructive or Soft Errors: in this category are SEE's that do not destroy the device upon their appearance. The capacitance and voltage levels of the logic circuits play a crucial role in the occurrence of soft errors. When these parameters have higher values, the probability of generating soft errors decreases. For example, in a Field Programmable Gate Array (FPGA), the critical charge depends on the specific node under consideration: as the capacity of the internal nodes of Static Random Access Memory (SRAM) is lower than that of the Flip Flops (FFs), less charge is required to change the stored value. Fig. 1.9, provides a visual representation of the basic mechanism behind soft error generation [21]. When charged particles pass through the device material, they produce electron-hole pairs (a). Reverse-biased p-n junctions are generally the areas most vulnerable to these effects. The high electric field, along the depletion region of the reversely polarised junction, collects through the drift process the particle-induced charge to the nearby node, where a current/voltage transient is created. Due to the conductive nature of the charged track and the charge separation by the depletion region, the charge generated along the particle path can locally disrupt the electric field of the junction. This local perturbation extends the electric field of the junction beyond the junction itself and deep into the substrate (b). As a result, the collection of charges in the junction increases, extending the range of the electric field. The charges deposited at some distance from the starting junction can be effectively collected due to the efficient drift process. This phenomenon contributes significantly to the increased charge collection in the junction. The drift process is followed by a diffusion process as visible in Fig. 1.9 (c).

  Three main types of soft errors can be distinguished:

  - Single Event Transient (SET): is a current or voltage spike generated by the impact of particles on a circuit [23]. It can manifest itself as a glitch in the circuit or can be caught in the Flip Flop (FF) or other memory elements, potentially leading to a functional error in device operation. It is worth noting that not all SETs are harmful to the device, as they are transient. However, the higher the clock speed of the digital circuit, the greater the probability of the event being captured [24]. Since SET captures occur asynchronously, they cannot be predicted through static timing analysis.
  - Single Event Upset (SEU): the SEU is a soft error caused by a transient signal

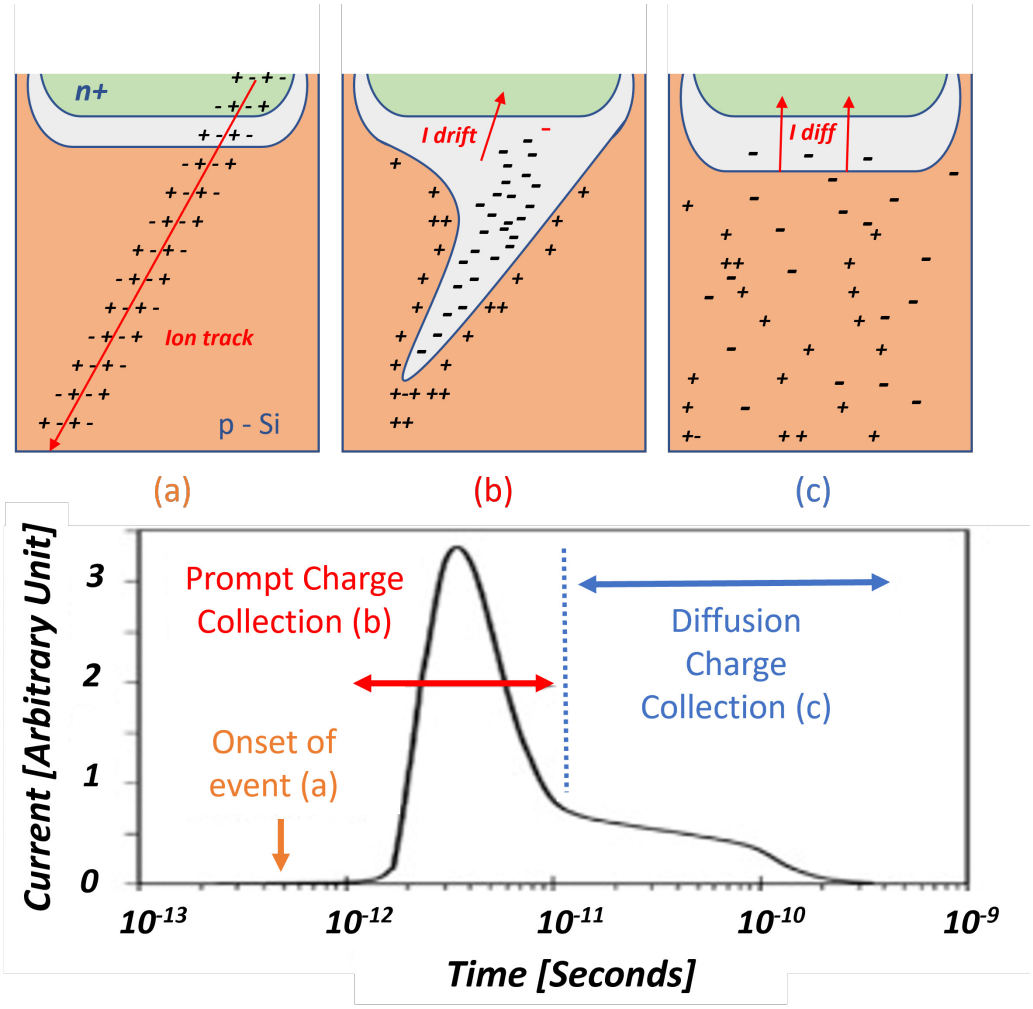


Figure 1.9: A reverse-biased junction in which are depicted the charge generation and collection phases. The current pulse resulting from the passage of a high-energy ion is also depicted during each phase. Figure adapted from [22].

induced by the strike of a single energy particle whose deposited charge is greater than the critical one required to cause a change of state of a memory cell, register, latch or FF. The most well-known example of an upset is the one occurring in Complementary Metal-Oxide Semiconductor (CMOS) technology SRAM. When an energetic particle strikes a sensitive location in this type of SRAM, for example, the reverse biased drain junction of the MOS in the OFF state, the charge collected by the junction results in a transient current flowing in the transistor hit. Fig. 1.10 depicts a graphical example of the different steps following the SEU event which leads to a change of state in the memory element.

The current flowing through the activated MOSFET, discharges the input capacitance of the opposite CMOS structure, causing its P-MOS to be switched on. Consequently, its activation and current flowing charges the input capacitance of

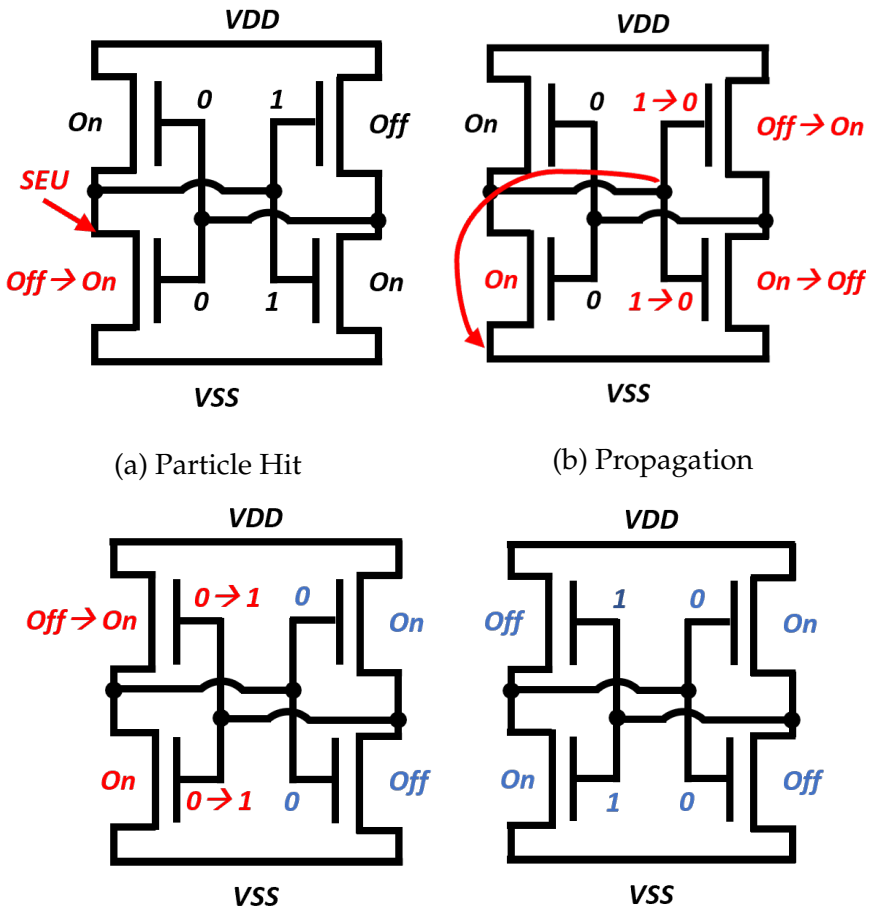


(a) Particle Hit

(b) Propagation

(c) Further Propagation

(d) Resulting Change Status

Figure 1.10: (a) Particle hits the drain of a transistor in the off state in a CMOS SRAM. (b) The charge collected, results in a current flowing in the left NMOS, which discharges the input capacitance of the right transistors. (c) Right transistor states are switched and a current flows through the Right PMOS, charging the input capacitance of the left transistors. (d) Left PMOS is finally switched off and the circuit reaches a stable condition. SEU has occurred [21].

the CMOS structure initially affected by the SEU. As a consequence, the N-MOS whose drain was hit by the particle, is turned on and retains the state created by the occurred SEU. Consequently, the P-MOS of the left CMOS structure is turned off. This process resulted in a permanent change in the state of the SRAM.

– Single Event Functional Interrupt (SEFI): the above-mentioned SEEs can cause the device to stop working as stuck in a logic state. In this case, the system requires a reset or a power cycle to recover its functionalities. A mitigation scheme, which will be discussed later, can also be applied to the design to detect and mitigate the error.

- Destructive or Hard Errors:

  - Single Event Latchup (SEL): the event caused by the activation of the parasitic bipolar junction (Thyristor) typical of CMOS structures and normally in the off-state. If one parasitic transistor is activated, it begins to feed the base of the other, creating positive feedback that leads to an increase in current in the device. If not detected and removed in time, it can lead to permanent loss of device functionality.

  - Single Event Burnout (SEB): event caused by the activation of a parasitic bipolar junction structure in silicon devices which triggers a regenerative avalanche breakdown effect. This event leads to an increase in the current in the device that may damage it by thermal heating if not detected and mitigated in time. It is typical of power electronics [23].

  - Single-Event Gate Rupture (SEGR): the incident particle creates an accumulation of charges at the silicon/oxide interface, which can create a strong electric field capable of opening a conductive path through the plasma created in the oxide layer separating the gate from the semiconductor body. This results in a shortage of the gate with the source and/or drain, making it impossible to drive the device by applying a gate bias. [23]

To quantify the probability of having a specific SEE in a device or a system, the metric used is called cross-section which is defined in equation (1.10).

$$\sigma = \frac{N}{\Phi} \tag{1.10}$$

With

- $N$: the number of the specific SEE observed during the test [adimensional]
- $\Phi$: the fluence of particles with a specific Energy or LET [$pp \cdot cm^{-2}$ ]

Given their criticality, the use of components with cross-sections greater than 0 for SEB and SEGR is avoided [25]. Similarly, components with possible SEL can be discarded or tolerated depending on the criticality of the application and the rate concerning SEFI, as will be discussed in Chapter 2.

#### Radiation Mitigation Techniques for digital circuits

To prevent SEFI from causing malfunctions within a system, different types of mitigation techniques exist and are used to detect soft errors, correct them, or reset the component, restoring the functionalities of the system or the component itself. ECC (Error Correcting Codes) or EDAC (Error Detection and Correction) are used to protect memory content against soft errors. These schemes use extra parity bits to detect and possibly correct the corrupted data. Since the errors can occur even when the memory is not accessed, a circuit called a scrubber is used to continuously sweep the RAM. Hamming Codes [26] and triple modular redundancy are typically used as traditional error-correcting codes. This type of scheme is widely used in mitigating SEUs in the configuration memory of SRAM-based FPGAs. For these devices, another approach consists of using an external scrubber that uses a golden configuration bitstream with no frame-by-frame readback and no ECC circuitry but periodically writes the correct configuration bitstream to the configuration memory. This was demonstrated in [27] to be more effective than an internal scrubber.

Another way to improve system reliability and correct any soft errors, is hardware redundancy schemes. These schemes consist of adding redundant hardware to the design to detect and in some cases correct any errors. The first approach is Duplication With Comparison (DWC): in this case, the combinatorial logic is duplicated and a comparator is used to check whether an SEU has occurred. As visible in Fig. 1.11, this scheme allows the SEU to be identified, but since it cannot identify which output is incorrect, it cannot correct it.

Triple Modular Redundancy (TMR), unlike DWC, can correct the SEU. In this case, the combinatorial logic is triplicated and a majority voter is used to select the correct output. This approach is mainly used in FPGAs where, due to their versatility in terms of design synthesis, it is possible to implement these techniques at the hardware level. In commercial microcontrollers and microprocessors used under radiation, the implementation of this technique can be complicated and impact the performance of the device. Indeed, at the software level, it is possible to triple the computational algorithms and correct SEUs. In [28], the authors show how the Trikaya algorithm, which consists of triplicating the subroutine constituting the algorithm with a majority voting, can reduce corrupted calculations by five to ten times. However, as has been reported, its implementation causes an increase in execution and energy consumption, and multiple SEUs can still cause the algorithm to fail. An improved mitigation scheme is proposed in [29]. In this case, the algorithm is always triplicated, but the three subroutines are not always executed. If the output of 2 first-executed

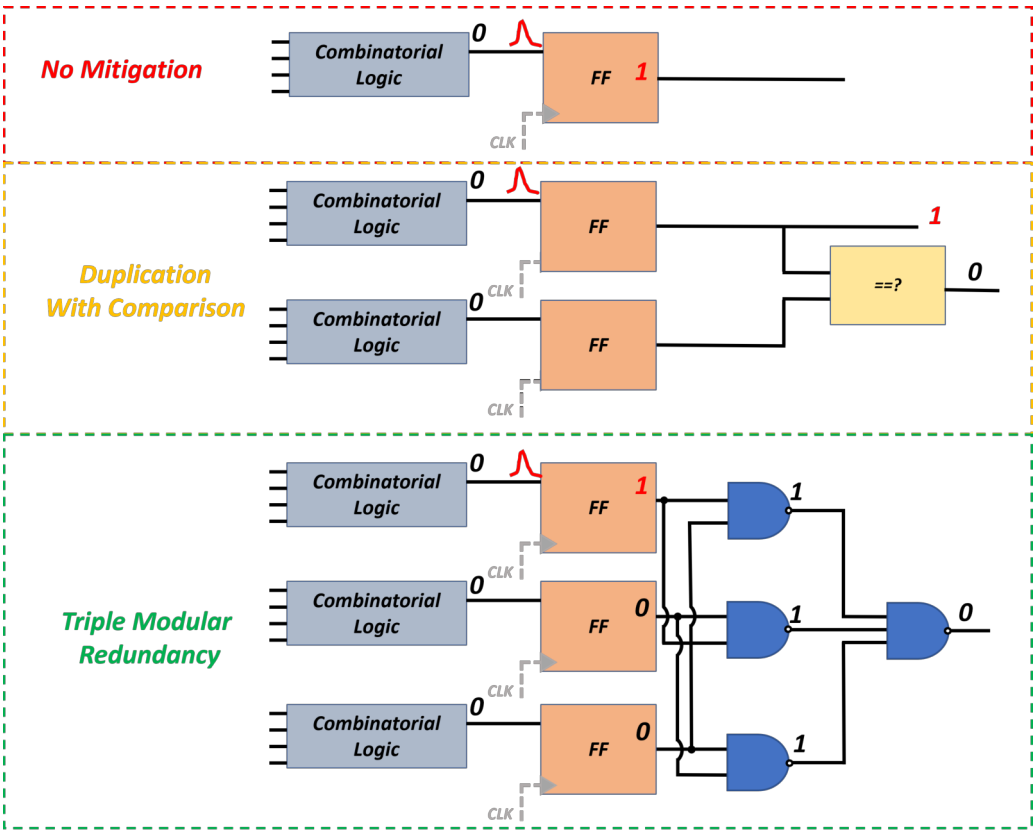


Figure 1.11: In the Figure, different mitigation schemes are applied to a combinatorial logic followed by an FF. In the case of no mitigation, when the SET occurs and is caught by the FF, no correction and detection is possible and the error propagates into the design. Using DWC, it is possible to detect the SEU but not recognize the correct output. Using TMR, on the other hand, it is possible to detect the SEU and correct it, propagating the correct output.

subroutines is equal, the third one is skipped. Conversely, if the two outputs do not match, it is executed and the output is corrected by a majority voting. This approach, compared to [28], reduces execution time and power consumption, maintaining the performance of the previous work in terms of reducing damaged calculations. Automatic tools that allow the entire algorithm to be triplicated exist such as [30]. However, as already mentioned, the increase in execution time and energy consumption can be a strong constraint for some applications and Selective Triple Modular Redundancy (STMR) would be necessary. A further alternative is the watchdog timer. This is a hardware component or internal feature commonly found in microcontrollers and embedded systems, whose purpose is to monitor the correct execution of a program and take corrective action if it detects a malfunction or software error. It works on the principle of periodically resetting or feeding a timer before a timeout is reached. The device monitored by the watchdog must update the timer by writing to a specific register or toggling a General Purpose Input/Output (GPIO). If the watchdog timer is not updated, the system is reset. The watchdog timer serves as a safety mechanism

to prevent the system from getting stuck in an infinite loop, deadlock, or other unwanted states that may result from soft errors. It can be internal (already embedded within the component) or external. In the latter case, as will be seen in Chapter 4, this mitigation scheme is not always able to detect an error that may be invisible to the watchdog and remain hidden. Software mitigation schemes are necessary for certain types of systems and will be introduced in Chapter 3.

## 1.4 Displacement Damage

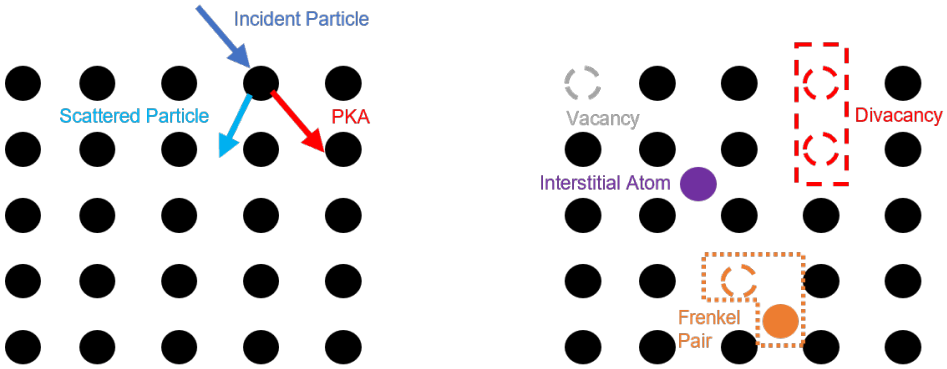


Figure 1.12: Impinging particle and possible defects generated by Atoms displacement effects.

As mentioned in Section 1.1, charged particles and neutrons can cause Displacement Damage by interacting with the matter through Coulombic and nuclear interactions. This phenomenon occurs when the impinging particle has enough energy to displace the atom from its original lattice position and create a defect inside it. The atom knocked on is called a Primary Knock-on Atom (PKA). The possible defects that can be created by this type of interaction, depicted in Fig. 1.12, are:

- Vacancy: absence of an atom from its normal position in the lattice
- Interstitial: atom knocked on and in an abnormal position in the lattice
- Divacancy: two adjacent vacancies
- Frenkel Pair: an Interstitial Atom and an adjacent vacancy.

The minimum energy required to generate a Frenkel pair is 21 $eV$ [31]. If the PKA generated has enough energy, it can create other defects in the lattice. Based on the kinetic energy of the PKA 3 groups can be identified as depicted in Fig. 1.13.

PKAs with low energy ( < 1-2 $keV$ can create Frenkel pairs or small defect clusters. PKAs with low intermediate energy ( 2-12 $keV$ can create a single defect cluster, a region with high density defects. Finally, the one with high energy ( > 12 $keV$) produces multiple or large cascades of defects.

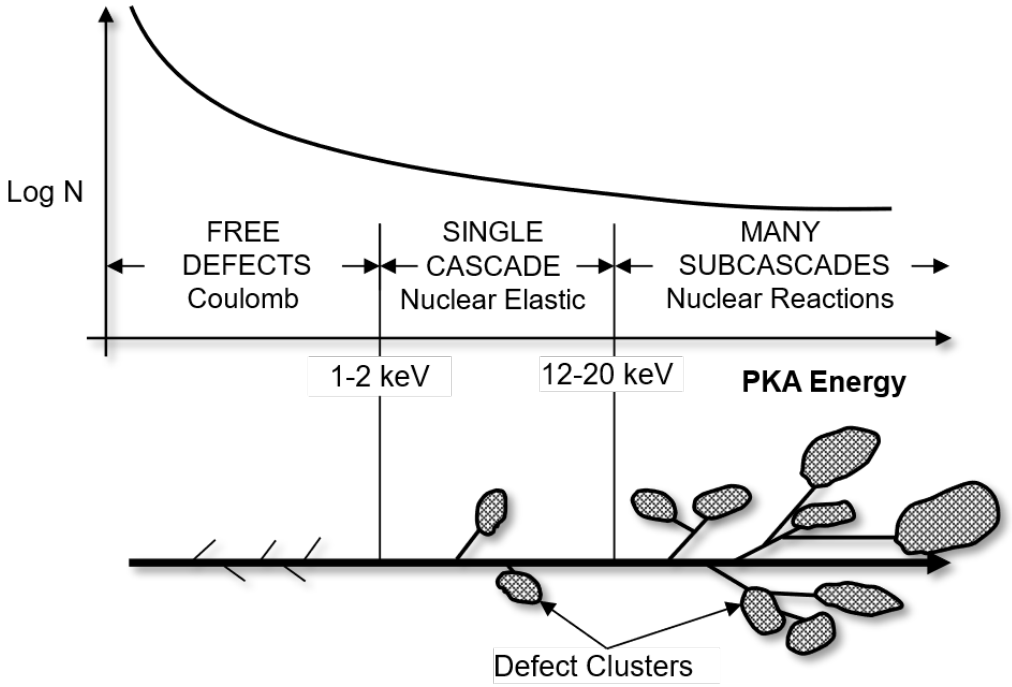


Figure 1.13: Schematic representation of defects and subcascade formation as a function of PKA Energy [1, 32].

Charged particles through Coulombic scattering can create low-energy PKAs already with a low Energy (<10 $MeV$ in Si). While electrons, due to their low mass can only create low-energy PKAs, heavy-charged particles can create intermediate energy and high energy PKAs respectively with an energy of about 10 -20 $MeV$ and > 20 $MeV$. Neutrons can already produce low-energy PKAs with an energy of 25 $meV$ (Thermal Neutron) through nuclear scattering. The number of Frenkel pairs created during a cascade is directly proportional to the PKA energy and the impinging particle NIEL. The NIEL depends on the material, the energy, and the type of incident particle as it is visible in Fig. 1.14.

The Displacement Damage Dose (DDD) generated by a particle can be obtained by dividing its NIEL by the density of the material as defined in equation (1.11) [1]. s

$$DDD = \frac{NIEL(E)}{\rho}\Phi(E)\Big|_{\Phi(E)=1} \tag{1.11}$$

The effects of DD are commonly quantified by using an equivalent fluence of 1 $MeV$

neutrons, which is representative of the particle of the environment of interest and would generate equivalent effects in the given environment. This metric is obtained by multiplying the particle fluence by a hardness parameter $\kappa$. This parameter is obtained by the ratio of the particle NIEL and the one of 1 $MeV$ Neutron as described in equation (1.12) where the Displacement Damage Enhancement Factor (DDEF) is given.

$$DDEF = \Phi_{1MeVneq.} = \kappa_{n_{1MeV}}(E) \cdot \Phi(E) = \frac{NIEL(E)}{NIEL(n_{1MeV})} \cdot \Phi(E) \tag{1.12}$$

As in the case of TID, by summing the different contributions it is possible to obtain the DDEF deposited by all particles belonging to the spectra of the radioactive environment of interest, as defined in (1.13).

$$DDEF = \sum_{p} \int_{0}^{E_{max}} \kappa(p, E) \cdot \Phi(p, E) \cdot dE \tag{1.13}$$

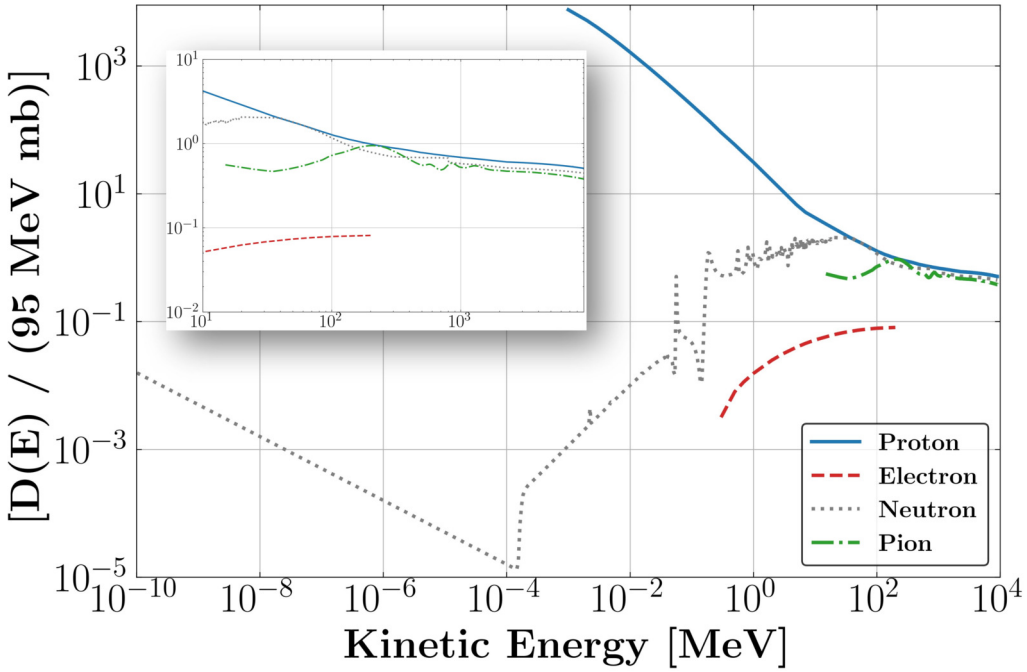


Figure 1.14: Displacement damage cross-section D in Silicon is depicted as a function of the Kinetic Energy for different types of particles. This quantity is equivalent to the NIEL and hence the proportionality between the NIEL value and the resulting damage effects is referred to as the NIEL-scaling hypothesis. Data from [33].

## 1.5 Chapter Summary

This chapter provided an overview of the different effects of radiation on electronics. To better understand and define these effects, the mechanisms by which particles interact with matter were explored. It has been shown that particles lose energy when interacting with matter until they stop; these losses are classified as ionizing (IEL) and non-ionizing (NIEL). Regarding electronic components, IEL and NIEL are associated with three distinct radiation-electron effects: TID, DD, and SEE. Each of these effects has been discussed in detail.

Section 1.2 focused on TID, distinguishing between contributions induced by photons and charged particles. Different formulas were introduced to evaluate the TID contribution for each type of particle. Furthermore, the impact of TID on the functionality of MOS structures was shown as an example.

In Section 1.3, SEE effects were defined and classified under the categories of destructive or non-destructive. The most relevant types of SEE for further investigation were described in detail. The concept of cross-section was introduced, which quantifies the sensitivity of a system to a particular SEE. The evaluation of this quantity becomes crucial in determining the probability of a component or system being affected by a specific SEE in a given radiation environment. Techniques used in digital circuits to mitigate non-destructive SEEs were also outlined. However, it has been observed that these techniques present difficulties when applied to microcontroller-based systems without affecting their performance, making alternative approaches necessary. Chapter 4 will extensively discuss the new mitigation techniques developed within this thesis work, presenting the results obtained from radiation tests and their direct applications.

Finally, in Section 1.4, the damaging effects of DD were presented, accompanied by a formula to evaluate the Displacement Damage Enhancement Factor (DDEF).

Knowing these effects is essential for the upcoming chapters of this manuscript as they significantly impact various analysis aspects. Firstly, understanding them will help to identify the cause of failures in components or systems, a crucial skill required in radiation testing. As will be discussed, the response of a component/system especially for an accelerator environment, may depend on the ratio of TID and DD experienced, and it is therefore necessary to have a correct understanding of both cumulative effects. On the other hand, the knowledge of SEEs is particularly important in digital design. Then, their knowledge plays a crucial role not only in Chapter 2, in which the different phases of the CERN Radiation

Hardness Assurance (RHA) procedure are introduced, but more particularly, in the qualification process of the wireless radiation monitoring system which is discussed in Chapter 3. This system will be a significant topic of this manuscript, and only through proper knowledge of the effect of radiation on electronics will it be possible to understand its behavior under radiation. Finally, the information provided in this chapter will also help to define the effects of radiation on electronics in specific test facilities and environments, enabling their selection according to the desired induced effects. This last skill will be particularly important for the final objective of Chapter 3.

# CHAPTER 2

## Radiation Hardness Assurance for CERN Accelerator Sector

After presenting an overview of the impacts of radiation on electronics in Chapter 1, this chapter introduces the main topic on which this study focuses: the Radiation Hardness Assurance (RHA) procedure.

The highly distributed nature of systems in particle accelerators is one of the most challenging aspects of their operation. This becomes even more challenging when the need to keep infrastructure costs sustainable requires the use of commercial systems as much as possible. Such systems, not designed to operate in a radiation environment, may be more sensitive to radiation to electronics effects and may stop operating due to a radiation-induced failure. Although in a particle accelerator, unlike a space environment, the failure of equipment could be considered tolerable to a certain extent, since it is always possible to access the accelerator to replace the failed equipment, the availability of the machine remains a very critical parameter for its proper functioning. If the accelerator's availability is reduced due to radiation-induced failure, the annual number of delivered collisions decreases, which significantly lowers the prospect of notable discoveries by the organization.

It is therefore necessary to protect the systems considered critical to the operation of the accelerator or to move them to areas where radiation levels are lower. However, this is not always possible because some of these systems must operate in close proximity to the accelerator. To make this distributed network of systems highly reliable and consequently improve machine availability, It is necessary to have a set of well-defined procedural steps

that can lead to a commercial system being reliable in a radiation environment. This procedure was developed taking into account the unique and non-uniform (in terms of spectra) environments of the accelerator.

Considering its importance, this chapter introduces the RHA concept with some generic examples. Then before presenting the CERN RHA procedure, an overview is given of the CERN's and the world's most complex particle accelerator (CERN Large Hadron Collider (LHC)) and its future upgrade (High-Luminosity Large Hadron Collider (HL-LHC)), describing its structure, the working principle, and the associated availability concept, as well as the radiation environment in the most important areas. The introduction of these concepts will make it possible both to understand the challenges and the choices made for the development of the CERN RHA and to compare the results presented in the rest of the thesis with those of various accelerator environments.

The remainder of the chapter is dedicated to CERN's RHA for the accelerator sector, through an exhaustive description of its main phases. An in-depth analysis of the different steps that make up this procedure, allows its main vulnerabilities to be identified. In particular, the 'Radiation Environment Analysis' and 'System-Level Testing' phases, which emerge as critical and vulnerable points of the entire procedure, are detailed in the corresponding sections. The need to improve these phases plays a crucial role in achieving the requirements in terms of availability and radiation tolerance for the next upgrade of LHC and constitutes the starting point for the development of this thesis. This work focuses on the optimization of these steps and, consequently, on the entire RHA procedure. Subsequent studies are structured around this refinement objective and justify the importance of this chapter.

## 2.1 Principle of Radiation Hardness Assurance

The process that ensures that electronic components or systems can withstand and function reliably in a radioactive environment is called RHA. It is a comprehensive set of activities and actions to be followed to know the behavior of the system under radiation (characterization) and validate its use in a specific radioactive environment (qualification). The main objective of RHA is to design, develop, and qualify electronic components and systems to meet specific radiation tolerance requirements. This typically involves understanding the radiation environment, predicting and detecting the effects of radiation on the system, im-

plementing appropriate mitigation schemes capable of mitigating these effects (SEE), and conducting tests under radiation to ensure and validate compliance with specified radiation requirements. The RHA procedures, which enable the above-mentioned objectives to be achieved, include several steps such as the analysis of the radiation environment through simulations, component characterization and selection of the best parts, system-level validation, and risk and reliability analysis. Standards and methodologies to follow and improve these analyses are defined and followed in each procedure to ensure the reliability of the system in operation. In the following section, prior to focusing on CERN RHA, several basic RHA instances will be provided in order to understand the general scheme of an RHA procedure.

## 2.2 Radiation Hardness Assurance Literature Review

All RHA procedures present similar structures made of several phases such as design study, environment analysis, characterization, and testing phases.

[34] is an example of a generic-purpose RHA standard for Electrical, Electronic, and Electro-mechanical (EEE) components developed by the European Space Agency (ESA), national space agencies, and European industry. The requirements of this Standard are defined in terms of objectives to be achieved, rather than in terms of how the necessary work is to be organized and performed. Four different phases are foreseen.

- Phase 0 - Mission analysis: the mission environment is characterized and high-level radiation requirements can be determined. RHA requirements, such as Radiation Design Margin (RDM), are defined to meet the specific needs of the project.

- Phase 1 - Preliminary definition: the requirements and radiation constraints are established and the initial electronic design and spacecraft layout are finalized. This phase covers the scheduling of the test phase.

- Phase 2 - Detailed definition: radiation characterization tests are carried out and analyses are conducted on shielding and circuit design, such as worst case scenarios and SEE failure risks. If necessary, the impact of the radiation effect on the design is not studied at the component-level but at the system or subsystem-level. This phase includes the drafting of reports on the results of the analysis and tests.

- Phase 3 - Qualification and production: a final radiation characterization on flight lots is performed.

Although generically, several development phases typical of RHA procedures can be highlighted within this procedure, such as the study of the environment, the definition of margins, the testing phase, and the analysis of results. However, normally each institution, depending on the spectra of the radioactive environment in which the electronic systems will operate, customizes these phases, enriching them with test and analysis methodologies that enhance the characterization process and allow reaching the operational reliability and availability requirements. [35] is an example of a more specific RHA developed by NASA in 2002 for the characterization of space systems. In this procedure, more specific testing guidelines and specifications, such as testing procedures, are provided by the Institute. It is always based on a top-level phase structure, of which four main steps can be identified:

- Phase A - Description of the mission radiation environment and definition of the radiation levels within the spacecraft: the particle spectra for the specific mission are defined and are used to establish the radiation levels within the spacecraft and/or the radiation specification levels.

- Phase B - Assessment on parts radiation sensitivity: the radiation tolerance of the selected components is established through data provided in radiation databases (if available) and/or radiation tests. In this part, instructions on testing standards to be followed are provided. Considering the TID case, 2 approaches are proposed: step stress (measuring the device's electrical characteristics every a certain amount of TID) and in-flux testing (continuously monitoring the electrical characteristics of the device). In terms of biasing, the worst possible condition has to be applied. Two standards are the US MIL-STD-883 Test Method (TM) 1019.5, whose dose rate is 0.5 to 3 $Gy \cdot s^{-1}$, and the ESA/SCC 22900, whose is 0.01 to 0.1 $Gy \cdot s^{-1}$ are recommended to be followed for TID Testing. An interesting methodology is proposed for low dose rate tests. Since TM 1019.5 does not provide dose rate specifications for low dose rate tests, ESA/SCC 22900 is recommended. Since this standard dose rate test, is very low (0.1 to 1 $mGy \cdot s^{-1}$), and thus time-consuming and generally not compatible with the time frame of a space project, an alternative approach is proposed using the test standard ASTMF 1892 whose block diagram is depicted in the Fig. 2.1.

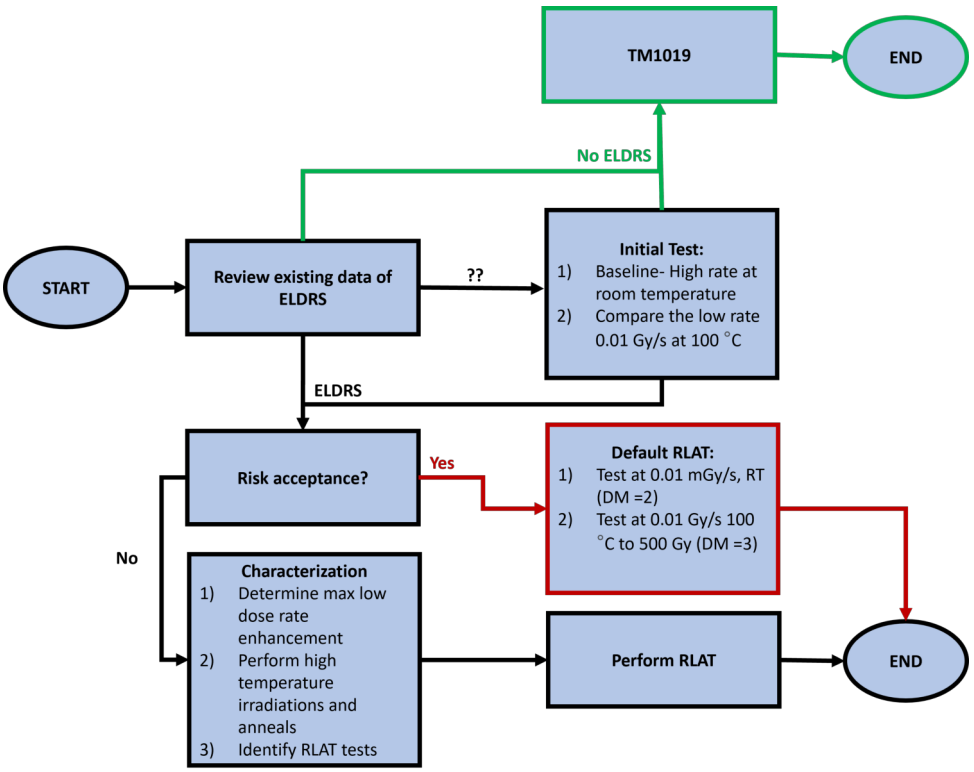


Figure 2.1: Flow Diagram of Enhanced Low Dose Rate Sensitivity (ELDRS) re-adapted from [35]. RLAT stands for Radiation Lot Acceptance Testing.

This approach introduces the concept of risk margins, which is widely used in the RHA procedure. The first step is to determine whether the component is sensitive to low dose rate effects, based on existing data or testing. If existing data confirm the non-dependence of the ELDRS, TM 1019.5 can be used to characterize the device. If no data are available, ASTMF 1892 suggests performing two types of tests: a high dose rate test at room temperature and a low dose rate test, with at least a factor of 3 difference. If no effect of the low dose rate is observed, TM 1019.5 can be used. If dependence exists, two possible approaches can be followed, introducing the concept of risk acceptance. If the risk can be accepted, the approach is a pragmatic test method using reasonably low dose rates and recommending higher radiation Design Margins (DM) than those used for CMOS devices. This approach involves testing with a low dose rate of 0.1 $mGy \cdot s^{-1}$ with a standard DM of 2 or with a temperature of 100 °C and a dose rate of about 10 $mGy \cdot s^{-1}$, with a DM of 3 for doses up to 500 Gy. Although this approach is simple, there is a potential risk of not fully capturing the response of the tested part at low doses. The second approach is more comprehensive and involves testing under various conditions to determine the appropriate test conditions for the specific part being evaluated. This approach aims to ensure comprehensive testing and to identify

the appropriate test conditions to accurately represent the radiation response of the part. In this section of the guideline, SEE and DD testing instructions are provided similarly. It should be noted, that for DD, the procedure consists of following a similar approach to that for TID, however, unlike the latter, not many specifications are given on how to perform the test. For proton-dominated space environments, proton tests may deliver enough TID to estimate DDD/TID-induced degradation, otherwise, they must be combined during Phase C.

- Phase C - Radiation aspects in Worst Case Analysis (WCA) of system and circuit design: sensitivity obtained in phase B for the different parts can be used to perform a WCA of the design. A radiation failure level can be determined for each component by combining their radiation response and usage in the design

- Phase D - Part Categorization: in this phase, the different parts tested are compared with the expected radiation level defined in phase A. The factor used to select which category the part falls into for each radiation environment is the RDM. RDM is defined as the ratio of the part failure level to the part radiation environment. Three categories are identified and reported in Table 2.1.

Table 2.1: RDM categories for [35].

| **RDM** | **Categorization** |
|---|---|
| < 1-2 | Unacceptable |
| 1-2 < RDM < 10-100 | Hardness Critical |
| > 10-100 | Hardness non Critical |

For parts classified as unacceptable, three possible scenarios are foreseen:

  - Investigation: a more estimated evaluation of the environmental radiation conditions and a radiation test biasing the device with operating conditions can help to obtain a more realistic RDM.
  - System or equipment level countermeasure: introduce shielding and mitigation scheme into the design to improve the response of the component.
  - Part replacement: exchange the component with a more reliable and radiation tolerant one.

Hardness Critical are instead components that do not exceed the RDM but are still close to the threshold margin. For these components, further tests of the flight lots are

suggested. If the parts exceed the RDM, they can be used in this application without any further action required.

[35], suggesting test guidelines through existing standards and defining RDMs, allows those who follow it to be able to characterize their system while remaining compliant with NASA standards. A standardized process helps to improve the reliability of spacecraft (in the case of NASA) in operation, as all their parts must pass the same stages. The standardization of the process to achieve more reliable systems prompted CERN to develop its own RHA procedure to standardize the qualification process of the electronic system and improve the accelerator reliability over the years. As explained in the next sections, the adoption of a comprehensive and well-defined RHA procedure is indispensable for ensuring the reliability of electronic systems and enabling CERN to achieve superior results. However, the large number of distributed systems, the use of Custom Commercial Design to keep low the cost, a spectra composed mainly of neutrons with energy varying from the energy of $meV$ up to $TeV$ are some of the unique challenges that the LHC presents, which cannot be addressed by existing standards and which have required the development of specific qualification procedures to ensure reliability under radiation. In the next Section, the LHC structure and its radiation environment will be presented: its knowledge will allow to motivate the choice taken within its RHA procedure.

## 2.3 LHC Structure and Radiation Environment

The Large Hadron Collider (LHC) is the world's largest and most powerful particle accelerator. With a circumference of 27 kilometers, the energy of the particles passing through it is increased by the use of superconducting magnets and various acceleration structures. With two beams of high-energy particles whizzing by almost at the speed of light, there are four detectors where they collide at 13.6 $TeV$. These beams travel in opposite directions through separate tubes maintained under high vacuum conditions. Superconducting electromagnets, consisting of coils of specialized electric wires operating in a superconducting state, guide the beam of 2 particles along their circular trajectory. This enables efficient electrical conduction without resistance or loss of energy. To achieve this state of superconduction, it is necessary to cool the magnets to a temperature of -271.3 $^{\circ}C$, even colder than space. To achieve this, a complete liquid helium distribution system connects a significant part of the accelerator, ensuring that the magnets receive essential cooling and other vital services.

In particle physics, the particles of interest in interactions are exceptionally rare, requiring a high number of interactions to generate them. In the case of the LHC, the luminosity is used to quantify the number of interactions per unit of surface area and time ($cm^{-2} \cdot s^{-1}$). By integrating the luminosity over time, it is possible to determine the accelerator's capability to generate collisions relevant to high-energy physics. The unit of integral luminosity is expressed as an inverse surface area and is commonly defined in inverse Femtobarn ($fb^{-1}$). To improve the LHC operation there are two possible ways: by increasing the instantaneous luminosity (Higher beam intensity) or by improving the availability of the accelerator. While the first can be obtained through an upgrade of the machine, as it will be for the HL-LHC, the second depends on the different control equipment of the accelerator. In Fig. 2.2, it can be observed over the last 10 years, increasing integrated luminosity values have been reached with increases in beam intensity. As will be shown in the next paragraphs, an increase in luminosity will lead to an increase in the radiation levels to which electronic components are exposed. The availability of the machine could be impacted by an increase of the radiation to electronic-induced failures. This scenario allows an understanding of the impact of the RHA procedure on the operations of the accelerator: the accurate definition and fulfillment of all its phases are essential to ensure the proper functioning of the accelerator.

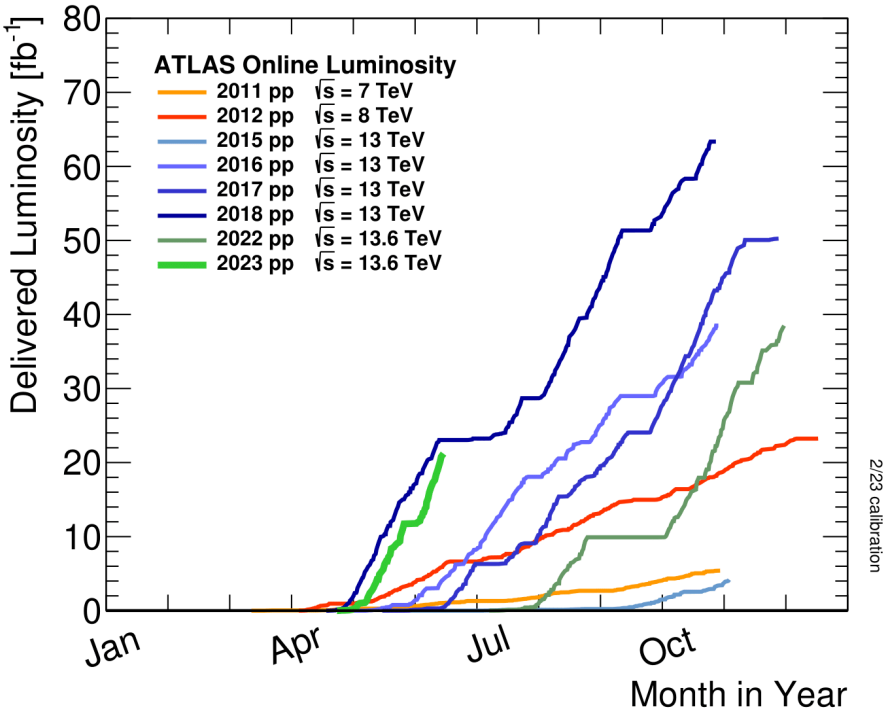


Figure 2.2: Cumulative luminosity versus day delivered to ATLAS during stable beams and for high energy proton–proton (p-p) collisions. In Fig. $\sqrt{s}$ is the Center of mass energy.

### 2.3.1 LHC Layout

Before presenting the radiation environments of the LHC, it is fundamental to describe the layout of the machine and its basic operation. These principles play a crucial role in advancing the thesis, as they facilitate the categorization of the various areas and ensure clear guidance through them.

The LHC is divided into eight Octants within which it is possible to distinguish eight arcs and eight straight sections, also called Insertion Region (IR) and long 528 meters [36]. The IRs are not used in the same way: four are designed for the collision points and the detectors (IR1, IR2, IR5 and IR8) while the others are used for different Machine Tasks. IR4 hosts radio frequency cavities, IR6 beam dumps, and IR3 and IR7 collimation (referred to as Cleaning in Fig. 2.3) [37]. A schematic of the layout is shown in Fig. 2.3.

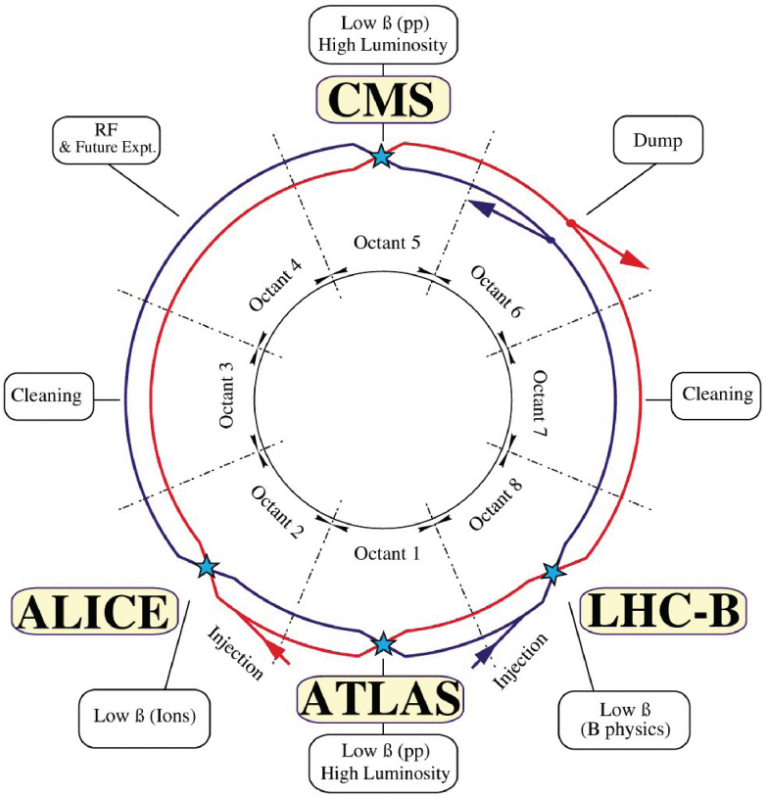


Figure 2.3: A schematic diagram depicting the layout of the LHC, showing the eight octants and IRs. Beam 1 circulates in a clockwise direction, while beam 2 in an anticlockwise. [38].

The accelerator has a modular structure in which each IR is located between two arcs [38]. The basic modules, which constitute the machine, are the half-cells: 54 meters long, they consist of a string of three twin aperture main dipole magnets (MB.Axx, MB.Bxx, and MB.Cxx) and one short straight section containing a quadrupole (MQ.xx). Each arc, between the 2 IRs, has 42 half-cells. At the end of each arc, and thus at the beginning of each IR, is

the Dispersion Suppressor (DS), which serves to minimize the machine's dispersion in the vicinity of the IRs. This is followed by the almost straight sections, called Long Straight Sections (LSS). They can consist of Matching sections, which consists of a set of quadrupole and dipole used to change the trajectory of the two separate beam tubes into a shared vacuum one, and the Inner Triplet (IT), which is a set of three quadrupole magnets and serves to reduce optical $\beta$-function and thus, focus the beams to collide. The IT is present at the four collision points. Finally, in the middle, there is the Interaction Point (IP). A block diagram of the Octant structure is provided in Fig. 2.4.

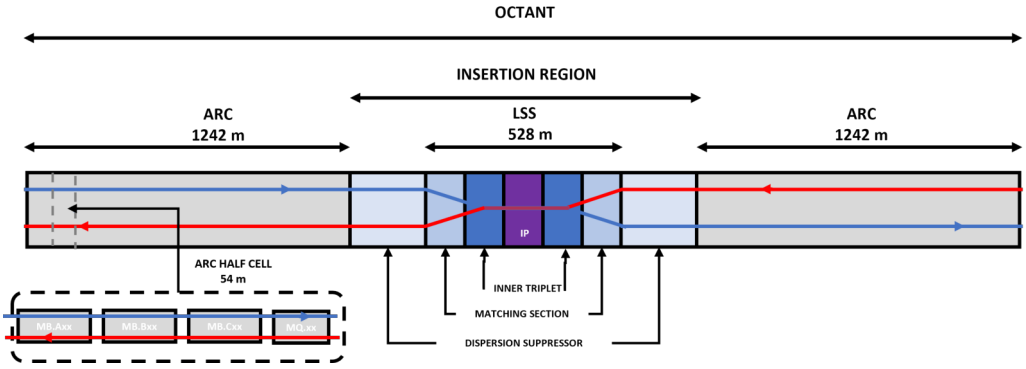


Figure 2.4: The regular octant layout of the LHC can be divided into different sections according to their specific functions. Each part is made of different half-cells, the basic element of the machine. The IT occupies half-cells from 1 to 3, followed by the matching section (4 to 7). The DS is located in half-cells 8 to 13, while the Arc extends from half-cells 14 to 34.

Along the LHC tunnel, there are other infrastructures called Service Alcoves designed to accommodate large amounts of accelerator equipment since in the proximity of the tunnel the radiation levels would be too high to accommodate rad-hard designs. However, not all the accelerator equipment can be hosted in these areas and they require to be directly exposed to the radiation produced by the accelerator. For example, Quench Protection Systems (QPS), used to protect magnets from destruction in case of a quench, have to be placed as close as possible to the beam for operational reasons [39] [40].

The equipment, depending on their usage, may be installed in environments characterized by different particle spectra and radiation level intensities. This variability of the radiation environment has a direct impact on the qualification processes and thus, on the RHA procedure making it more challenging. The choice of components (Rad-tol, qualified COTS, commercial system), and the number and type of tests will depend on the specific worst case environment in which the final system will operate. To better understand the choices made for CERN's RHA, it is essential to understand the working principle of the machine and the related source of radiation.

### 2.3.2 LHC Operation Modes

To understand why the concept of availability and the need for a proper RHA are fundamental for Machine operation, it is important to introduce the operating modes of an accelerator. The LHC functioning is based on 3 main operation cycles called Fill, Ramp, and Stable beam [20].

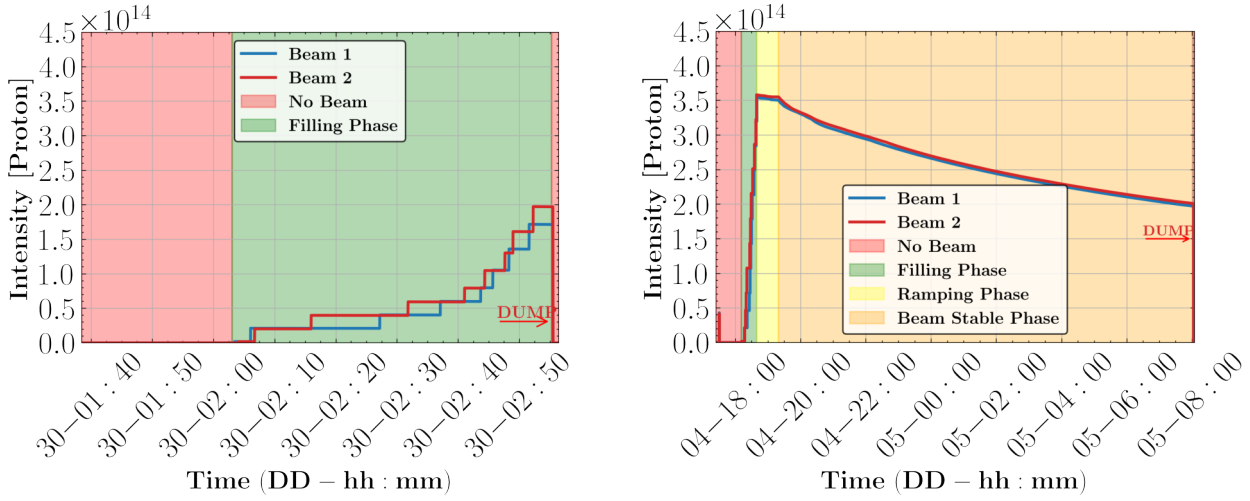


(a) Fill 8844: example of aborted Fill

(b) Fill 8873: example of a successful Fill

Figure 2.5: Two filling processes are depicted. In Fig. 2.5a, the filling process, highlighted in green, is started but remains incomplete. Consequently, the beam is dumped, and the process is aborted. In Fig. 2.5b, the filling process (in green) is completed and followed by the ramp period (in yellow). After that, the stable beam phase (in orange) starts and lasts for approximately 13 hours. Subsequently, the beam is dumped, and the process is concluded.

During the "fill" operation mode, the protons are injected into the two vacuum pipes. Once injected, their intensities are increased (ramp mode) to the maximum possible energy, which in 2022 was 13.6 *TeV* (collision). Once and if the target energy is reached, the last phase begins. During the Stable Beam mode, collisions between protons of the 2 beams are produced within the IPs: it is during this phase that data useful for experiments are recorded and then extrapolated. During this operational phase, the protons available for collisions are reduced not only by the collision itself but also by unwanted losses in other areas of the accelerator. As a result, the instantaneous luminosity is reduced and the beam degrades. When the beam degrades, it is up to the operator to decide whether to interrupt the run and start a new one or prolong it, since it is not possible to start a new one quickly. Normally, stable beams last from 5 to 15 hours and are interrupted through a dump [1]. However, not always the filling stopped because of the beam degradation (Controlled Dump) but is often terminated because of a fault (Uncontrolled Dump). In Fig. 2.5, two examples of fills are

depicted. While in Fig. 2.5b all the operations are completed and the beam is terminated with a Controlled Dump, this is not the case for Fig. 2.5a. In this case, the beam is stopped through an Uncontrolled Dump, during the filling phase. After a controlled Dump, some operations are mandatory before starting a new fill. If the dump is Uncontrolled, this time is increased by the extra interventions required to detect the fault, restart, or in the worst case replace the equipment. As a consequence, the delivered luminosity at the end of the year is reduced by those interventions. To quantify these losses of time on the overall functionalities of the machine, the concept of Availability applied to the Machine is defined as the time the machine is functional concerning the overall functioning time [41]. A higher availability would allow for reaching a higher value of delivered luminosity during a year of operation. Reducing the number of uncontrolled dumps caused by radiation effects on electronics and increasing the accelerator availability and the delivered luminosity, has been the main mandate of the Radiation to Electronics (R2E) project [42]. Starting at CERN in 2012, its main objective consisted of quantifying the danger of radiation-induced failures and introducing mitigation to minimize the risk of failures to less than one per week, not only for nominal beams but also for any future scenarios that may arise. At the beginning of the mission, the radiation levels in the tunnels were unknown, so only short-term measures were taken while radiation-induced failures occurred. These measures consisted of moving the systems to safer areas, increasing the protective shielding [43], and, replacing the malfunctioning systems with more robust ones. As visible from Fig. 2.6, thanks to these measures it was possible to reduce the number of dumps per year from 12 $\frac{dump}{fb^{-1}}$ in 2011 to 3 $\frac{dump}{fb^{-1}}$in 2012. [44] Then, the knowledge of the radiation environment of the LHC obtained through simulation and the radiation monitoring systems developed in-house, together with the development of strategies for qualifying the systems to be used, leading to better results [45]. During Run 2, (2015-2018) the number of $\frac{dump}{fb^{-1}}$ was drastically reduced as visible in Fig. 2.6.

Most of the dumps depicted in Fig. 2.6, were caused by SEEs. In the case of non-destructive ones, the average downtime per dump was relatively short since most of the time the system could be restarted remotely. A destructive SEE not detected in time or failure caused by degradation caused by cumulative effects (TID and DD) have a greater impact because the system degraded may require change increasing the Accelerator downtime. To reduce the downtime, the R2E project has relocated most of the equipment and improved the shielding when possible to reduce the absorbed radiation keeping the system far from their design margins [45]. This was the case for Power Converters (PCs) [46], which were moved

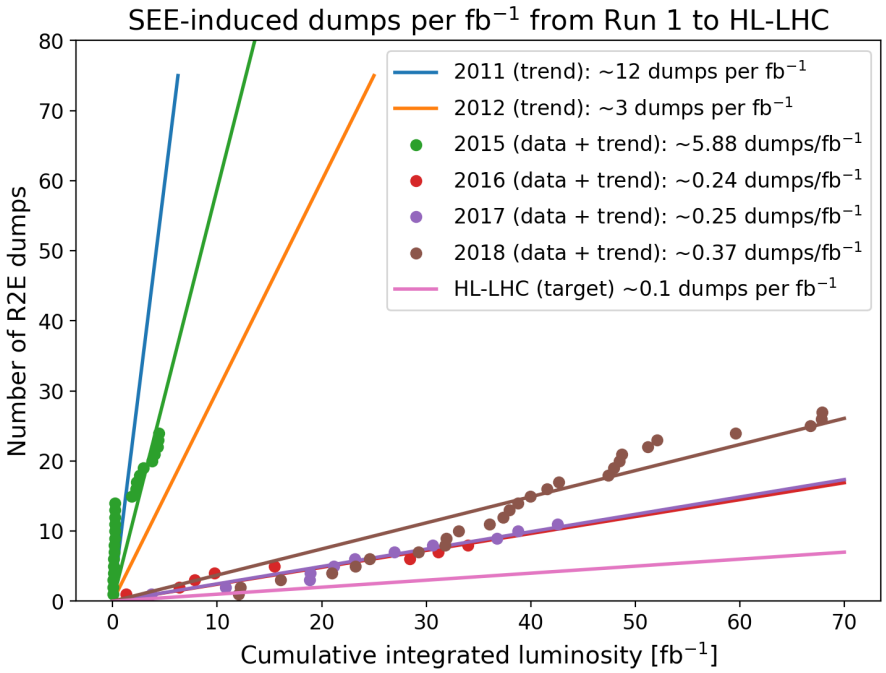


Figure 2.6: Dump related to R2E fault as a function of the cumulative integrated luminosity in 2011-2012 (Run I, trend only), 2015-2018 (Run II, data and trend). The number of acceptable dumps due to R2E failures for HL-LHC is also given [45]

to areas with lower radiation levels (e.g. from UJ14/16 to UL14/16) or, when possible, to radiation safe ones. In addition, actions in terms of the redesign were taken for the system suffering from destructive SEEs. In the case of PC, a radiation tolerant power MOSFET was added to the design to prevent SEB observed in Run 1, improving the reliability of this type of system [47]. For the upcoming LHC Run 3, the target is achieving a similar level of R2E performance as in Run 2. This accounts for further improvements in the performance of the LHC, such as increased beam intensity and annual integrated luminosity. For the HL-LHC upgrade the target is 0.1 $\frac{dump}{fb^{-1}}$. This upgrade aims to increase the delivered luminosity by a factor of five compared to 2018. To ensure the smooth operation of the upgraded system and maintain high machine availability, it is essential to design systems with higher radiation tolerance margins to prevent failures due to cumulative effects. The achievement of the set target values for HL-LHC will only be possible by following an RHA procedure that accurately assesses the radiation environment and incorporates qualification steps that are as realistic as possible. However, only by improving the existing procedure through new test techniques or a better understanding of the radiation environment will it be possible to achieve the predefined target values for HL-LHC. The RHA must also adapt its qualification margin to the expected radiation levels of HL-LHC and make its qualification steps as realistic as possible.

### 2.3.3 LHC Radiation Source

This section presents the different radiation sources of the LHC and the resulting radiation scenarios. Understanding these sources is essential for understanding the challenges and choices made in the development of the CERN RHA and for contextualizing the results presented in the other chapters.

Depending on the position along the LHC, the main radiation sources are three: the inelastic collisions in the IPs, the generic beam interactions with LHC elements (typically collimators), and the interactions of the beam with residual gas molecules in the beam pipes [38]. Particle debris from the inelastic proton-proton (p-p) interaction dominates the mixed IP field (IP1 and IP5). Secondary particles originate from these interactions, with an average multiplicity of 120 per proton-proton collision. This secondary particle shower is made of protons, pions, kaons, electrons, photons, and muons. They range from thermal energies up to $GeV$ and can induce all three electron-effect radiations presented in the previous chapter. At 5 $mm$ from the point of interaction, the secondary particles are photons (~50 %) and charged pions (~30 %). Even if most of them are intercepted by the detectors, a small part, emitted at very small angles to the beam, reaches the accelerator equipment. The spectrum changes with distance from the IP. Other important sources of radiation for the accelerator equipment are the halo particles caught in the debris collimators around the experiments and initiating hadronic and electromagnetic showers. This is a major radiation source not only for the collimation points (IR3 and IR7) but also for the experiment areas. The gas-beam interaction is the last source of radiation in the LHC and is due to the interaction of the beam with the residual gas density in the vacuum pipes. While the first two radiation sources mentioned are dominant in the IRs, the last one prevails in the ARCs region. The inelastic collision in the IPs is defined luminosity driven since it is proportional to the luminosity of the machine. The other two radiation sources are instead called intensity driven since they depend on the beam intensity. The collimator setting and quality of the vacuum pipes also respectively impact the radiation generated by the interaction of the beam with machine elements and with residual gasses [1]. While intensity-driven radiation sources are emitted during each of the operation cycles, luminosity driven is generated only during beam stable phases. The future upgrade of the LHC (HL-LHC) is expected to increase the luminosity and the intensity respectively by a factor of 5 and 2.5 [1]. An increase in the radiation level in all the LHC areas is expected according to [38]. To optimize the beam size and maximize luminosity, the HL-LHC upgrades imply changes to the IR1 and IR5 pairing

sections, which include larger physical apertures. As a result, the number of debris particles entering the matching section per primary collision will be significantly higher. To protect the cold magnets from collision debris, a network of collimators is present and is called Target Collimators Long (TCL). While not all TCLs are necessary to protect the magnets in the current machine, all TCLs become indispensable in the HL-LHC due to the increased amount of debris particles. Their usage will strongly reduce the radiation levels in the area within which they will be deployed. The debris from the collimations will increase the radiation level in the service alcoves, increasing the radiation levels there. As visible in Fig. 2.7, the radiation levels outside the RR53 (An Alcove of IP5) change by roughly a factor of 10 depending on the TCL settings showing the impact of the collimator on the radiation environment.

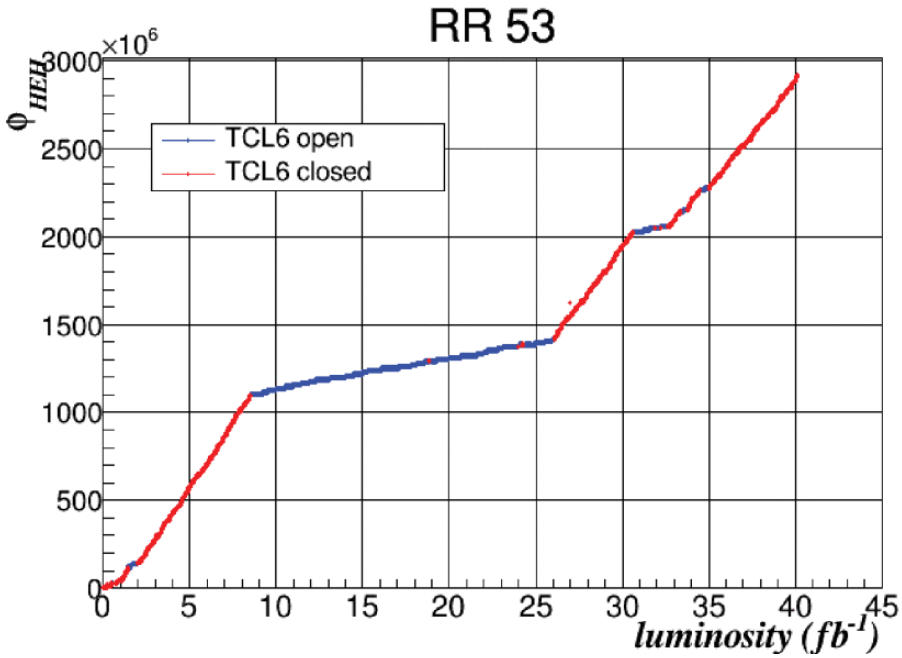


Figure 2.7: HEH fluence as a function of the luminosity measured along the tunnel (outside RR53) for different TCL settings [38].

Different radiation sources and configurations (i.e. TCL in IP5), lead to a significant variability of radiation levels within the LHC. This combined with the presence of all radiation to electronics effects, poses challenges in establishing an RHA procedure that can be universally applied to all systems operating within the machine. It would be a significant mistake, both in terms of cost and time, to apply the same qualification process to a system used along the tunnel and one used in a service alcove. Therefore, the RHA procedure is customized to include an analysis phase that investigates the specific environment in which the system will be installed. This analysis is conducted through simulations or by radiation monitoring, as

elaborated in the following sections. As a consequence, different qualification strategies are foreseen based on the expected level of radiation the system may withstand. The following sections provide current (LHC) and foreseen (HL-LHC) values of radiations along different areas of the accelerator.

### 2.3.4 Radiation Levels Along Different LHC Areas

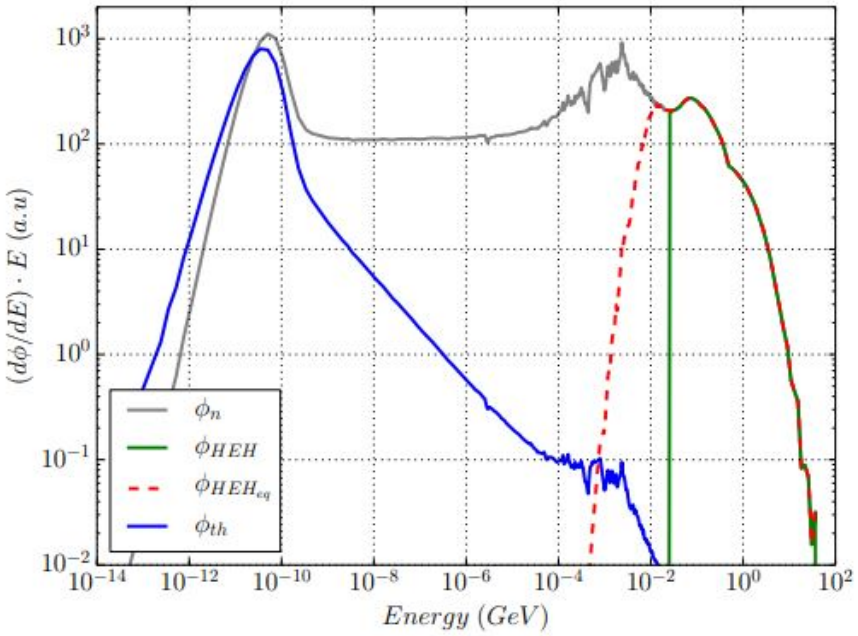


Figure 2.8: Neutron Lethargy fluence derived using FLUKA for a tunnel position of the LHC. The Contribution of Th, $HEH_{eq}$ and HEH are highlighted. In this plot only neutron contribution is considered [20]. Lethargy is defined as the differential flux times the geometrical mean of the bin energy and is often used to represent neutron spectra [48, 49].

At CERN, as will be detailed in the next sections, radiation monitoring systems or Simulations are used to evaluate the radiation levels in the different accelerator areas. The TID is expressed in Gray ($Gy(Si)$) while the DD uses the DDEF(Si) unit, expressed in 1 $MeV\ neq. \cdot cm^{-2}$. To quantify SEEs effects the High Energy Hadron (HEH) fluence and Thermal Neutron (Th) fluence magnitude are used [20]. The HEH fluence ($\Phi_{HEH}$ is defined as the fluence of Hadrons with an energy above 20 $MeV$ [50, 51]. There are two reasons for this definition: Hadrons a) with energy above the given value have a similar probability of generating an SEE, while b) with energy below the given value, they are still capable of producing an SEE, but with a lower probability. The latter motivation is justified by the drop in energy within standard device packages and the rapid reduction in the cross-section

of the nuclear reaction below this energy. These particles are therefore negligible from the point of view of SEEs [52]. HEH fluence is expressed in $HEH \cdot cm^{-2}$. Since energy losses do not apply to neutrons, the HEH equivalent ($\Phi_{HEH_{eq}}$) is used which corresponds to the HEH fluence plus the intermediate neutron fluence (neutron contribution in the 0.2 - 20 $MeV$ energy range). In addition to HEHs, Th fluence ($\Phi_{Th}$ is also monitored since, as is known in the literature, Th can cause SEUs in electronic components containing boron 10 ($^{10}B$) [53, 54] and many areas of the LHC have a higher Th fluence per year than that of HEH. Th is defined as the neutron fluence cumulated weighed by the $^{10}B\ (n,\alpha)^{7}Li$ cross-section normalized to the value at thermal energy (0.025 $eV$). In Fig. 2.8, these contributions are highlighted for a spectrum made of only neutrons. To quantify the SEE rate impact of ($\Phi_{Th}$) and ($\Phi_{HEH}$) to the Accelerator operations, the R-Factor is defined in equation (2.1) [55].

$$R = \frac{\Phi_{Th}}{\Phi_{HEH}} \tag{2.1}$$

As mentioned in previous paragraphs, electronics are normally hosted in the alcoves but according to the requirements they can also be placed close to the tunnel. In the next sections, the radiation levels of these two types of areas will be analyzed.

#### Tunnel

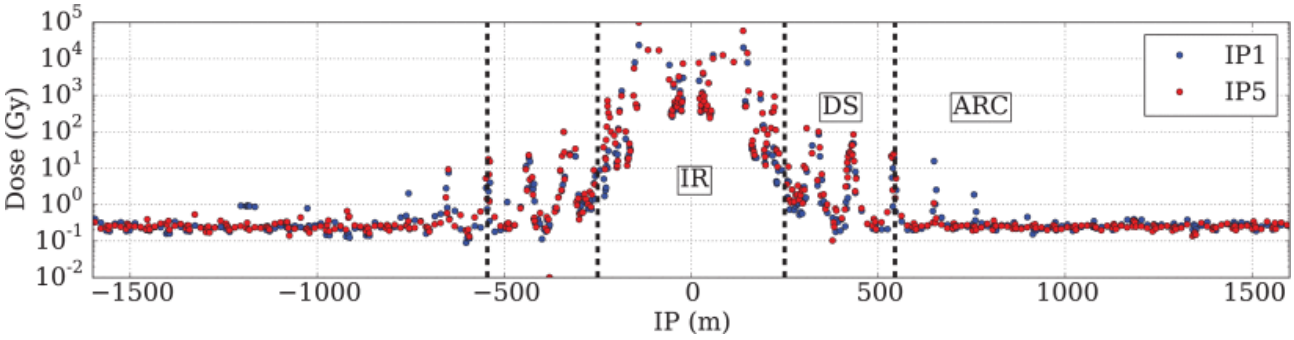


Figure 2.9: Integrated TID measured by the BLMs in IP1 and IP5 during the p-p 2016 run where a delivered luminosity of 40 $fb^{-1}$ was reached [38].

The integrated TID measured by Beam Loss Monitors (BLMs) during the proton-to-proton run of 2016 is depicted in Fig. 2.9 and allows evaluating the TID of different tunnel areas. As mentioned in the previous paragraphs but visible from Fig. 2.9 the IR does not allow the usage of Commercial design and custom boards with COTS with its dose rate of 10 $kGy \cdot y^{-1}$. The same applies to the DS area, where there are peaks of 100 $Gy \cdot y^{-1}$. Here Custom COTS design can be used for the location below the dipole magnets where the TID

is 10 $Gy \cdot y^{-1}$. In the Arc regions, where there is less than 1 $Gy \cdot y^{-1}$, custom boards with COTS design suit these margins for a radiation damage lifetime perspective. The ratio between the DDEF and TID is around $10^{10}$ 1 $MeV\ neq. \cdot cm^{-2} \cdot Gy^{-1}$ while for the HEH is $10^9$ $HEH \cdot cm^{-2} \cdot Gy^{-1}$ [52]. This HEH value is not negligible when evaluating the SEE failure risk taking into account the number of systems that will need to be deployed in the area. For example, a system with a failure cross-section of $10^{-11} cm^2$ would be considered safe for this environment. Extending this consideration to 10 units installed in this area, there is already a ~10 % probability of system failure over the 10 deployed, making this fluence non-negligible. The expected Radiation level for HL-LHC has been evaluated in [38]. The simulations have been carried out using FLUKA [56] [57], which is a general purpose Monte Carlo code for studying the interaction and transport of hadrons and photons from cosmic rays to thermal energies within any material. Since LSS is too harsh an environment to host electronics already in the LHC, the other areas of the tunnel are treated (DS, Arc). In the DS area, near the dipole magnets where the electronics is hosted, the maximum TID per year reached will be 200 Gy, but it will vary along the different half cells reducing also a factor of 10. The electronic equipment in this area is placed below the magnets and so is subjected to lower radiation levels (factor 3). Thus, in the DS area electronics will experience a TID ranging from ~80 to ~800 $Gy$ during the whole lifetime of HL-LHC (3000 $fb^{-1}$). Areas below the dipoles in the DS HL-LHC should have annual TID levels of less than 10 $Gy \cdot y^{-1}$. The expected radiation levels of Arc and DS areas are reported in Table 2.2.

Table 2.2: Simulated radiation levels for HL-LHC considering one year of operation and a luminosity of 250 $fb^{-1}$. For DS, the areas downstream of the dipole magnets are considered in the table [38].

| **HL-LHC [250 $\mathbf{fb^{-1}}$]** | **HEH [$\mathbf{cm^{-2} \cdot y^{-1}}$]** | **DDEF DDEF [$\mathbf{1MeVneq. \cdot cm^{-2} \cdot y^{-1}}$]** | **TID [ $\mathbf{Gy \cdot y^{-1}}$]** |
|---|---|---|---|
| DS | $5{\cdot}10^{10}$ | $5{\cdot}10^{10}$ | 100 |
| Arc | $10^9$ | $10^9$ | 2 |

### Service Alcoves

The Service alcoves are often referred to as shielded areas inside the LHC terminology. They can be divided into two groups:

- Heavily-shielded areas: service alcoves that are placed close to the IP. Two zones can be identified composing these areas: the Underground Junction chambers (UJs) and the Underground Liaison galleries (ULs). Fig. 2.10 presents the layout of UJ16 and UL16, heavily-shielded areas of the right side of IP1, and their FLUKA simulated radiation levels in the x-z plane at beam height. The left side of IP1 is symmetrical.

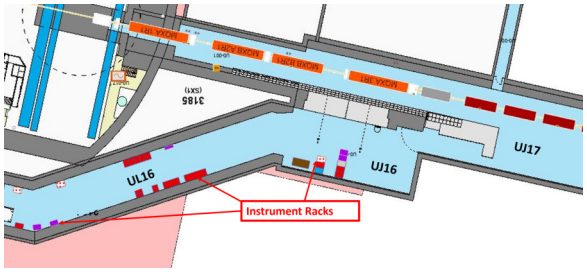


(a) Layout showing the instrument racks position in the heavily shielded areas UL16, UJ16

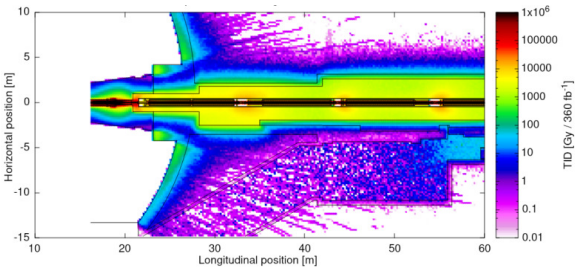


(b) Expected TID for HL-LHC in the x-z in UJ16-UL16

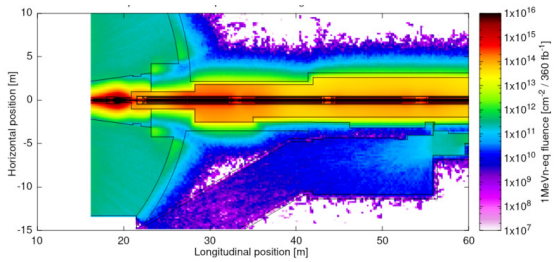


(c) Expected DD for HL-LHC in the x-z in UJ16-UL16

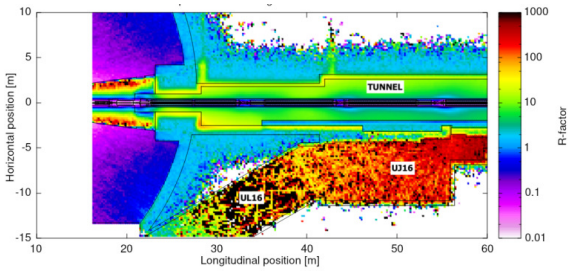


(d) Expected R factor for HL-LHC in the x-z in UJ16-UL16

Figure 2.10: FLUKA simulation of annual (360 $fb^{-1}$) radiation levels in the x-z plane at beam height on the right side of IR1, in the vicinity of the experimental cavern. The instrument rack position (Fig. 2.10a) and the foreseen level of HL-LHC in UL16 and UJ16 (Figures 2.10b,2.10c and 2.10d) are depicted [58].

- Lightly-shielded areas: less shielded Service alcoves because subject to a harder (In terms of energies) but less intense spectrum respect the heavily shielded areas. Placed at the DS/LSS intersection are called RR. Fig. 2.11 presents the layout of RR17, a lightly-shielded area of the right side of IP1, and their FLUKA simulated radiation levels in the x-z plane at beam height.

In Table 2.3 the radiation levels cumulated during the proton to proton run of 2018 are

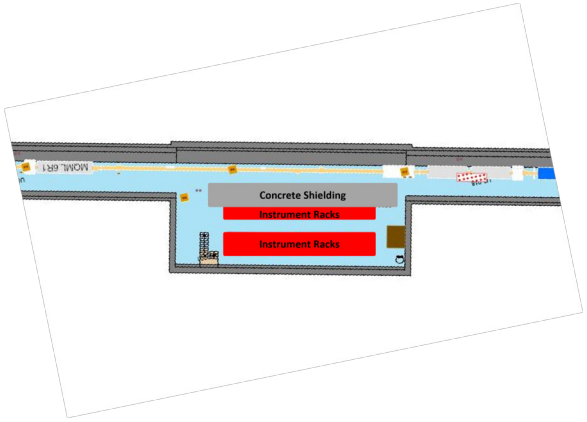


(a) Layout showing the racks position in the heavily shielded areas RR17

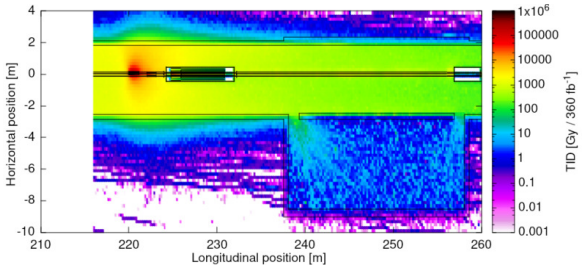


(b) Expected TID for HL-LHC in the x-z in RR17

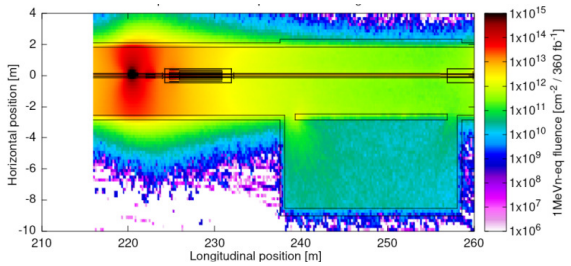


(c) Expected DD for HL-LHC in the x-z in RR17

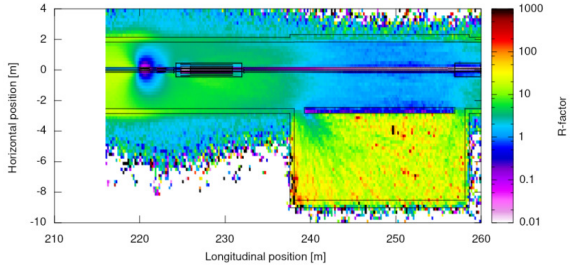


(d) Expected R factor for HL-LHC in the x-z in RR17

Figure 2.11: FLUKA simulation of annual (360 $fb^{-1}$) radiation levels in the x-z plane at beam height on the right side of IR1, in the service alcoves of RR17 where the electronics is hosted. The instrument rack position (Fig. 2.11a) and the foreseen level of HL-LHC in RR17 (Figures 2.11b,2.11c and2.11d) are depicted [58].

presented for ULs, UJs, and RRs of IP1 and IP5. RRs in IP5 are identical to the ones in IP1. There is a difference in the UJ and UL geometry but the radiation levels are similar.

Table 2.3: Shielded areas radiation levels of IP1 and IP5 obtained during 2018 run [1].

| **LHC 2018** | **Tunnel Areas** | **Shielded Areas** | | |
|---|---|---|---|---|
| **60 [fb$^{-1}$]** | **RRs** | **RRs** | **UJs** | **ULs** |
| HEH [$cm^{-2} \cdot y^{-1}$] | $3 \cdot 10^9$ | $3 \cdot 10^8$ | $3 \cdot 10^8$ | $10^7$ |
| DDEF [1 $MeV\ neq. \cdot cm^{-2} \cdot y^{-1}$] | $10^{10}$ | $10^9$ | $10^9$ | $<10^9$ |
| TID [ $Gy \cdot y^{-1}$] | 11 | 0.4 | 0.4 | 0.02 |

These levels have been measured with the TCL collimators opened. As shown in the previous paragraphs, this is the best possible condition for the electronics hosted in these areas. With HL-LHC, they will need to be in closed positions and this will lead to an increase in the radiation levels that the electronics in these areas will need to withstand as shown in Table 2.4. The shielded areas present the highest increase compared to Tunnel areas. This will have a strong impact on the qualification of components and usage of Commercial design.

Considering the lifetime of HL-LHC (3000 $fb^{-1}$, a system in UJs will have to withstand 120 $Gy$ and a DDEF of 3.6 $\cdot 10^{11}$ 1 $MeV\ neq. \cdot cm^{-2}$, which are not negligible quantities making it prohibitive to use fully commercial systems without additional shielding.

Table 2.4: Shielded areas expected annual radiation levels of IP1 and IP5 [38].

| **HL-LHC [250 fb$^{-1}$]** | **Shielded Areas** | | |
|---|---|---|---|
| | **RRs** | **UJs** | **ULs** |
| HEH [$cm^{-2} \cdot y^{-1}$] | $3{\cdot}10^{9}$ | $5{\cdot}10^{9}$ | $10^{8}$ |
| DDEF [1 $MeV\ neq. \cdot cm^{-2} \cdot y^{-1}$] | $3 \cdot 10^{10}$ | $3{\cdot}10^{10}$ | $10^{9}$ |
| TID [ $Gy \cdot y^{-1}$] | 6 | 10 | 0.2 |

## 2.4 CERN RHA Overview

As defined in Section 2.3, CERN's electronics systems, both in the accelerator and in experiments, are exposed to the peculiar harsh radiation environments induced by the different particle accelerators. As such, these systems are required to withstand all three radiation effects on electronics to avoid failures that would impact the machine availability and as a consequence, do not permit to reach higher luminosity per year.

To ensure the reliability of systems exposed to these environments, they must pass a battery of qualification tests in specific conditions described in the CERN RHA procedure. This procedure, much like those used in other fields such as space, provides different phases and detailed instructions on how to qualify components and systems. However, due to the unique radiation environments present in accelerator areas, the qualification procedure foresees several distinct challenges that have been overcome through the development of dedicated test methodologies that are now integrated into the whole qualification process.

One of the primary challenges in LHC systems is their distributed nature. Unlike many other environments, these systems can be composed of thousands of individual units, which creates two major constraints. Firstly, Commercial Off The Shelf (COTS) components and commercial systems should be used whenever possible to keep costs down. CERN RHA must therefore define the boundaries that distinguish when and where a commercial system, a Custom COTS board, and a rad-hard system can be used. Secondly, systems are exposed to a diverse range of radiation environments, imposing different challenges both in terms of source and type of radiation effects, and multiplicity of the conditions to be tested.

Unlike space, the accelerator environments are mainly neutron dominated, leading to

specific challenges to be assessed. One of the most significant threats to system reliability is the estimation of Displacement Damage on optoelectronics, caused by NIEL scaling violation between neutrons and other particles typically used for qualification. Optoelectronics are often the most vulnerable components in a system exposed to a neutron environment and a specific qualification methodology was developed to ensure the degradation estimation reliability.

Another challenge is the large predominance of thermal neutrons in shielded areas, as certain technologies can be susceptible to thermal neutron-induced SEEs. A systematic approach must be followed to evaluate this risk as was shown with FPGAs for instance in these areas thermal neutrons can be by far the main contributor to the failures and their underestimation can have dramatic consequences.

Another unique challenge of the LHC is the fact that components and systems are exposed to a wide variety of TID and DD levels that induces combined TID-DD effects at the circuit-level or system-level that can lead to various degradation rate and profiles depending on the TID/DD ratios there are exposed to, and a very careful test process must be followed to assess this issue.

To take care of all these challenges led by the radiation environment and components, the CERN RHA has been tailored to integrate different qualification phases that assert all these issues.

### 2.4.1 Functional Description Blocks and Radiation Requirements

Before describing CERN's RHA procedures in detail, a distinction needs to be made. In this work we will focus on the RHA applied to the AcceleraTor Sector (ATS). The experiments do not follow this procedure but have their own specific procedures.

At CERN the only systems which do not require passing the RHA procedure, are the ones installed in R2E safe areas. These areas are characterized by TID and DD levels which are expected to not impact the functionalities of the systems and HEH fluence $< 3 \cdot 10^6$ and Th fluence $< 3 \cdot 10^7\ cm^{-2}$ per year [59]. In Fig. 2.12, the different levels of various LHC installations in terms of HEH fluence, TID, and DDEF are depicted for the different types of electronic systems. As it is visible, R2E safe areas are not the rule, but the exception in the LHC. In non R2E safe areas, systems need to pass all the steps of the RHA process.

To stay within cost budgets, the only solution is to develop electronic systems based

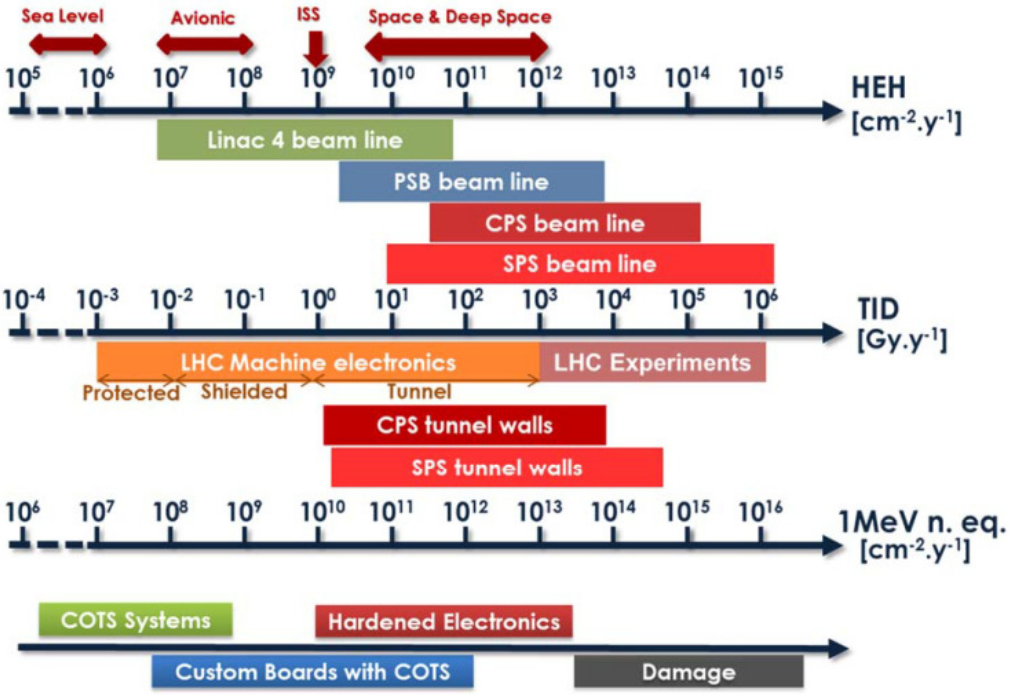


Figure 2.12: The block diagram illustrates the different radiation levels found in the LHC's different installations. The types of systems that can be employed according to specific environmental requirements are also shown.

mainly on COTS devices while rad-hard components are rarer. Fig. 2.13 describes the different phases that compose the RHA process for custom-built systems designed at CERN and details its evolution during the development and production life cycle of the system. The phases marked in light blue, are the ones dedicated to radiation effects on electronics.

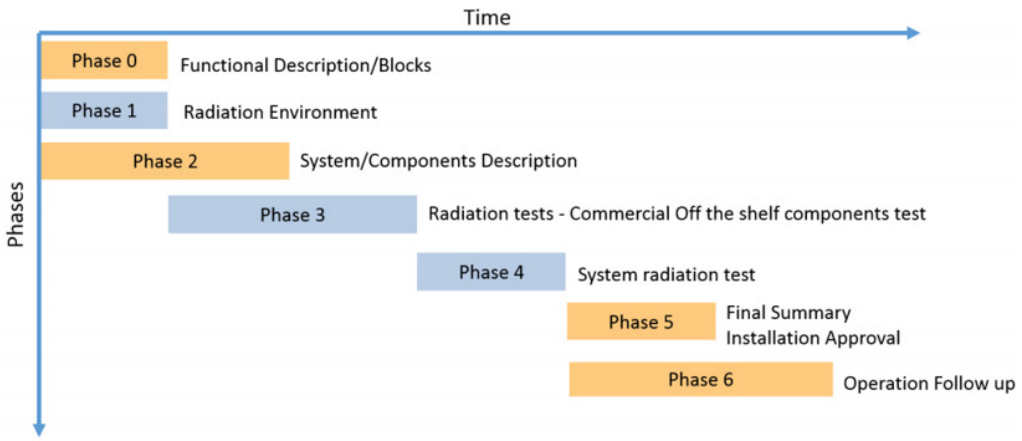


Figure 2.13: RHA process block diagram for custom-built electronic systems designed at CERN.

Concerning the single phases:

- Phase 0: is used to tailor the functional description of the equipment and the specifications for its use in the accelerator.

- Phase 1: in the Radiation environment phase the CERN, Monitoring and Calculation Working Group analyzes all the operational environments within the system that will be installed and identifies the worst case environment scenarios within them. In this phase, the system radiation requirements are established.
- Phase 2: the development of the system architecture starts. The Radiation Design Requirements (RDR) derived from Phase 1, are applied to the different design parts with a top-down approach (system-level, functional block-level, and device-level). In this phase, the components considered critical for the system functionalities are detected. In addition, circuits for monitoring the performance of these critical parts (Point of observability), mitigation schemes, and fault tolerance strategies are also identified and implemented.
- Phase 3: the sensitivity of each component to radiation is evaluated, and the radiation test results for each component are used to determine the system's overall tolerance.
- Phase 4: the performance of the system design is evaluated through a final test to verify that it respects the initial requirements derived from Phase 1.
- Phase 5: based on the results obtained during phases 2-4, evaluates the suitability of the equipment installation in the radiation areas specified in Phase 1.
- Phase 6: the system becomes operational and anomalies/faults happening during operation are reported.

In order to be compliant with R2E CERN Regulation, a system to be used in the accelerator in a non-safe area, must pass all the above phases. In case of failure in phase 4 or rejection in phase 5, the phases must be repeated with a new design solution starting from phase 2. In the LHC, for cost reasons, not only custom boards with COTS components are employed but also COTS systems. They are fully commercial systems and with an unknown architecture and bill of material, a dedicated approach is required when they need to be used in no radiation-free areas. Examples of these types of systems used in the accelerator are: Uninterruptable Power Supplies (UPSs), commercial solutions to monitor the voltage distribution of the area, and Programmable Logic Controller (PLC) used to monitor and control machinery and equipment. When they are required to operate in non-safe R2E areas, they need to pass a shorter RHA procedure. This procedure does not take into account Phases 2 and 3, as the architecture of the system is not known, which results in a "black box". Therefore, the first

and only level of verification is system radiation testing. The RHA assurance for the COTS system is depicted in Fig. 2.14.

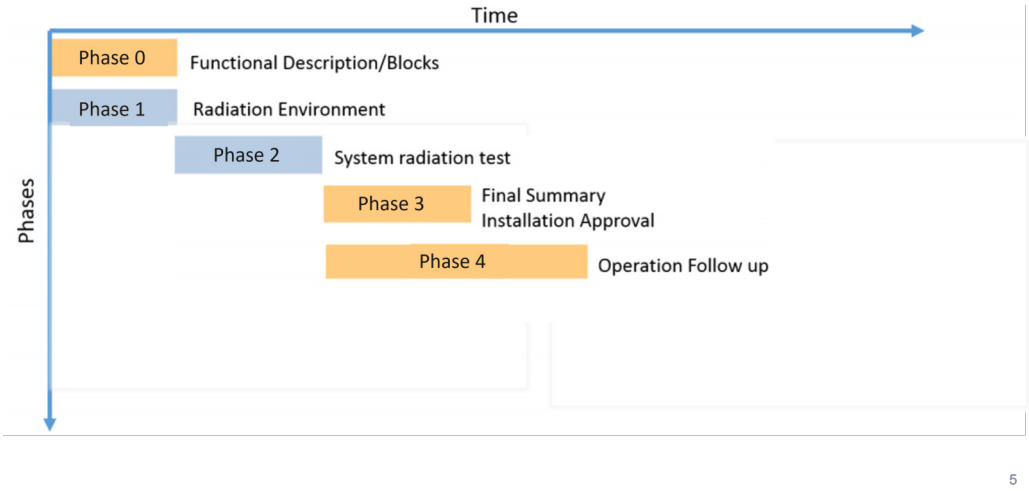


Figure 2.14: RHA process block diagram for COTS Systems.

Modified off-the-shelf (MOTS) systems, which are fully COTS systems whose architecture is known, follow the shorter RHA procedure presented in Fig. 2.14. In this case, the Final Summary Installation Approval phase is not passed, knowing the architecture, it is possible to replace the failing components with qualified COTS components and improve the system performance. For COTS systems, this is not possible and an analysis of the system architecture would be required which is normally avoided for cost reasons. In case of not passing the qualification process, the system is just replaced with another commercial one. In the remainder of this chapter, some of these steps of the RHA procedure for custom based on COTS components of greatest interest for this doctoral work will be discussed in detail. Their in-depth study will provide insights into the current weaknesses of the procedure. These represent the starting points of this thesis work, from which methodologies have been developed that will allow further improvement of the procedure. In the next sections, the phases more relevant to the manuscript are described.

### 2.4.2 Radiation Environment Analysis

The values of radiation expected for HL-LHC are known for the most important locations of the machine and are available in [38] [58]. For areas not covered by [38] [58], dedicated radiation level assessments are carried out using either measurements, simulations (FLUKA) [56, 57] or both, of the radiation field at the locations where electronic racks are typically placed.

For the measurements different dosimeters are available. The most famous and used for the machine functionalities are the BLM system [60, 61]. The operating principle of these detectors is to measure deposited energy. These systems are capable of measuring TID rates with a resolution of 40 $\mu s$. Their main purpose is to detect particle showers caused by beam losses and to trigger beam discharges to protect the machine equipment from unintentional energy deposition, thus preventing the magnet quenches and damaging machine components. In addition to their machine protection role, BLM measures are used for TID measurements and optimization of the accelerator, to detect the position of loss cause [62] and to validate simulation codes via benchmarks [63]. They are placed in the most likely loss position along the accelerator. After being deployed in the Proton Synchrotron Booster (PSB) [64] and Proton Synchrotron (PS) [65], in LS2 another TID monitoring system has been deployed in SPS and LHC DS of IP1, IP5 and IP7. The Distributed Optical Fibre for Radiation Sensing (DOFRS) based on radiation-sensitive optical fibers (OFs) provides a linear map of the TID with a resolution of 1 $m$, helping to accomplish online and distributed dosimeter measurements. More versatile sensors, with a faster deployment time are the Radio-Photo-Luminescence (RPL) dosimeters [66, 67]. The main limitation of this sensor is that it is passive and does not provide online measurements. However, during Technical Stops (TS), when the short access time can make the deployment of other more complex dosimeters difficult, RPL represents a valid alternative to evaluate the TID level in areas not covered by other dosimeters.

The RadMonV6 [68] is a radiation monitoring system based on a full custom COTS design, able to measure all radiation to electronics effects thanks to specific sensors. TID measurements are asserted using radiation-sensitive p-channel MOSFETs (RadFETs) [69], the DDEF through 3 photodiodes [70]. The HEH and Th fluences are measured by using the usage of two different well-calibrated parallel SRAMs, whose sensitivity to both Th and HEH is known, and by applying the equation (2.2) [55, 68].

$$\begin{cases} SEU^{SRAM1} = \sigma_{HEH}^{SRAM1} \cdot \Phi_{HEH} + \sigma_{Th}^{SRAM1} \cdot \Phi_{Th} \\ SEU^{SRAM2} = \sigma_{HEH}^{SRAM2} \cdot \Phi_{HEH} + \sigma_{Th}^{SRAM2} \cdot \Phi_{Th} \end{cases} \tag{2.2}$$

Where SRAM1 and SRAM2 indicate the two different well-calibrated parallel SRAMs, SEU is the sum of the bit flips for each bank, $\sigma_{Th}$ is the cross-section of the memory to thermal neutrons, whereas $\sigma_{HEH}$ is the cross-section of the memory to high energy hadrons. The

importance of radiation monitoring in the implementation of this phase is evident. Among the systems described, the only one capable of providing online measurements and that can be easily moved to different locations appears to be RadMon. However, this instrument has major limitations in terms of mobility and distribution, which prompted the development of a wireless monitoring system. **The qualification of this system was one of the topics of this research work. Its use will bring multiple benefits to the organization, including improvement in RHA Phase 1 (Fig. 2.13). Since this phase also evaluates the choice of possible shielding layers to protect the systems and measures their effectiveness, it requires a high-mobility instrument or this can be only carried out with simulation for deployment time requirements which may provide more conservative results. The system we will describe in Chapter 3 meets this and other requirements**.

### 2.4.3 System/Components Description

To design a radiation-tolerant system compliant with CERN regulations in terms of availability and reliability, the RHA assurance has foreseen a phase called System/Components description. In this phase, availability and reliability requirements at the system and component-level are defined from the LHC Requirements. A V-cycle approach is proposed by RHA as visible in Fig. 2.15.

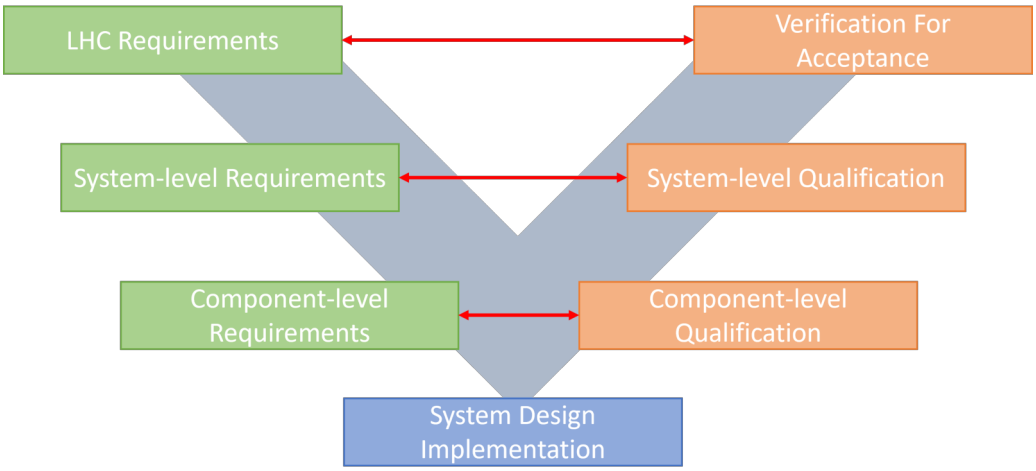


Figure 2.15: Block diagram of the V-cycle process implemented in the CERN RHA procedure for the qualification of Custom COTS Design. The definition of the margins of phase 2 (green) is tailoring the different qualification phases and the final verification and acceptance phase.

Starting from the LHC requirements, the system and device requirements are tailored and the design implementation starts. Afterward, the phase of component, system-level

qualification, and verification for acceptance are performed. As it is visible from Fig. 2.15, this phase is fundamental and draws the next phases of qualification and verification. In the next paragraphs, it will describe how the SEE and Cumulative effect requirements are chosen. Once the LHC requirements in terms of fluences and cumulative effects have been established during phase 1, the system developer can evaluate the target availability and reliability for the system to be designed.

#### Target Availability Requirement Definitions

As mentioned in the previous Section, the availability target for HL-LHC is 0.1 $\frac{dump}{fb^{-1}}$. It must be noted that this is the target referred to the whole machine. A conservative approach is followed defining the $\frac{dump}{fb^{-1}}$ allowed for each system. This approach is unfair because systems in harsh environments exposed to stronger radiation environments will end up requiring much lower system-level and device-level cross-sections than systems in weaker environments. The main problem is that those margins could be difficult to respect for a custom COTS design system while having a $\frac{dump}{fb^{-1}}$ proportioned to the environment the system would have to withstand, could allow all the systems to have larger margins.

Table 2.5: Example of a radiation requirement hierarchy for a generic system availability.

| ID | Requirements |
|---|---|
| LHC-R001 | Each system in the LHC can cause $10^{-5}$ $\frac{dump}{fb^{-1}}$ |
| LHC-R002 | In UJ16 are expected 8.3 $\cdot 10^6$ $HEH \cdot cm^{-2} \cdot fb$ |
| LHC-R003 | In UJ16 are expected 8.3 $\cdot 10^8$ $Th \cdot cm^{-2} \cdot fb$ |
| SYS-R001 | The system has one device (FPGA) whose failure can cause a dump |
| DEV-A001 | One of the FPGA selected for the design has an HEH cross-section of $10^{-11}$ $cm^2$ and a Th cross-section $10^{-12}$ $cm^2$ |
| DEV-A002 | One of the FPGA selected for the design has an HEH cross-section of $3 \cdot 10^{-12}$ $cm^2$ and a Th cross-section $5 \cdot 10^{-14}$ $cm^2$ |
| DEV-A003 | One of the FPGA selected for the design has an HEH cross-section of $10^{-12}$ $cm^2$ and is not sensitive to Th |
| FAI-A001 | Using DEV-A001, SYS-R001 has a failure rate expecting to cause 1.1 $10^{-4}$ $\frac{dump}{fb^{-1}}$ |
| FAI-A002 | Using DEV-A002, SYS-R001 has a failure rate expecting to cause 8 $10^{-6}$ $\frac{dump}{fb^{-1}}$ |
| FAI-A003 | Using DEV-A003, SYS-R001 has a failure rate expecting to cause $10^{-6}$ $\frac{dump}{fb^{-1}}$ |

It has been estimated that the number of units capable of inducing a beam dump is in the

order of ten thousand and thus, its unit should produce $10^{-5}\ \frac{dump}{fb^{-1}}$. The environment that the system will have to withstand is known from phase 1 and can be used to evaluate the respect of the margins. By multiplying its Th and HEH cross-section by the corresponding expected fluence per $fb$, it is possible to evaluate if the expected failure rate per $fb$ is lower than the margin ($10^{-5}\ \frac{dump}{fb^{-1}}$). An example of the process is provided in Table 2.5.

The system in the example has one device whose failure can cause a dump of the beam and has to be placed in UJ16 whose expected Th and HEH have been taken from [58]. In this example, three different FPGAs have been tested at the component-level. As it is visible DEV-A001 is not suitable for the application because is outside the spec (LHC-R001). DEV-A002 and DEV-A003 are below the spec and can be chosen for the application. The device with the highest margin should be considered. The verification of the respect of these metrics has to be carried out in parallel with the component-level qualification. The system may have more critical devices and in such cases, their combined cross-section has to be below the system margins.

#### Target Reliability Requirement Definitions

In the context of the LHC machine Radiation reliability is not a problem since repair and replacement operation can potentially extend the Accelerator lifetime indefinitely and differently from space it is possible to access the instruments. However, extraordinary intervention due to system failure may reduce the budget available to the equipment in terms of availability, since the operation required can be long compared to one LHC cycle. During the year, CERN has foreseen windows called TS (generally 1 week), Year-End Technical Stop (YETS), and Long Shutdown (between two different runs), during which preventive maintenance can be carried out to the systems. TID and DDEF margins are tailored, taking into account the expected radiation value of the operational area provided in phase 1, the whole lifetime of the accelerator (12 years), and design margins. Those design margins are defined according to the expected level for the 12 years. When it is possible, margins above factor 2 are taken called RDM to consider the statistical distribution of the radiation responses of devices from the same LOT. Differently from the availability previously described, the components need all to withstand the design margins. The components that may exhibit a degradation profile within specs defined by the design developer over the RDM defined are considered eligible for the design. Components with a degradation profile (within the de-

fined RDM) conforming to the specifications defined by the project developer are considered suitable for the project. An example is provided in Table 2.6.

The system is planned to be used in the UJ16 area where for the whole HL-LHC operation a TID of 144 $Gy$ and a DDEF of $6 \cdot 10^{11}$ 1 $MeV\ neq. \cdot cm^{-2}$ (LHC-R001 and LHC-R002) are foreseen [58]. A RDM margin of 3 is taken (SYS-R001). The system in the example needs the DC-DC Converter output voltage to not deviate more than $\pm 10$ % or it will not be able to provide the correct power to the rest of the system (SYS-R002). Three candidates are listed. DEV-A001 and DEV-A002 have to be discarded because they do not respect the RDM margin. DEV-A003 can be selected as a candidate for the final design.

Table 2.6: Example of a radiation requirement hierarchy for generic system reliability.

| **ID** | **Requirements** |
|---|---|
| LHC-R001 | In UJ16 are expected 144 $Gy$ in 12 years of operation of HL-LHC |
| LHC-R002 | In UJ16 are expected $6 \cdot 10^{11}$ 1 $MeV\ neq. \cdot cm^{-2}$ in 12 years of operation of HL-LHC |
| SYS-R001 | Considering RDM of 3, all the components have to remain within the defined specs after absorbing 432 $Gy$ and $1.8 \cdot 10^{12}$ 1 $MeV\ neq. \cdot cm^{-2}$ |
| SYS-R002 | The 1.2 $V$ DC-DC converter shall not deviate more than $\pm 10$ % to not compromise the functionalities of the system |
| DEV-A001 | This DC-DC converter stopped working after cumulating 200 $Gy$ and $3.2 \cdot 10^{11}$ 1 $MeV\ neq. \cdot cm^{-2}$ |
| DEV-A002 | At the RDM, the device was functional but the output was changed of -12 % |
| DEV-A003 | At the RDM, the device did not exhibit any degradation remaining within the specs |

#### Component Database Selection

When defining the components for the design, CERN RHA suggests also checking them from the existing CERN Radiation Database, developed during the years by the organization. When considering the use of other sources, caution should be applied. The simple possession of radiation data for a device does not automatically imply its suitability for usage. Many existing data sets are obsolete or lack adequate documentation, such as a specific bias condition used, unknown radiation for some characteristics, or measurement techniques used not compliant with standards. Even if the device has been selected by one of those databases, the production lot qualification phase is compulsory.

### 2.4.4 Component-Level Qualification

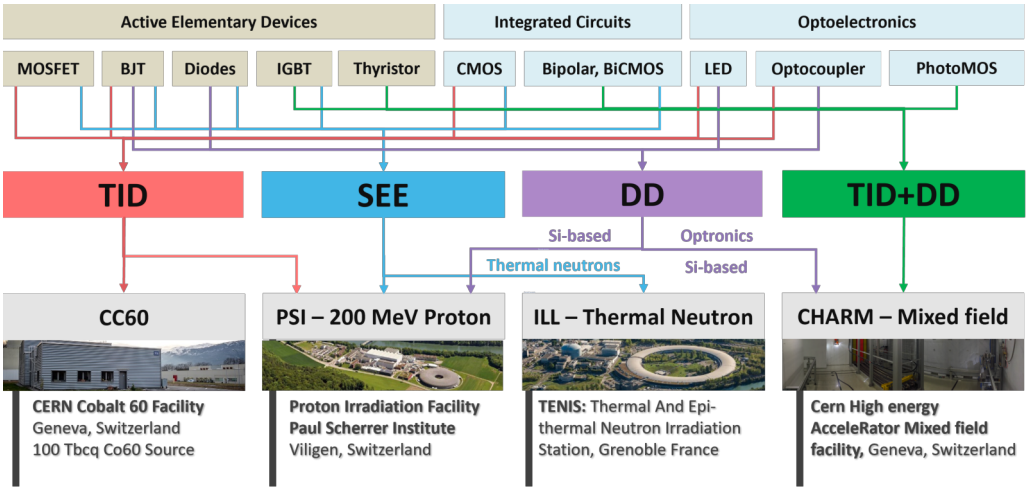


Figure 2.16: The following block diagram describes the choice in terms of test type and facility depending on the type of effects or components to be qualified for the CERN Radiation environments.

The component-level qualification represents one of the most important and longer parts of the CERN RHA. During this phase, the components selected are qualified for each radiation to electronics effect to have a complete characterization. This procedure is not only necessary for the choice of the best candidates: a deep analysis may allow tracing the eventual cause of system failure in the next phase and detect the weaker part of the system to be replaced in case of a required update to get better performances. Choosing the best part through a more realistic characterization enhances the system's chances of successfully passing the next RHA steps. For TID, CERN developed its test procedure based on the existing methodologies and standards available in the literature. However, its unique environment did not allow it to do the same for DD and SEE (Th). More robust strategies for these effects were required to obtain realistic results. The component-level qualification in CERN RHA can be distinguished into 2 macro qualification phases: the test lot and the production (part selected for system design) lot characterizations. Both the phases foresaw qualification for each effect and the minimum number to be tested for each part is 11 in agreement [71]. This number may be lower if the components are expensive or if the size does not allow for such a large number of devices to be tested at one time. A summary of the different component qualifications per device type and for which the different guidelines are applied is provided in Fig. 2.16 [72].

#### Total Ionizing Dose Testing Guidelines

TID testing is performed by exposing a device to an ionizing radiation environment and by measuring its electrical performance for a variety of operating conditions. Two approaches can be used to characterize the response: step stress and in-flux testing. Step-stress testing is performed by first characterizing the electrical performances of the device, exposing it to a fixed dose of ionizing radiation, and then measuring again the electrical parameters to determine their shift. In-flux testing shall be preferred, when feasible, over step-stress irradiation. Nevertheless, some quantities can only be tested through step-stress irradiation (i.e. device reprogrammability, and power-cycle functionalities). When in-flux testing cannot be performed, it is recommended to perform step-stress irradiation by having steps at least 10 times lower than the Target TID. The TID test has to be carried out testing the device up to the RDM established in phase 2. The biasing condition should be the worst one (for re-usability of the data in other applications) or equivalent to the operational one. Two tests are foreseen: high dose rate and low dose rate. The first one has to be carried out with a dose rate in the range of 36 $Gy \cdot h^{-1}$ and 360 $Gy \cdot h^{-1}$ according to ESA-ESCC-22900 standard. For devices containing bipolar technologies, low dose rate tests are mandatory to evaluate ELDRS. The dose rate has to be chosen in the range of 0.36 and 3.6 $Gy \cdot h^{-1}$ according to ESA-ESCC-22900. The device has to be irradiated at room temperature and their temperature has to be monitored during the test.

#### Total Non-Ionizing Dose Testing Guidelines

As discussed in [1], DD testing represents a huge challenge for CERN. Components may have different degradation rates according to the DDEF/TID ratio that they will have to withstand during operation. As shown in Fig. 2.17, the LM334 displacement damage responses change according to the DDEF/TID condition of the test.

To cope with this problem, CERN has developed its own specific DD qualification methodology for components. While different Silicon devices verify NIEL scaling hypothesis (NIEL can be used to scale the DD generated by particles at different energies [74]), there are different examples of optoelectronic devices with different semiconductor materials for which systematic scaling violation was witnessed between high and intermediary energy protons (i.e. Si charge-coupled devices (CCDs) [75], AlGaAs LEDs [76], SiC LEDs [77], and GaAs [78]). Such as the case of the LM334, the qualification using protons could underestimate

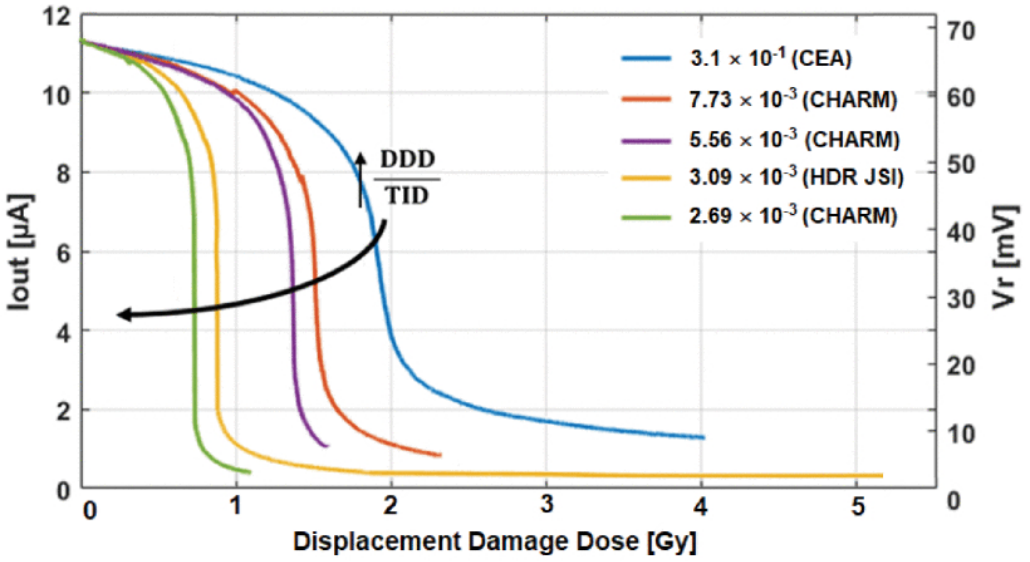


Figure 2.17: The LM334 responses is depicted for different DDEF/TID ratio obtained in different facilities [73].

the degradation in operation.

NASA has proposed its optocoupler test methodology which foreseen tests at different proton energies to evaluate the effective damage factor energy dependency for the component instead of using the NIEL scaling hypothesis based on the data obtained through single energy test [74]. The demand for more realistic and accurate results required by CERN has driven the development of a more robust methodology. This methodology is illustrated in Fig. 2.18. For optocouplers, LEDs and photo transistors [49], once defined TID and DD levels for the environment in which the system will be deployed (Phase 2), the Most Important Electrical Parameter (MIEP), which for this component is the Current Transfer Ratio (CTR), degradation of the device due to DDEF + TID is obtained exposing it to the closest spectrum environment the system will encounter during operation. The TID CTR response is in parallel tested under only the TID effect. Finally, the response obtained allows to extrapolate the CTR degradation due to DDEF only. For Bipolar discrete components, a similar methodology can be applied with a higher level of freedom (Red arrow path in Fig. 2.18). The DDEF + TID response can be recorded under a 200 *MeV* proton beam since the NIEL scaling hypothesis is verified. In this case, the MIEP is the Beta Gain. For Integrated Circuits sensitive to both DD and TID, a methodology based on DDEF/TID ratio tests was proposed in [79] and is depicted in Fig. 2.18. It consists of first identifying the ratio to which the system will be exposed in operation, by measurements or simulations, and second by irradiating the devices to a certain number of ratios representative of the target operational environments.

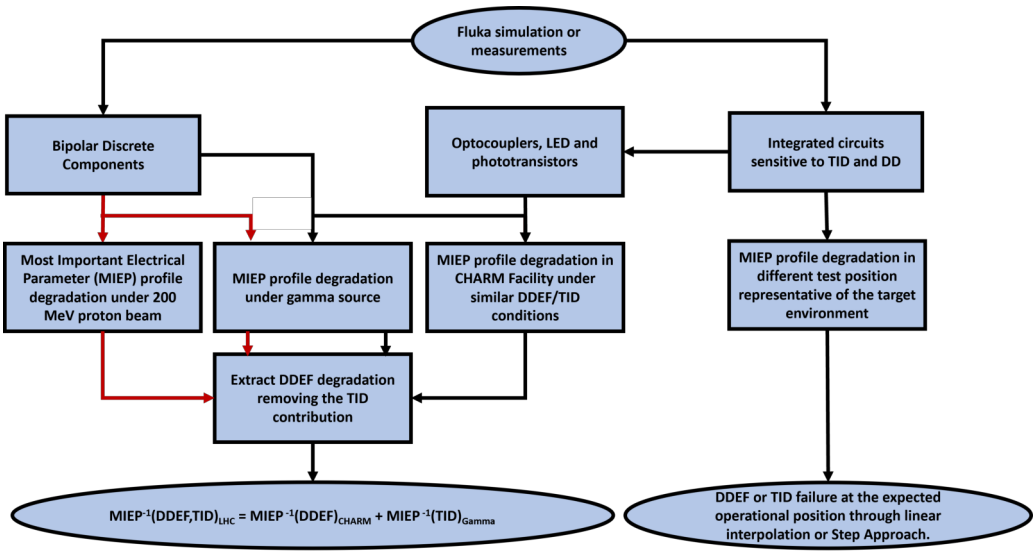


Figure 2.18: This block diagram shows the different methods to extrapolate the DDEF from the knowledge of component responses under DD+TID and TID alone. For discrete bipolar components, two methods can be used: while the TID is recorded under gamma sources, the TID+DD can be obtained using 200 $MeV$ protons or a test environment with a spectrum close to the operational one. This method cannot be applied to integrated circuits due to their complexity, as they may have multiple bipolar components within them, making it difficult to extrapolate the unique degradation due to DDEF. On the other hand, part of the method for discrete bipolar components can be applied to some optoelectronic devices.

This allows to evaluate the $\lambda(R_{DDEF/TID})$. The degradation of a specific operational position can be obtained either by performing a linear interpolation between the two closest failure levels obtained during the test, or through a step approach, keeping the previous failure level up to the second one. The criticality of the components and its sensitivity are the main actors in the choice of the method. Even providing a more realistic degradation evolution of the component, the linear interpolation can underestimate the failure level if not enough test positions are considered. On the other hand, the step approach provides a too conservative result if there are not enough points since the worst case scenario is considered. An example is provided for LM334 in Fig. 2.19 in [73].

Then the final step is to calculate the failure levels (expected lifetime) of the device according to the system requirements against the different ratios and to verify that it is compliant with the radiation levels associated with the different ratios in operation. To do it the following equation (2.3) can be used.

$$Lifetime(x) = \frac{\lambda(R_{DDEF/TID}(x))}{R_{level}(x)} \tag{2.3}$$

Where x is the location in the LHC, $R_{DDEF/TID}(x)$ is the DDEF/TID ratio in this location,

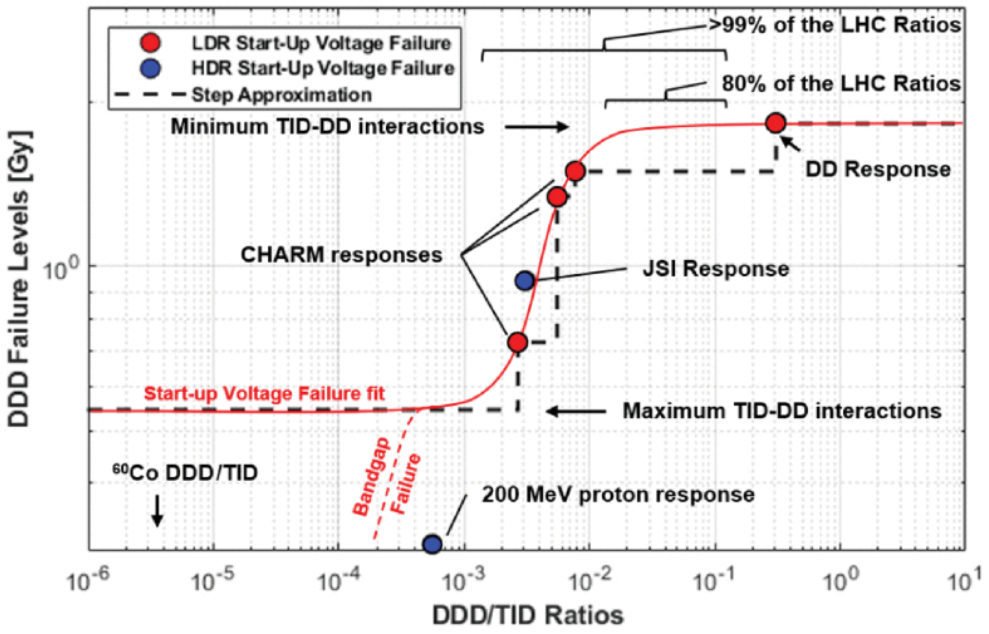


Figure 2.19: For the LM334 device, through the application of linear interpolation and of step approach is possible to extrapolate the $\lambda(R_{DDEF/TID})$ for different DDEF/TID ratio [73].

$\lambda(R_{DDEF/TID})$ is the failure level for this ratio expressed either in $Gy$ or DDEF and $R_{level}(x)$ is the annual radiation levels expressed in the same unit as $\lambda(R_{DDEF/TID})$. In terms of in-flux and step-stress testing, the same rules defined in TID testing guidelines applied to DD.

#### SEE Testing

Devices are normally sensitive to multiple types of SEEs, representing a challenge in SEE testing since multiple tests are required to evaluate the fault risk for each stochastic effect. If SEB and SEGR are considered, it can be noted that the worst case conditions for them are already different and they cannot be tested together. As a consequence for each SEE, CERN RHA foresees a specific testing methodology. For SEB, the test methodology explained in [80] is used and foresees a high resistance between the Drain pin of the MOSFET and the power supply. The value of the resistance has to be carefully chosen to avoid the SEB being suppressed by too high a value. The circuit is tested in the worst case scenario which for SEB is gate biased to have the device turned off and room temperature [20]. For SEGR since there is no method existing, the device cannot be protected from the event occurrence [20]. In this case, the worst gate condition is the room temperature but the gate is biased at the maximum voltage. Since the power MOSFET is destroyed in the case of SEGR, an accurate estimation of its cross-section is possible only by testing a high number of devices. Normally the sensitivity for this SEE is expressed in terms of fluence cumulated up to the

moment of the failure. For SEL the effect can be mitigated by removal of the Bias. Other than the cross-section, the amplitude of the high state current is also measured to verify the possibility of mitigating the event in the final design (Phase 2). For non-destructive SEE the test is carried out by reaching the target fluence and by recording enough statistics. SEFIs have to be removed upon occurrences or by reset or power-cycle. Other than the cross-section, for single SETs it is necessary to measure the amplitude and the duration of each pulse to apply system mitigation if required. For digital devices, the flux shall be as low as to guarantee the independence of the cross-section from the flux. High-flux conditions may induce SEFIs whose rate is strongly dependent on the actual flux. No general worst case pattern exists for SET, therefore it is suggested to test under all the conditions under which the device can operate in the equipment. The worst condition suggested for Soft SEE testing is lower biasing and higher frequency speed possible. For components suspected to contain ($^{10}B$), non-destructive SEEs are also tested under thermal neutron sources to evaluate their sensitivity.

### 2.4.5 System-Level Qualification

A component can be defined as any electronic device that cannot be physically partitioned without affecting its capability of delivering the intended functionality [81] [82]. According to this definition, all designs ranging from the simplest consisting of 2 discrete components up to a complex system such as a satellite, are classified as systems. The competitiveness of system-level testing in terms of cost versus component-level testing makes it very attractive for low-cost, high-risk space missions such as satellites. For this type of space application, the extensive and costly process of component-level qualification poses challenges in terms of scheduling and cost constraints. Conversely, system-level testing offers a potential solution by providing a greater level of confidence in the successful execution of the mission, while also reducing testing time and costs. For COTS custom design, CERN foresees already inside its RHA a system-level-testing phase as a complementary part of the component-level one. The two characterization phases are not considered as two mutually exclusive things, but as complementary steps to have the most reliable system possible, System-level testing goes beyond simply irradiating the system and confirming its functionality at the end of the test. System-level testing allows the verification of the following [82]:

- Functional reliability and availability verification of the current design.

- Functional availability verification of the current design also in terms of embedded firmware.
- If implemented, assessment of the system's self-recovery capacity.
- If implemented, assessment of the efficiency of the mitigation schemes implemented (e.g., transient filtering, TMR, error correction codes).
- Criticalities arising from the radiation effects of individual components or combined degradation of several components.
- Criticalities caused by the design itself.
- Assessment of the need for additional system-level mitigations to be implemented at the hardware or software level.

The achieving of these results is crucial for attaining the availability and reliability targets of HL-LHC and is only possible through realistic and rigorous testing. Despite the importance of this topic and its complementary to component-level testing, CERN's RHA does not provide information on how (testing methodology) to perform this step, but only which facility to use. The mixed field facility of CERN High energy Accelerator Mixed field (CHARM) at CERN facility [83] is a mixed-field irradiation facility designed to qualify entire systems within a realistic field that is fully representative of the mixed-field environment of the high-energy accelerator. This facility will be discussed in more detail later in a dedicated paragraph. However, the absence of a specific methodology for executing this phase is a major limitation that affects the qualification of systems. Another limitation is the absence of an alternative test procedure for this RHA phase in the absence of CHARM. In this research work, one of the main objectives was to develop and assess test approaches for system-level testing and to define a comprehensive system-level qualification methodology that can be used when CHARM is not available (during the Long Shutdown). To provide more information about system-level testing, which is one of the main topics of this research work, its challenges are discussed.

### 2.4.6 Challenges of System-Level Qualification

In system-level tests, four parameters can be distinguished that can be played upon to maximize the test results and make the test as realistic as possible. Those are Testing condi-

tions, the definition of parameters to be monitored during the in-flux testing, flux selection, and test facility selection.

#### Challenges of Representative Test Conditions in System-Level Radiation Testing

As shown, to obtain a better characterization of the component, it is possible to test selecting the worst biasing conditions [80]. For system-level radiation testing, the choice of the most representative test condition for a system to obtain realistic information for availability and reliability is one of its main challenges [82].

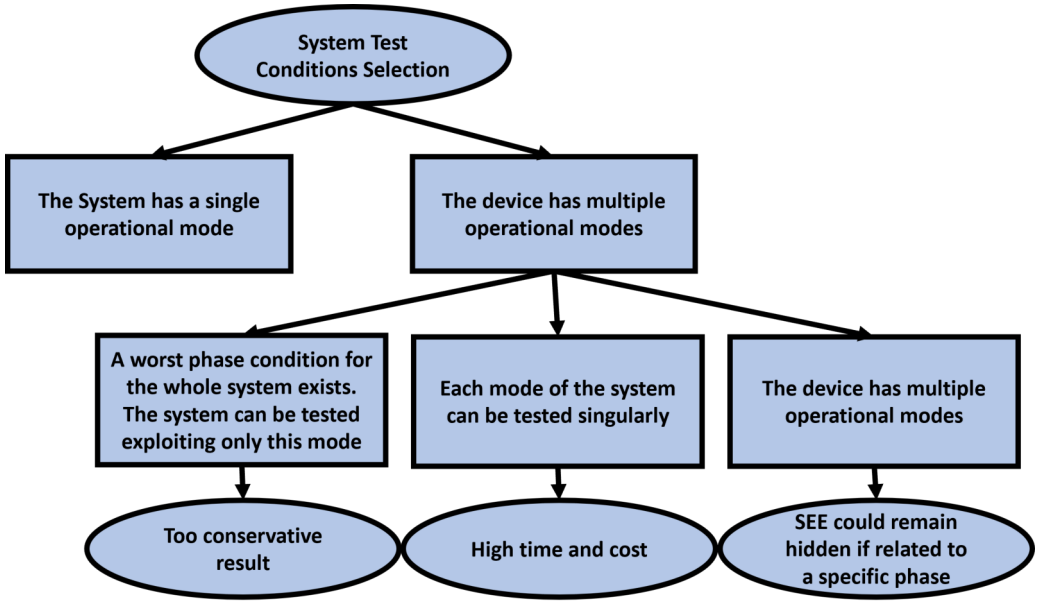


Figure 2.20: The block diagram shows the different Test conditions that can be selected based on the system working modes.

It is uncommon for a system to be exclusively designed for a single working mode, as is often the case that systems operate in different modes. For this type of system, testing in one operational mode may be not representative of its behaviour in operation. A complex system can be made of different subsystems, which may exploit different working modalities during each operation. In a so complex design, all the subsystems rarely exploit their worst case operating condition within a single phase. Therefore, finding a worst case condition for the whole system may be challenging due to the concurrent effects and sensitivities between devices within the system. When the worst case working mode can be identified, the system can be tested by exploiting only this mode. However, the too conservative result obtained could make it necessary to perform another test in a more realistic working mode to meet the target requirements. On the other hand, if the system has a low number of working

phases, it is still possible to test each mode singularly. This approach is time-consuming and costly.

A possible solution could be to test the system in the same way as it will work, thus exploiting all the working phases that are supposed to be executed during operation as it was done in [84]. This approach can lead to underestimating or not detecting existing SEE affecting a component or more in a specific working mode but can be coped with the number of systems tested. A block diagram summarizing the different approaches is proposed in Fig. 2.20.

#### System-level Test: Importance of In-flux Test Parameters Monitoring

During component-level testing, all device pins can be accessed, including those of complex components such as transceivers, FPGAs, and microcontrollers. When these components are connected together in a system, the capability to characterize individual components is often reduced to some extent. As a result, the observability of monitoring parameters (e.g., Voltages, current, etc.) during system-level testing is typically reduced and it may not be feasible to perform tests for every internal configuration of components within the system. The problem of not having access to all points of the design (Point of Observability) is another challenge in system-level testing.

The observability impacts the quality of system-level testing for monitoring of events during irradiation and for assessment of the system health during or after irradiation. The quality of the test is impacted by the number of points of observability. Monitoring of some events occurring during the test, could not be possible during at the end of the irradiation (step-stress test) if test points are not available or not properly chosen. If present, they may allow tracking of failure path cause in the system as it was in [85].

On the contrary of COTS commercial systems, in custom boards with COTS components, since the architecture and software are well known, the addition of observability points at strategic locations is an option not to be missed. The better knowledge on how to monitor specific parameters of the system. The integration of the system itself is the main limitation from the observability point of view since not all the points can be tested. This limitation is not always a problem since not all the parameters of the components are required to be monitored and by implementing dedicated interfaces, it is possible to monitor the most critical parameters of a system [86].

The absence of Points of observation can have a strong impact on SEEs rather than cu-

mulative effects in system-level testing. For the latter, the step-stress test can still allow to evaluate of the cause of failure by checking the parameters (through measurements on the board) at the end of each step test. SEE evaluation needs in-flux testing, and thus not having a point of observability will make them invisible during the tests. However, even in the case of cumulative effects, it could be difficult to detect the cause of failure without points. This is the case in [87], even if the system was still working at the end of the test, it was not possible to track the source of functionality errors occurring during the run.

#### Impact of Flux Selection on System Characterization

When component SEE sensitivity data are not available, the flux should be ramped up only when flux-dependent events are not observed [82]. However, there are challenges in this approach. Firstly, the flux may not always be tunable to the desired value, and secondly, the limited availability of experimental time may cause testers to select a higher flux level to obtain higher statistics and reach the target fluence. In the qualification of a system but also of System-on-Chip (SoC), choosing an inappropriate flux can result in the invalidation of a test. Several examples of flux-dependent effects can be found in the literature.

An SRAM-based FPGA can be affected by SEUs in Configuration RAM (CRAM) and for this reason, are supported by correction modules to mitigate these effects. Unfortunately, their effectiveness can be influenced by the flux of the radiation environment. Different examples can be found in the literature. In [88], the qualification of an SRAM-based FPGA is carried out to assess its suitability for non-critical CERN applications. The cross-section of its CRAM is rated in different radiation environments. As a mitigation scheme, a commercial scrubber of Xilinx ((Soft Error Mitigation (SEM) controller) is employed. If a Single Bit Upset (SBU) is detected, it corrects the error and triggers a report. The cross-section is evaluated in two different flux conditions: under a 25 $meV$ equivalent neutron flux of $1.37 \cdot 10^8$ $n \cdot cm^{-2} \cdot s^{-1}$, during which the SEM crashed during the test due to the high flux, and a lower one of $1.2 \cdot 10^6$ $n \cdot cm^{-2} \cdot s^{-1}$, where it worked properly during the whole run. COTS Microcontrollers (MCU) and Microprocessors are also component flux-dependent. Since they are called upon to perform many complex operations, if the flux is not selected properly, the ICs can stop working before completing their tasks and provide results significant for the test. An example is provided by the usage of benchmarks and, CoreMarks [89] to evaluate the performance of CPUs. Coremark is an open-source general-purpose benchmark that presents a very representative set of operations for the most common microcontroller work-

loads. Normally it consists of 3 main operations: memory access, Arithmetic Logic Unit (ALU) operations, and branch operations. Its final result has two important parameters, the result and a normalization factor which is the number of iterations per second. For the test under radiation, it is clear that the selected flux impacts the number of iterations chosen. In [90] the performance of a microcontroller implemented in a flash-based FPGA is evaluated through a Coremark of 201 iterations which takes about twelve minutes to be completed. When no hardening in the design was implemented, the number of iterations chosen combined with the high (respect the MCU cross-section) test flux of $5.6 \cdot 10^6\ n \cdot cm^{-2} \cdot s^{-1}$, caused the 25 % of the iterations to timeout requiring an external reset. From this example, it is possible to observe that the choice of a not optimal flux can invalidate part of the test and not allow all iterations to be completed correctly, requiring a reset of functionality.

Another example of flux dependency can be observed in [91]: an Ethernet-based solution on an SoC, in which a flash-based FPGA and an MCU coexist, is tested under radiation. The performance of the communication protocol is evaluated through different configurations. Tests are carried out under a 200 $MeV$ proton beam and at the CHARM facility. In the first case, a higher bit error rate cross-section is obtained, which is related to the dependence of the protocol on the flux and data rate. The flux selected may not only impact system behaviour during testing in terms of a lifetime but it can also invalidate the verification of the mitigation scheme implemented in the design which is one of the main features when performing system-level testing. In the EDAC (a Single-Error Correct and Double Error Detect (SECDED)) scheme the probability of a failure may depend on the flux selected since only one-bit error can be corrected while two bit-flips can only be detected [92, 93]. Some techniques exist to evaluate if a system or a component is flux dependent. An example is the "tri-flux" test developed by the Jet Propulsion Laboratory (JPL) [94, 95, 96]. In this method, the predicted failure rate and the measured failure rate of the mitigation scheme are compared for different fluxes. When the curves do not match, there could be a secondary failure mode affecting the system or a breakdown of the mitigation scheme [92]. Flux dependency can affect both the result of the system and the verification of mitigation schemes. The problem of flux selection is a big challenge of system-level testing. Testing at low flux would be time consuming and extremely expensive. On the other hand, a test at high flux could lead to invalid results as it was shown in the different examples provided.

The selection of the flux is also closely related to the problem of observability within a certain range. In [88], it was possible to determine the cause of failure because the system

was a 'simple' one. In a more complex one, the cause of the error may remain hidden and only the selection of an appropriate flux could improve the detection of the fault part. Another problem with flux selection can occur in a complex system based on several working modes. If the system is more sensitive to SEE in one specific working condition than in others, this mode may mask the failure mode that only appears in the other phases, making it difficult to observe.

**In this research work, part of the investigation focused on demonstrating the existence of a dependency between SEE observability and flux selection and the development of a flux selection methodology to optimize the observability of SEE failures within complex systems based on different operating modes. It will be dealt within Chapter 4**.

## 2.5 Test Facilities

The main factor determining the facility selection is the desired homogeneity of the beam, both in terms of depth and over a sufficiently large area. According to the existing standards, to achieve uniform irradiation of a system, homogeneity must be kept within a range of $\pm$ 10 %. Achieving homogeneous irradiation in depth is crucial and can only be achieved with highly energetic and penetrating beams. It is important to choose a beam that does not fragment significantly as it passes through the different layers of matter. Reduction of the beam intensity and change of its composition are triggered by the fragmentation process.

For component-level testing, CERN RHA foresees different facilities as was depicted in Fig. 2.16. For system-level testing, however, the selected facility to have more realistic results of the future operation is CHARM. The different facilities are discussed in the next paragraphs.

### 2.5.1 Paul Scherrer Institute PIF Facility

The Proton Irradiation Facility (PIF) is located at the Paul Scherrer Institute (PSI) in Villingen (Switzerland) and was built in cooperation between PSI and ESA [97]. The proton beam is provided by the cyclotron-type accelerator COMET to PIF with a maximum of 230 $MeV$ energy. Energy can be lowered up to 10 $MeV$ through the use of various Cu plates. The maximum and minimum usable current is 10 and 0.1 $nA$, above and below which the beam is unstable. A current of 10 $nA$ corresponds to a 230 $MeV$ and a proton flux of ~$2{\cdot}10^9$ $p \cdot cm^{-2} \cdot s^{-1}$


Figure 2.21: PIF irradiation room with 5 *cm* collimator mounted.

and scales linearly with the current. The beam size and shape can be modified through a copper collimator whose max diameter is 9 *cm*.

Two ionization chambers upstream and downstream of the collimators are calibrated to measure the beam flux at the position of the DUT by comparing their counting with the output of a scintillator detector. The beam profile is typically flat within ~20 %.CERN uses this facility for the component-level qualification for TID, DD, and SEE testing.

### 2.5.2 Institute Laue - Langevin TENIS Facility

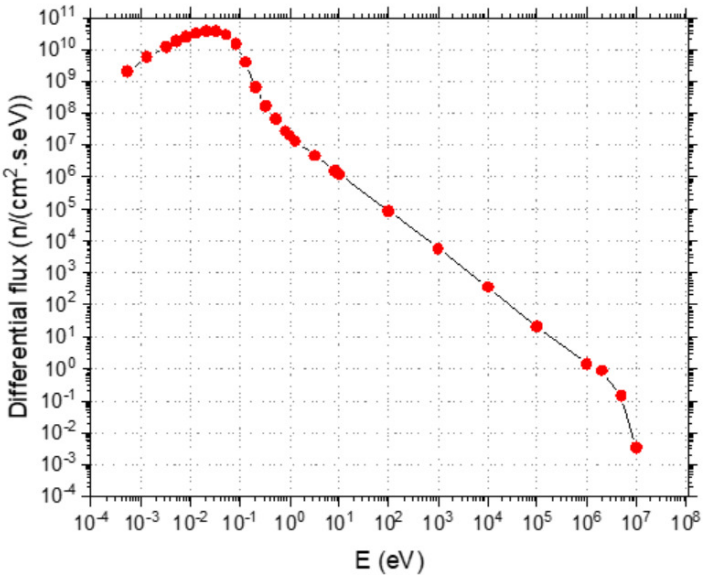


Figure 2.22: Beam characteristic: fission spectrum at TENIS.

The Thermal and Epi-Thermal Neutron irradiation Station (TENIS) is located at Institute Laue - Langevin in Grenoble and has been re-adapted for Radiation to electronics qualification [98]. A neutron field with a fission spectrum is extracted from the reactor core and delivered to the test position. A non-negligible gamma photon contribution is also present. Gold foil activation measurements performed by the facility showed that the equivalent flux of thermal neutron (25 $meV$ equivalent at nominal reactor power 58.3 $MW$) is ~2.8·$10^9$ $n \cdot cm^{-2} \cdot s^{-1}$. This flux is 60 % composed of pure thermal neutrons and 40 % of epithermal neutrons. In Fig. 2.22, the spectrum is shown. The Beam Size is ~3 $cm^2$ but the beam profile is typically flat within ~20 % of 2 $cm^2$ as it is visible in Fig. 2.23. The facility is used by CERN for components SEE testing but also for the calibration of Th detectors [55].

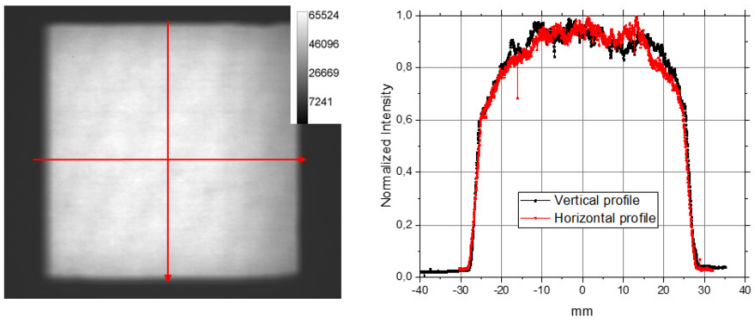


Figure 2.23: Beam Size and homogeneity.

### 2.5.3 CERN CHARM Facility

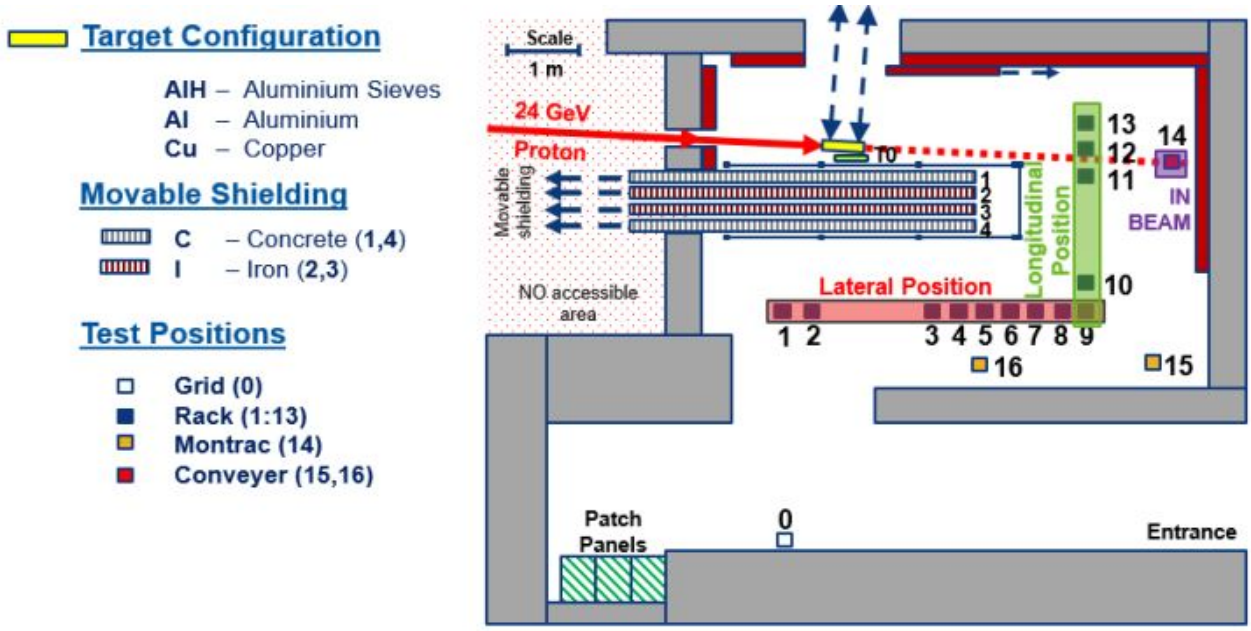


Figure 2.24: Layout of the CHARM facility in which the 17 test positions are depicted.

CHARM is a mixed-field irradiation facility designed to qualify entire systems within a realistic field that is fully representative of the mixed-field environment of the high-energy accelerator [83]. The layout of the CHARM irradiation room is depicted in Fig. 2.24. The complex mixed field that characterizes the facility is generated through the interaction of a mono-energetic 24 $GeV$ proton beam and a target. The facility is configurable: 3 types of target (Copper, Aluminium, and Aluminium Sieves), 4 movable shieldings of 20 $cm$ thick (2 of Iron and 2 of Concrete), and 14 different testing positions allow testing under different representative spectra in terms of radiation to electronics effects different TID/DDEF ratio and R factor in a room of 70 $m^3$. The different positions are available through different installation supports. In position 1-13 the setup is installed on a rack moved using an automated conveyor system. In position 15 or 16 it is installed on a mini rack moved by an overhead conveyor. in position 14, the system is mounted on the Montrac movable through a rail system. The test area interfaces with the control room using a patch panel with an array of different connections (same on the control room side). In between, there are ~40 $m$ of cables. The beam is pulsed (~10 $s$ between each Spill) with a quasi-uniform-spill lasting roughly 350 $ms$ and made of $5 \cdot proton \cdot spill^{-1}$ [99]. The radiation levels for TID, DDEF, HEH, and Th normalized per day are depicted in Fig.2.25. As it is visible, the positions close to the target have radiation characterized by higher levels. It can also be noted that in the position close to the target, using the Aluminium one higher values of TID, DDEF, and

HEH are obtained compared to the Copper one. This is due to the higher density of Copper, which deflects more particles. Irradiations normally last 5 days and the dosimetry is provided by the means of RadMon [68] or through the usage of calibration factor evaluated at the beginning of the year using the latter instrument.

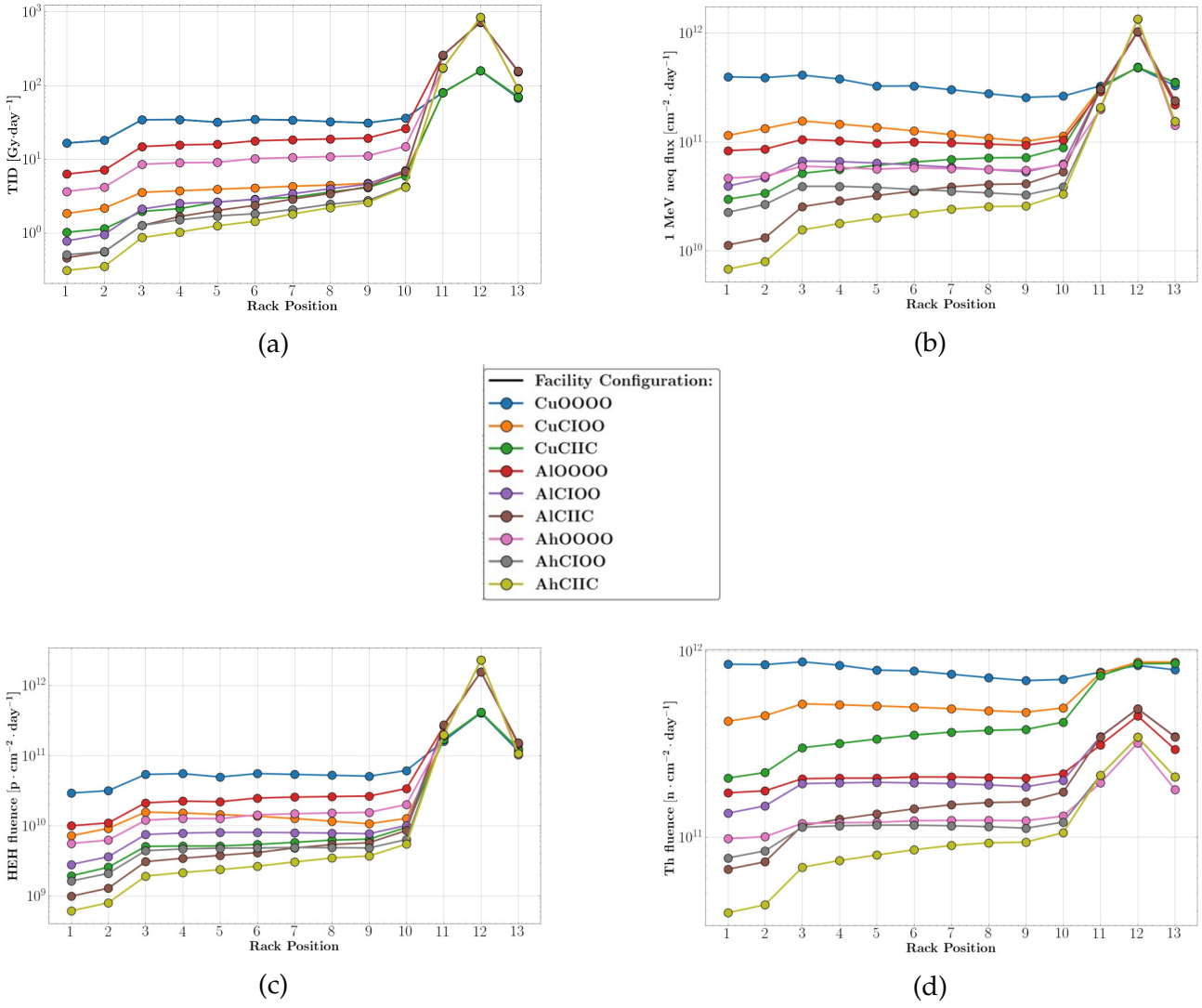


Figure 2.25: TID (Fig. 2.25a), DDEF (Fig. 2.25b), HEH (Fig. 2.25c) and Th (Fig. 2.25d) for different positions and configurations at CHARM facility from FLUKA simulation [100]. The first two letters are used to define the target (Cu: Copper, Al: Aluminium, Ah: Aluminium with holes) and the last four to define the shielding (O: no shielding, C: Concrete shielding, I: Iron shielding).

### 2.5.4 CERN Co60 Facility

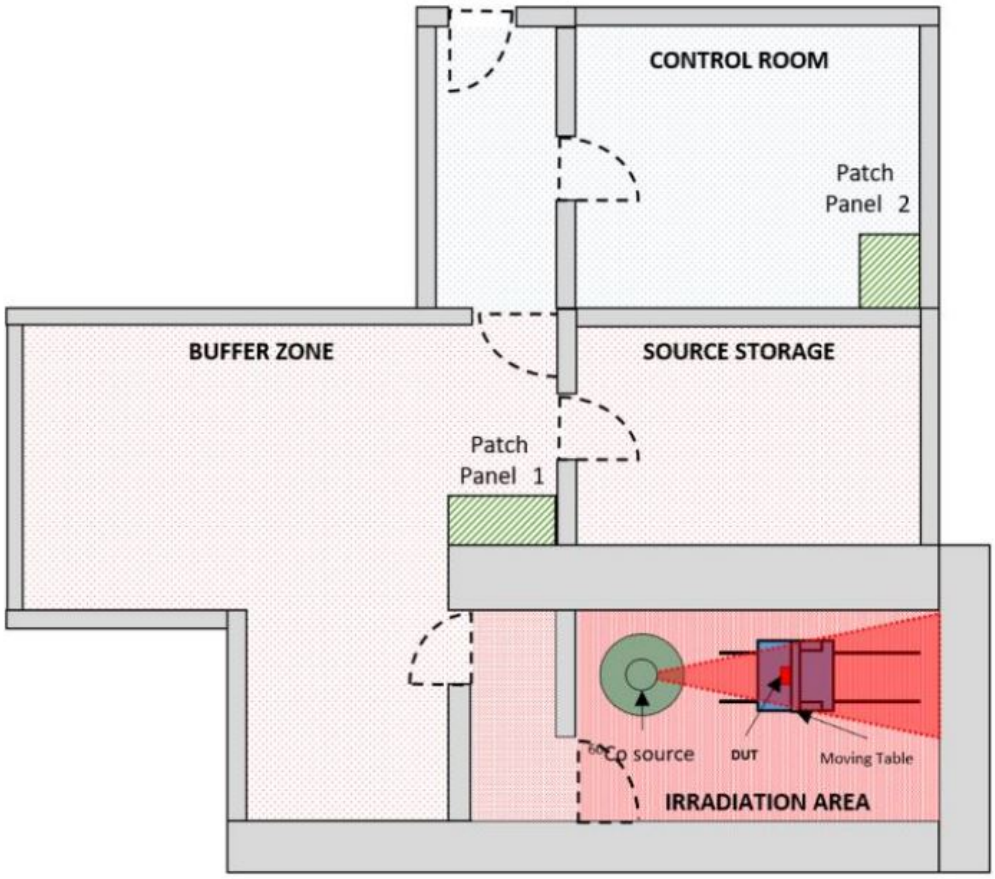


Figure 2.26: Layout diagram of CERN's Co60 facility with emphasis on the irradiation area. The irradiated area is indicated in red. A moving table is used to bring the device under test closer to the source point.

The CERN Cobalt-60 (Co60) facility is located in the French CERN complex [101]. It is a type of irradiation facility very common and several can be found in Europe. It exploits the decay of $^{60}Co$ isotopes into 60 Nickel isotopes through the emission of beta particles. The highly activated nickel nucleus emits two gamma rays with an energy of 1.172 and 1.332 $MeV$ to reach the stable ground state. At this energy, the gamma radiation is considered to have enough penetrating power to pass the devices. Concerning the source point, the dose rate reduces with distance squared. The facility allows irradiating devices from a minimum dose rate of 120 $mGy \cdot h^{-1}$ on a surface of a 100 $cm^2$ area up to 20 $Gy \cdot h^{-1}$ on a surface of a 20 $cm^2$. It is possible to reach a dose rate of 650 $Gy \cdot h^{-1}$ on a surface of a 3 $cm^2$ mounting the device on support available on the sarcophagus aperture. An air-filled ionization chamber is used to measure the dose in the position of the test device before starting the test. A layout of the facility is depicted in Fig. 2.26.

### 2.5.5 PTB - PIAF Facility

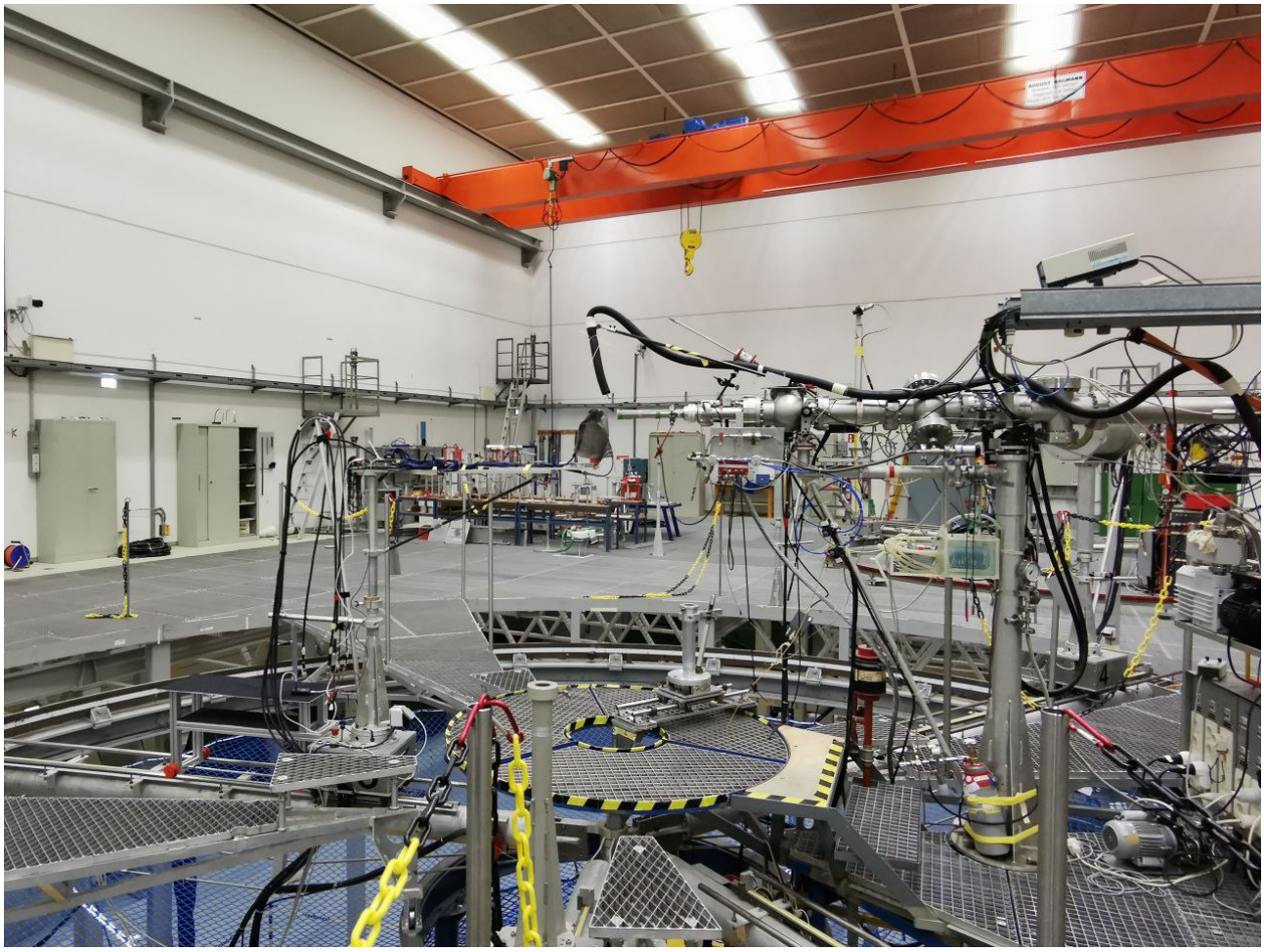

Figure 2.27: Image of the irradiation room of PIAF. A device is mounted in the Center in front of the source.

The PIAF facility of the Physikalisch-Technische Bundesanstalt (PTB), the national metrology institute of Germany [102, 103, 104, 105] is a low and intermediate neutron facility able to provide energies from 24 $keV$ up to 19 $MeV$ [105]. The monoenergetic neutron spectrum is obtained by the nuclear interactions of light ion beams (proton (p) and deuteron (d) gas) with a target of lithium (L) deuteron (D) or tritium (T). To avoid scattering with wall floor and ceilings, the irradiation room is 24 x 30 x 14 $m^3$ and the beamline is located in the middle as visible in Fig. 2.27. The different energies and corresponding flux for this facility are reported in Table 2.7. This facility is not used normally to test electronic devices. It is normally used to calibrate dosimeters. CERN uses it to evaluate the response of SRAM detectors [106].

Table 2.7: The different neutron reactions of PIAF with corresponding energy ($E_n$), flux ($\phi_n$), and distance [107].

| Reaction | $E_n$ [MeV] | $\phi_n$ [$cm^{-2} \cdot s^{-1}$] | Distance [cm]) |
|---|---|---|---|
| 0.144 | Li(p,n) | $4 \cdot 10^5$ | 5.5 |
| 1.2 | T(p,n) | $1.8 \cdot 10^6$ | 5.5 |
| 2.5 | T(p,n) | $1.9 \cdot 10^6$ | 5.5 |
| 5 | D(d,n) | $8.2 \cdot 10^5$ | 6.6 |
| 8 | D(d,n) | $2.7 \cdot 10^6$ | 6.6 |
| 17 | T(d,n) | $5.2 \cdot 10^5$ | 2.5 |

### 2.5.6 JSI TRIGA MARK II

At the JSI TRIGA (Training Research Isotopes General Atomics) Mark II research reactor it is possible to irradiate components and system using neutrons and gamma-rays [108]. The different irradiation positions have been extensively characterized by the use of dosimetry fission and gamma ray flux measurements [109] and Simulation [109]. The neutron environment is very attractive for the CERN experiment and has been used already for components RHA [49] in an alternative of CHARM. The irradiation positions are depicted in Fig. 2.28.

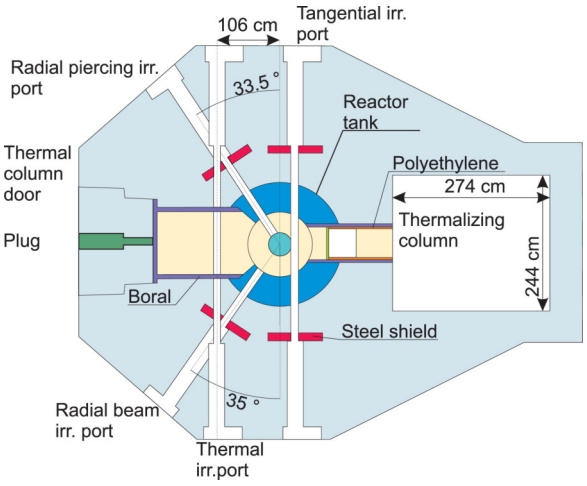


(a) Top view of the JSI TRIGA Mark II reactor [108]

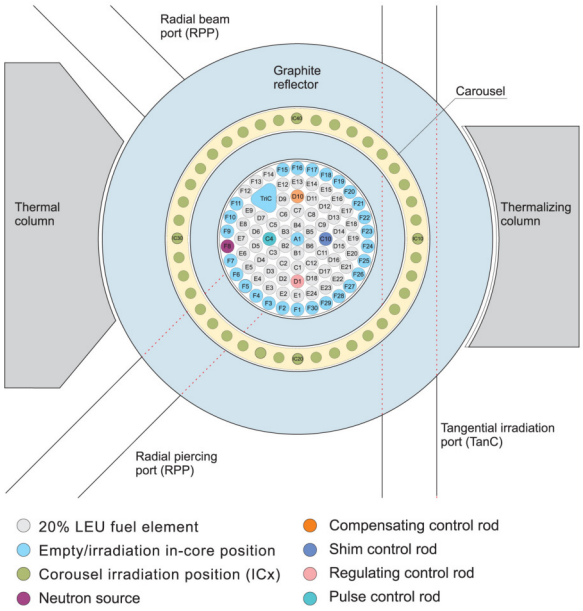


(b) Top view of the JSI TRIGA Mark II reactor core [108]

Figure 2.28: The layout of JSI TRIGA Mark II reactor, with Thermalizing and Thermal column in Fig. 2.28a. A layout of the only core with the different test position is shown in Fig. 2.28b.

Not all the testing positions available can host large electronics. Inside the reactor tank,

40 cylindrical positions with a diameter of 3 $cm$ and a length of 23 $cm$ are available. Outside the reactor core, the two largest positions can be used for large equipment tests (the Thermal and the Thermalizing columns). At full power, the reactor can provide a neutron flux ranging from ~1 to $6 \cdot 10^{12}$ $p \cdot cm^{-2} \cdot s^{-1}$. In terms of dose rate from 50 to 150 $kGy \cdot h^{-1}$. Then the radiation levels can be decreased by reducing the nuclear power reactor. With a power of 0.5 $kW$, a dose rate of 0.5 $Gy \cdot h^{-1}$ and flux ~$4{\cdot}10^{6}$ $p \cdot cm^{-2} \cdot s^{-1}$ are provided [108]. The lethargy spectra for the different irradiation positions is shown in Fig. 2.29.

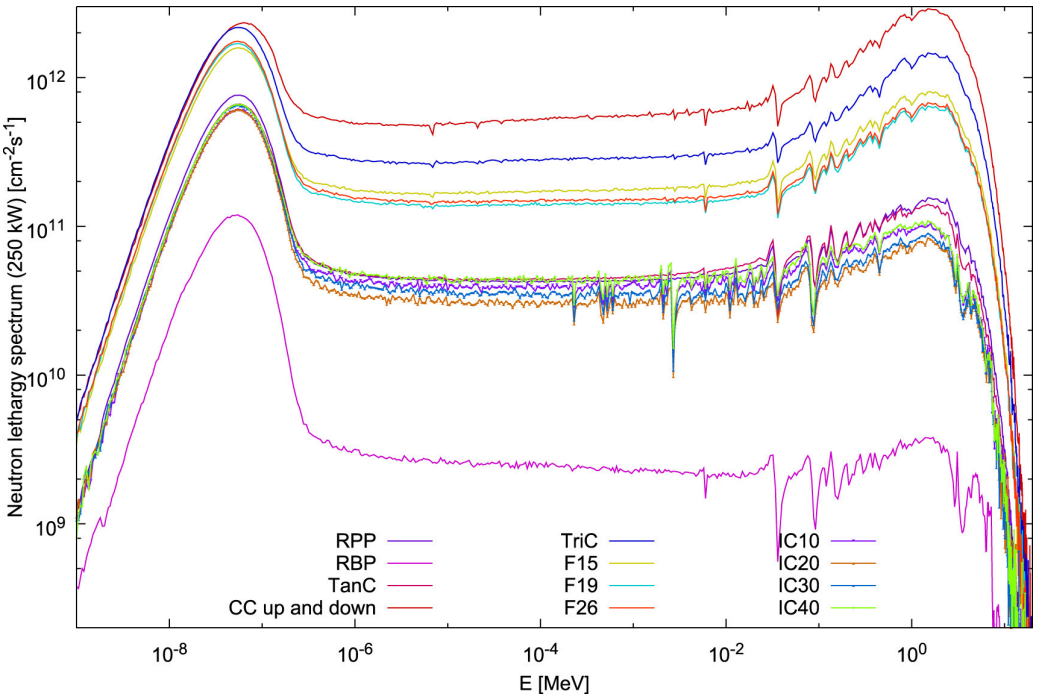


Figure 2.29: Neutron lethargy spectra are depicted for different test positions when JSI TRIGA reactor operating at full power (250 $kW$) [108].

## 2.6 Chapter Summary and CERN RHA Challenges

In this chapter, the concept of RHA was introduced and the corresponding procedure developed by CERN to improve the availability and reliability of the electronic equipment used in its accelerator chain was analyzed in detail. To understand its impact on machine operation, the structure and the working principle of the LHC were first presented in Section 2.3. As it turned out, to increase the probability of having relevant results for the organization, there are two possible ways: either by increasing the instantaneous luminosity (higher beam intensity through Machine Upgrade) or by improving the availability of the accelerator. Both actions lead to an increase in the radiation levels to which the electronic systems are subjected. Consequently, the availability of the machine may be reduced by the failure of the electronic systems due to the higher radiation level experienced.

Shielding and relocation of equipment, as described in Section 2.3, is not always possible and therefore equipment must withstand radiation effects. At the same time, the use of custom boards with COTS components and Commercial COTS systems, the distributed nature of systems, and their large number within the machine could make it very difficult to achieve the objective of maximizing its availability. To counteract these radiation increases and maintain optimal machine performance, the only available means is a proper RHA procedure. CERN followed the latter strategy and developed its own procedure for the accelerator sector, introduced in Section 2.4. The most important steps of this procedure have been discussed in dedicated sections.

As far as the system-level testing phase is concerned, this analysis has shown that the process still has weaknesses but a great margin for improvement. While great efforts have been made to implement component-level test methodologies that allow standardization and reliable results, system qualification is still a weak and non-standardized phase. As described in Section 2.4.5, the current CERN RHA only suggests "where" to test, not "how".

Another major limitation of the current RHA is that CHARM is not always operational, and this is particularly critical during the LS, which lasts several years (the facility is unavailable for the entire period). In addition, the number of test slots available in the facility during the operational part of the year is also limited. Therefore, the qualification process of a system could be very slow and the repetition of Phase 4 could take years due to the unavailability of the facility. Therefore, in order to cope with the limited availability of CHARM, the number of tests required for a system to pass Phase 4 must be reduced and optimized

as much as possible. The only way to achieve this objective is to ensure that this phase is carried out as accurately as possible. As described within the Chapter, if system-level testing is not performed correctly (for example, incorrectly selected flux, reduced observability of possible causes of failure or unrealistically tested system), the benefits of this testing methodology defined in Section 2.4.5 cannot be exploited, and the risk of failing this phase increases. On the other hand, if the test is performed correctly, there is a greater chance of finding the cause of the problems observed during the test and of passing this phase at the next attempt. An alternative and reliable methodology (as the current one) to complete Phase 4 without CHARM and test guidelines that can answer the questions of "how" to perform this phase are essential. The development of this testing strategy, as an alternative to the use of CHARM, will enhance the system-level testing capability, allowing testing to be carried out during the LS period.

In addition to the above-mentioned issues, with the next LHC upgrade, with a predicted luminosity of 300 $fb^{-1}$ per year, radiation levels are expected to increase enormously. In the safe areas, where most of the electronics are hosted, annual radiation levels will no longer be negligible or tolerable as in the past. For example, a TID of 10 $Gy$ in UJs is expected during a year of HL-LHC operation, which is much higher than the 0.4 $Gy$ experienced in 2018. This also has an impact on the whole process, increasing the requirements and the number of systems to be qualified and making them difficult to meet when large RDMs (factor 2 or 3) are applied. In this case, in order to avoid or significantly reduce the use of RDMs and continue to obtain reliable results, it is necessary to improve methodologies at the system level, as this is the phase with the greatest room for improvement.

A more accurate estimate of the radiation requirements obtained from CERN RHA Phase 1 would also help to reduce the RDMs and meet the challenges of the HL-LHC in terms of the RHA process. As described in Section 2.4, this phase is crucial to the whole RHA process, as the requirements for a system are based on its analysis. Currently, as described in Section 2.4.2, the only instrument capable of providing all the radiation to electronics quantities requires to characterize an area of the accelerator, is the RadMon. However, this system has several operational limitations in terms of infrastructure integration and mobility. As a result, rapid deployment of this application is difficult, and a network of highly distributed RadMon around the LHC is complex to set up.

For these reasons, CERN has decided to develop a new Wireless Radiation Monitoring System capable of overcoming all the limitations of RadMon and drastically improving the

RHA Phase 1. This system thanks to its improved mobility and fast deployment will help to improve the Radiation Environment Analysis phase covering a higher number of points of the accelerator. Its use will also benefit the FLUKA simulations themselves, allowing benchmarking and reducing their uncertainty. This system is presented in Chapter 3 and the benefits of its development are demonstrated by the operational cases presented in Chapter 5.

Regarding Phase 4 improvements, the new system's qualification (Chapter 3) presents an ideal opportunity to develop and validate an alternative procedure for executing this RHA phase and to assess the functionality of a system when CHARM is unavailable. This new procedure will complete Phase 4 providing the possibility to qualify a system without CHARM and increasing the number of system-level tests possible. This will result in a more accurate procedure and more reliable results. The practical examples of system-level testing presented during the qualification process of the new platform, provide insights into how to perform system-level qualification in radiation test facilities when irradiation of the entire system is not feasible. This provides a comprehensive overview and guidance for the qualification process.

Finally, within the context of testing at the system-level and enhancing result reliability, Chapter 4 of this dissertation analyses the relationship between flux selection and fault observability. The impact of this investigation is significant in a context such as the accelerator, where there are a large number of distributed systems. In this context, it is crucial to reduce the possibility of low-probability failure modes to a minimum in order to avoid their occurrence during operation. The impact of their occurrence would be significant, requiring re-qualification of the system to identify the failure. In such cases, without a methodology, replication of the fault could be very complicated, as will be shown in Chapter 4. Therefore, Chapter 4 is dedicated to the definition of a methodology for selecting the most appropriate flux to decrease testing time and improve the observability of low cross-section failures. This in turn will improve the reliability of the CERN RHA procedure.

# CHAPTER 3

# A New Radiation Wireless Monitoring System for the LHC: Design and Radiation Qualification

In Chapter 2, the CERN RHA procedure and its main limitations were presented. As pointed out in Section 2.6, with the higher radiation level expected with HL-LHC, it will be more complex to complete this procedure using large safety RDMs. It is therefore necessary to reduce these while maintaining the reliability guaranteed by the current procedure.

With the aim of improving the overall qualification process, the system-level testing phase has been highlighted as the one with the highest potential for enhancement. Unlike the component-level testing, this phase is non-standardized and has a "structural" limitation tied to the availability of CHARM. These weaknesses affect the quality of the test phase and prevent the execution of a high volume of tests in a short period of time.

At the same time, in order to decrease the RDMs applied for the system requirements definition, it is imperative to enhance another aspect of the process, specifically Phase 1. As outlined in Chapter 2, this Phase marks the beginning of the full RHA procedure, and the uncertainty on the radiation requirements and thus the choice of RDMs, depends on its outcomes. Among the various instruments available for measuring radiation levels within the accelerator and extrapolating the relevant values for CERN's operational requirements (Phase 2), RadMon is the only instrument that can measure all the radiation to electronics effects. However, this instrument has some limitations that prevent its quick deployment and limit its distribution within the LHC.

The demand for increased mobility, flexibility, and cost-effectiveness has driven the development of a novel Wireless IoT radiation monitoring system for electronics, also called BatMon, designed to overcome the drawbacks of the RadMon instrument. This platform will allow measurements in locations where the mobility of RadMon falls short, while also allowing for the deployment of a larger number of devices in a shorter period of time, thus extending coverage to more areas of the accelerator. These enhanced capabilities will, in turn, improve the simulation estimates through benchmarking with system measurements, thereby reducing their uncertainty. These operational benefits will enable Phase 1 to provide estimates with less uncertainty and consequently, reduce RDM without compromising the quality of the process itself.

At the same time, the qualification of the system will validate a new system-level test procedure developed as an alternative to CHARM. This alternative procedure will allow Phase 4 to be completed in the absence of CHARM and will also allow a greater number of tests to be performed. The practical examples of system-level testing presented during the qualification process of the new platform, provide insights into how to perform system-level qualification in radiation test facilities when irradiation of the entire system is not feasible. This provides a comprehensive overview and guidance for the qualification process.

The chapter focuses on two main topics and is structured accordingly. The first part details the system design choices driven by the need to address the limitations of RadMon. The second part outlines an alternative system-level testing methodology, whose effectiveness is demonstrated through its direct application to the new system.

Furthermore, the chapter explores the benefits and limitations of implementing an IoT network within the framework of particle accelerators. In particular, as the newly developed wireless system is the first instance of an IoT device at CERN, it will demonstrate the network's feasibility in a particle accelerator.

The content of this Section refers to the two publications [98] and [110].

## 3.1 RadMon V6: Limitation

This section outlines RadMon's limitations, classified under Operational, Sensor Capabilities, Electrical, and Radiation Tolerance. Understanding these limitations, is crucial for introducing the design choices made for the new Wireless IoT system, outlined in Section 3.3.

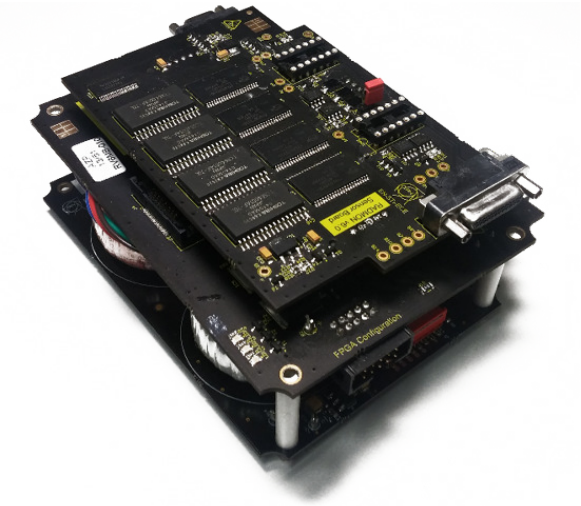

Figure 3.1: The RadMon V6.

### 3.1.1 Operational Limitation

As highlighted in Section 2.4.2, CERN RHA foresees a Phase (Radiation Environment) during which the expected radiation level for all the operational environments within the system will be used, are analyzed. These analyses are fundamental to defining the radiation requirements of the systems that will go through the RHA process and are carried out by simulation or real measurements. The latter are fundamental to anticipate electronic degradation, benchmark simulations, and help in the investigation into the cause of failures. Between the different instruments used by CERN to carry out these studies presented in Section 2.4.2, the RadMon is the only one capable of measuring all quantities related to radiation effects on electronics (TID, DD, HEH, and Th). This system is fully integrated into the CERN infrastructure [79]. To work it requires two cables: a power cable and a communication cable, which is connected to Front-End Computer (FEC). The protocol used is the worldFIP [111], in which up to 32 devices can be connected to the same Fieldbus [68]. The use of cables gives the system low mobility and, together with the complex infrastructure in which it is integrated, makes it slow to deploy. The low mobility and the complex infrastructure makes difficult the quick deployment of RadMons. During the operation of the

LHC, it is very common for users to request measurements in places where RadMons are not installed. Satisfying these requests can be very challenging, especially when it is necessary to track failures of specific equipment or evaluate the effectiveness of shielding. Limitations arise from the limited time available to deploy new cables or register a new RadMon within the current infrastructure. For these operational cases, a wireless battery powered radiation monitoring system could represent the perfect solution. However, implementing such a solution presents several challenges that need to be addressed:

1. Wireless communication: finding a wireless communication technology with a range of a few hundred meters to several kilometers, while maintaining a data rate of about 1 $kB$ per hour.

2. Low power electronics: having a system battery capable of functioning for at least one year requires the use of low power components or capable of reducing their power consumption when needed. This type of component introduces new challenges in terms of radiation qualification, requiring dedicated testing strategies, which are currently not addressed by CERN RHA.

3. Radiation tolerance and sensitivity: ensure that the new system meets or exceeds the radiation tolerance and sensor sensitivity capabilities achieved by RadMon.

4. Infrastructure integration: integration of a new system into its dedicated infrastructure must be simple in terms of device preparation and short in terms of time, allowing for quick deployment of new devices.

5. Low cost: all the above requirements must be met while keeping the cost of the application low using COTS components.

### 3.1.2 Radiation Sensor Limitation

As reported in [112], the HEH sensor used by the RadMon is the 8 $Mb$, 90 $nm$, Cypress SRAM CY62157EV30. An effect called burst was discovered in this memory, which consists of read corruption caused by the arising of Multiple Cell Upset events, characterized by a non-negligible number of SEUs. This event was never experienced during the calibration phase and therefore, there was no mitigation applied when it first appeared. Initially, it was thought to be related to the specific radiation operating environment, but then it was

observed that burst events were occurring in most of the system. This event is potentially harmful because, by corrupting the SEUtot number, i.e. the total number of SEUs recorded throughout the irradiation period, it leads to erroneous data reading and loss of precision. The burst can be divided into two categories [113]:

1. Type A: particles passing through the sensitive volume of the memory array generate clusters with a low SEU number by inducing currents in neighboring cells. Referred as type A are depicted in Fig. 3.2a.

2. Type B: cluster that comprises a larger number of SEUs located in adjacent rows over the entire width of the memory block (8 $B$). Generated by micro-latchups in the address sector, they have a roughly rectangular shape, as shown in Fig. 3.2b. They are referred to as type B [112].

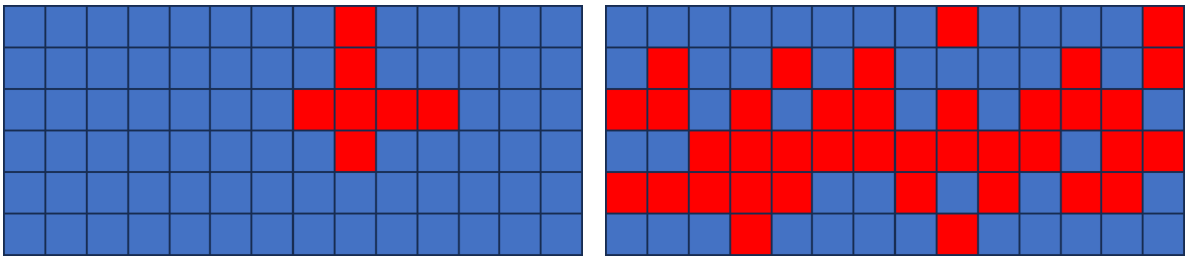

(a) (b)

Figure 3.2: On the left (Fig. 3.2a) an example of Type A cluster. On the right (Fig. 3.2b) an example of Type B cluster. [1].

To detect and mitigate bursts inside the RadMon, a specific algorithm was developed and is described in [112]. The different addresses are read row by row and block by block, along both the direction (top to bottom and bottom to top) of the chip, accessing the SRAM through a descrambled reading scheme called physical addressing. A threshold SEU value ($Th_{SEU}$) is used to is used to determine the occurrence of a burst event. If, during a sector reading, the number of measured SEUs within the same sector exceeds this threshold, the event is classified as a burst. The optimum value of this threshold was studied in [112] and observed a good trade-off was found with a value of $Th_{SEU}$ in the range of 30 to 40. The RadMons installed in the LHC implement this algorithm and are able to detect and mitigate bursts above the defined $Th_{SEU}$. This algorithm effectively mitigates type B clusters, but its efficiency for type A depends on the radiation level of the monitored area. In areas with a high number of SEUs, their distribution is similar to that obtained during calibration, so

they are taken into account by the cross-section used. In areas with a low numbers of events, the appearance of a type A cluster has a greater impact since the relative error introduced is high if not enough events are accumulated.

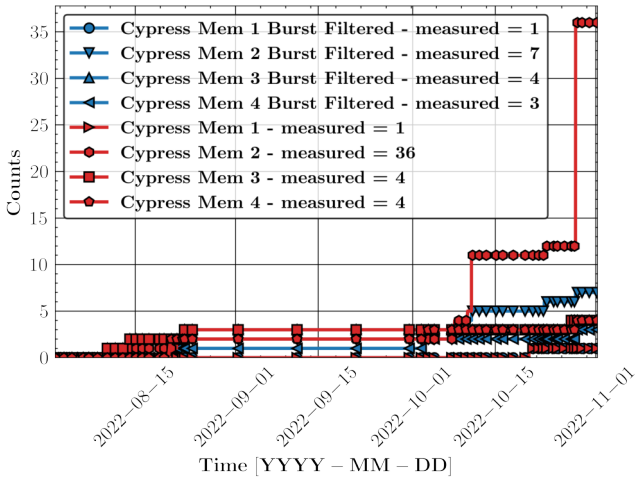


(a) Cluster Event - SEU Level

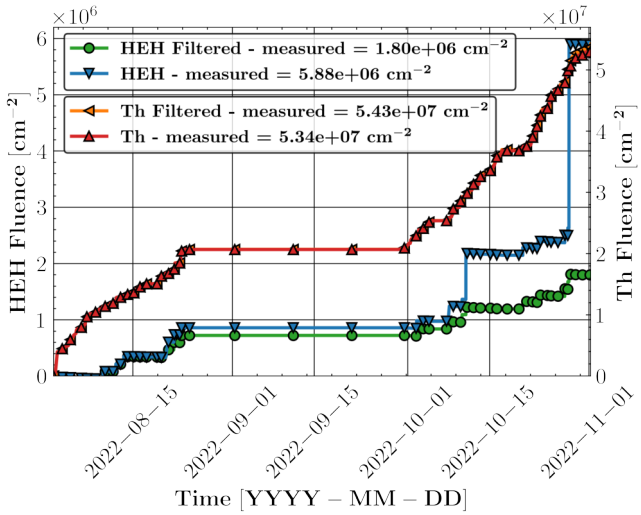


(b) Cluster Event - Fluence Level

Figure 3.3: In Fig. 3.2a a burst event affecting the measurements of the RadMon V6 installed in UL14. The event caused an artificial increase in Cypress Memory 2. In Fig. 3.2b the corresponding fluences have been calculated both with the Cypress affected by the Type A cluster and without (post-processing correction). As can be seen, the HEH measurement result is ~5 times larger.

In Fig. 3.3a an example of a cluster appeared in low radiation area (P1-UL14) on Cypress Memory 2 and impacts on the final measurement (Fig. 3.3b) are provided. A post-process correction can be implemented, as was done in Fig. 3.3, considering the burst event as a single SEU and reducing the uncertainty on the final measurements. It should be noted that type A clusters are accounted for in the memory calibration process, and when applying this correction, it may be necessary to apply the cross-section evaluated by filtering these

events, which was not done in this example since not available. This action would reduce the memory sensitivity and increase the HEH obtained. However, this process cannot be generalized since it fails in mid-count areas where clusters or MCUs caused by different particles passing through the sensitive volume cannot be differentiated.

Another limitation in this context is the resolution offered by the TID sensor used. The RadFET biased at 5 $V$ can provide a resolution of 57 $mGy$, higher than the one obtained with a biasing of 0 $V$ (212 $mGy$). This resolution can be a major limitation, especially when considering measurements within shielded areas (ULs IP1 and IP5 reported in Table 2.3).

### 3.1.3 Electrical Hardware Limitation

In the LHC, in particular in the experimental areas, the functioning of systems can be influenced by the presence of a magnetic field. RadMons is part of this group of systems. During operation in the experimental areas, they experienced electrical malfunctions caused by the magnetic field. To investigate this issue, the system was tested in a CERN Magnet, whose magnetic field was ramped up to 0.5 $T$. As it is visible from Fig. 3.4, the system stops transmitting after a few minutes of magnet functioning reaching a Magnetic field of ~70 $mT$.

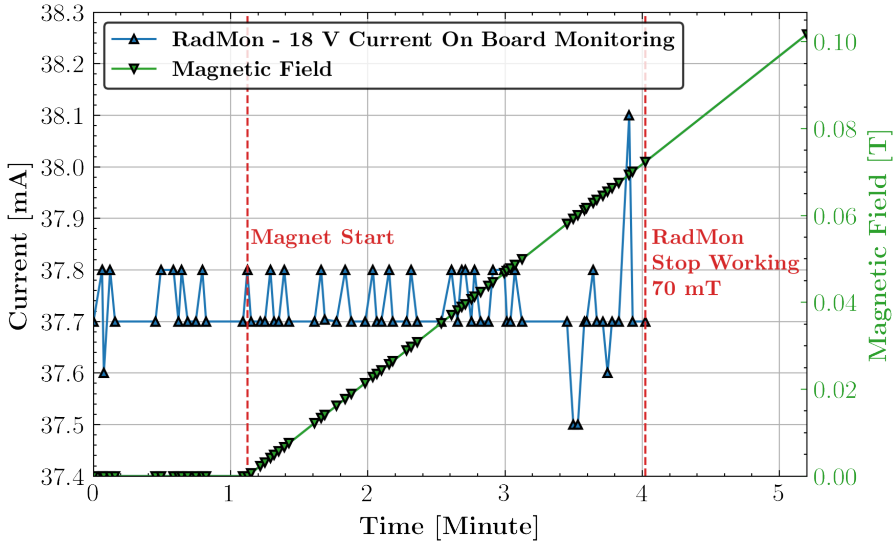


Figure 3.4: The RadMon V6 - 18 $V$ Converter output current on-board monitoring. After a few minutes the Magnet was started (start and stop indicated with dashed red line), the noise on the current increased showing spikes, and after their appearance (Minute 3.4), the system stopped communicating (Minute 4).

### 3.1.4 Radiation Hardware Limitation

The RadMon is a complex design within which, several subsystems providing the different functionalities, can be identified and are illustrated in Fig. 3.5a. To ensure that each subsystem is properly powered, several regulators are used, as highlighted in Fig. 3.5b.

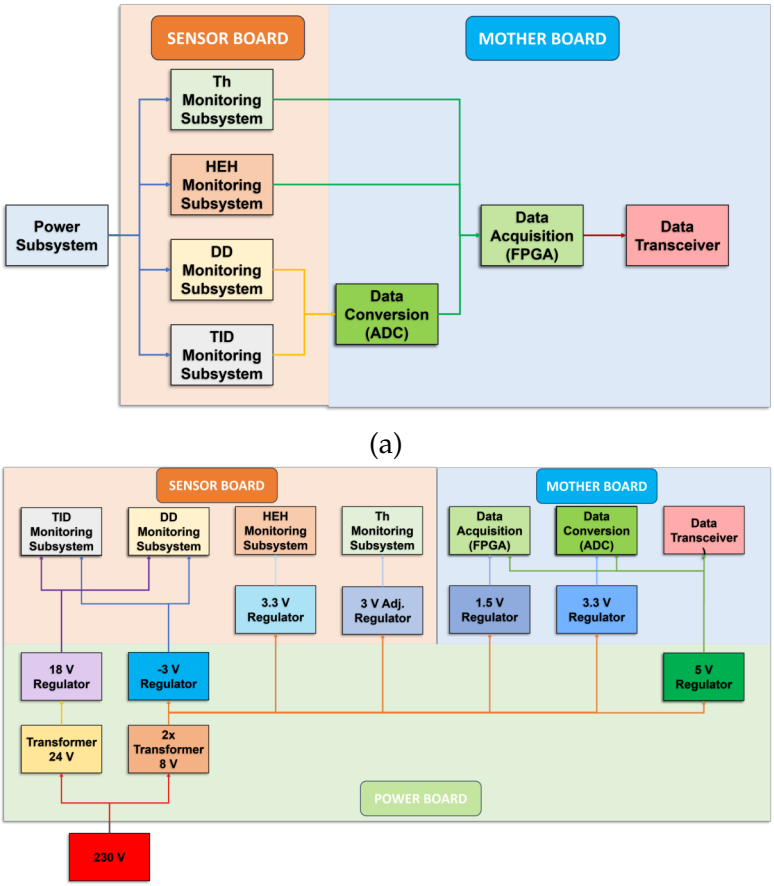


Figure 3.5: In Fig. 3.5a, a simplified block diagram showing the various subsystems that make up the RadMon and how they are interconnected. In Fig. 3.5b, a detailed focus on the complex power supply subsystem of the RadMon, showing specifically each regulator, by what it is powered and which subsystem or other regulator it powers [1].

From the point of view of radiation's impact on the functioning of the system, different failure modalities can be identified that lead to the loss of system functionalities.

1. Failure of the Current Source: the current source is used by RadMon to inject current into the RadFET sensor and measure the degradation of the sensor. The lifetime of this component depends on the DDEF/TID ratio experienced. The higher this ratio, the shorter the lifetime in terms of TID. When this failure event occurs, the system is unable to provide one of the monitored quantities (TID) but is still able to provide Fluences and DDEF measurements.

2. Current increase of ADC and FielDriver Transceiver: the effects of radiation on electronics cause the ADC and FielDriver transceiver to require more current for their proper operation. This increase propagates to the 2x8 $V$ transformers used to power the various regulators that bias the two components. As the current load increases, the response of the transformers changes and the output voltage decreases. When it reaches 4.2 $V$, it can no longer power the ADC, which shuts down. Without the ADC, the device cannot provide measurements for TID and DDEF, while it can still provide measurements for the two fluences. When it drops below 3 $V$, the transceiver also shuts down. Without communication, the system can be considered not functional anymore.

3. Uncertain increase in Th fluence monitoring: a drop in the voltage regulator output biasing this subsystem ($3V$) causes an increase in memory Th sensitivity, which depends on the voltage applied [55]. The drop starts at 50 $Gy$ and decreases by 3 % at about 180 $Gy$. Thereafter, the drop begins to be more rapid, losing another 1.5 % over the next 20 $Gy$. As the cross-section used is the one evaluated at 3 $V$ bias, the uncertainty in the final measurements is increased and the fluence is overestimated.

A reliability study of the different RadMon subsystems was carried out in [1] and the remarks obtained are reported in Table 3.1.

Table 3.1: The Reliability of the different RadMon functionalities considering independent sudden failures and combined/dependent gradual degradation's are reported concerning the TID [1].

| **System Functionality** | **R(99 %) [Gy]** |
|---|---|
| **Th Fluence Mon.** | 265.3 |
| **HEH Fluence Mon.** | 279.5 |
| **TID Mon.** | Depends on DDEF/TID ratio<br>$< 10^9$ 1 $MeV\ neq. \cdot cm^{-2} \cdot Gy^{-1}$: 577<br>$10^{10}$ 1 $MeV\ neq. \cdot cm^{-2} \cdot Gy^{-1}$: 200<br>$5 \cdot 10^{10}$ 1 $MeV\ neq. \cdot cm^{-2} \cdot Gy^{-1}$: 110<br>$5 \cdot 10^{11}$ 1 $MeV\ neq. \cdot cm^{-2} \cdot Gy^{-1}$: 55 |
| **DDEF Mon.** | 597.5 |
| **ADC** | 210.8 |
| **Data Acquisition** | 281.6 |
| **Data Transfer** | 278.1 |
| **RadMon** | **278.1** |

As can be seen, the average dose at which the system stop communicating is 278.1 $Gy$, but other system functionalities such as TID Mon. and ADC (its failure includes TID Mon.,

On Board Mon. and DDEF Mon.) stop working before this TID value, leading to the loss of major system functionalities. In addition, the Th Fluence Mon. degrades from 50 $Gy$, leading to an increase in the uncertainty of the Th measurement. A more stable regulator is required for this sensor.

The different limitations introduced, represent a starting point from which to develop a new wireless platform capable of overcoming all the problems presented.

## 3.2 Internet of Things: a Possible Solution to Improve LHC Operations

Most of the requirements listed in the previous paragraph (i.e. high mobility and flexibility, low power, and wide-area coverage (LHC)) are typical features of the Internet of Things (IoT). The term IoT denotes everything that is connected to the Internet, representing a concept that includes devices, networks, services, and data. Cisco's 2014 reference model provided definitions of the seven layers within the IoT ecosystem. These layers are not unfamiliar for particle accelerators, where all sensors, devices, and equipment are interconnected and well embedded in what is usually referred to as the 'control system' [114]. A significant distinction between the two lies in the connectivity options. Particle accelerators are mainly dependent on wired networks (e.g. "copper cables" and optical fibers [114]) and infrastructure, while the IoT concept has become increasingly popular, especially with the advent of a new generation of wireless technologies. Its integration in particle accelerators will allow: a) quick connectivity, b) easy installation, and c) no cabling requirements. These features will have a substantial impact in terms of:

1. Accelerator availability: enables quick installation, reducing the accelerator downtime.

2. Observability: Currently, the number of RadMons that can be installed in a given area of the LHC is limited by the maximum number that the Front-End Computer (FEC) can accommodate, i.e. 32 devices per FEC. Furthermore, the FEC is not dedicated to the RadMon but is shared with other equipment, so this number can be lower. An IoT network does not have this limitation and allows a greater number of distributed devices and a better coverage of the machine surface.

3. Cost reduction: reducing operating and infrastructure costs.

On the other hand, the application of the IoT infrastructure to the Accelerator context introduces further constraints:

1. Low Power requirements: this is a typical feature of IoT projects, which again leads to the need to extend the current CERN RHA procedure with test methods that take into account the different modes of operation that may include this category of components.

2. Wireless protocol: finding a wireless protocol capable not only of working under radiation and able to provide long-range coverage but also of being compliant with LHC Radio Frequency (RF) requirements.

3. Availability compliance of the application: as defined in Section 2.3.2, the machine availability is normally considered more critical than reliability in the accelerator sector, as it is always possible to access the equipment and perform preventive maintenance, extending its life indefinitely. The introduction of IoT systems in the accelerator equipment, when used for critical applications, must respect the CERN availability constraint. This is not the case for the side applications of the accelerator whose malfunctioning does not impact the functionalities of the LHC.

**A further objective of this thesis will be to demonstrate the feasibility of applying IoT in the context of accelerators despite these challenges.**

## 3.3 Platform Choices and Challenges

The several challenges introduced in the previous paragraphs for the design of a battery-powered Wireless IoT monitoring system, combined with the unique radiation tolerance requirements for a system exposed to intense radiation, lead to several design choices that, in turn, impose some new radiation qualifications challenges to be evaluated. The following paragraphs outline the design choices that shaped the development of CERN's **battery-powered Wireless IoT monitoring system for electronics**, also called BatMon, and outline the qualification challenges they introduced.

### 3.3.1 System Modularity

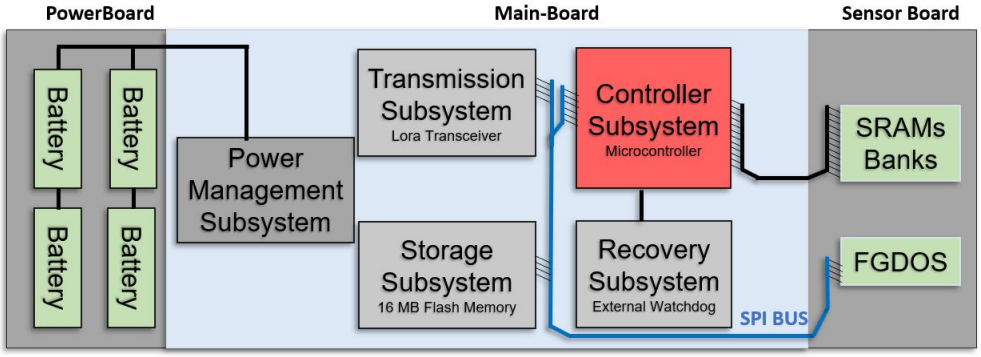


Figure 3.6: Conceptual diagram of the BatMon System.

The first requirement of the system, which must be able to easily integrate new sensors and modules, is modularity. In fact, in parallel to designing a flexible and easily maintainable radiation system, the aim is also to provide CERN users with a generic platform that can be used for different applications. Therefore, four layers compose the system: 1) the Power-Board; 2) the Main-board; 3) the Sensor Board; and 4) the deported module. The Main-board is the only application-independent part, while the power and Sensor Boards can be interchanged according to the needs and purposes of the application. The Main-board offers the possibility of deporting the Sensor Board away from it and providing measurements in the presence of radiation levels it would not withstand. When the Sensor Board is deported away from the Main-board but still connected to it, it is called a deported module and represents a possible fourth level of the design.

The PowerBoard can fit up to four lithium batteries, providing up to 7.2 $V$ with a battery capacity of 17 ampere-hours ($Ah$). The choice of batteries has been made to ensure safety

by opting for non-rechargeable batteries, thus avoiding the potential radiation problems associated with rechargeable batteries [115]. As visible from Fig. 3.6, The four batteries are configured in a parallel of two branches. Each branch consists of two batteries connected in series. This arrangement increases the energy capacity of the system to 17 $Ah$ and provides a voltage of over 5 $V$ (2 x 3.6 $V$), which is essential for its operation. For applications with less demanding time requirements, it is possible to choose to install only two batteries, which provide a cost-saving but 8.5 $Ah$ capacity. The platform itself would be fully compatible with a single battery since all the components of the Main-board require 3.3 $V$. However, to provide flexibility for the Sensor Board, a 5 $V$ design was chosen to allow the use of multiple batteries.

Several subsystems can be identified on the Main-Board: the Controller Subsystem, the Transmission Subsystem (a wireless transceiver), the Storage Subsystem, the Recovery Subsystem, and the Power Management Subsystem. The latter provides the electrical bridge between the Main-board and the PowerBoard through the use of two linear regulators, which convert the voltage coming from the PowerBoard to low-noise voltages of 5 and 3.3 $V$ DC, which are also required for the Sensor Board. The usage of DC-DC converters was avoided, since they are generally more sensitive to destructive SEEs [116]. In addition, a design made of MOSFET and Bipolar Junction Transistor (BJT) allows the three separate power rails (the output of the Low Dropout (LDO) regulators and the battery voltage) to be read via resistance dividers, without compromising current consumption performances. A conceptual diagram of the Main-Board is shown in Fig. 3.6.

### 3.3.2 Low Power Components

As introduced in Section 3.1, one of the requirements of the system is to run for at least one year with the same set of batteries. This condition imposes a limitation on the current consumption of the system and prompts the selection of components according to low power specifications: low leakage current, and low quiescent current. However, this approach alone may not be sufficient. To further reduce the average power consumption of the system, the implementation of a duty cycle mode (includes wake-up, measurement, storage, and transmission of information, followed by sleep) becomes crucial. The need to implement this type of operating principle places additional demands on component selection, which must incorporate low power modes that can drastically reduce power consumption when

needed. In addition, radiation sensors capable of cumulating and storing measurements through their operating principles must be used. These choices introduce new challenges to the CERN RHA component qualification procedure, where the screening of low power components or components with different operating modes is not adequately covered. To address the potential impact that these components and their embedded mode will have in radiation environments, it is necessary to extend CERN's traditional RHA by introducing new testing strategies that consider the different operating modes that the component can exploit.

### 3.3.3 Communication Technology

An effective wireless sensor network must be energy efficient, scalable, real-time, reliable, and highly portable. In addition to these characteristics, other parameters, such as the effects of radiation on electronics and RF interference, must be considered when applied to particle accelerators. In CERN's underground and experimental areas, regulation of permitted radio frequencies is coordinated with host states (ANFR in France and OFCOM in Switzerland). The main purpose of these regulations is to avoid interference with external RF services. Additionally, the frequencies used must avoid overlapping with the ones used by the RF systems installed in the area for physics and operational purposes. An example, are the RF cavities used by the accelerators to perform their duties. Another constraint is given by the radiation effects. The wireless technology emitter and receiver must be radiation tolerant if not installed in safe R2E areas. This constraint is even more strict when considering that the LHC has a part longer than 1 $km$ with no shielded areas. To cope with this problem and provide wireless connectivity along the accelerator and experimental areas, 60 $km$ of radiating cables with more than 50 injection points located in non-radiation areas, were deployed by CERN [117, 118]. Radiating cables are coaxial cables with slots cut into the outer conductor to allow controlled levels of electromagnetic energy to be radiated from and into the cable. The high length of the cable imposes the use of frequencies below 1 GHz to reduce losses in the cable since they are directly related. It is already employed for TETRA and TETRAPOL (400 $MHz$ band) by the CERN's fire brigade and public safety agencies, 5G (700 $MHz$ band), LTE (800 $MHz$ band) and UMTS (900 $MHz$ band). The ISM band, which in Europe is 868 $MHz$ was not employed yet and was a good candidate to apply the IoT concept to the accelerator and exploit its features (Flexibility, low power requirements, and wide-area coverage

(LHC)) that perfectly fits the application design constraints.

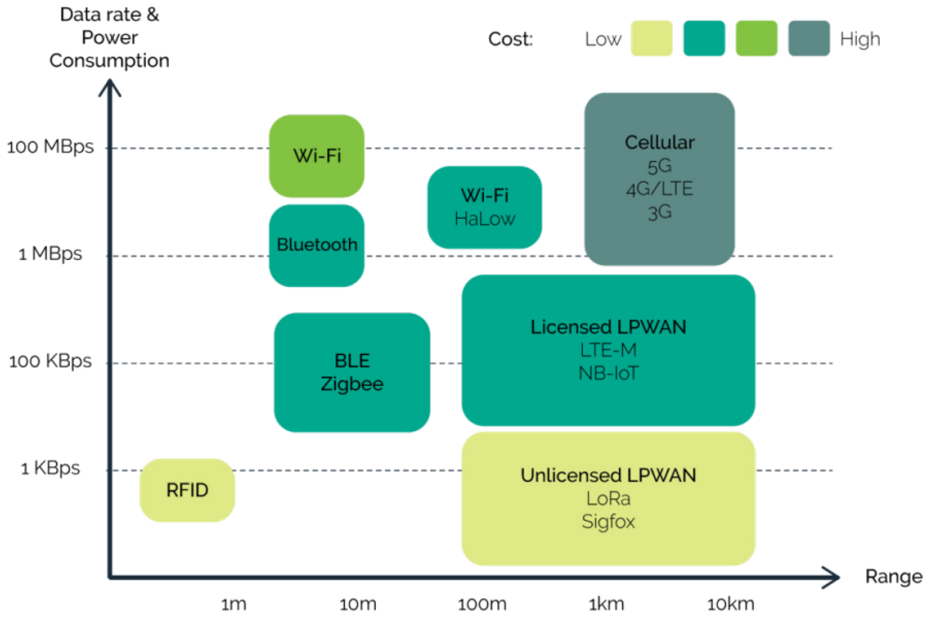


Figure 3.7: Different Wireless Solutions are depicted according to their characteristics of power consumption, data rate, and coverage.

In addition, between the different wireless possibilities as depicted in Fig. 3.7, Low Power Wide Area Network (LPWAN) solutions, mainly used in industrial IoT infrastructures, perfectly fit the constraints of long range, data rate, and low power consumption required for radiation monitoring of electronics in the CERN accelerator complex.

The LPWAN LoRaWAN, SigFox, and NB-IoT, similar in terms of scope and features, were investigated [119]. The different features of the three solutions are reported in Table 3.2. The NB-IoT presents two main limitations in terms of frequencies and the possibility of creating a private Network (Cost). SigFox respects the frequency requirements but it does not allow private network creation and the data rate is too low for the radiation monitoring of electronics requirements. On the other hand, LoRaWAN, being provider independent allows us to exploit this feature and create a network with open-source tools.

The frequency band, being below 1 $GHz$, fits the CERN radiating cables constraints. In

Table 3.2: The characteristics of the three LPWAN network solutions selected (LoRaWAN, SigFox, and NB-IoT) are reported in the table.

| | **LoRaWAN** | **SigFox** | **NB-IoT** |
|---|---|---|---|
| **Frequency** | Unlicensed ISM | Unlicensed ISM | Licensed LTE |
| **Data Rate** | 50 $kbps$ | 100 $bps$ | 200 $kbps$ |
| **Range** | 5-20 $km$ | 10-40 $km$ | 1-10 $km$ |
| **Private Network** | Allowed | Not Allowed | Not Allowed |

addition to these characteristics, the LoRaWAN network embeds redundancy since the data transmitted by each node are received by all gateways that receive the message and are all transmitted to the network server. This feature guarantee also has high coverage with the disadvantage of possible collisions and communication bottlenecks. LoRaWAN addresses these limitations by employing suitable RF modulation techniques and incorporating extra layers for data acknowledgments. LoRaWAN is a Media Access Control (MAC) protocol designed to enable wireless communications for battery-powered devices. The LoRaWAN protocols are specified by the LoRa Alliance and standardized in the LoRa Alliance Technical Specifications [120].

After selecting the wireless technology and protocol, radiation effects on electronics are still a constraint, particularly about the LoRa transceiver, and some RHA actions need to be considered. Being a commercial solution, the sensitivity of this component to radiation effects may cause connectivity or transmission problems, requiring the implementation of dedicated mitigation schemes. On the other hand, since it is a wireless solution, packet loss and thus loss of measurements, may occur due to network unavailability or low Received Signal Strength Indicator (RSSI). Therefore, to improve the reliability of the system, a 16 $MB$ nonvolatile flash memory with a Serial Peripheral Interface (SPI) (storage subsystem) was added to the design. The integration of this component allowed the storage of information in situations where wireless communication is disrupted due to radiation effects or network unavailability. In addition, LoRa functions such as Confirmed Uplink, Adaptive Data Rate, and Downlink Custom Message can be used to identify network unavailability and to change the configuration by setting different spreading factors and transmission power, thus improving the reliability of the system.

### 3.3.4 Controller Choice

The choice of the control subsystem, which is responsible for interfacing with the various components, including sensors and onboard peripherals such as the communication subsystem, must meet several critical constraints, such as the need for low power consumption, the need for flexibility, and ease of scalability. In the context of the effects of radiation on electronics, the FPGA appears as the best choice for radiation-tolerant designs for several reasons:

1. Flexibility: in terms of design, the FPGA provides considerable hardware flexibility,

enabling the development of highly customized and complex designs, and allowing the implementation of hardware-level mitigation techniques, such as TMR, for a final design more reliable under radiation [121].

2. Scalability: FPGAs are available in various sizes and configurations to provide, if needed, a large number of GPIOs and enable the control subsystem to meet the needs of an evolving design.

3. Parallel processing: FPGAs excel in parallel processing, enhancing the general system performances.

On the other hand, the MCU, having a design that cannot be customized but only configured, offers less flexibility. However, with integrated peripherals, such as the Analog-to-Digital Converter (ADC), Real Time Clock (RTC), and communication bus (SPI, Universal Synchronous and Asynchronous Receiver-Transmitter (USART), I2C), it enables easy control of on-board hardware and integration of new sensors into the design. Power-saving modes are also typical for this type of component, whereby low power requirements that cannot be achieved with an FPGA can be met. As stated in Section 1.3, the impossibility of applying mitigation at the hardware level in Commercial MCU makes it necessary to use an External WaTchDog (Ext WTD) to increase the reliability of the system and recover its functionality in case of SEFI. The working principle of the Ext WTD is described in Section 3.5.2. If the MCU is selected as controller, it becomes necessary to identify an additional component that meets the system requirements, thus adding complexity to the RHA phase of component-level testing. However, the ease of integrating LoRa transceiver control using existing C code-based LoRa libraries compliant with LoRaWAN, along with the low power capabilities of the MCU, pushed for its choice.

### 3.3.5 Radiation Sensor Selection

The selection of sensors for radiation monitoring is ruled by several constraints, some of which were introduced by previous choices:

1. Low power: this constraint has always been central to the design of the wireless radiation monitoring system and continues to be so in the choice of sensors. The sensor should not affect the overall power consumption of the system or incorporate low power modes.

2. Duty cycle mode: the sensors need to be capable of cumulating and storing measurements through their operating principles

3. Integrability: the choice of MCU as the controller offers the possibility of easily integrating new sensors due to the embedded peripheral. However, the number of available GPIOs is a limitation, which may also affect the choice of radiation sensors.

In addition to these hardware features, sensors must be able to perform their main task of providing the measurement of metrics of interest for the CERN accelerators, such as TID, DD, HEH, and Th as shown in [38]. The sensors used in the CERN RadMon represented a good starting point.

#### HEH and Th Sensors

As discussed in Section 2.4.2, in the RadMon [68], two different well-calibrated parallel SRAMs, whose sensitivity to both Th and HEH is known, allow retrieving the different fluences by combining their measurements as shown in [68]. However, as it was presented in Section 3.1.2, the HEH sensor SRAM used, due to the still existing Type A cluster, results in high uncertainty in the HEH measurement. This limitation pushed the research of a new candidate. Since the search for candidate SPI SRAMs providing the same capabilities is still ongoing, the 16 $Mb$, 65 $nm$, Cypress SRAM CY62167GE30 was selected. For the Th fluence measurement, the 4 $Mb$, 400 $nm$, Toshiba SRAM TC554001AF, used on the RadMon with 3 $V$ Biasing, was kept. In Table 3.3, the different sensors' sensitivities to HEH and TH evaluated respectively under 200 $MeV$ proton beam and Thermal and Epi-Thermal Neutron sources, are reported. As it is visible the CY62167GE30 has a slightly higher HEH sensitivity with respect to the CY62157EV30 (HEH sensor in the RadMon V6), making the sensor a good candidate.

Table 3.3: The Sensitivity to HEH and Th of different SRAM is presented.

| **Sensor** | **Size [Mb]** | $\sigma_{\mathbf{HEH}}$ **[cm$^2$]** | $\sigma_{\mathbf{Th}}$ **[cm$^2$]** |
|---|---|---|---|
| **CY62167GE30** | 16 | $1.46 \cdot 10^{-6}$ | $2.01 \cdot 10^{-8}$ |
| **CY62157EV30** | 8 | $1.31 \cdot 10^{-6}$ | $8.24 \cdot 10^{-9}$ |
| **TC554001AF** | 4 | $2.09 \cdot 10^{-7}$ | $1.01 \cdot 10^{-6}$ |

The limited available amount of Inputs and Outputs (IOs) in the MCU forced the use of SPI GPIO expanders to cope with the parallel interface of SRAMs. This necessary choice

increases the read and write time of the memories and, as will be seen, is the cause of the long active time required by the device to make measurements.

#### TID Sensor

Regarding the TID, the RadFET has two main limitations for the application:

1. Read Circuitry: to read the RadMon, different components in a complex circuitry are required. Those components are power-consuming and difficult to replace. In addition, the lifetime of the current reading circuitry, depended on the DDEF/TID experienced by the system (Section 3.1.2).

2. Resolution: as described in Section 3.1.2 the RadFET resolution can be a major limitation, especially when considering measurements within shielded areas ($> 20\ mGy \cdot y^{-1}$ in ULs IP1 and IP5 as reported in Table 2.3).

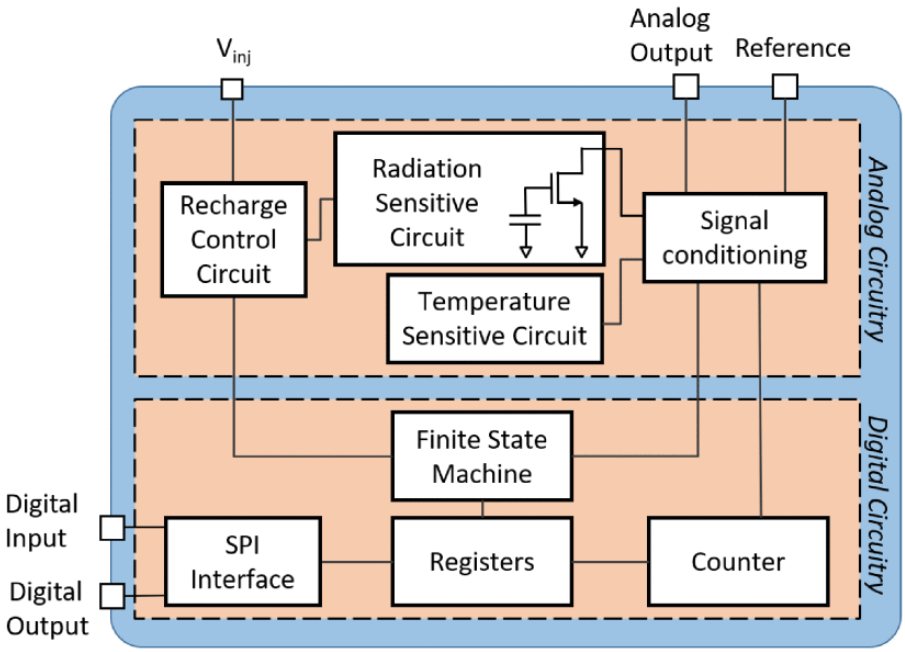


Figure 3.8: Block diagram of the FGDOS architecture [122].

For many years, CERN has been cooperating in the development of a new fully digital Floating Gate DOSimeters (FGDOS) [122]. Each chip contains two independent FGDOS. A single transistor with a floating gate composes the radiation-sensitive circuit (Fig. 3.8). To enhance radiation sensitivity, the gate area extends over the field oxide, increasing the radiation-sensitive volume. The sensor is modeled as a capacitor connected to the gate of a readout transistor. To quantify the radiation dose, the capacitor is initially positively charged

through an injector transistor. When ionizing radiation interacts with the field oxide, it generates electron-hole pairs. The electric field separates the generated pairs pushing the holes toward the substrate, while the electrons are captured by the previously charged floating gate. Consequently, the radiation-generated electrons neutralize the charge stored in the capacitor, leading to a change in the drain current of the transistor. A square-wave signal of 5 $V$ is generated by an internal conditioning circuit, the frequency of which is based on current drift. The absorbed dose can be measured through the converted frequency. An internal counter, integrated into the FGDOS, measures this frequency, which is then stored in a dedicated register accessible via SPI. The radiation response of the sensor is not linear in general, but by exploiting a specific frequency range (Linear Range ($\Delta_{LR}$)), a linear response can be retrieved. To work in this range, the sensor embeds a recharge control circuit, which compares the output frequency with the threshold frequency ($f_{th}$) (Bottom Limit range). If it is below this value, it enables the recharge, and when the configured target frequency ($f_{tg}$ (Upper Limit range) is reached, it disables the process.

Different working modes can be exploited that impact the sensor's current consumption.

1. Autonomous mode: operating mode in which the sensor works independently, without the need to either externally control the recharge process or continuously read the frequency. Knowing the Number of recharge ($R_{Cnt}$), the frequency before irradiation ($f_{BegIr}$), and the frequency at the end ($f_{EndIr}$), it is possible to know the TID taken by the sensor (Cumulative property) as shown in equation (3.1) [122]. As a disadvantage, the sensor is always active and the current consumption is impacted.

$$TID = \frac{(R_{Cnt} - 1)\Delta_{LR} + (f_{BegIr} - f_{th}) + (f_{tg} - f_{EndIr})}{Sensitivity} = \frac{(R_{Cnt})\Delta_{LR} - (f_{EndIr} - f_{BegIr})}{Sensitivity} \tag{3.1}$$

With:

- $R_{Cnt}$: recharge counter
- $f_{BegIr}$: frequency before irradiation [$Hz$]
- $f_{EndIr}$: frequency at the end of the irradiation [$Hz$]
- $f_{tg}$: configured target frequency [$Hz$]
- $f_{th}$: configured threshold frequency [$Hz$]
- $\Delta_{LR}$ = $f_{tg}$ - $f_{th}$: operating Linear Range [$Hz$]
- $Sensitivity$: sensor Sensitivity [$Hz \cdot Gy^{-1}$]

2. Passive mode: operating mode in which the sensor is kept in the reset state, reducing power consumption, and is read only when needed. The benefits of Autonomous mode are not available, and charging can only be triggered by SPI command when the controller detects that the frequency is below the threshold. To prevent the FGDOS from working outside the linear range or completely discharging the capacitance, the sensor access frequency should be adjusted according to the experienced dose rate.

In addition to the low power and integrability features required by the application, it also offers a higher TID resolution than RadFET, as visible in Table 3.4. It will allow the platform to provide measurements in ULs (> 20 $mGy \cdot y^{-1}$ Table 2.3), but more specifically inside protective shieldings where the dose may be even lower than 10 $mGy \cdot y^{-1}$.

Table 3.4: RadFET and FGDOS Resolution capability performances [122].

| Sensor | BIAS [V] | Resolution [mGy] |
|---|---|---|
| **RadFET** | 0 | ~212 |
| | 5 | ~57 |
| **FGDOS** | - | ~2 |

With these features, this sensor is the perfect candidate for this application as a TID sensor. However, further studies on the passive mode are needed. The implications of using FGDOS passive mode and lessons learned from its direct application to the Wireless IoT monitoring platform are discussed in Section 3.5.3.

### 3.3.6 The Wireless IoT Platform

As presented in Section 3.3.1, to fulfill the requirements of modularity the system is made of four modules: 1) the Power-Board; 2) the Main-board; 3) the Sensor Board; and 4) the deported module. A description of the Power Board was given in Section 3.3.1, while in this paragraph a summary of the Main and Sensor Boards hardware designs is presented.

As defined in Section 3.3.4, the core of the system is the MCU which is positioned in the middle of the design and is highlighted in red in Fig. 3.9. Through its GPIOs, it interfaces and controls the other components on board. In particular, the SPI bus is used to control a LoRa transceiver, used for wireless capability, and a 16 MB nonvolatile External Flash memory, which is used as a backup solution when the wireless capability is not available. An Ext WTD, placed in the bottom right of the design (Fig. 3.9), is used to recover the

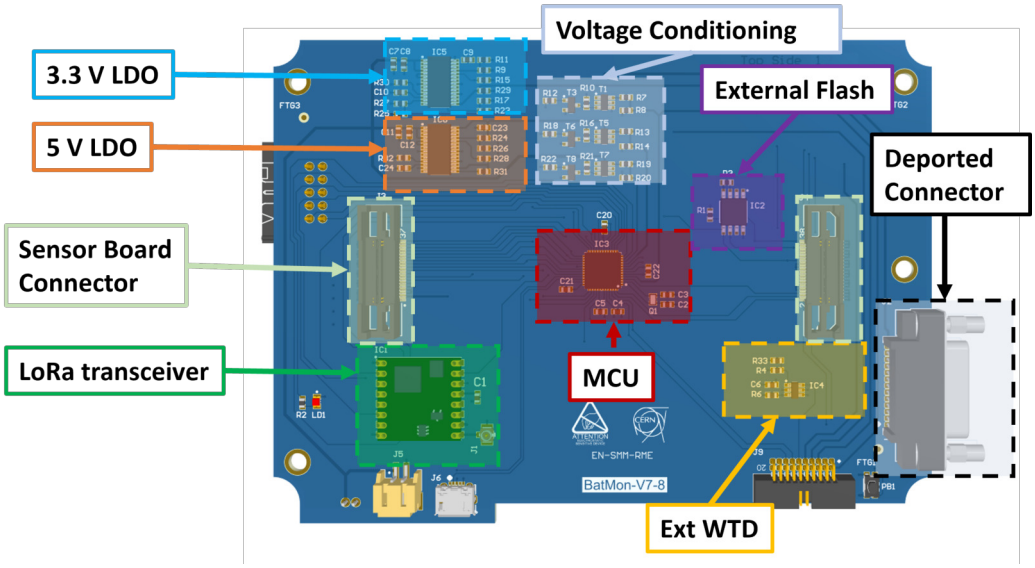


Figure 3.9: The different parts composing the Main-board design are highlighted.

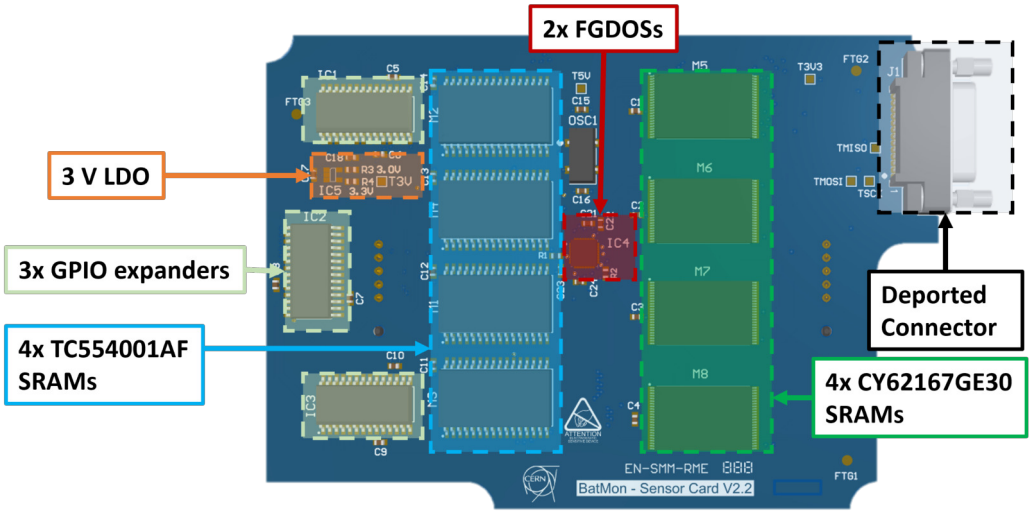


Figure 3.10: The different parts composing the Sensor Board design are highlighted.

system functionalities in the case of SEFIs. All the components are powered with a 3.3 $V$ LDO regulator placed in the upper left of the design. An additional 5 $V$ LDO regulator is also provided to supply this value of voltage if required by the equipped Sensor Board. Both the Main-board's LDO outputs and the battery voltage are monitored with a low power solution made of MOSFET, BJT, and resistor dividers (referred to as Voltage Conditioning in Fig. 3.9).

The Main and the Sensor boards are interfaced via two Sensor Board Connectors. Through these connectors, selected MCU's GPIOs are connected to the Sensor board to provide three independent analog inputs (ADCs), one of which is usable for signal generation via an internal Digital-to-Analog Converter (DAC). The remaining lines can be configured to provide

all three main protocols (I2C, SPI, and USART) for communication and control of the digital sensors. Alternatively, they can always be used as digital signals. The Radiation Monitoring Sensor Board is composed of a larger number of components as visible in Fig. 3.10. In particular, three SPI GPIO expanders are used by the MCU to control four CY62167GE30 and four TC554001AF SRAMs. The latter are powered with a dedicated LDO embedded on the sensor board, which converts the input 3.3 $V$ provided by the motherboard to the required 3 $V$ (For higher Th Sensitivity [55]). Finally, in the middle of the design, the TID sensor (FGDOS) is positioned.

Both boards are equipped with a Deported Connector that allows for deporting the Sensor Board away from the Main-board and providing measurements under radiation level conditions not sustainable by the latter. The three boards, stacked vertically, are enclosed within a custom 3D-printed enclosure and are depicted in Fig. 3.11.

Figure 3.11: The BatMon.

## 3.4 Dedicated RHA Concerns

The design choices discussed in Section 3.3, introduce several qualification challenges specific to this family of wireless and low power systems. These challenges are not addressed in the traditional RHA process. Consequently, dedicated test and validation methodologies are needed to extend the standard CERN RHA procedure, ensuring a complete validation of a wireless and low power radiation monitoring system. The proposed additional testing methodologies take place in two phases (3-4) of the traditional RHA for custom-built electronic systems (Fig. 2.13) and are expanded by the proposed additional testing methodologies.

1. Component-level qualification phase: specific test methodologies and considerations were introduced to extend those already defined for CERN's radiation environments. These concerns aim to address the unique challenges posed by the use of wireless and low power components in such environments.

2. System-level qualification phase: as an alternative to the qualification process using the CHARM facility, as foreseen by CERN's traditional RHA, new test steps were added to complete this phase and introduce new test strategies for this type of system.

   (a) Electrical validation phase: it includes new functional tests in which the primary information for system radiation qualification is extracted.

   (b) System-level qualification phase: a new test plan is proposed that includes tests under different types of particle spectra. Its application allows information to be obtained on performance degradation, expected lifetime, and failure rate that will define the use of the system and possible improvements.

   (c) Sensor calibration phase: an innovative step compared to the traditional RHA at CERN. The sensors are an important part of the system and require specific qualification and calibration processes. This step is added as a final qualification step to complete the methodology and is made possible by the characteristics of the system.

All these phases and their challenges are discussed in the following Sections.

### 3.4.1 RHA Implications on Component-Level Qualification

The highly distributed nature of the CERN system, as in the case of the radiation monitoring system, required the use of qualified COTS [123] components to reduce costs. As presented in Section 2.4.4, valuable information on component testing strategies is provided by the RHA. In addition, the CERN database provides a large selection of already qualified components for a wide range of applications.

However, since very few wireless and low power applications were developed in the previous years at CERN, not many components suitable for this application are available in the database. In addition, the test methodologies used to screen components may not be adapted to their characteristics and a component selected from the database may require further testing. In fact, low power components may embed different internal features, such as power saving and different operating or sleep modes, as well as operate with much lower internal biasing. Therefore, such components may exhibit different degradation and failure modes depending on usage. This testing problem, together with the high radiation levels expected for the HL-LHC, up to 100 $Gy$ and $10^{11}$ 1 $MeV\ neq. \cdot cm^{-2}$ per year in the tunnel [38], has made the search for a suitable candidate difficult.

Consequently, it is necessary to follow several recommendations when conducting tests on these types of components. It is worth noting that while other factors such as dose rate effects are addressed in the RHA process, the usual practice of employing worst case bias conditions during testing could potentially lead to an underestimation of component degradation rates compared to what will occur during effective operation. It is more reasonable to replicate test conditions similar to operational conditions. It is important to recognize that this approach may reduce the radiation margin and thus imply greater confidence in the responses obtained. However, the radiation margin must always be taken into account to consider the problem of variability of COTS components. In addition, the data obtained may not be reused for other applications but will be specific to the one to which the test refers. For battery-powered IoT applications, it must be considered that the system will spend most of its time in a sleep or powered-down state, which can significantly affect the component's overall lifetime. Section 3.5.1 will present a component qualification case whose response depends on the biasing conditions proving the impact that the different operating modes can have on the test results.

### 3.4.2 System Electrical Validation

Some initial tests can be carried out without radiation to assess whether the performance of the system meets the initial requirements, such as the expected battery life of the system based on its power consumption. In detail:

1. Duty cycle life: the lifetime requirements can be partially evaluated before performing radiation tests. At this stage, it is already possible to assess whether the system meets the original requirements and evaluate the impact of the measurement period chosen on the lifetime. However, since radiation effects can lead to current consumption increases, this evaluation needs to be repeated after obtaining degradation rates.

2. Functionality and firmware validation: at this stage, tests can be performed to evaluate system functionalities, such as storage, transmission, and firmware stability, thus avoiding misidentifying bugs as radiation-induced effects.

3. Tests under magnetic field: as experienced with the RadMon and described in Section 3.1.3 section, the possible presence of magnetic fields is a parameter to be taken into account during system design, since the system would experience this during its operation, particularly in the experimental area. Performance degradation due to the magnetic field can be evaluated during this validation phase.

System-level testing under radiation will be impacted by this electrical validation phase. For example, the lifetime as a function of the measurement period also delineates the subsequent usage of the device, as it allows us to know those "real working conditions" that will permit a more realistic test of the system under radiation. Knowing the behaviour of the system in the presence of magnetic field will allow to avoid unexpected failure during operation and in the case of sensitivity, will allow more attention to be paid to installation in experimental areas of the accelerator.

### 3.4.3 System-Level Qualification

As described in Section 2.4.5, traditionally CERN RHA considers component-level and system-level qualification as two complementary characterization steps. In the case of wireless and low power systems with different modes of operation during which components exploit different biasing conditions, this is even more true, since some verification may be difficult to perform with component-level testing alone.

1. Component Biasing replication: during component-level qualification, it can be difficult to accurately reproduce the dynamic biasing conditions that components will use over the lifetime of the system. This is even more the case for low power components where the biasing conditions are highly dependent on the operating mode of the system, such as the value of the duty cycle.

2. DDEF/TID ratio: this ratio can affect component degradation rates and its effect at the system-level can be difficult to predict from only the component-level test data [79].

3. Mitigation schemes and system functionalities evaluation: only through system-level testing can the effectiveness of mitigation schemes be assessed, such as the ability of the Ext WTD to detect SEFI and restore system functionality, or the reliability of the communication link when both the MCU and LoRa module are used.

4. System characterization: system-level testing allows knowing the real radiation lifetime and cross-section of the system.

The above reasons demonstrate the need for system-level validation, which allows the qualification of functionalities and parameters that cannot be verified at the component-level. However, some aspects may compromise the quality and validity of the tests that need to be considered during system-level qualification. The different subsystem composing the application, may not exploit their worst case biasing condition during the same work phase. This can be overcome by testing the equipment exploiting duty cycle mode. However, this is not enough. A realistic duty cycle must be chosen and the system should be tested by emulating, as far as possible, the behaviour it will have during real operation [84]. The test may be invalidated if the system is tested in a duty cycle mode without the correct facility being selected. Flux is an important parameter for this selection [82]. Pulsed beam testing is risky because not all operating conditions may be correctly tested using a realistic duty cycle if there is no synchronization between the system and the beam. The tunability of the flux is another important feature. The beam flux can have a significant effect on systems based on digital circuits such as MCUs and FPGAs. Bearing in mind that the system should be tested under realistic duty cycle conditions if the flux is too high, it may not be able to take advantage of all the different working conditions, restarting or stopping before the end of a complete working cycle. In this case, not all operating conditions would be tested. Therefore, the system would not be fully qualified. On the other hand, it is not possible

to test with low flux and achieve high fluence and dose at the same time, as beam time is limited in most facilities. A hybrid solution to this problem may be to ramp up the flux during different irradiation runs to estimate system SEE sensitivity at low flux and lifetime at highest flux. This solution is described in Section 3.5.5. Thus, the sensitivity of the system can be tested using all operating conditions and a high dose value can be achieved in an acceptable time. Finally, it will be possible to know the cause of the failure and improve the system in the future, only enhancing observability of the electrical parameters during all the tests, as highlighted in Section 2.4.6.

### 3.4.4 Choice of the Appropriate Facilities

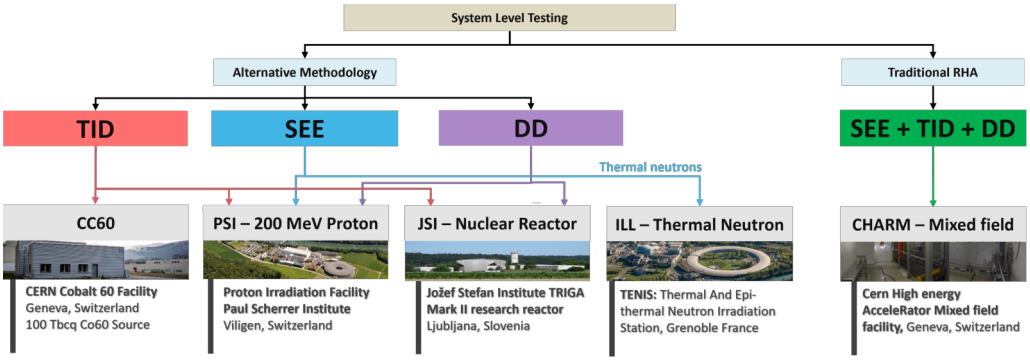


Figure 3.12: Block Diagram showing the two possible approaches to carry out system-level testing.

As described in Section 2.4.5, the facility specified by the Traditional CERN RHA for system radiation level qualification is CHARM. This facility, described in Section 2.5.3 offers the possibility of testing complete electronic systems in a realistic field, fully representative of the mixed-field environment of the high-energy accelerator. However, it is not always available and this is particularly critical during the long LHC shutdown period. Indeed, during this period, system-level testing following Traditional CERN RHA is not possible and an alternative methodology is required. This alternative methodology, illustrated in Fig. 3.12, consists of dividing the qualification process into several validation steps using other facilities.

1. TID: Co-60 facilities are perfect for a first qualification phase: they allow testing only TID monitoring performances of the entire system combining the different system and sensor working modes to verify the accuracy achieved. In addition, the only gamma contribution in the spectrum allows exploiting all the working modalities of the sys-

tem without having to worry about the reset problem induced by SEFI that occurs in the case of CHARM. Moreover, testing in a Co-60 source enables the possibility of easily fine-tuning the dose rate allowing investigation of dose rate effects and possible dependencies with duty cycle used.

2. SEE (Th): as described in Section 2.3.4 Th can represent a problem for electronics inducing SEE. In general, a system based on COTS components could be sensitive to Th effects as there is no information on their manufacturing process. This sensitivity could lead the system to soft failures (recoverable - partial loss of functionality). Testing the system under Th is necessary to know its sensitivity to this type of neutrons and avoid unexpected behavior during operation. The readout capability of the Th fluence sensor can also be investigated using an appropriate flux.

3. TID+DD+SEE (HEH): as described in Section 2.4.4, the traditional CERN RHA uses high-energy proton beams to test components against all electronic radiation effects. This solution can also be extended to test small systems or parts of them (several subsystems together) against combined SEE, TID, and DD effects. The readout capability of the HEH fluence sensor can also be investigated using an appropriate flux.

4. TID+DD: the TID/DD ratio experienced by a bipolar component can strongly influence its degradation profile. As shown in [79], the choice of ratios representative of the LHC environment is crucial. The conditions covered by the proton tests are only a fraction of the ratios that will be experienced in the LHC. On the other hand, more representative ratios can be obtained with neutron irradiation from nuclear reactors or mixed fields such as CHARM. This also applies to systems, as in the case of RadMon (Section 3.1.4, which if they contain bipolar components, may show different degradation behaviour as the ratios vary).

However, not all systems allow the whole design to be irradiated, whereas in most cases it is possible to irradiate a part of the system. During the development of this thesis, several system-level test approaches were developed to perform the different tests based on the available irradiated area and are presented in the test description part of the section.

### 3.4.5 Sensor Calibration

While high-energy proton testing is sufficient to evaluate the SEE and TID sensitivity of components according to the CERN RHA, more detailed characterization is required for radiation sensors. For SRAM sensors, in order to measure HEH and Th fluences, it is necessary to know the sensitivity of the component to both quantities. To evaluate the HEH cross-section, characterization is performed through a high-energy proton beam of 200 $MeV$ while for Th sensitivity, a thermal and epi-thermal neutron source is used. The process consists of writing a pattern in the memory, irradiating with the specific beam, and reading the number of bit flips after reaching a certain fluence. With the reference fluence provided by the facility and the total number of bit flips occurring, the cross-sections are evaluated. This operation is carried out on different chips from the same batch to take into account the uncertain variation within the batch in the final cross-section and is repeated for each batch. For the TID sensor, the calibration process can be performed in the Co60 structure with a pure gamma spectrum, inducing only the TID effect. However, in the case of FGDOS, there are different operating modes and it is important to assess their impact on the different sensor parameters (resolution, accuracy, and sensitivity degradation). In previous work [122], analyses were already performed on the chip, but the passive mode, defined in Section 3.3.5, still requires further investigation. This mode will be analyzed in the next section, focusing on the degradation of the sensor in terms of current consumption and sensitivity when used in passive mode.

In general, for sensor calibration, there are two possible approaches:

1. Lot Calibration: it consists of evaluating the responses of several samples belonging to the same production batch to a specific radiation effect and, from the measurements taken, obtaining an average sensitivity with a certain uncertainty.

2. System Calibration: this method, being time-consuming, is not typically followed. However, calibrating each system by assessing the true sensitivity of each system's sensor, may increase the precision of measurements.

The latter approach is usually too complex to execute, requiring extensive cabling to test many systems, but with battery-powered wireless applications, the only difficulty is to calibrate the test locations. An example of such a process is shown in Section 3.5.6.

## 3.5 System Validation

The additional validation and qualification steps added to the standard RHA were applied to the Wireless IoT system to validate it. This system represents the validation vehicle for the methodology and innovation in terms of the monitoring platform. In this section, several testing approaches are proposed that complete the methodology by allowing reproducibility of operations for a different system and proving its validity.

### 3.5.1 Component-Level Qualification

The component-level testing is the first validation step of the methodology and as suggested by Traditional CERN RHA, it was performed at the PSI facility under a 200 $MeV$ Proton Mono-energetic beam. A replacement rate of one faulty unit every three years has been assumed as a requirement. In most critical areas where the System is expected to work (HL-LHC DS Area), it corresponds to a dose of about 300 $Gy$ and a DDEF of $1.5{\cdot}10^{11}$ 1 $MeV\ neq.\cdot cm^{-2}$. As discussed in Section 3.4.1, when performing component-level qualification for low power components, several implications must be considered. The different bias modes can lead to different degradation rates depending on the bias used during operation. For a more realistic result, it would be optimal to replicate the operational conditions during the screening or to test all the different modes embedded in the component.

Interesting qualification requirements and results were found for some of the components tested. Between them, the 16 MB NOR flash memory used in Wireless IoT for data storage in case of communication failure or loss presents different operating modes that were tested individually.

1. ON Mode: no power safe mode is enabled, the memory is turned on and the current consumption is maximized.

2. OFF Mode: the memory is turned off during the irradiation.

3. Deep Power Mode: internal biasing mode through which it is possible to reduce the memory current consumption. When in this mode, it is not possible to read and write the content of the memory.

During the test, nine memories, divided into groups of 3 (One working modality per group), were initialized with a fixed pattern and were checked at different dose steps (Static

Test). In addition, a Dynamic Test on the other 3 chips in ON Mode was also performed: in this case, during the irradiation, the three memory contents were continuously read and compared to the initial pattern. The results of the test are reported in Table 3.5. As can be seen, the best results were obtained using the memory in OFF mode, while using it in Deep Power mode, which is the mode expected to be used in the system, reduced performance by a factor of 2.5. The higher lifetime achieved in OFF mode is an expected result: the non-recombined electron-hole pairs in the oxide of the MOS structure are split by the electric field, which since the device is turned off, is lower and as a consequence, the degradation may be reduced. It should be noted that during operation, the memory is used in dynamic mode, using both active and low power modes, and therefore, considering the results obtained in active mode (dynamic), a longer duration is expected concerning the result obtained using only Deep Power Mode. These results show that for low power components, the bias conditions are crucial, and special care must be taken when testing: testing under the worst conditions, even if they can be identified, does not guarantee realistic results. Furthermore, as the number of saves (entering in ON mode) depends on the duty cycle used, it is necessary to test the component by emulating this behaviour to know its lifetime. This emulation can be complex at the component-level and only by testing at the system-level would it be possible to obtain this information.

Table 3.5: Average TID ($Gy$) and DDEF ($1\ MeV\ neq. \cdot cm^{-2}$) failure levels of three samples irradiated per each mode at which the Flash memories were completely corrupted.

| **Mode** | **ON** | **ON** | **OFF** | **Deep Power** |
|---|---|---|---|---|
| **Test Type** | **Dynamic** | **Static** | **Static** | **Static** |
| **TID** | 346 | 400 | >500 | 200 |
| **DDEF** | $5.85{\cdot}10^{11}$ | $6.76{\cdot}10^{11}$ | $>8.45{\cdot}10^{11}$ | $3.38{\cdot}10^{11}$ |

The MCU and LoRa transceiver showed intriguing behaviours, as the occurrence of SEFI resulted in a loss of functionality, which could only be recovered by a power cycle. For these two components, the total measured SEFI cross-section corresponded to $3.51 \cdot 10^{-11}$ $cm^2$, while they reached a TID of 500 $Gy$ and DDEF of $8.45{\cdot}10^{11}$ $1\ MeV\ neq. \cdot cm^{-2}$, without suffering any failure. The existence of SEFIs makes it necessary to use an Ext WTD to recover when they occur. Besides, the effectiveness of the mitigation solution can only be assessed through system-level testing. The two LDOs of the power subsystem were also tested, facing the same TID and DDEF as the previous digital components and showing no degradation. No SET was observed despite a total fluence of $8.6{\cdot}10^{12}$ $p \cdot cm^{-2}$. None of the components

exhibited increased current consumption. As noted above, system-level testing is essential to assess the true life of the system due to the challenges of replicating working conditions and to verify the effectiveness of the recovery mitigation strategy (Ext WTD).

### 3.5.2 Electrical Validation

As described in Section 3.4.2, some tests can be performed without radiation. This section describes the different electrical tests carried out on the system that did not involve radiation testing, but which still allow the system to be validated and provide valuable information for the system-level qualification phase.

#### Firmware Description

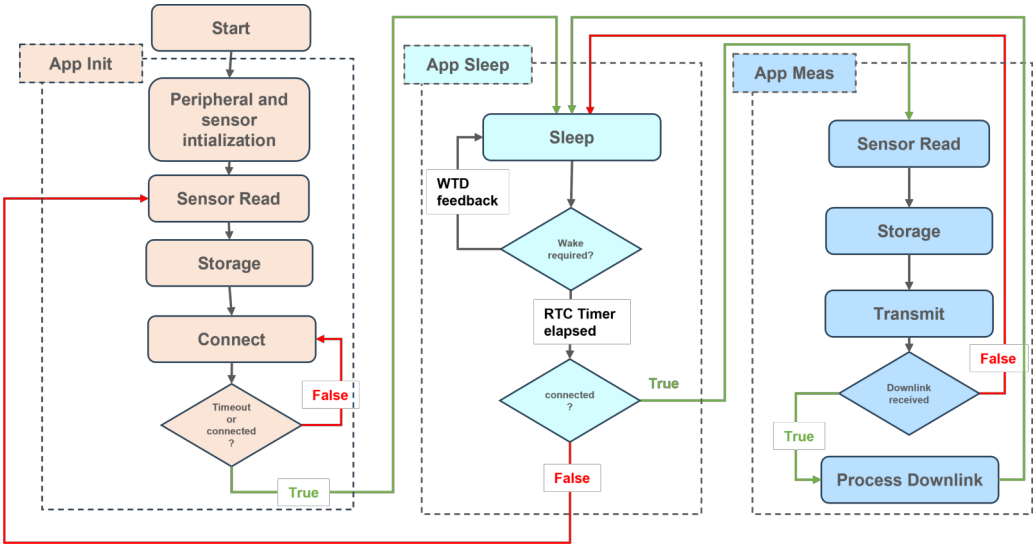


Figure 3.13: Flow Chart of the Wireless IoT Monitoring system firmware.

The duty cycle mode presented in Section 3.3.2 and required to minimize device current consumption, is implemented in the Wireless IoT firmware through a Finite State Machine (FSM) composed of three main states. This FSM, depicted in Fig. 3.13), controls the system functionalities and schedule the different operations. After start-up (setting up of the different clocks and GPIOs), the system initializes the sensors and peripherals required for operation. Once completed the sensors are read, the results are stored in the Flash memory and it starts the network join process. To take into account the possible unavailability of the network, a timeout is defined after which the system stops trying to connect and enters sleep mode (App sleep). On the other hand, if it connects, the previous measurements are transmitted and App sleep is reached. In this mode, the system reduces power consumption

by disabling the MCU's unneeded internal peripherals (e.g. ADC) and setting the external component to power save mode (e.g. Flash set in deep power mode, FGDOS reset enabled). An MCU internal Real Time Clock is used to wake up the system when a specific timeout is elapsed (Duty Cycle Time). When this timeout is reached, the system can reach two different states:

1. App Init: the initial state is reached again if the connection was not possible at the previous wake period.

2. App Meas: this state is reached in case the system manages to join the network.

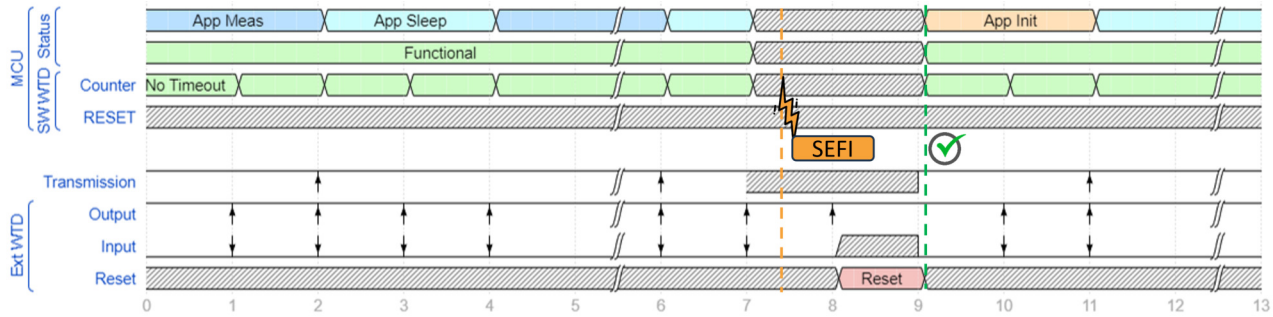


Figure 3.14: The Ext WTD recovery working principle is shown in the figure. When the MCU Status is undefined (Not functional), it cannot reply to the Ext WTD request and the latter reset the MCU. After the reset, the MCU reboots, starting from the App Init state.

In both cases, the operations performed are the same (Read sensor, store the measurements). The only difference stays in the operation related to the transceiver. If the device is not connected, it tries to connect again (App Init in Fig. 3.13). If it is connected, it simply transmits the measurements respecting the LoRa Protocol Class A timing (Opening of Tx and Rx windows) and it goes back to App Sleep. Once connected, the system no longer enters the App Init phase. During all phases, the MCU feeds the Ext WTD via an external interrupt. The working principle of the Ext WTD is described in the flowchart of Fig. 3.14. During the normal MCU operation, the Ext WTD triggers the controller every 60 seconds through a GPIO toggling. If the MCU replies to the trigger (e.g. toggling another GPIO connected to the component), it recognizes that the system is still functional. If not, the component resets the MCU, restoring system functionality.

#### Power Requirements Validation

As described in Section 3.4.2, some tests can be performed without radiation. For battery-powered systems, this may include assessing whether the system's performance matches the

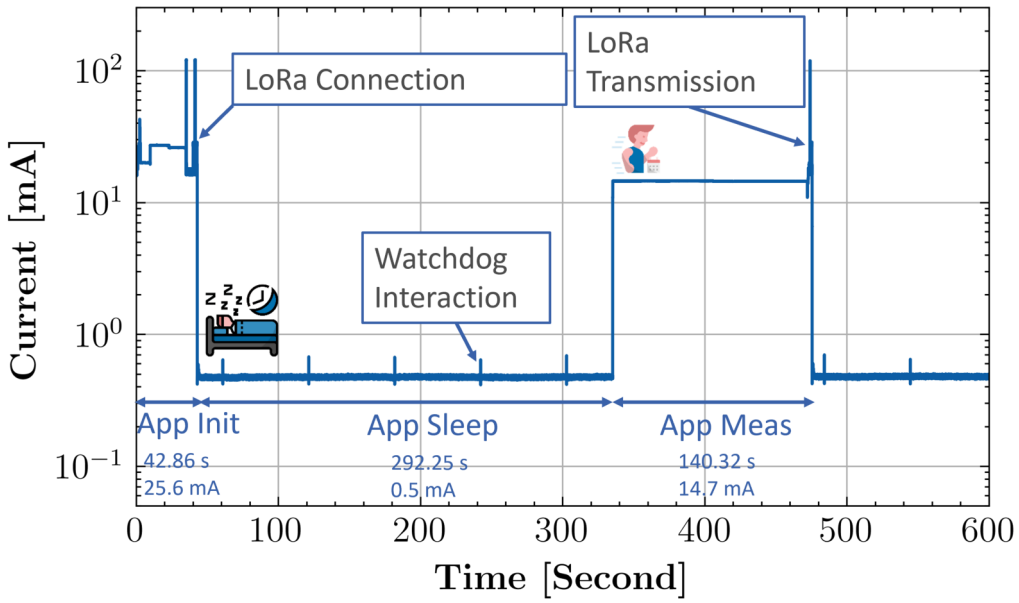


Figure 3.15: Wireless IoT power consumption. After the App Init period (Average Power consumption ($P_{avg}$): 184.3 $mW$), the device enters App Sleep ($P_{avg}$: 3.6 $mW$) for a configurable period. At the end of this period, it starts the App Meas operation ($P_{avg}$: 105.8 $mW$): wakes up, measures, stores, transmits, and enters App Sleep again. The cycle is then repeated. Each phase's duration and average current are reported.

original requirements, for example, the expected system life based on power consumption. The Wireless IoT implements the duty cycle mode described in Section 3.5.2, which allows the daily power consumption to be reduced and the battery life to be improved. In Fig. 3.15 the current consumption of the system is shown. As it is visible the current consumption in App Sleep is much lower compared to the one in App Meas, thanks to the power saving mode of the Controller and of the different components. The duration of App Meas can be adjusted based on the required measurement precision. Increasing the number of measurements and increasing the duty cycle will result in decreased battery life of the system. This counter-effect can be observed in Fig. 3.16, where the expected lifetime of the system, calculated from the power consumption data of the system, is plotted as a function of the duty cycle. These design choices allow operation for over three years in an LHC environment as visible in Fig. 3.16. However, cumulative effects may affect the component's performance in terms of current consumption, leading to an increase in this parameter, which in turn may reduce the system's battery life. In addition, the behaviour of the component may change depending on the dose rate experienced. It is therefore essential to carry out further analysis to investigate if the current consumption increases due to radiation effects and if the dose rate can affect this parameter. The analyses carried out on this system about current degradation due to cumulative effects are presented in Section 3.5.3.

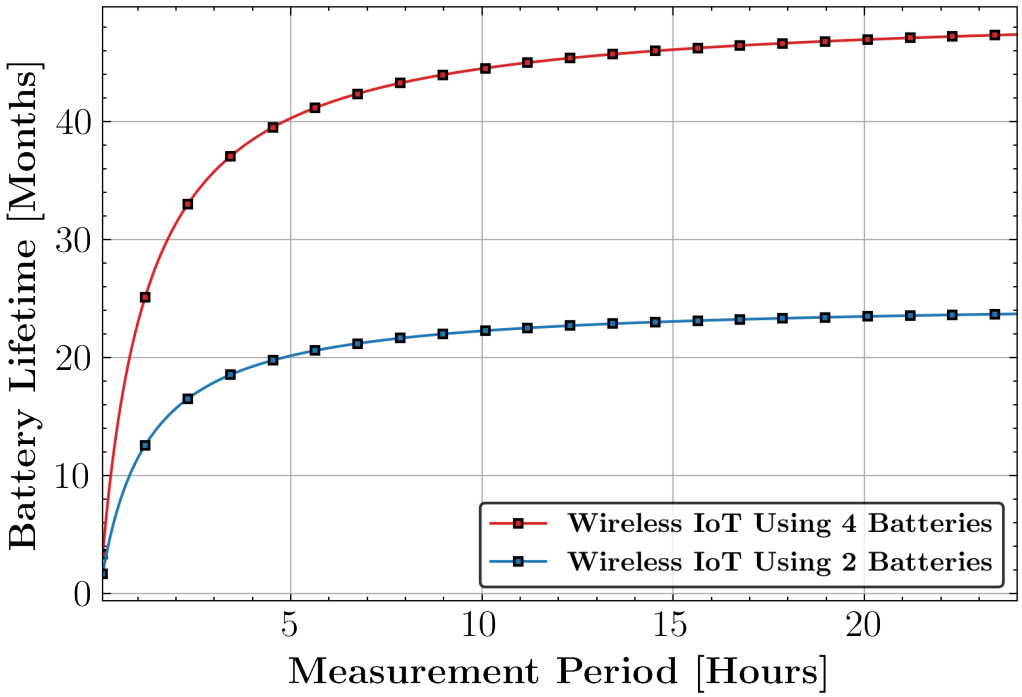


Figure 3.16: The Battery Lifetime is depicted as a function of the measurement period. As visible increasing the measurement period it is possible to extend the lifetime of the BatMon.

#### Test Under Magnetic Field

(a) CERN CMS M1 Magnet

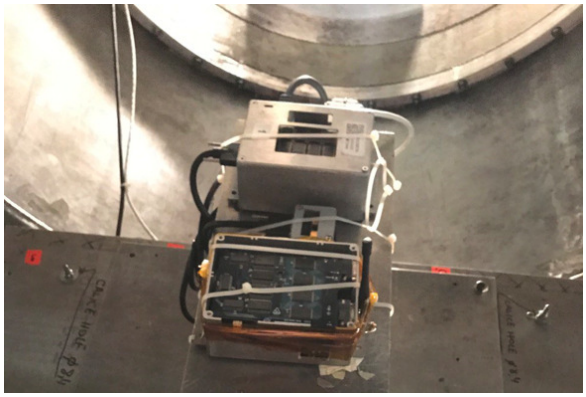

(b) Test Setup installed in CMS M1 Magnet

Figure 3.17: In Fig. 3.17a, the CERN CMS M1 Magnet is depicted while Fig. 3.17b shows the setup (a Wireless IoT platform and a RadMon) installed within it.

As defined in Section 3.4.2, another step in the system qualification was to check its capability of working in environments characterized by the presence of a Magnetic Field. The test was carried out at CERN using the CMS M1 Magnet (Fig. 3.17a). This magnet can provide a 3-T horizontal magnetic field in its center, and 3.6 $T$ in the center of each coil. The magnet is located in a large experimental hall at CERN in the North Area, on the Prévessin site in France, in a radiation supervised area. The test was divided into two phases:

1. Ramping up: the magnetic field is ramped up reaching the target value. The device behaviour is checked.

2. Stable field: the Magnetic field is taken stable and tests are carried out.

The functionality of the Wireless IoT was monitored during both phases and steps of 0.5 $T$ up to 3 $T$ were performed. The field experienced during the test is shown in Fig. 3.18. Data from the Wireless IoT Monitoring system were collected wirelessly. An indoor LoRa gateway RAK7258, configured with a static IP and connected to a personal computer, was used to collect the data. It was placed in the control room, outside the area of interest of the magnetic field. During this time, the Wireless IoT Monitoring system showed no degradation in transmission capability and on-board functionality. No issues were observed on the different voltages on board, as visible in Fig. 3.18. No resets were experienced and thus the system seems to be immune to the presence of an active magnet. The immunity of the system to the presence of a magnetic field allows the use of the BatMon in the experimental areas where the RadMon cannot be used as described in Section 3.1.3.

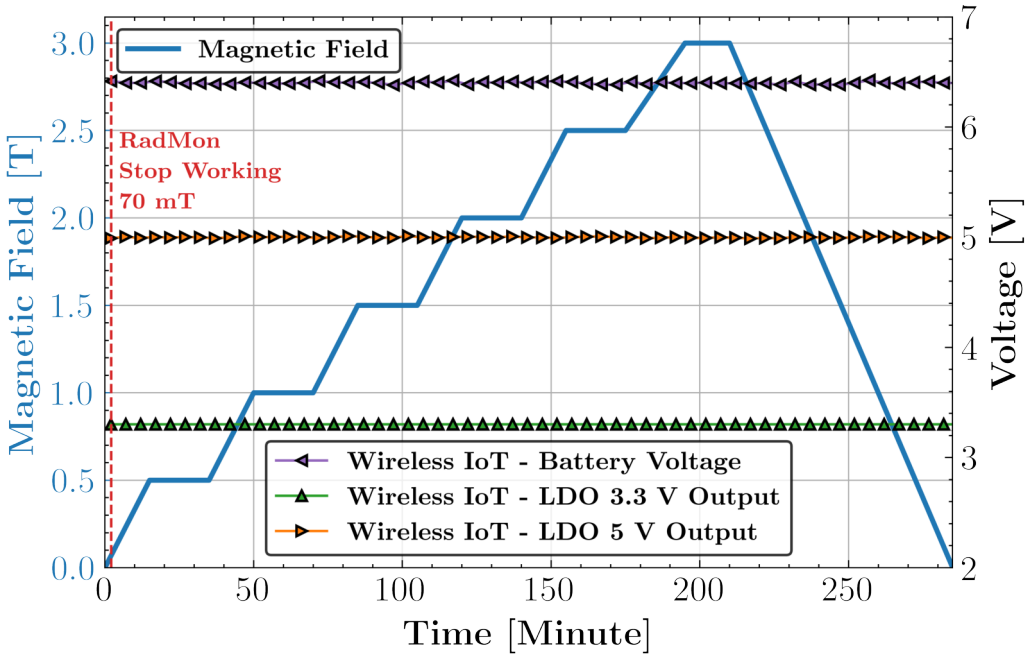


Figure 3.18: Magnetic field provided by CMS M1 over time experienced during the test. The on-board voltages ADC readings, retrieved through the LoRa packet collected, are shown. As can be seen, the RadMon stops working at around 70 $mT$, while the Wireless IoT shows no degradation up to 3 $T$ (Correct packet transmitted during the whole test).

**LoRa Validation in Tunnel**

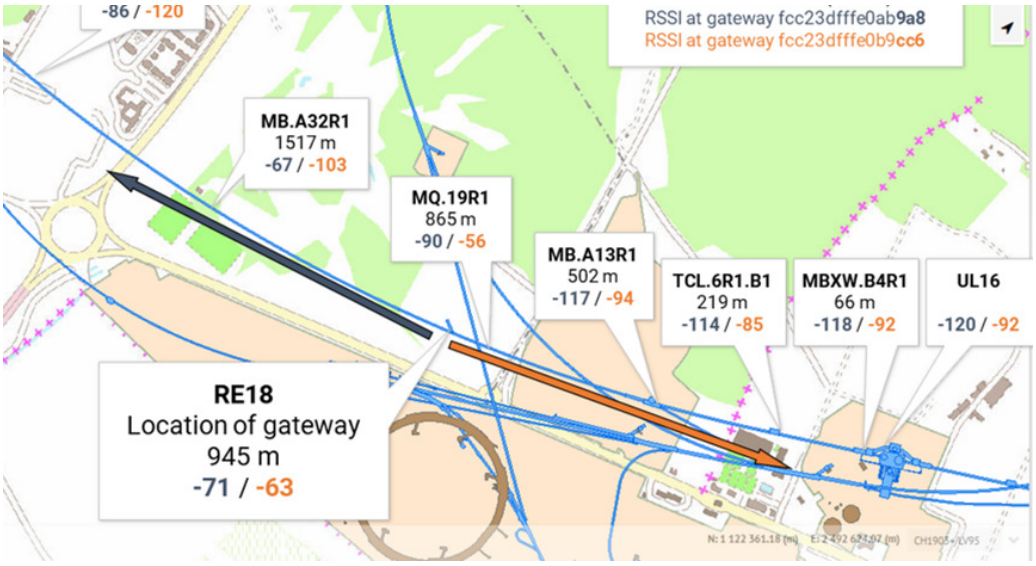


Figure 3.19: The RSSI expressed in $dBm$ decreases as the distance from the gateway increases, but communication is still solid [124].

Also tests on the wireless capability of the IoT monitoring platform wireless can be carried out without radiation. To evaluate the long-range capability of the technology chosen and prove its validity as a network in the accelerator, a test was carried out in LHC P1. Two LoRaWAN gateways were installed in UPSRE18 alcoves. Moving further away from the gateways, five packets were collected every 200 $m$. The RSSI reported by the two gateways, were used as magnitude to analyze the quality of the network. The results of the test are displayed in Fig. 3.19. As visible, the transmitted packets were successfully received by at least one gateway at a distance exceeding 2 $km$, demonstrating that LoRa technology is compatible with the long-range requirements of this application in an accelerator environment.

### 3.5.3 System-Level Validation Under TID

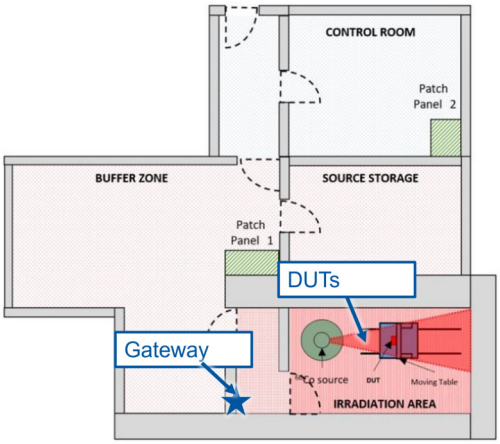


(a) Co60 layout and equipment Position

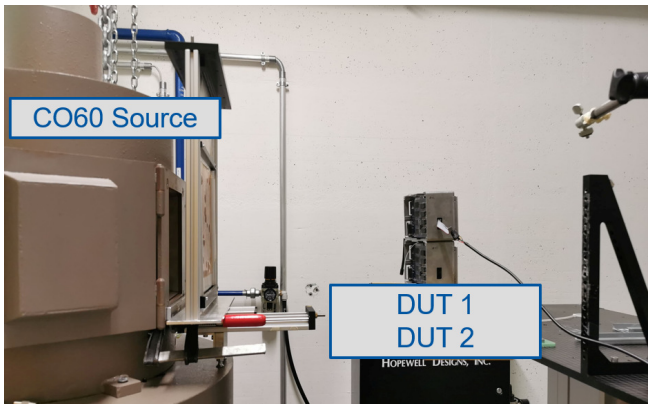


(b) Test Setup at Co60

Figure 3.20: the CERN Co60 layout is presented with the different positions of the test setup (Fig. 3.20a). In Fig. 3.20b, the two Wireless IoT platform placed in front of the source and tested at the Co60 facility.

Due to the unavailability of CHARM, further tests, divided into different types of facilities, are required to complete the system-level validation as described in Section 3.4.4. The first tests can be performed at the Co-60 facility as foreseen in the developed alternative methodology. In this test facility, it is possible to evaluate the degradation of the system under only the TID effect. In addition, thanks to the gamma contribution alone, it is possible to test all operations without interruption, since no SEFI can be generated. Different tests were performed to validate and qualify the system.

#### Firmware Validation

A first test was carried out to validate the firmware and the procedure used to read the FGDOS. During the test, the packets were logged. An indoor LoRaWAN Gateway RAK7258 was installed outside the irradiation area as shown in Fig. 3.20a and configured to establish a private LoRa network. The Wireless IoT was placed in front of the source and its position was calibrated using an ionization chamber. The dose rate measured at its position corresponds to 0.45 $Gy \cdot h^{-1}$. It has to be noted that the Ionization Chamber provides measurements in $Gy(Air)$. The gamma emitted by a $^{60}Co$ source has energy of 1.172 and 1.332 $MeV$. It was observed that at 1.25 $MeV$ energy, the difference between TID in Air [125] and Si [8] is negligible. During the test, two issues were observed.

1. Overcharge: when a value below the threshold frequency is reached and the charge is

enabled, the process does not end with the end of the charge (Bit disabled). A residual charge continues to charge the FGDOS, overcharging it. The value transmitted, which corresponds to the frequency read at the end of the charge indicated by the sensor, is an underestimation as the process is not finished and at the next acquisitions are higher.

2. Recharge Lost: since the sensor uses passive mode, charging is not autonomous. The sensor is read at each measurement period and therefore only at the reading, the MCU can detect if a recharge is needed and enable the process. As a result, the frequency can fall below the frequency threshold. If the latter frequency is used as the start frequency of the charging process, the TID may be underestimated.

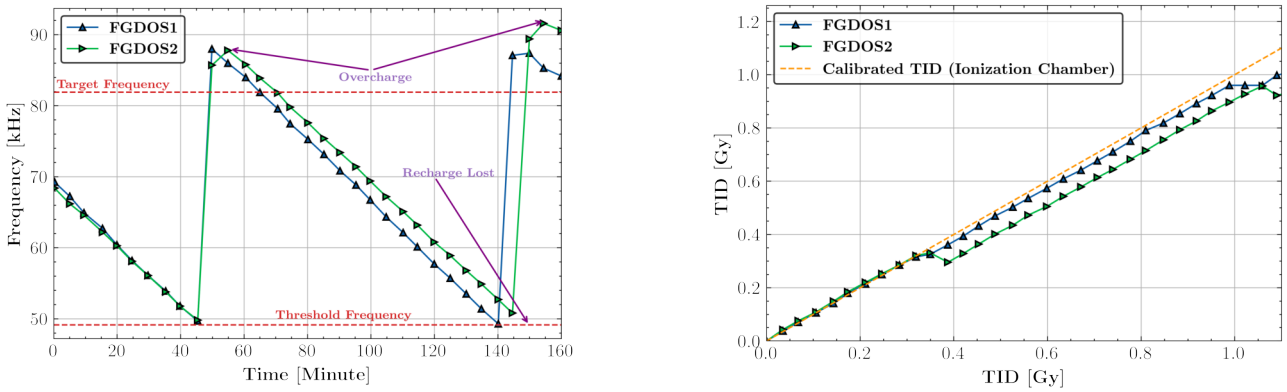


(a) (b)

Figure 3.21: Result of the first test carried out to validate the firmware used to read the FGDOS. In Fig. 3.21a, the two FGDOS output frequencies respect the test time, and the "Overcharge" and "Recharge Lost" issues are indicated. In Fig. 3.21b, the TID from the two FGDOSs compared to the one expected (Ionization Chamber). As visible the two problems are leading to a strong underestimation of the TID.

As visible in Fig. 3.21, The two FGDOS underestimate the TID compared to the reference TID (ionization chamber). The missing TID contributions are due to the "Overcharge" and "Recharge Lost" problems described above. For example, as shown in Fig. 3.21a, at minute 150 the frequency read by FGDOS2 is lower than the next reading. This phenomenon is caused by the "Overcharge" problem and as a result, the TID contribution corresponding to these two consecutive readings is erroneously negative. Always at minute 150 and with reference to FGDOS2, since the frequency at which recharging occurs is not transmitted, it is not known how much the sensor has discharged below the Threshold frequency, and using the latter as an approximation, the TID is underestimated. This is particularly critical not only in a high dose rate environment but also in the event of network unavailability and

packet loss. The two problems were issued with a firmware upgrade and another test was carried out following the same procedure.

To solve the Overcharge, the frequency transmitted when a recharge occurs is not the one immediately read at the end of the process ($f_{realendcharge}$), but a delay of 200 ms has been added to allow the process to be effectively completed. For the Recharge Lost, a variable containing the value of the frequency at which the recharge starts ($f_{startrecharge}$) has been added to the payload transmitted. Positive results were obtained through these modifications. In particular as visible in Fig. 3.22a, the overcharging problem is not occurring anymore since the frequencies are always decreasing. In addition, the exact shape of the sensor outputs can be rebuilt knowing the exact frequency at which the recharge has started. These upgrades are necessary to exploit the passive mode of the sensor and reduce the uncertainty of the final measurements. However to compute the TID the autonomous mode formula (Equation (3.1)) cannot be used since would lead to an underestimation as previously demonstrated. The following formula needs to be applied:

$$TID = \frac{f_{BegIr} - f_{realendcharge_0} + \sum_{i=0}^{N}(f_{realendcharge_i} - f_{startrecharge_i}) + f_{startrecharge_0} - f_{EndIr}}{Sensitivity} \tag{3.2}$$

in which N is the number of recharges that occurred. So for N equal to 0, the equation can be reduced to:

$$TID = \frac{f_{BegIr} - f_{EndIr}}{Sensitivity} \tag{3.3}$$

It is clear that to use this formula, none of the packets transmitted must be lost. If the packet sent when a recharge occurs is lost, $f_{realendcharge}$ and $f_{startrecharge}$ would be unknown if they are not stored and sent in the next transmissions. In this case, $f_{tg}$ and $f_{th}$ can be used to approximate these values. Due to payload size constraints, only $f_{startrecharge}$ is transmitted as an additional variable in the packet, so if this critical packet is lost, only this value can be known from subsequent packets. However, if the system was reset and the value of this variable was not stored in non-volatile memory, it would assume a value of 0 on reboot. If the reset occurred immediately after recharging and the corresponding packet was lost or not transmitted because the system failed during this process, then the next packet sent after resetting the system would contain incorrect information. According to the information transmitted, recharging would start at 0 $Hz$ (measurement overestimation). To avoid

this problem, this variable should be stored in non-volatile memory so that it is only set to 0 if no recharging has ever taken place or if the sensor has been effectively discharged at 0 $Hz$. At the same time, if there is a longer period without data transmission due to the unavailability of the network, during which sensor recharges occur, not all differences of $\sum_{i=0}^{N}(f_{realendcharge_i} - f_{startrecharge_i})$ would be known and it would not be possible using equation (3.2) to compute all TID contributions. In this case, the unknown differences can be approximated with the $\Delta_{LR}$ as done in equation (3.1). To keep track of the number of reloads that have taken place, the reload counter is also transmitted. This is a critical variable and must be stored in non-volatile memory in order not to be reset and lose information. It is the variable that guarantees the cumulative property of the sensor, even when used in passive mode.

As illustrated in Fig. 3.22b, computed using equation (3.2), both using the average sensitivity (sensitivity assessed by calibrating multiple FGDOSs, the process of which will be presented in Section 3.5.6) and the actual sensor sensitivity (Calibrated), the relative error concerning the reference (ionization chamber) is reduced to $\pm 1$ %.

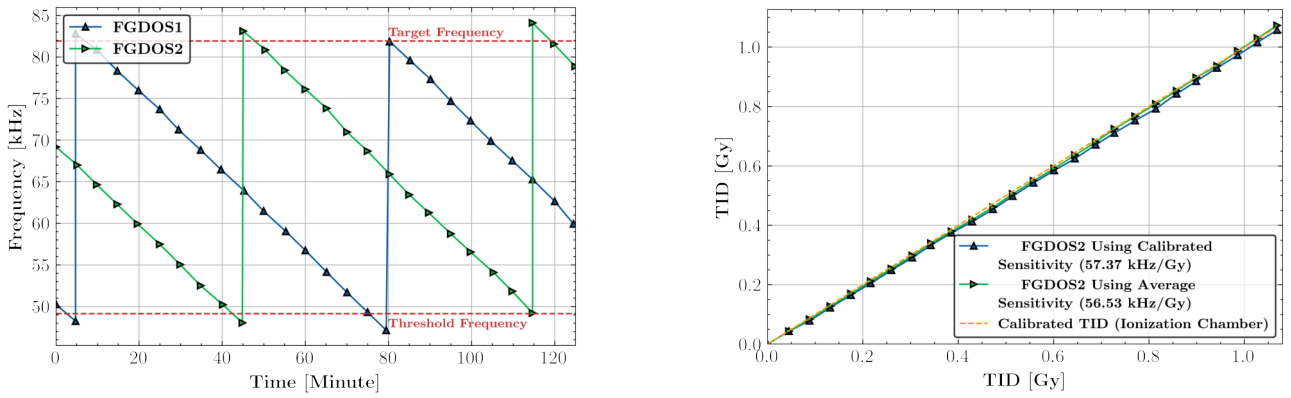


(a) (b)

Figure 3.22: Result of the second test carried out to validate the firmware used to read the FGDOS. In Fig. 3.22a, the two FGDOS output frequencies respect the test time, while in Fig. 3.22b, the TID from FGDOS evaluated using an Average and its Calibrated sensitivity evaluated respect the TID of the Ionization Chamber.

This test is a demonstration of how testing a radiation monitoring system in the presence of the TID alone can be beneficial to verify the functionality of the firmware and the sensor reading. This result will allow to obtain measurements in operation with a lower uncertainty.

#### Evaluation of Performances with Different Duty Cycle

As stated in Section 3.4.3, the BatMon may show different degradation rates if different duty cycles are used in different operating modes. The implementation of a realistic duty cycle can enable the evaluation of system degradation with outcomes that closely resemble those that will be achieved during operation. The duty cycle of the Wireless IoT will depend mainly on the radiation environment in which it operates. In alcoves, due to the low radiation rate, it is expected to read the sensor every 1 hour or even once a day. In harsher environments, in order to prevent the FGDOS from operating outside the Linear Range, it will need to access the sensors with higher frequencies (lower measurement period). An initial test was performed to evaluate the system TID degradation and sensor sensitivity with two different duty cycles. The duty cycle ($DC_{Bat}$) of the Wireless IoT Monitoring system can be defined as defined in equation (3.4).

$$DC_{Bat} = \frac{T_{AppMeas}}{T_{MeasPeriod}} \tag{3.4}$$

where $T_{AppMeas}$ is the period of time spent in Acrive Mode while $T_{MeasPeriod}$ is the measurement period (App Meas + App Sleep). As shown in Fig. 3.15, the most time-consuming part of App Meas State is the reading of the sensor and, in particular, the SRAMs. The use of SPI GPIO expanders increases the time required to read and write each SRAM due to both the SPI speed used by the MCU, the increased number of operations required to control the expanders, and especially, they need to be read one by one. For this reason, one system was programmed with the firmware (Device Under Test (DUT) 1) presented in Section 3.5.2 and a $T_{MeasPeriod}$ of five minutes, giving a $DC_{Bat}$ of ~53 %. The second system (DUT2) was always configured with the same measurement period as DUT1 in order to obtain as much data as possible and avoid the FGDOS from operating outside the LR since one of the scopes of the test was to evaluate the sensitivity degradation with different $DC_{Bat}$. However, a modified firmware was used to reduce the duty cycle. Since the SRAMs are not important for this type of test, their reading and writing have been removed from this firmware version, so basically only the FGDOS was read during the App Meas period, reducing $DC_{Bat}$ to ~15 %.

As illustrated in Fig. 3.20b, both DUTs were positioned in front of the beam, at a distance from the source such that the dose rate was 3.06 $Gy \cdot h^{-1}$. An indoor LoRaWAN Gateway RAK7258 was installed outside the irradiation area as shown in Fig. 3.20a and configured to establish a private LoRa network. Packets received were recorded in specific log files. The

test was stopped when 320 $Gy$ was reached and the devices were removed. The contents of the two external flash memories, using both ON and Deep Power modes, were checked and found to be still functional. The collected data allows investigating the sensitivity degradation of the FGDOS with different $DC_{Bat}$. The behaviours are depicted in Fig. 3.23. As can be seen, the FGDOS of the two systems exhibits the same behaviour, proving the independence of the $DC_{Bat}$ used. A reduction in the slope of the curves can be observed around 80 $Gy$.

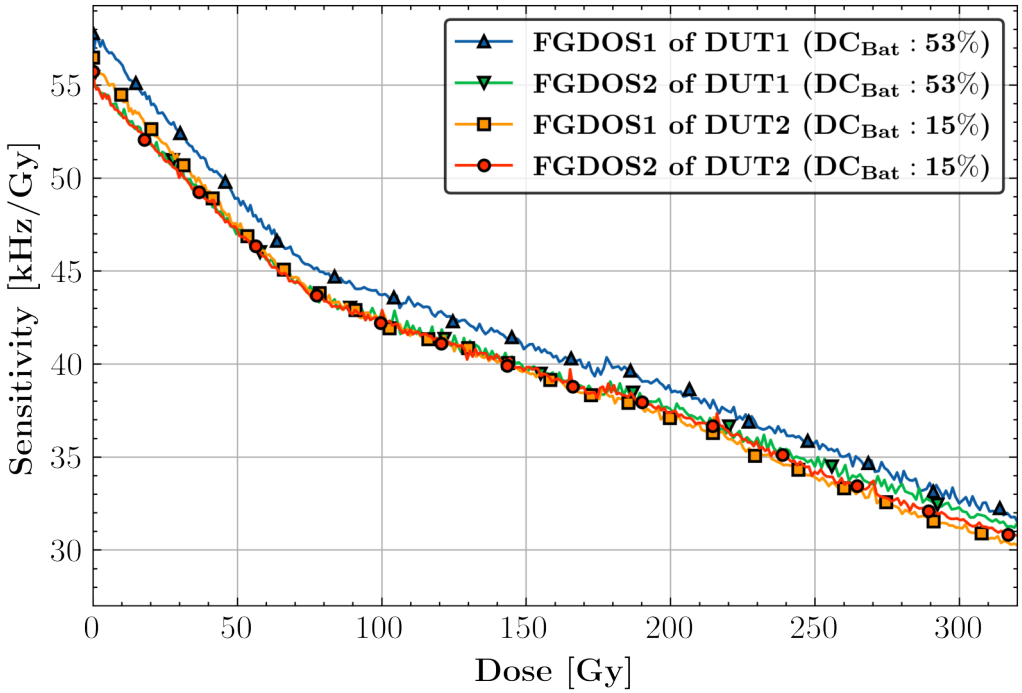


Figure 3.23: In passive mode the FGDOS sensitivity degrades with the TID. It does not depend on $DC_{Bat}$ selected.

Another interesting observation concerns the base current required by the two systems. This was measured and found to have increased by the end of the test. Both systems showed similar behaviour. The cause of the increase concerned the Sensor Board and was independent of the operating mode (App Sleep or App Meas). To detect the cause of the fault, the 5 $V$ rail, powering the FGDOS, was disconnected (Cut) and the individual component was supplied from an external source. The cause of the current increase has been identified in this component. This last result motivated the planning of a further test to evaluate the current increase due to the TID. Two other new systems (DUT3 and DUT4) were tested, recording their current consumption every second. A feature of this facility is the possibility to test the system without SEE-induced interruption, which allows all its operating modes to be exploited as presented in Section 3.4.4. This is a perfect environment to qualify performance degradation due to TID alone, and this test is another example of exploiting this feature. A

Setup similar to the previous irradiation was used, but the dose rate measured during this test was 3.96 $Gy \cdot h^{-1}$. The campaign was completed once 350 $Gy$ were reached and the device was removed. No degradation was observed on the on board hardware, since all the components were still functioning. The current measurements taken during the test allowed the rate of current degradation due to TID to be assessed. Its behaviour has been analyzed and is shown in Fig. 3.24. As visible, at around ~80 $Gy$, the system's current consumption starts slowly increasing and reaches a slope of 0.5 $mA \cdot Gy^{-1}$ at ~150 $Gy$.

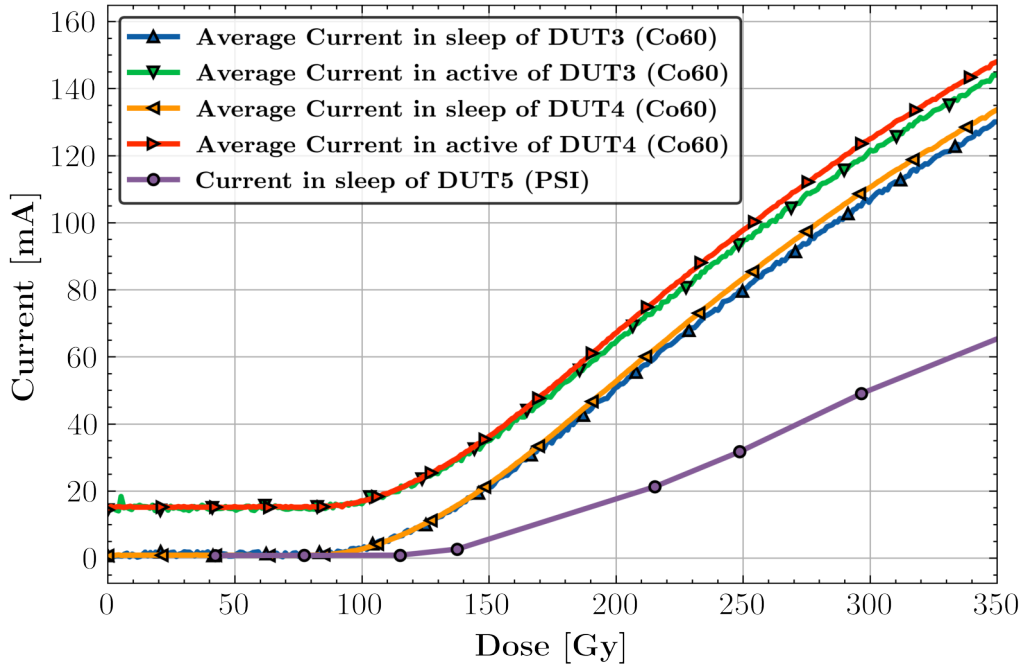


Figure 3.24: Current consumption of the system is increasing as the TID increases. The increase in current is compared with that observed at a high dose rate (>46 $Gy \cdot h^{-1}$) at PSI (DUT5), the testing of which is described in Section 3.5.5.

The current consumption degradation rate measured was used to evaluate the expected lifetime of the system for different dose rates per year different from 0. As illustrated in Fig. 3.25, the lifetime of the Wireless IoT is not impacted in an environment where the dose rate per year is less than or equal to 20 $Gy \cdot y^{-1}$ (Shielded areas in HL-LHC). On the other hand, in harsher environments like the DS Area of future HL-LHC (dose rate of around 100 $Gy \cdot y^{-1}$ as reported in Table 2.2), it is still possible to achieve a lifetime of more than one year by using a Measurement Period longer than 30 minutes (Fig. 3.25b). However, the lifetime will also become independent of the selected measurement period for values of the latter greater than 1 hour. Those results will be very important when selecting the measurement period in operation. In fact, favoring lifetime, selecting a measurement period longer than 1 hour will be useless in environments such as the DS area.

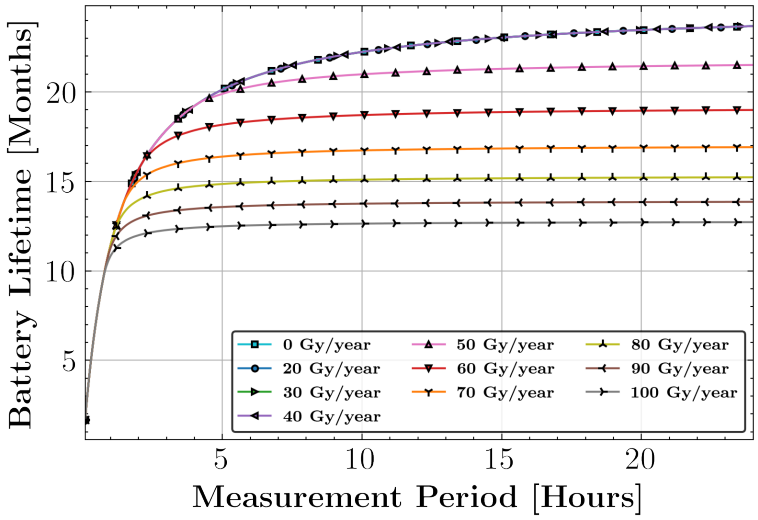


(a) Battery life for different yearly dose rates when the system battery capacity corresponds to 8.5 *Ah* (2 Batteries)

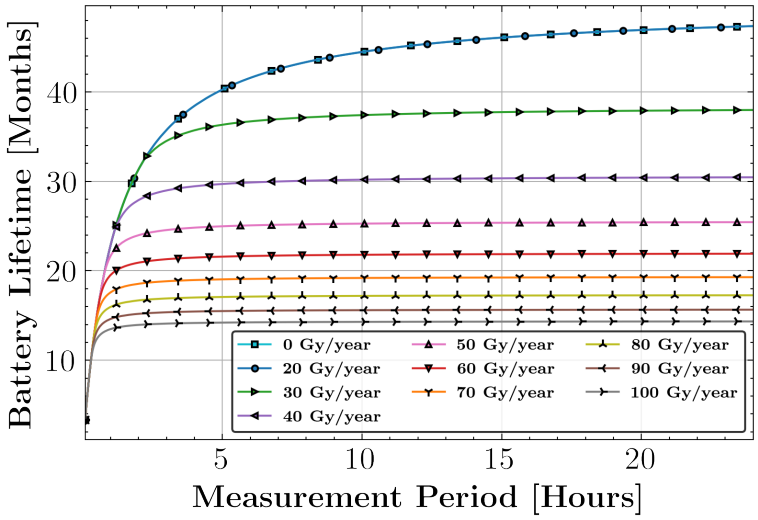


(b) Battery life for different yearly dose rates when the system battery capacity corresponds to 17 *Ah* (4 Batteries)

Figure 3.25: Battery life as a function of the measurement period. The expected dose rate per year may impact the lifespan, resulting in independence from the measurement period.

These outcomes provided a comprehensive view of system performance degradation, proving the importance of this phase of the methodology and its validity.

### 3.5.4 System Level Validation Under Thermal Neutron

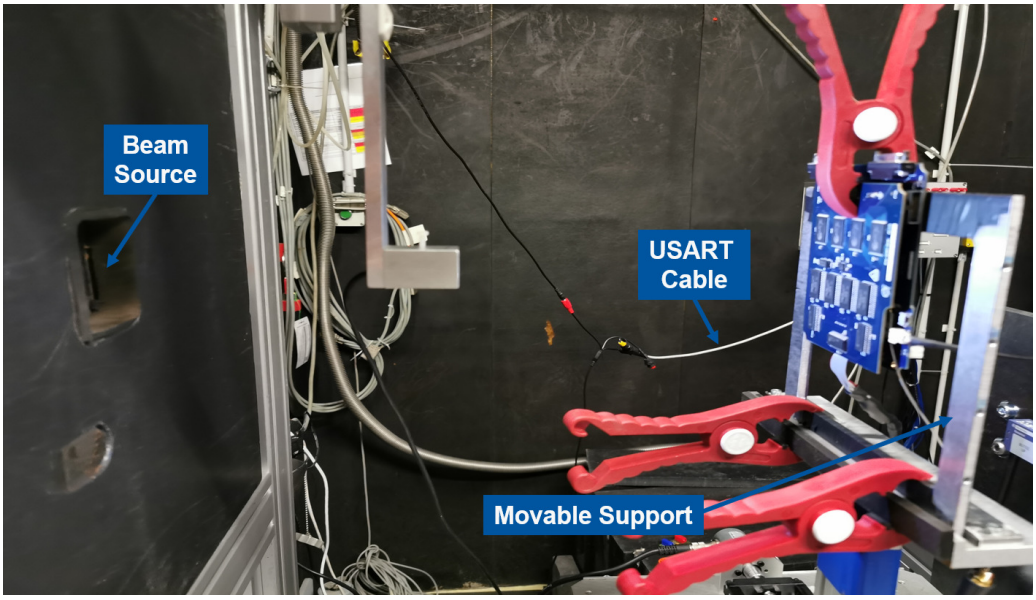


Figure 3.26: Wireless IoT placed in front of the beam and tested at TENIS.

Once the TID performance degradation was known, the Wireless IoT has been qualified under a Thermal and Epi-Thermal Neutron beam at the TENIS facility presented in Section 2.5.2. One limitation to system-level qualification at this facility is the 2 *cm* beam size available, which does not allow the entire system to be irradiated, nor many subsystems together. In the case of Wireless IoT, the design does not allow more than one subsystem to be tested at a time. The different subsystems were tested one at a time, but always with the whole system in operation, as the total SEE sensitivity of the system is the sum of the sensitivities of the different subsystems. This test methodology allows the identification of the thermal neutron sensitive parts. It also allows the qualification at the component-level to be completed if no previous data is available. The system was placed on mobile mechanical support that allowed the different subsystems to be positioned in front of the beam, as illustrated in Fig. 3.26. All the control instrumentation of the system was placed outside the experimental area. A power supply was used to power the Wireless IoT. An indoor LoRa gateway RAK7258, configured with a static IP, was employed to provide a private LoRa network and was placed in the control room with the other test equipment. A custom cable with a TTL-232RG connector was used to read data via USART provided by the system. A computer was employed to record the LoRa and USART transmission data.

For the test, some modifications were made to the MCU firmware in order to improve the observability of code execution and on-board functionalities. Specifically:

1. Storage Subsystem: whenever a record is saved in the Flash Memory, the content of the flash is checked to evaluate its correctness. If the previous attempt to save fails, the memory is reset via the SPI command. Another attempt is then made to ensure that all functions are restored. Messages are transmitted via USART, summarizing the result of these operations.

2. Recovery Subsystem: when an interaction with the EXT WTD occurs, a message is displayed. The timestamp of the interaction is also saved, to check if the timing (60 $s$) is respected.

3. Transmission Subsystem: packets are all recorded, but when a confirmed uplink is requested, a message is displayed indicating whether or not the confirmation was received.

4. Power Management Subsystem: the output value of the LDOs and the battery read out through the ADC is transmitted by the operating firmware every measurement period, so no changes were necessary.

Table 3.6 reports the different fluences cumulated for each subsystem. During the tests, no malfunctions were observed in the subsystems tested. Higher fluence levels were reached for the transmission and control subsystems, as they had a higher probability of containing $^{10}B$, being fully digital components. The value achieved corresponds to more than one year of operation in the DS area ($2 \cdot 10^{11}\ n \cdot cm^{-2}$) [38], guaranteeing high operational reliability concerning SEE effects induced by thermal and epi-thermal neutrons in harsh DS-like environments.

Table 3.6: Each subsystem was irradiated individually, accumulated different fluence values, and showed no sensitivity to neutrons belonging to this energy spectrum.

| **SubSystem Under Test** | **Fluence Absorbed [n $\cdot$cm$^{-2}$]** |
|---|---|
| **Transmission Subsystem** | $1.35 \cdot 10^{12}$ |
| **Controller Subsystem** | $1.14 \cdot 10^{12}$ |
| **Recovery Subsystem** | $4.61 \cdot 10^{11}$ |
| **Power Management Subsystem** | $4.06 \cdot 10^{10}$ |

### 3.5.5 System-Level Validation Under HEH, TID, and DD

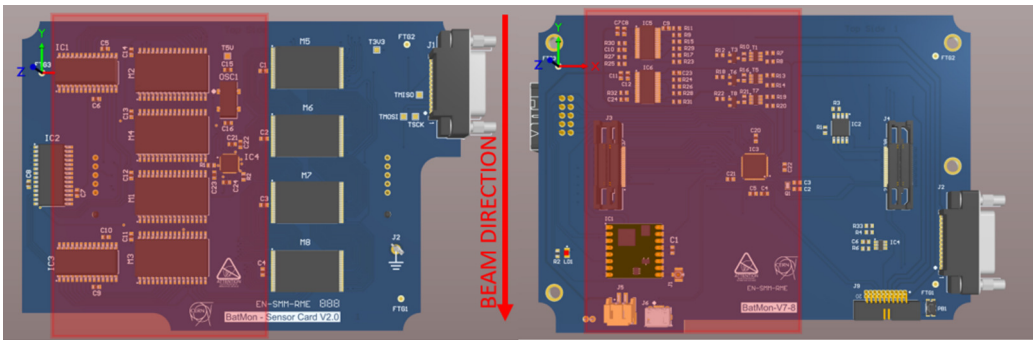


Figure 3.27: In red, the area irradiated in Wireless IoT 1 Test. It contains the Controller, the Transmission, the Power Management Subsystems and the TC554001AF sensors.

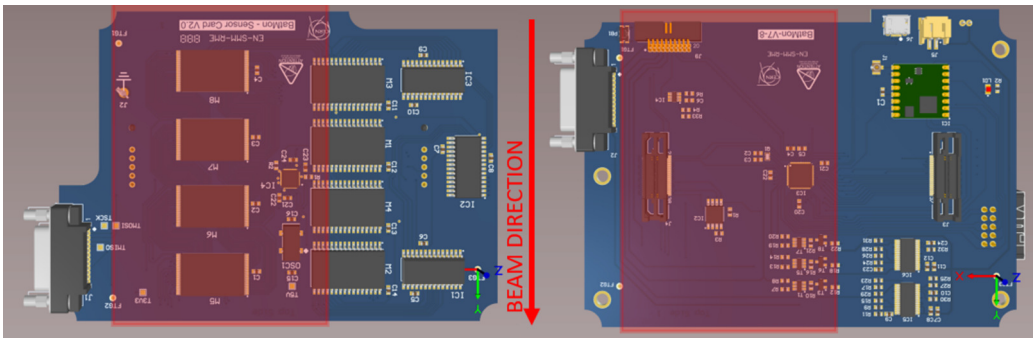


Figure 3.28: In red, the area irradiated in Wireless IoT 2 Test. It contains the Controller, the Recovery, the Storage Subsystems and the CY62167GE30 sensors.

To complete the system sensitivity evaluation, and estimate the expected failure rate and lifetime during operation, the alternative methodology for system-level qualification proposes a test campaign under HEH. As described in Section 3.4.4, this qualification is performed at PSI with a 200 *MeV* mono-energy proton beam, as foreseen by CERN RHA for component screening. As always stated in Section 3.4.4, this facility was selected because it provides a tunable and continuous flux. The possibility of reducing the flux can help in testing a system based on MCU and FPGA allowing it to perform all the operations of one working cycle (full duty cycle). In general, the use of low flux to characterize system life may not be cost-effective due to the time required to reach a given level of fluence and TID and the hourly cost of the beam. To overcome the above problem, a hybrid test approach can be used to evaluate both the cross-section and the degradation under TID and DD of the system. The methodology consists of increasing the fluence through several runs to estimate the SEE cross-section at a low flux and then testing the lifetime at the highest fluence. One issue presented by this particular irradiation facility when it comes to system-level testing

is the limited 5 *cm* beam size. Due to this, the whole system cannot be irradiated. Nevertheless, unlike TENIS, it is possible to test different subsystems simultaneously. Based on the data of component-level qualification, it was known that the two HEH-sensitive components were the transmission and control subsystems. As visible in Figures 3.27 and 3.28, one system was irradiated by having in beam the Controller with the Transmission, the Power Management Subsystems and the TC554001AF sensors (Wireless IoT 1) while the other having the Controller with the Recovery, the Storage Subsystems and the CY62167GE30 sensors. (Wireless IoT 2).

Both systems were placed in front of the beam with their sides facing it. This allowed us to perform both tests simultaneously. To ensure that the fluence was homogeneous throughout the irradiated area, Wireless IoT 2 was used, which had HEH sensors in the beam. As can be seen in Fig. 3.29, two acquisitions of its HEH (CY62167GE30) sensor were performed, which showed similar behaviour on all SRAMs. A relative difference of <4 % was noted between the memories with the highest and lowest bit flip measured. This value aligns with the uncertainty observed during calibration at PSI on the same batch (10 %), indicating a fairly homogeneous irradiated area.

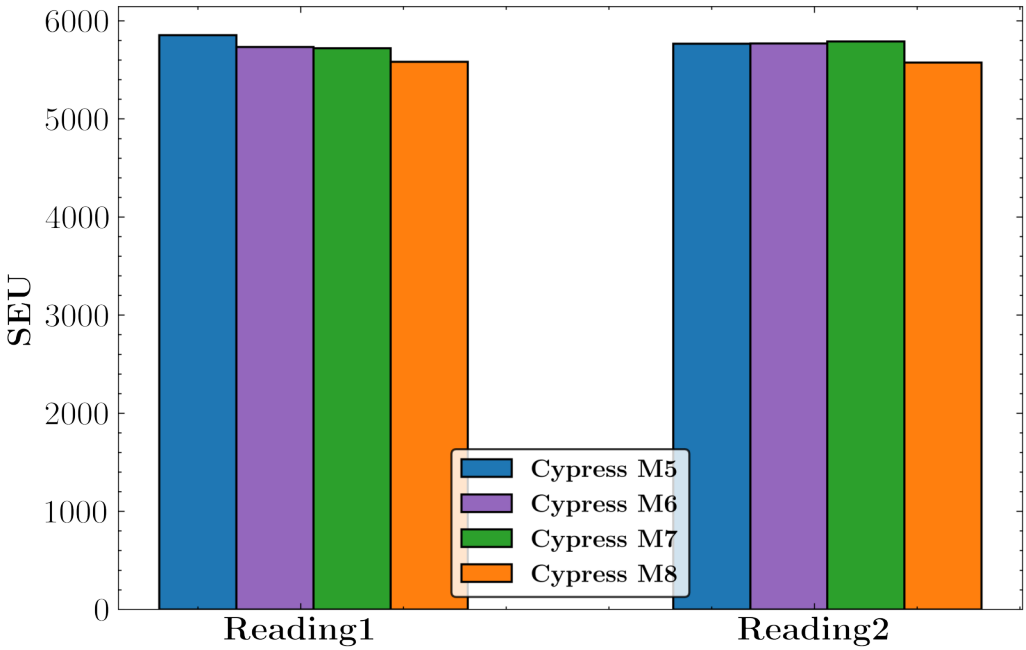


Figure 3.29: Bit flips measured on the CY62167GE30 SRAM (HEH sensor) to assess the homogeneity of the beam in the irradiated area.

In terms of the equipment used to power and monitor system status, a similar configuration was used to that used in TENIS. The only difference was the addition of observability points by monitoring the output voltages of the LDOs and the reset line via a cable con-

nected directly to an oscilloscope. These observability points were added to ensure that no SETs on the output of the LDOs would cause the system to reset.


(a) (b)

Figure 3.30: In Fig. 3.30a, the two Wireless IoT systems are mounted with their side part facing the source. They are stacked on top of each other to be tested together. In the figure, the different cables connected to increase the observability of the device are listed. A Gafchromic film was also mounted on the side of the two systems to check the effective irradiated area. At the end of irradiation, the targeted area was all black as visible in Fig. 3.30b, proving that the test setup was correct.

Thanks to the setup depicted in Fig. 3.30, different runs were carried out with different flux and are reported in Table 3.7. As visible the cross-section of the Wireless IoT is inversely proportional to the flux. This is a consequence of using the Ext WTD as a mitigation scheme. When a SEFI appears, the recovery time can range from a few seconds to a minute since the MCU's state is monitored by an Ext WTD with a set time interval. Additionally, software mitigation techniques inside the MCU allow it to reset itself, which brings the recovery time down to a few milliseconds. For these reasons, when using a high flux, some Single-Event Upsets can be hidden by the long recovery time combined with the high flux and thus, not be visible and quantifiable.

Table 3.7: Recoverable fault cross-sections of the group of subsystem irradiated during Wireless IoT 1 and 2 tests.

| **Flux** $[p \cdot cm^{-2} \cdot s^{-1})]$ | **Wireless IoT 1 Recoverable Faults Cross-Section** $[cm^2 \cdot Device^{-1}]$ | **Wireless IoT 2 Recoverable Faults Cross-Section** $[cm^2 \cdot Device^{-1}]$ |
|---|---|---|
| $2.20 \cdot 10^{7}$ | $6.50 \cdot 10^{-11}$ | $3.25 \cdot 10^{-11}$ |
| $6.89 \cdot 10^{7}$ | $5.81 \cdot 10^{-11}$ | $2.33 \cdot 10^{-11}$ |
| $1.51 \cdot 10^{8}$ | $3.49 \cdot 10^{-11}$ | $3.49 \cdot 10^{-11}$ |
| $2.31 \cdot 10^{8}$ | $1.73 \cdot 10^{-11}$ | $1.52 \cdot 10^{-11}$ |

Another possible observation is the higher cross-section of Wireless IoT 1 with respect to number 2. As there were no observed SET on the Regulators' outputs resulting in an

MCU reset, it is reasonable to attribute the cause of the increased failure rate to the Transmission Subsystem. Its malfunctions may result in the Controller Subsystem getting stuck and requiring a reset.

At 275 $Gy$ and $4.65{\cdot}10^{11}$ 1 $MeV\ neq.\cdot cm^{-2}$, a malfunction due to the Ext WTD was observed on the Wireless IoT 2. The failure of the recovery subsystem causes the whole system to fail as it pulls down the reset line (it was visible through the oscilloscope) and keeps the MCU in a reset state. This component showed no degradation during the tests under only TID at Co60. It has to be noted that gamma rays also induce DD and the DDEF/TID ratio is two orders of magnitude lower than PSI [73]. It is therefore reasonable to say that its lifetime depends on the DDEF/TID ratio experienced. Finally, at the end of the test, a failure not recovered by the Ext WTD was observed on the Wireless IoT 1. The event cross-section was measured to be $9.32{\cdot}10^{-13}\ cm^2\cdot Device^{-1}$.

During this test, it was also possible to evaluate the degradation of system power consumption due to high dose rate effects. Due to the high flux and the presence of SEFIs, it was not possible to record a full duty cycle. Discrete points were therefore taken. In Fig. 3.24, the degradation rate measured during this test at PSI is compared with that of Co60, which, as can be seen, is more critical. This difference could be partly due to the type of particles used in the tests, but mainly to the low dose rate effects, which according to the presented results, have a greater impact on the performance of the system.

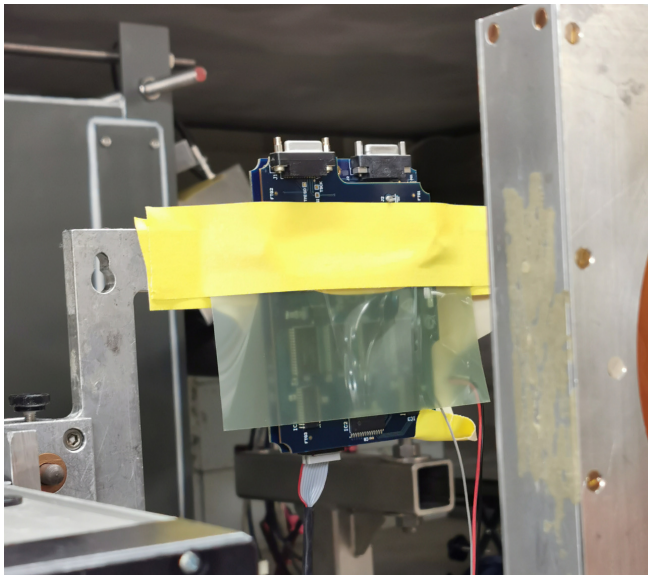

Figure 3.31: Wireless IoT 3 test setup. The Controller, Transmission, and Power Management Subsystems are in beam and the internal watchdog is enabled. The Ext WTD is not mounted.

As the system also embeds an internal watchdog and the Ext WTD was operating below

the desired target TID, a further test was performed enabling this peripheral. The Wireless IoT 3 was placed in front of the beam, targeting the same subsystem irradiated during the Wireless IoT 1 test, as it was found to be more sensitive to HEH. However, the internal watchdog solution was discarded as it was not always able to recover the system, showing a not recoverable fault cross-section of $1.18{\cdot}10^{-11}\ cm^2 \cdot Device^{-1}$ and never being able to recover the system after 100 $Gy$.

The presented phase of the proposed test qualification methodology made it possible to obtain the sensitivity of the system to HEH and its lifetime. It was also possible to identify the component that caused the system failure, i.e. the Ext WTD. To improve system performance, it will be necessary to replace this component with a more reliable one or to implement a new hardware solution to replace the Ext WTD with a different type of component.

#### Expected Failure Rate in Operation

The importance of this phase in the methodology and its validity are demonstrated by the results obtained using this test approach, which allows an evaluation of the expected failure rate in operation. The Homogeneous Poisson Process (HPP) can be used to estimate the probability of the system failure rate for specific HL-LHC environments and years of operation using the expected radiation levels for specific accelerator areas and the system cross-sections. A constant failure rate and independence between failures are taken into account in this process. This analysis considered one year of operation in two worst case scenarios: the Arc and DS areas. These areas represent two harsh environments in which the BatMon will be deployed since they host electronic equipment that needs to be close to the beam and magnets. The BatMon self-recoverable ($6.50 \cdot 10^{-11}\ cm^2 \cdot Device^{-1}$) and permanent failure ($9.32{\cdot}10^{-13}\ cm^2 \cdot Device^{-1}$) cross-sections obtained during HEH qualification (Section 3.5.5) were used for this analysis.

The HPP results are depicted in Fig. 3.32. The curve represents the probability that a Wireless IoT will experience between 0 and 5 independent self-recoverable or permanent failures in a year of operation in Arc and DS areas. As visible, the probability of having a self-recoverable failure in Arc (HEH = $10^9\ HEH \cdot cm^{-2}$) in one year of operation is 5 %, while for a permanent failure, it is negligible (<0.1 %). In the harshest environment like DS (HEH = $5 \cdot 10^{10}\ HEH \cdot cm^{-2}$), this probability increases reaching for permanent failure 5 % while for self-recoverable failure 20 % of having 2 or 3 resets per year [38].

Of the two cases presented, the Arc is the more interesting one. In fact, the Wireless IoT system will mainly be used in shielded areas, where the radiation levels in terms of HEH per year are expected to be less than or equal to this worst case. The probability of having one permanent failure is already negligible in the Arc region ($< 0.1$ %).

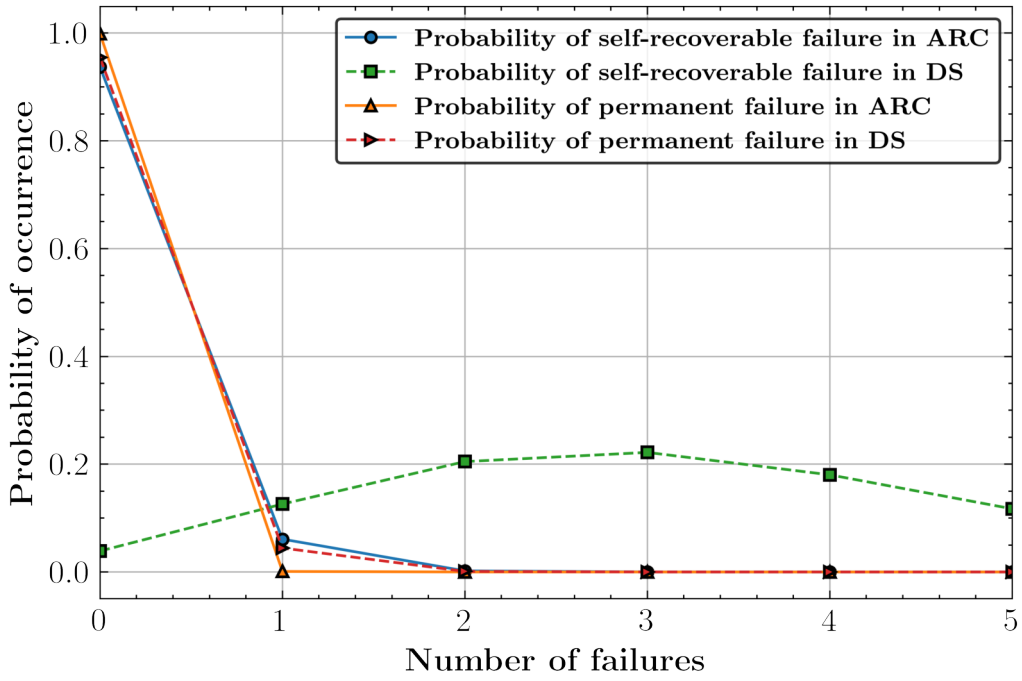


Figure 3.32: Probability of having a self-recoverable or permanent failure in the tunnel region of Arc and DS for HL-LHC.

This type of failure analysis can also be extended to a space application. For the space environment, the expected radiation levels can be obtained using specific software such as Outil de Modélisation de l'Environnement Radiatif Externe (OMERE), as done in [126].

### 3.5.6 System Calibration

In Section 3.4.5, the benefits of calibrating each system individually in terms of reducing the uncertainty of the final measurement were discussed. It was also pointed out that this process can be time-consuming. This is especially true for generic monitoring systems, which require a complex setup (cables).

However, as wireless, battery-powered monitoring systems do not have the need for cables, a method can be defined for the calibration of each system alone. Calibration of the FGDOS was performed at the Co60 facility and ten Wireless IoTs (twenty FGDOSs) were placed in front of the beam as depicted in Fig. 3.33a. Considering that there are two sensors on each chip, the dose rates of the ten positions were measured using a one-cc Ionization

Chamber (PTW 23331) and are listed in the figure. The lower TID in the left corner was due to the presence of another DUT in the line of sight tested closer to the source. The distance from the source, and therefore the dose rate, was chosen to give a sufficient number of points per sensor discharge. Then, for each FGDOS, some complete discharges were collected and the middle part of the discharge curve was taken into account to avoid uncertainties introduced by the overcharging problem. Knowing the timestamp for each point, the expected TID was evaluated using the time of the two extremes of the discharge curve portion considered. The sensitivity of each FGDOS was calculated using the equation (3.5) and the data retrieved during the test for each BatMon.

$$Sensitivity = \frac{f_{1stpoint} - f_{Lastpoint}}{DoseRate \cdot (Time_{f_{Lastpoint}} - Time_{f_{1stpoint}})} \tag{3.5}$$

The resulting distribution of the twenty FGDOSs tested is shown in Fig. 3.33b. For three sigma, the dispersion is approximately 10 %, which therefore defines the measurement uncertainty of the system when using average sensitivity.

The flexibility of the system made this procedure relatively easy to perform and it can therefore be part of a methodical calibration procedure that can drastically improve the final measurements in operation.

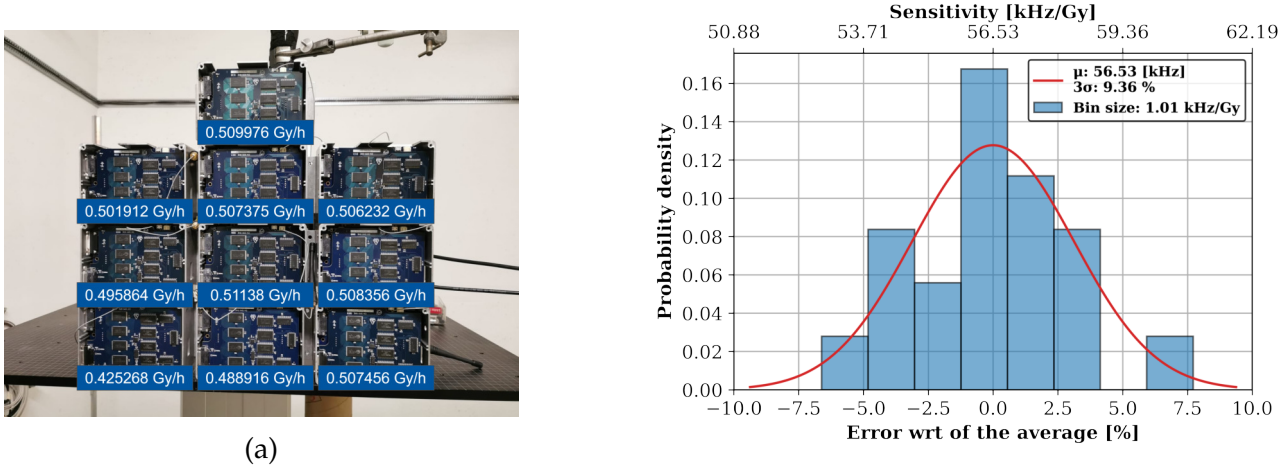


(a) (b)

Figure 3.33: On the left (Fig. 3.33a), the ten Wireless IoT tested with the corresponding dose rates. On the right (Fig. 3.33b), the probability density of the measured FGDOS TID sensitivity and error made with respect to an experimental average value.

## 3.6 Chapter Summary

System qualification under radiation for the traditional CERN RHA depends on the availability of CHARM. In the absence of this facility, during Year-End Technical Stop (YETS) or Long Shutdown (LS), it is not possible to perform this phase being compliant with what is defined by CERN's RHA. This prompted the search for an alternative way to perform this radiation qualification step, and the development of this alternative methodology was coupled with the need to qualify a new generation Wireless IoT radiation monitoring system, the BatMon, developed to overcome the various limitations (electrical, radiation tolerance, radiation resilient hardware, and flexibility) encountered with the RadMon presented in Section 3.1. This system was the perfect test vehicle to validate this new test approach, but the fact that it was wireless and represented the first IoT platform for the radiation environment at CERN prompted discussion on how the IoT world could represent an interesting solution for the future of the LHC, and in particular for longer accelerators such as Future Circular Collider (FCC), but whose feasibility has yet to be demonstrated (Section 3.2). The choices made in the development of this new system were justified in Section 3.3, where their RHA and design implications were also examined.

One of the RHA implications discussed was that of component-level qualification. As far as low power is concerned, CERN's traditional RHA does not provide specific component-level test guidelines for devices with different modes of operation; the implications of these choices on the RHA process have been discussed in Section 3.4. The results of qualification at the component-level for the platform were presented in Section 3.5.1. In addition, to demonstrate the impact of different biasing or operating modes on device degradation rates, the example of Wireless IoT non-volatile memory was used to show that testing only the worst case can lead to a severe underestimation of device lifetime, whereas replicating operating conditions can provide greater confidence in the response obtained. However, this is not always possible at this qualification stage and can only be done at the system-level.

Next, the new system-level qualification approach is introduced with its three phases, presented in Section 3.4. They are electrical validation, alternative system-level radiation qualification, and sensor calibration, specific to systems based on a sensor.

During the first of the three phases, different tests without radiation were carried out:

1. Lifetime requirement test: the implementation of the duty cycle within the system, made it possible through the analysis of the current consumption to validate the initial

design requirements (battery lifetime of more than 1 year). By varying the measurement period, it is possible to meet these requirements (Section 3.5.2).

2. Magnetic field test: this test made it possible to demonstrate the Wireless IoT platform's immunity to magnetic fields of up to 3 $T$. This represents a major success for the system as, unlike the RadMon, it can be used anywhere in the experimental areas (Section 3.5.2).

3. Transmission Test: a wireless transmission capacity test was carried out that demonstrated the wide-area coverage capability of the chosen wireless technology (LoRa). This result also proved that there exists a wireless protocol that can be used under radiation (Section 3.5.1, can cover a wide area, and complies with the radio frequency (RF) requirements of the CERN LHC (Section 3.5.2).

Following this initial qualification, the alternative system-level radiation qualification began. Due to the unavailability of CHARM, it was decided to split Phase 4 of Traditional RHA into several stages. The different tests performed and their results were discussed in the corresponding sections. During the Co60 test described in Section 3.5.3, it was possible to test the system by evaluating its degradation performance with the TID effect alone. It was possible to validate the functionality of the firmware (i.e. TID sensor acquisition) by using the full-duty cycle due to the impossibility of SEFIs. The representative dose rate was also used to assess the effect of the duty cycle on system performance. In the Th and epi-Th neutrons spallation, it was possible to validate the sensitivity of the system to neutrons belonging to this spectrum, and, as shown in Section 3.5.4, no malfunction was observed. Finally, under a 200 $MeV$ proton beam, the degradation of the system due to the combination of TID and DD was studied, and the sensitivity and lifetime of the system were evaluated using a hybrid test approach consisting of increasing the flux during the different phases of the test (Section 3.5.5). With these data, it was possible to estimate the expected failure rate during operation, given always in Section 3.5.5. Finally, thanks to the flexibility and wireless capability of the design, Section 3.5.6 demonstrated the possibility of a methodical approach to calibrating the TID sensitivity of each specific system, which will drastically improve the final measurements in operation. Calibration of sensors for other types of measurements (fluences and DD) is also possible in dedicated facilities.

The alternative approach presented in this chapter will allow systems to be qualified at CERN even when CHARM is unavailable, without the need for delayed deployments. The

practical examples of system-level testing presented in this chapter will also help to answer the question of "how" to perform system-level qualification in irradiation facilities when it is not possible to irradiate the whole system. This is an important result that will have an impact on the system qualification at CERN, allowing this process to be accelerated without the need for CHARM. The same approach used for BatMon can be applied to qualify any system designed for a particle accelerator. For instance, in cases of higher complexity with a greater number of components, the PSI test can be conducted by subdividing the system into a larger number of subsystems, each including the most sensitive or critical component. However, for this approach to be effective, it is crucial that the test board is designed symmetrically. Placing the most sensitive component in one corner rather than the center of the board could hinder its inclusion during the testing of various identified sub parts. If data are already available on the effect of the DDEF/TID ratio on system sensitivity or on the sensitivity of Th, tests at JSI and TENIS facilities may be avoided. However, it should be noted that CHARM provides a test environment that replicates that of the LHC, and therefore for a more realistic system response and to assess the impact of the DDEF/TID ratio that the system will experience in operation, a final CHARM test is always recommended.

Finally, during the process of design and qualification of the Wireless IoT platform presented within this chapter, it was also possible to demonstrate the non-problematic nature of two constraints for an IoT network in the context of the accelerator environment, introduced in Section 3.2 (qualification under the radiation of low power components and the existence of a protocol compliant with LHC requirements). The last one, i.e. compliance with LHC availability requirements, is discussed in the next chapter.

# CHAPTER 4

# An In-Depth Investigation into Flux Selection and Failure Observability

In system-level testing, the flux selected and the observability of the failure are closely related parameters. Depending on the one chosen, systems sensitive to flux-dependent effects may show different responses. As an introduction to the issue of flux selection in system-level testing, several examples of flux-dependent effects on test results were given in Section 2.4.6.

In [127], for proton testing, it is advisable to select the flux based on two considerations: 1) the time required to attain the desired fluence, and 2) the expected error rate. Flux is selected with the intention of preserving beam time, thus reducing the cost, by testing at the highest achievable flux. However, it is important to note that flux-dependent effects can impact systems and SoCs, which can in turn influence test results. A number of study cases can be found in the literature, starting from the component-level testing. A first example is given by SRAM-based FPGAs, which can be affected by SEUs in the CRAM. To mitigate these effects, correction modules are implemented. As happens in [88], the effectiveness of this technique would decrease as the flux increases. In the context of a microcontroller, an example is given in [90], where the performances of the device are evaluated using a Coremark. Due to the flux used, the device is unable to complete all iterations and requires an external reset. If the flux-dependencies effects impact are already evident at component-level, the related problems may be even more evident when testing SoCs and complex systems. For

example, as discussed in [91], the performances of systems using high data-rate communication protocols can vary with the flux rate selected. On the other hand, when low data-rate protocols are used, the system may fail before enough transmissions have been made to observe a failure mode. Finally, the mitigation schemes implemented in the design may behave differently depending on the flux selected, and may appear ineffective at certain flux rates, as is the case with error detection and correction.

In order to avoid the occurrence of these effects on the final results, different approaches for flux selection have been developed over the years and are available in the literature, which allows to obtain better system lifetime and sensitivity estimations. They are discussed in Section 4.4.1. However, those methods do not provide any specific approach to quantify the relationship between flux and failure observability and improve the latter one. For systems with different operating modes along their working cycles, this characterization is particularly necessary. In fact, they can exhibit, failure modes that occur only in specific operating modes, which may be masked by more general failures. Their detection may also not be immediate, requiring a complete working cycle to be performed. For this type of event, flux selection plays a key role in their observation.

The BatMon, which belongs to this category of systems, exhibited unexpected failure modes when tested at CHARM under different flux conditions. Due to these unexpected failures, the device was partially non-functional and its availability was drastically reduced using only an Ext WTD as a mitigation scheme. In order to detect and investigate these less probabilistic failures, it was necessary to implement dedicated Software Mitigation Schemes (SMSs). Their application proves that the IoT device can provide high availability even in harsh environments. In addition, it was possible to identify and characterize these failures in terms of cross-section. The value obtained makes it possible to study the probability of their observability with respect to the flux used, demonstrating the link between flux selection and failure observability. Further analysis was also carried out to understand if it was possible to determine a system-level testing methodology to improve the observability of low-probability failure modes by determining the optimal test flux for a generic system. This chapter presents the process that was applied to the Wireless IoT to develop such a methodology. By applying it directly to the failure modes exhibited by the platform, it was possible to demonstrate that the non-recognition of these failures in the application of the methodology presented in Chapter 3, did not invalidate it. On the contrary, it has been shown that the proposed approach is necessary for any qualification of systems with different operating

modes that are suspected of having failure modes with different probabilities of occurrence. The proposed methodology will complete the system-level qualification phase and improve the result obtained. Its use avoids unexpected failures during operation, which would require further tests and investigations, which would have been in turn very complex without the selection of an appropriate flux rate.

The content of this Section refers to the two publications [128] and [129].

## 4.1 Less probabilistic Failures in Wireless IoT Design

Once the system has been qualified according to the methodology described in Chapter 3, it was decided to perform a further system-level test in CHARM to confirm the SEE sensitivity result obtained. As far as lifetime is concerned, the test in CO60 and PSI proved the dependency on the DDEF/TID ratio, CHARM may provide more realistic results related to this parameter. Compared to the other radiation facilities used during Chapter 3, in CHARM it is possible to test the whole design (not part of it) under all radiation to electronics effects. An indoor LoRa gateway RAK7258 was installed outside the irradiation area (CHARM Control Room) and configured to establish a private LoRa network. Due to the shielding of the facility, the antenna of the gateway was deported in the irradiation room through the available patch panel. Since the main scope of the test was to evaluate the system functionalities and sensitivity in a more realistic environment without destroying the system, it was irradiated in the G0 position. The system was tested without the USART cable and powered by batteries to reduce setup time (preparation/installation) as this test was only a validation of the system.

As visible in Fig. 4.1 from the LoRa Frame Counter (FCNT) trend, the device exhibits unexpected behaviour during the test: long periods without data transmitted were observed (In yellow and red). This is a counter transmitted in the LoRa packet that is incremented by one with each transmission performed by the end node (i.e. a packet counter). When the counter goes to 0, it means that the device is rejoining the network (App Init). This happens when the system is reset.

The duration of these periods was not fixed and ranged from tens of minutes to hours. At the end of them, the device resumes its normal functioning not allowing to detect any specific failure pattern only through the data transmitted. Similarly, the setup used did not allow any useful information (power consumption and USART data) to be extracted from

the test performed. The observability was dramatically reduced. However, some useful information was retrieved by dumping the external non-volatile flash memory of the Wireless IoT platform at the end of the test.

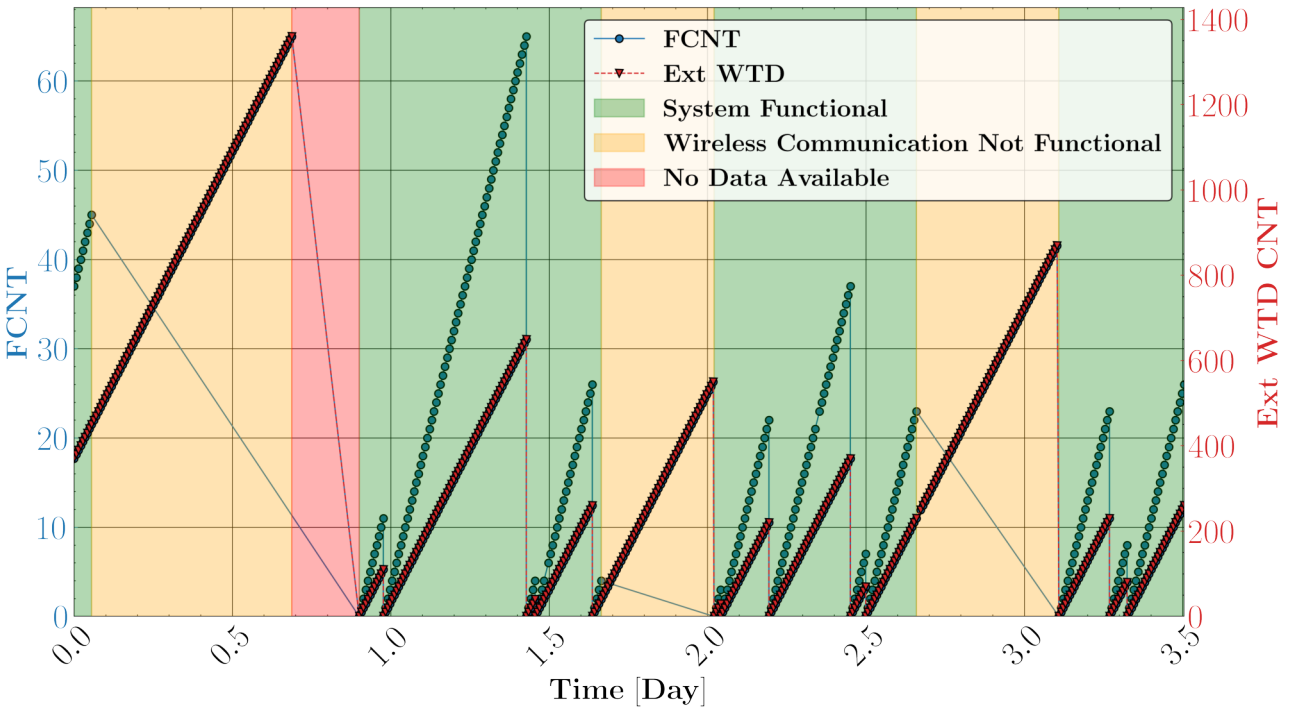


Figure 4.1: Behaviour of the Wireless IoT during the test in CHARM-G0. The transmitted packets are expressed in terms of the FCNT, a counter incremented by the MCU with each transmission. The ExtWTD counter (CNT), a counter incremented by the MCU at each interaction with the component, was obtained from the contents of the flash memory. Different periods are highlighted: in green when both wireless communication and memory are working. Yellow when only the latter is available, and red when both are unavailable.

Cross-checking the two data sets, two main observations were possible.

- Part of the non-transmitted data was available in the data downloaded from memory (Test periods highlighted in yellow in Fig. 4.1). In particular, it was possible to verify the functionality of the external watchdog from this data. It was found that interactions were still taking place during these periods without transmission, and therefore, the failure that occurred was invisible to the Ext WTD. In this failure-induced case, only some functionalities of the device were not available causing the system to not be able to transmit. Two Potential Failures (PFs) can be identified:

  1. PF1: the transceiver was not functional anymore and the MCU was controlling it without any effect.

  2. PF2: the MCU is controlling the transceiver through an internal state machine

whose operations are scheduled by a Timer Control. If the timer or the FSM itself crashes, the MCU is not able to detect it.

- In a case, the data not transmitted were also missing from the Flash (Test period highlighted in red in Fig. 4.1). The content of the flash was again available when the device was restarted together with the transmitted data. However, the FGDOS showed interesting behaviour, being completely discharged. This behaviour could be triggered by two possible causes.

  1. PF3: the content is missing due to a malfunction of the component itself or caused by a bit flip in the MCU SRAM (it cannot control the component properly). The MCU is still capable of feeding the Ext WTD. This PF does not explain the FGDOS completely discharged.

  2. PF4: the MCU is in an undefined state which allows it to reply to the Ext WTD and thus, the fault state is undetectable by this mitigation scheme. At the same time, the MCU is not able to perform other operations as if it were blocked. It can be due to a malfunction of the RTC causing the device to sleep for a longer time or to a never-ending while loop. This PF explains why the FGDOS was completely discharged. The passive mode of the sensor requires the recharging to be enabled by the MCU. If the latter is blocked, this action cannot take place and the sensor is completely discharged.

To counter these identified PF modes, software mitigation techniques have been developed that can detect such types of failures and restore system functionalities. Those techniques are presented and their effectiveness is demonstrated in the next Sections.

## 4.2 Software Mitigation Schemes to Improve MCU Availability

As described in Section 4.1, several anomalies were observed during the Wireless IoT validation test performed in CHARM. By comparing the transmitted data and the content of the external flash, it was possible to identify different possible causes of failure, called PFs. This section presents and describes the mitigation schemes implemented in the MCU firmware to deal with these failures.

### 4.2.1 Software Watchdog to Detect PF4

As described in Section 4.1, one of the potential failures that caused the MCU to be unable to perform operations was related to a stack in the MCU firmware execution (PF4). As described in Section 3.3.4, the Wireless IoT design embeds a recovery subsystem made of an Ext WTD. This PF may be invisible to this external mitigation scheme since the device may still be able to execute the Interrupt Service Routine used to feed the Ext WTD. The internal watchdog peripheral, when available, can be used as a complementary mitigation scheme, to detect failures invisible to the Ext WTD. In the case of the Wireless IoT platform the usage of this peripheral was discarded since its lifetime was limited to a TID of around 100 *Gy* (Section 3.5.5). An alternative mitigation scheme that is reliable and able to detect any blocks in the execution of the firmware by the MCU is required.

As a solution to this issue, an Internal Software WaTchDog (SW WTD) was designed. The RTC is used to check the time elapsed since the start of one of the main firmware FSM states (App Init, App Meas, and App Sleep). This check is performed each time the Ext WTD wakes up the MCU requiring an interaction. During this event, a timeout corresponding to the expected sleep and wake time (the Meas Period) is compared with the elapsed time measured by the RTC. If the measured time is greater than a defined timeout, it means that the MCU is stacked in one of three operating states, e.g. infinite while loop, no wake from sleep. In addition, if there is no change in this time from the previous interaction, the RTC is detected as malfunctioning. A self-reset is triggered in response to these problems. The faults mentioned above are examples of errors that may not be visible to the Ext WTD, as the MCU may always be able to feed the external peripherals. The working principle of the SW WTD is depicted in Fig. 4.2.

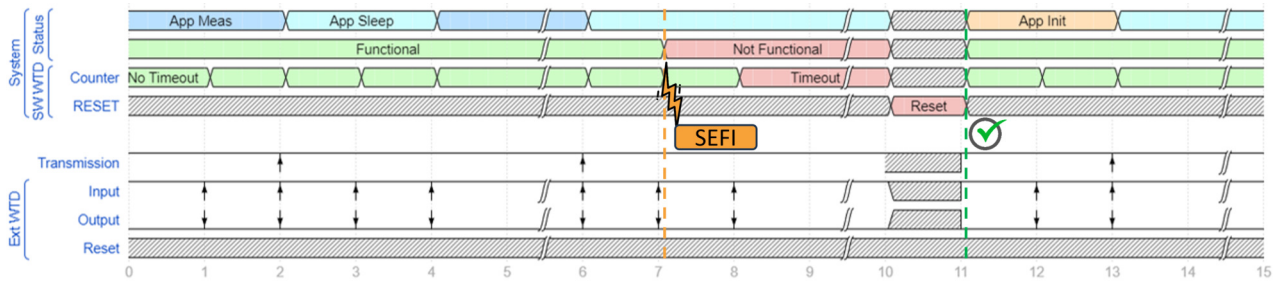


Figure 4.2: The working principle of the SW WTD recovery is shown. At tick 7 a failure occurs which the Ext WTD cannot detect because the MCU continues to respond. As a result of the failure, the MCU does not wake up and is in sleep mode. At tick 10, when the watchdog wakes up the system, the timeout has been reached. The SW WTD recognizes that the system is not functional and resets itself.

### 4.2.2 LoRa Link Check to Detect PF1

In Section 4.1, one of the PFs identified was related to a possible fault occurring internally to the transceiver. From a fault detection point of view, the transmission subsystem used for wireless communication has low observability. It can only be controlled and configured by the MCU via SPI, but there is no monitoring of its status. To verify the SPI chip functionalities, the signature of the chip can be read and compared to the expected value. However, If the internal components of the transmission subsystem that handle signal modulation and demodulation stop working properly due to radiation, the MCU will not be able to detect it. To detect such types of faults, a specific SMS is required.

The LoRa Confirmed Uplink (CU) feature can be used to verify if the transceiver is really functioning. A CU is requested from the Network Server (NS) for every configurable number of transmissions. The CUs are not requested at each transmission to not saturate the network when multiple systems are installed. If the confirmation is received, the transceiver is working correctly because both transmission (the request from the CU has reached the NS) and reception (the CU has been received by the device) have worked. On the other hand, if it is not received, this means that there is a problem. In such a case, in order to distinguish between a radiation-induced failure and a lost packet or a missed reception, it is also requested on the next two subsequent transmissions. It is repeated 2 more times, and not just once because it was observed that the possibility of two consecutive packets not being received by the NS was not negligible. If three consecutive CUs are not received, a transceiver failure is detected. A reset of the MCU and consequently of the transceiver (during App Init and via the hardware reset line) is performed. A flowchart describing the mitigation scheme is depicted in Fig. 4.3.

In addition to this scheme, as the operations of the LoRa Control FSM are scheduled by a Timer Control (TC) peripheral, a check has been added to the code to verify its functionality. At the start of each App Meas, the value of the timer is read before and after a time delay. At the end of the delay, the elapsed time of the TC counter is checked and if it differs from the expected value, the timer is considered not functional and the MCU resets itself.

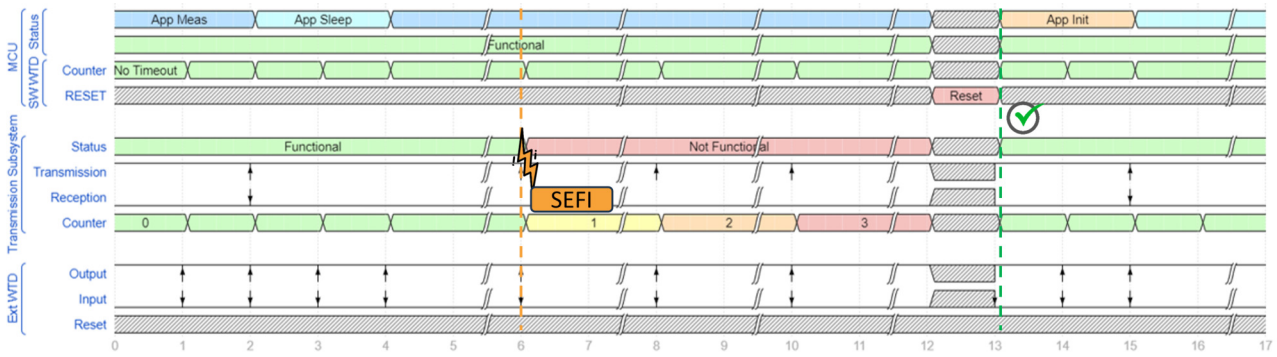


Figure 4.3: The mitigation scheme used to detect a failure of the LoRa transceiver is depicted. As visible, the failure of the transceiver is invisible both to the Ext and SW WTDs. For every configurable number of transmissions, the MCU requests a CU and updates a counter. If the confirmation is received (Tick 2), the transceiver is considered functional and the counter is reset to zero. If the confirmation is not received as in the occurrence of Tick 6, the counter is updated and the confirmation is requested again at the next uplink. In case it is not received three consecutive times, the MCU resets itself and the Transceiver.

### 4.2.3 Transmission Pending Variable to Detect PF2

To detect PF2, it was decided to add a Boolean transmission pending control variable to the firmware. The concept is very simple: when the transmission is started, the variable used to define that the transmission is pending is set to true. When the second Rx window is closed, i.e. the transmission operation is completed, this variable is set back to a false state.

The use of this variable allows the MCU to detect if something has failed in the execution of the LoRa Control FSM and the latter is crashed. The MCU checks this variable before starting each new transmission and if its value matches the true state, a crash of the LoRa Control FSM has occurred. As a reaction to the fault, the MCU executes a self-reset.

### 4.2.4 Reset of the Read and Write Pointers to Detect PF3

To understand how PF3 occurrence can be detected and cleared, it is important to introduce how the MCU controls the non-volatile external flash. Its content is organized as a circular buffer. Flash memory can be either erased completely or sector by sector. A full erase is not a good option to preserve memory integrity. So the best choice would be to erase only the sectors that have been written. A Write Pointer (WRP) is used to understand which sectors have been written and from where to continue the write operation. Instead, a read pointer is used to select the data address to be read (Read Pointer (RDP)). The values of these two pointers are defined at the beginning of the App Init: at boot-up, the flash memory is reset via an SPI command and read sector by sector. First, the last written sector is

identified and then, the positions of RDP (first record of first written sector) and WRP (last record saved of last written sector) are stored in the MCU's SRAM.

In order to maintain the integrity of this control algorithm, records must be stored continuously, with no sectors written separated by empty sectors. If the WRP changes due to a SEU occurring in SRAM, there are two possible outcomes.

- New records are not saved after SEU: if the bit flip causes the WRP to assume a lower value (SEU caused a change of a bit from 1 to 0), subsequent records will not be stored because the MCU will try to overwrite already written records. When the system is reset, the system is able again to store the new records in the correct positions because the WRP and RDP are redefined during initialization. This action does not cause the component corruption from the algorithm's point of view.

- Memory corruption after SEU: if the bit flip causes the WRP to assume a greater value (SEU caused a change of a bit from 0 to 1), the memory will be corrupted from the point of view of the FSM controlling it. The new records are stored in sector not consecutive. When a reset occurs, the algorithm will not be able to identify the WRP position. The process will therefore fail because there will be empty sectors between written ones. To clarify the problem, let's take an example: WRP is 10 and becomes 266 due to a bit flip. The device starts to store the following records from position 266, creating a new sector that is written far from the starting one. At reset, since there are sectors that are not empty (records written from position 266) after the sector containing the first 10 records, the memory appears to be corrupted and the WRP search algorithm fails.

The criticality of this counter requires a specific mitigation scheme to preserve its integrity. The use of software TMR applied to this variable is not an option as the MCU's SRAM has shown a tendency to bit flip even many consecutive worlds. It does not appear to be a safe place to store 'non-volatile' variables such as counters. A second, more reliable option is to perform a search of the WRP and RDP before each new storage operation. It would also be optimal to perform a hardware reset of the memory before such a search, to mitigate any permanent chip failures or bit flips within its registers. The chip used does not have a hardware reset pin, although a version exists with such functionality. However, it is possible to perform a software reset via the SPI of the memory. Therefore, the mitigation scheme consists of re-initializing the flash memory before performing any kind of write operation, avoiding keeping the critical variables (WRP and RDP) in the MCU SRAM. If the

write operation fails twice in a row, the system is reset, because this means that the problem is caused by something else, such as an incorrect writeable size retrieved from the device or another critical bit flipping within the MCU (such as a problem in the SPI driver), and requires re-initialization.

### 4.2.5 Additional Software Mitigation Scheme

In addition to these mitigation schemes, a further protection mechanism against MCU misconfigurations is implemented. An attribute instruction management function is assigned to all handler function definitions in the code and provides protection against misconfigurations that could result from SEEs. If the latter causes a setting change of a handler in the MCU, the above management function is executed, reporting the error and resetting the device. This mitigation scheme was already implemented during the qualification of Chapter 3. During the qualification process, it was observed that this type of error was also invisible to the Ext WTD and this mitigation scheme was able to detect and clear it.

In Table 4.1 the mitigation schemes presented are summarized and the PF concerned is mentioned. All these SMS require only a few clock cycles to perform their actions and therefore, have no significant impact on system performance.

Table 4.1: A summary of the different SMS implemented in the firmware of the Wireless IoT platform is provided. A description and the associated PF they are intended to detect and mitigate are provided. In the table, "ND" stands for Not Defined.

| **SMS Name** | **SMS Identifier** | **Description** | **Failure Concerned** |
|---|---|---|---|
| SW WTD | SMS1 | SW watchdog used to detect MCU blocks in the firmware execution | PF4 |
| LoRa Link-Check | SMS2 | CU is used to detect the functionalities of the transceiver | PF1 |
| TC Crash | SMS3 | TC control loss of functionalities | PF1 |
| Transmission Pending Variable | SMS4 | A variable is used to detect if the previous transmission operation has been completed | PF2 |
| WRP bit flip | SMS5 | WRP is identified before each save operation in the external Flash | PF3 |
| Attribute Instruction Management Function | SMS6 | Function assigned to all handler function definitions and protects misconfigurations | ND |

## 4.3 Low Probabilistic Failure Identification and Characterization

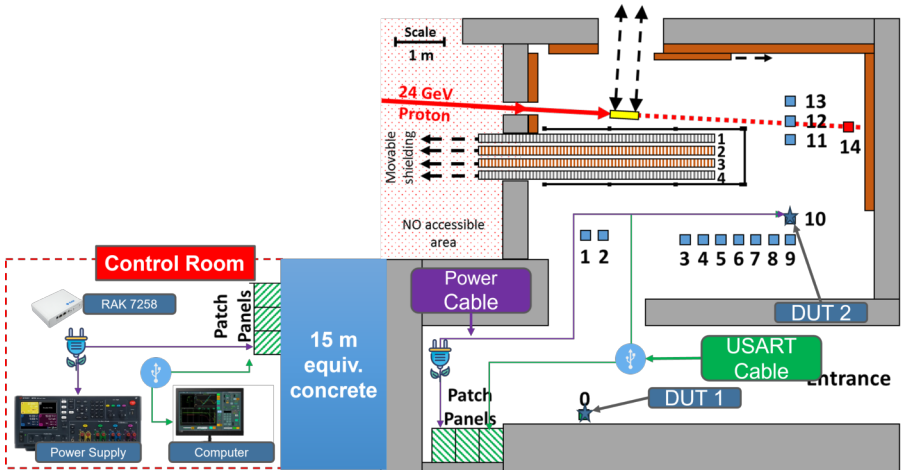


Figure 4.4: The test setup is depicted in the figure. The two Wireless IoT platforms were installed in R10 and G0 in order to evaluate the performance under two different flux conditions (Table 4.4). All the control equipment (Gateway, Power Supply, Acquisition Unit (Computer)) are installed in the control room.

To evaluate the efficiency of the new mitigation schemes and measure the cross-section of the different PFs, two devices were installed in two different CHARM positions: DUT1 was installed in G0 and DUT2 in R10. For the test, an indoor LoRa gateway RAK7258 was installed outside the irradiation area (CHARM Control Room) and configured to establish a private LoRa network. The two devices were both powered by a power supply in order to avoid the stop of the test due to a permanent failure. The device in the harsh position (R10) was connected via USART to the computer in the Control Room since it would have provided more events than G0. The setup is illustrated in Fig. 4.4. A RadMon was placed next to the two devices to measure the radiation to electronics effects.

The usage of the SMSs presented in Section 4.2 allowed for the identification of less probabilistic different failure modes (SubFailure (SF)) and validation of the mitigation implemented. In addition, it was possible to quantify their cross-section thanks to the USART data. This may be possible only through system-level testing.

### 4.3.1 Less Probabilistic Failures Identification

Thanks to the USART connected to the Wireless IoT, it was possible to identify the different failure modes and verify the effectiveness of the mitigation schemes implemented. In particular, all the recovery techniques implemented mitigate at least one failure once, con-

firming the existence of the PFs defined in Section 4.1. Only SMS 3 was ineffective as no TC failure was observed. Different failures were identified:

1. The first failure mode involves the transmission subsystem which, due to radiation, stopped transmitting. This failure was not detected by the MCU, which continued to operate normally, believing that the subsystem continued to function. The chip signature and configuration were still readable when the failure occurred. The SMS 2 was able to identify this issue and clear it. Without this SMS, the device's wireless functionalities would have been not available up to a more critical fault (Main Failure (MF)) occurring. This Fault detected is defined as SubFailure 1 and referred to as SF1 in Table 4.2.

2. Another failure was involving the duration of the App Sleep period. Due to bit flips in the RTC, causing an increase in the sleep time configured, or malfunction of the peripheral itself, periods of sleep longer than the expected sleep time were also observed. During these periods, the Wireless IoT was still able to feed the Ext WTD. The SMS 1 was able to identify this issue and clear it. Without this SMS the device would have continued to sleep up to a more critical fault (MF) occurring. This Fault detected is defined as SubFailure 2 and referred to as SF2 in Table 4.2.

3. In some minor cases, the device was blocked during the App Meas period within a "while loop". The block was due to a failure of the peripheral for which the while loop was used. Since the peripheral failed, the bit of the register that was expected to change, e.g. ADC conversion ready, never changed and the device was locked in that operation. During these periods, the Wireless IoT was still able to feed the Ext WTD. The SMS 1 was able to identify this issue and clear it. Without this SMS the device would have continued to wait in the loop up to an MF occurring. This Fault detected is defined as SubFailure 3 and referred to as SF3 in Table 4.2.

4. A case of transmission never completed was also observed. The SMS 4 was able to identify this issue and clear it. Without this SMS, the device's wireless functionalities would have been not available up to an MF occurring. This Fault detected is defined as SubFailure 4 and referred to as SF4 in Table 4.2.

5. A bit flip on the WRP was also detected. The SMS 5 was able to identify this issue and avoid the storage of the record in not correct positions. This failure would have

mined the integrity of the algorithm used to control the external Flash memory. Even in the occurrence of the MF, this failure may lead to a failure of the WRP detection algorithm and as a consequence an identification of corruption not due to radiation in the memory. Since this event occurred one time as the previously described fault, is defined as SubFailure 4 and referred to as SF4 in Table 4.2.

Since the SMS6 and the Ext WTD recovery were already available in the firmware used during the qualification described in Chapter 3, the failures that can be detected by those Mitigation schemes are considered as unique Critical Failure (MF). In Table 4.2, they are referred to as MF. The cross-section of these critical faults is compared to that observed in the test carried out at PSI and described in Section 3.5.5. To distinguish them, they are referred to as MF-CHARM and MF-PSI.

The cross-sections of these SF modes are depicted in Table 4.2. They have been evaluated considering the HEH fluence measured by the RadMon ($4.11 \cdot 10^{11}$ $HEH \cdot cm^{-2}$) with an error in the order of 30 %, while for PSI the error considered is 10 %. The Upper and Lower limits in Table 4.2 have been evaluated considering the uncertainty due to the low number of events' statistics (Poisson process) with a 95 % confidence interval. As visible the cross-sections of MF-PSI and MF-CHARM are compatible, validating the system-level testing methodology introduced in Chapter 3. The total average system cross-section ($8.7 \cdot 10^{-11}$ $cm^2 \cdot Device^{-1}$) is a bit higher with respect to the one evaluated at PSI. This can be due to the low number of events obtained at PSI, the uncertainty on the RadMon fluence measured (estimated at around 30 %) but also to the higher flux. It will be shown in Section 4.4.2, that the flux experienced in R10 is one order of magnitude lower with respect to the minimum one used at PSI. As introduced in Section 3.5.5, the lower flux allows a more accurate sensitivity

Table 4.2: Cross-sections of the different Wireless IoT failure modes. MF+SFs is the cross-section of the system considering all the platform failure modes and measured at CHARM.

| **Failure ID** | **Number of events** | **Lower Limit $\sigma$ [$\mathbf{cm^2 \cdot Device^{-1}}$]** | **Average $\sigma$ [$\mathbf{cm^2 \cdot Device^{-1}}$]** | **Upper Limit $\sigma$ [$\mathbf{cm^2 \cdot Device^{-1}}$]** |
|---|---|---|---|---|
| **MF-PSI** | 4 | $1.7 \cdot 10^{-11}$ | $6.5 \cdot 10^{-11}$ | $1.66 \cdot 10^{-10}$ |
| **MF-CHARM** | 24 | $3.1 \cdot 10^{-11}$ | $5.8 \cdot 10^{-11}$ | $9.1 \cdot 10^{-11}$ |
| **SF1** | 6 | $4.4 \cdot 10^{-12}$ | $1.4 \cdot 10^{-11}$ | $3.2 \cdot 10^{-11}$ |
| **SF2** | 3 | $1.1 \cdot 10^{-12}$ | $7.3 \cdot 10^{-12}$ | $2.1 \cdot 10^{-11}$ |
| **SF3** | 2 | $3.5 \cdot 10^{-13}$ | $4.8 \cdot 10^{-12}$ | $1.7 \cdot 10^{-11}$ |
| **SF4** | 1 | x | $2.4 \cdot 10^{-12}$ | $1.4 \cdot 10^{-11}$ |
| **MF+SFs** | 36 | $5.9 \cdot 10^{-11}$ | $8.7 \cdot 10^{-11}$ | $1.2 \cdot 10^{-10}$ |

estimation due to the uncertainty introduced by the recovery time of the ExtWTD.

The probability of occurrence of each failure with respect to the cumulated fluence can be modeled using Poisson's law, which is a distribution function that applies to rare events and is widely used for reliability analysis. Its definition is given in equation (4.1).

$$P(X = k) = \frac{e^{-\lambda}\lambda^{k}}{k!} \tag{4.1}$$

For k = 0 and lambda defined as the cross-section of a failure ($\sigma_{Failure}$) multiplied by the cumulated fluence ($\Phi$), this formula gives the probability that the fault considered will not occur as a function of $\Phi$. When its complementary function is considered (equation (4.2)), it gives the opposite, i.e. the probability that the system will fail for that particular event as a function of fluence.

$$P(\Phi)_{Failure} = 1 - P(k = 0) = 1 - e^{-\Phi \cdot \sigma_{Failure}} \tag{4.2}$$

Applying this formula to the average cross-section of the various failures reported in Table 4.2, the probabilities of occurrence of each failure are obtained and are shown in Fig. 4.5. As it is visible, the probability of occurrence of an SF is much lower compared to the MF. Considering a cumulated fluence of $10^{10}$ $HEH \cdot cm^{-2}$, while for MF the probability of occurrence is 48 %, for the others it is much lower, varying from 13 % in the case of most probabilistic SF1 to 2 % for SF4.

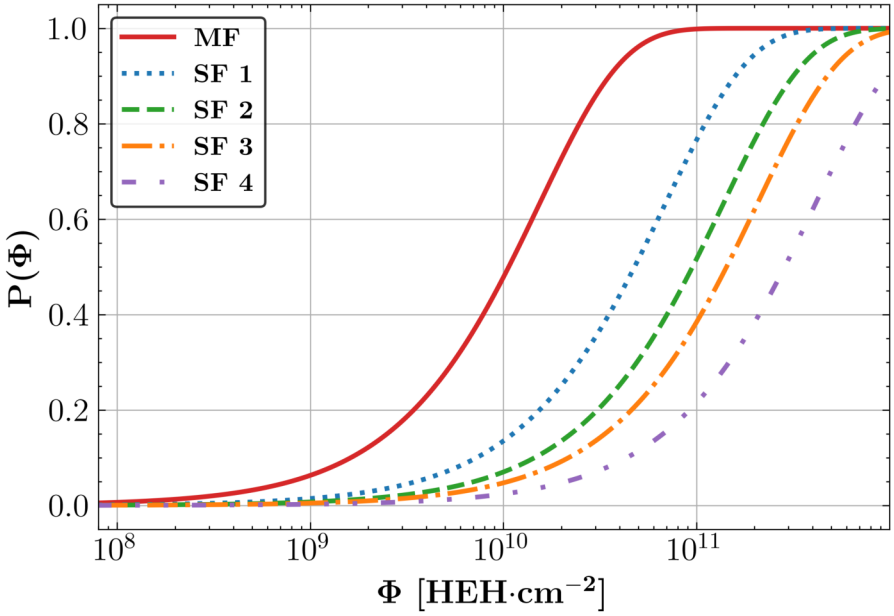


Figure 4.5: Probability of occurrence of the different Wireless IoT failure modes with respect to the fluence.

These numbers allow to understand how rare and complicated it can be to observe these failures. Their 'low observability' prompted an investigation into why they were not observed during the PSI test. This research highlighted how flux and observability of failures are two closely related parameters in system-level testing. The study of their relationship led to the definition of a flux selection methodology and demonstrated that the failure in the observation of these events at PSI was closely related to the test time and their low observability, but not to how the test was conducted. The test methodology presented in Chapter 3 has therefore not been invalidated by these results.

### 4.3.2 Using Software Mitigation Schemes to Improve the Availability of IoT Applications in Harsh Radiation Environments

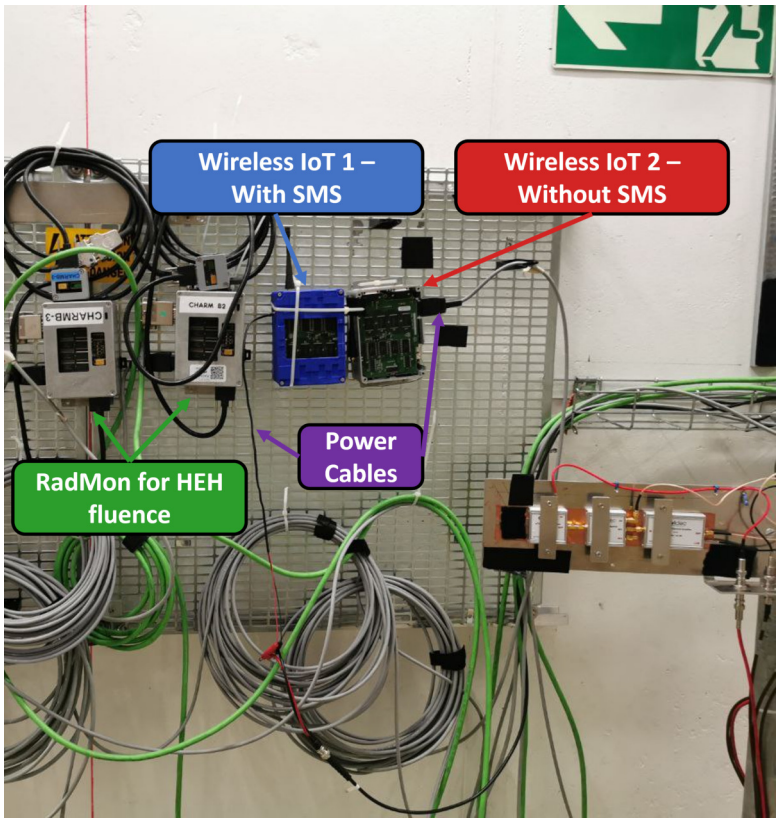


Figure 4.6: Setup of the CHARM test for the evaluation of the availability improvement through the use of SMS.

To better understand how these mitigation schemes impact the functionalities and performances of the system another test was carried out in CHARM in position G0. The scope of the test consists of comparing the performance of a Wireless IoT with mitigation schemes able to detect only MFs (Wireless IoT 2 - Without SMS: only SMS6 and Ext WTD used such

has been done in Section 3.5.5), with the one able to detect all PFs (Wireless IoT 1 - With SMS: All SMS implemented). Each Wireless IoT platform was powered by a power cable to monitor the device's power consumption (in case of other unidentified PFs) and to power cycle the device in case of an unrecoverable failure. A failure from which the system was unable to recover autonomously, requiring an external power cycle to restore its functionalities, was observed in Section 3.5.5. The use of a power cable allows the test to continue in the event of such a failure. As the reading performances of the HEH sensor have not yet been validated, a RadMon was used to measure the HEH fluence. The setup described is depicted in Fig. 4.6. For this test, Position 0 (G0) was chosen for two different reasons: a) the not harsh environment allows to test of a more realistic scenario b) these events are flux-dependent and a harsher environment would have triggered high probabilistic failure (MF) visible to the watchdog and SMS6, allowing the device also without SMS to exhibit better performances. To compare the behavior of the two devices, it was decided to use the FCNT as a metric.

Fig. 4.7 shows the FCNTs of the two devices recorded during the test in CHARM. An increase in FCNT is expected every 5 minutes as this was the chosen measurement period. As can be seen from Fig. 4.7, the device with SMS performs better than the other one, which has long periods without transmission that are only restored when an MF occurs (in Orange). During the test, the Wireless IoT 2 was silent for 3517 minutes, while the communication of the other was down for only 187 minutes. This time is due to the time it takes for each SMS to detect the failure and restore system functionality. Using SMSs, the downtime/uptime is reduced by a factor of ~19. In particular, it was reduced from 48.82 (Wireless IoT 2) to 2.58 % (Wireless IoT 1). This result proves the importance of using additional Software Mitigation Schemes complementary to the Ext WTD one, to obtain high availability performances under radiation.

### 4.3.3 Study of the Impact of Enhanced Availability on Future Operation

In Section 4.3.2, using the SMSs a downtime of 187 minutes was observed during the entire run, over a fluence of $9.33 \cdot 10^{10}\ HEH \cdot cm^{-2}$. This result does not represent a limitation for the application in terms of availability requirements. It must be considered that this fluence and those events were cumulated of a single run of CHARM which lasts less than one week. Considering the DS environment, where during 1 year of operation in the HL LHC $5 \cdot 10^{10}$

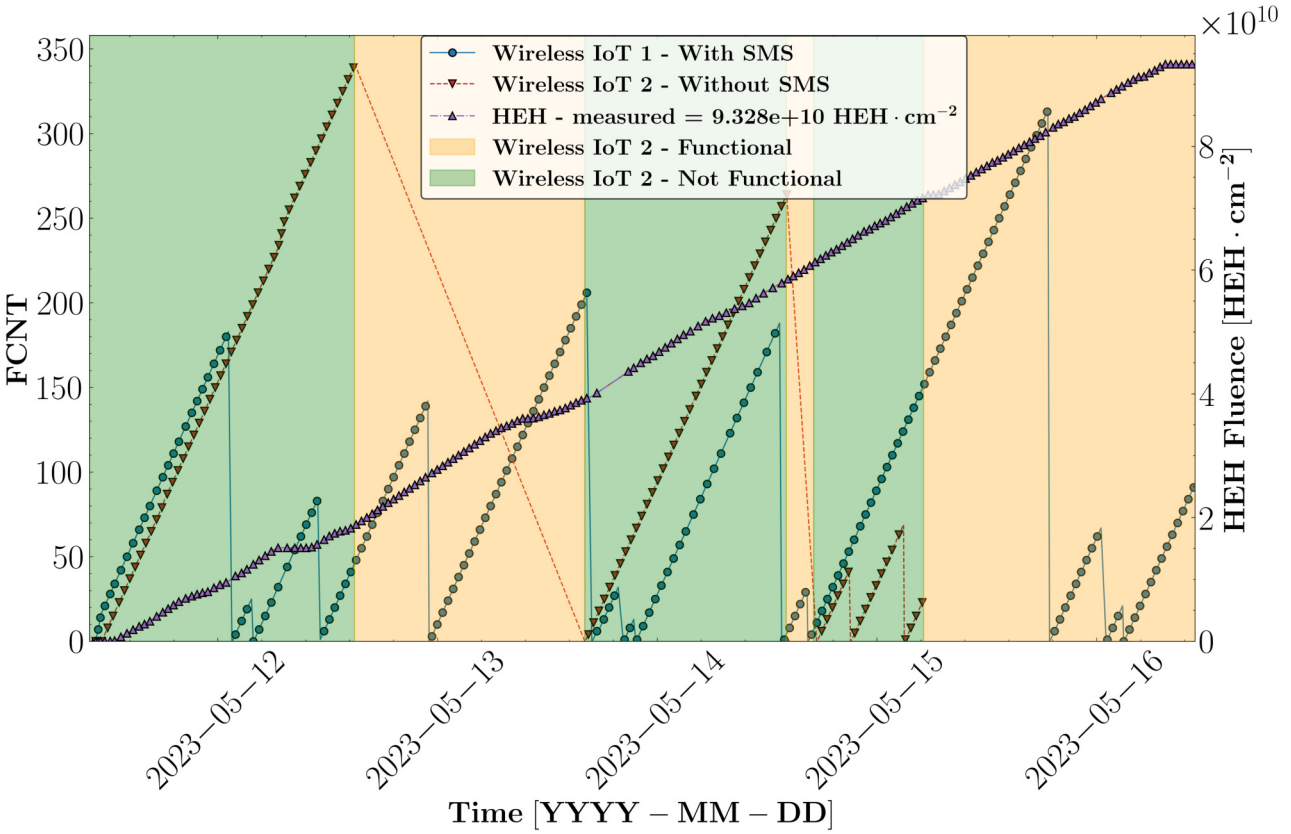


Figure 4.7: The LoRa FCNT is depicted for the two Wireless IoTs tested in CHARM. The Wireless IoT without the SMS (in red), was affected by SEFIs not detected by the only Ext WTD. During these malfunctioning periods (in Orange), the device was not able to transmit or was stacked in a while loop or sleep mode. On the other hand, when the SMS was implemented (Wireless IoT 1 in blue), the device ran without interruption throughout the test, with only a few intervals without any data due to error detection and recovery times.

$HEH \cdot cm^{-2}$ [38] is expected, the fluence taken during this test corresponds to 1.87 years of operation. Taking this time interval into account, and assuming behavior similar to that observed during the test (187 minutes of downtime), the expected unavailability per year considering only radiation induced failures, will be 0.01 % in the DS area.

The CERN's availability requirements establish that for each group of critical equipment (e.g. 100 critical systems performing the same action), a max of 20 minutes of downtime per day is considered acceptable [130]. Taking into account a safety margin of 3, each piece of equipment must have an availability of 99.54 %. An IoT application with the same performance as the Wireless IoT under radiation, i.e. an expected availability in the DS area of 99.99 %, can foresee 45 systems in this area while respecting the LHC constraints. However, this number would be higher in low-radiation areas where most equipment is installed. In fact, application availability depends on two factors: a) NS availability and b) the fluence experienced during operation. If the NS availability is excluded from this analysis, the appli-

cation availability is inversely proportional to the annual fluence and will therefore increase significantly in alcoves.

However, it should be noted that not all mitigation schemes have a fixed recovery time. The results presented are valid for a measurement period of 5 minutes, which was the period used in the test. If a longer measurement period, e.g. 1 hour, is selected, the recovery time can be as long as the measurement period. The situation is even worse for SMS2: in the worst case scenario, the failure of the transceiver occurs after the reception of CU. SMS2 to mitigate the failure, will take up to 6 times the measurement time, resulting in a downtime of up to 6 hours. For critical applications, the minimum measurement period should be used to maximize availability and minimize recovery time. It should be noted that the battery life decreases with the measurement period. For Wireless IoT in radiation monitoring, the significant duration of App Meas is related to the time needed to read SRAMs. In general, this time is much shorter for IoT devices: considering the LoRa Class A transmission time, it is typically around 5 $s$. The expected lifetime, considering only the Main-board (current consumption in the order of 1$\tilde{0}$0 $\mu A$) is depicted in Table 4.3. As visible, for different types of IoT applications, battery life will not be drastically affected by this choice.

Table 4.3: Lifetime of the system considering only the Main Board power consumption as a function of the Measurement Period chosen. The time required to read the Sensor Board is application-dependent. In this example, a 5 $s$ App Meas period has been considered.

| **Measurement Period** | **Avg. Current [mA]** | **Lifetime 2 Batt. [Months]** | **Lifetime 4 Batt. [Months]** |
|---|---|---|---|
| 5 Minutes | 0.29 | 41.18 | 82.36 |
| 1 Hour | 0.12 | 102.16 | 204.33 |
| 1 Day | 0.1 | 117.3 | 234.59 |

The results show that IoT devices can be a feasible solution for critical high-distribution systems in the future HL-LHC or even in longer accelerator projects such as FCC [131]. In addition, the Wireless IoT can be used for more critical applications such as wireless remote control of equipment due to its modularity and versatility. This topic and its advantages will be discussed in Section 5.5.3.

## 4.4 Study of the Flux Impact on the Observability of Wireless IoT Failures

As presented in Section 4.3.1 low probabilistic failure observed during the Test at CHARM prompted an investigation of the relationship existing between flux and failure observability. The research based on the data extrapolated in Section 4.3.1, introduced the definition of metrics which allowed us to quantify this link. Once the latter was demonstrated, further studies were carried out in order to define a method of flux selection to improve the observability of these types of failures. To understand the importance of the method that will be presented in Section 4.5, it is important to define the state of the art in terms of flux selection methodologies.

### 4.4.1 Flux Selection Methodology: State of the Art

Before starting to investigate the flux selection and observability link, a study of the state of the art on flux selection for radiation testing, has been carried out.

As introduced in Section 2.4.6, flux selection is a key parameter in system-level qualification and certainly influences its validity and effectiveness, as demonstrated by the various examples presented there. All the benefits listed in Section 2.4.5, may be lost if the wrong flux is selected. The question is therefore how to choose this parameter. The literature provides different approaches that can be employed to define this parameter. Increasing the flux from the lowest possible level to the point at which sufficient upsets can be obtained to provide robust statistics is the most common approach used in component-level testing, especially when no data are available on the device under test [82, 132, 92]. This recommendation was extended in [82] to include as a requirement for systems that the time between two hard losses of functionality must be at least 100 times the system's recovery time. To exclude the flux-dependent effects on the sensitivity analysis of the system, [133] also specifies that different levels of flux should be used to check whether the failure rate does not change with the flux chosen and, if so, to reduce it to satisfy this condition. However, apart from the need for a calibration step to define the flux, the approaches presented do not allow an optimal flux value selection to optimize the test results.

A more quantitative approach is given in [134], where the authors provide a methodology to minimize flux dependence within error cross-section computation. This methodology

is based on two scopes:

- Constant error bit cross-section: determine a flux range where the static cross-section of error bits for all significant bits in the design is independent for all fluxes within the range and a given LET.
- Exclude flux-dependent effects: establish a flux threshold that limits the unrealistic accumulation of errors in terms of system correction rates and other system parameters.

This methodology is mainly tailored for FPGA and may not be suitable in the case of complex systems or SoCs, where competitive modes are exploited throughout the operating cycle and may have multiple failure modes with different cross-sections. Moreover, none of these methods allows the quantification of the relationship between the fault observability and the selected flux, and thus of the optimal test flux that maximizes the observability of less probable events compared to a fault with a higher probability of occurrence.

For a system characterized by different operating modes with different timings (duty cycle type) and therefore possibly different failure modes, the flux can play a key role in observing such events. Consider the case of the Wireless IoT system: to observe a problem in transmission (PF1), several Full Working Cycles (FWCs) are required (App Sleep and App Meas). The choice of a non-optimal flux would have two consequences:

- If the flux is too high, high probability failures detectable by SMS6 or Ext WTD would occur, restoring system functionality. PF1 would be masked by high-probability failures (MF).
- If a lower flux is chosen, the probability of having an MF suddenly after the occurrence of a low probability one is reduced. However, as will be shown, choosing the minimum possible flux is not the best option because the opposite problem will occur, i.e. the failure would not be observable within a reasonable time.

Wireless IoT is not a unique case, as different types of systems, especially battery-powered ones, use duty cycle mode to operate (e.g. CubeSAT). For this particular category of systems, metrics are needed to characterize both the time required to observe such competitive failures and the optimal flux to reduce the observation time, i.e. the time required to observe the event for the first time. It is important to note that there is no general rule for flux selection because the optimal flux is determined by the system characteristics.

In the next section, these metrics are presented and applied to the failure cross-sections shown in Table 4.2, demonstrating the link that exists in system-level testing between observability and flux selection, and the importance and impact of selecting a non-optimal flux on the test outcomes.

### 4.4.2 Flux Comparison between CHARM and PSI

To better understand how the flux at CHARM played a key role in the detection of the failures, and to demonstrate that these events would have been very difficult to observe at PSI, the fluxes of the two facilities were compared and analyzed. Before presenting the flux intensities of the two study cases, it has to be reminded that in CHARM the beam is pulsed. Since the flux of PSI is continuous, for comparison reasons, the flux per second was evaluated in CHARM for the main positions. This average flux was computed considering the fluences measurement of the RadMon performed during the facility Calibration in 2021 and divided by the duration of the run.

Table 4.4 compares the fluxes for different CHARM positions with the flux normally used at the PSI facility for component and system qualification to favor, i.e. minimize, test time (max with 5 *cm* collimator).

Table 4.4: The average Th and HEH fluxes at different CHARM positions are given. The fluxes have been evaluated from the measurements taken by different RadMons at these positions during the calibration run of 2021. For comparison, the HEH flux at PSI is also reported as the maximum available, which is the one normally used by CERN RHA for component-level screening.

| **Test Position** | **HEH Flux** $[\mathbf{HEH \cdot cm^{-2} \cdot s^{-1}}]$ | **Th Flux** $[\mathbf{n \cdot cm^{-2} \cdot s^{-1}}]$ |
|---|---|---|
| PSI | $2.31 \cdot 10^{8}$ | - |
| CHARM-G0 | $1.16 \cdot 10^{5}$ | $3.68 \cdot 10^{5}$ |
| CHARM-R10 | $1.06 \cdot 10^{6}$ | $8.77 \cdot 10^{5}$ |
| CHARM-R13 | $4.50 \cdot 10^{6}$ | $7.97 \cdot 10^{5}$ |

As can be seen, the maximum flux at PSI is higher than the maximum one available at CHARM, which corresponds to position R13. Furthermore, since it is possible to irradiate the whole system rather than part of it as at PSI, this facility is ideal for system-level qualification. This feature combined with the low flux that characterizes the different test position, make CHARM a perfect test environment for:

- Observe flux dependence effects through the usage of different testing positions and

thus, fluxes as shown in Table 4.4.

- Demonstrate whether fewer probabilistic failures than an MF one that were not observable at PSI due to the choices of testing flux.
- Irradiating the whole system, observe whether the combined degradation of all embedded components due to radiation introduces new failure modes.

The test positions selected for this test were G0 and R10, where the average HEH flux is a hundred times lower than that used at PSI, and there is an order of magnitude difference between them.

### 4.4.3 Metrics for Optimal Flux Definition

From the study presented in Section 4.4.1, the necessity emerged of defining metrics capable of quantifying the link between flux and failure observability. As discussed, those metrics may be extrapolated and validated through the SF identified in Section 4.3.1. These metrics should be able to quantify both the probability of observing these failures ($P_{ob}$) and the required Mean Time Before the First Observation (MTBFO). They must take into account that the system is characterized by a failure mode (MF) whose high probability of occurrence makes it difficult to observe other failures. It must also assume that the system needs a minimum amount of time to detect these "other" failures (SF) and to complete all operations. This time defined as Full Working Cycle Time (FWCT), is the time required to complete an FWC from the moment of the boot, which in the case of the Wireless IoT corresponds to ~500 seconds (App Init + App Sleep + App Meas). This time is a function of the system under test. Thus defined, these metrics should be able to identify the flux that minimizes MTBFO and maximizes $P_{ob}$, i.e. the optimal flux. Once defined and validated, a methodology based on these metrics can be tailored to improve outcomes of system-level testing on duty cycle-based equipment.

The probability of observing each SFx, where 'x' represents a number ranging from one to four, without having the MF occurring, is the first metric to be defined. This metric will allow us to identify the optimal flux, but also to quantify the difficulty, in terms of test time (MTBFO), of observing such a failure with different flux intensities. Its formula is reported in equation (4.3). In the following analysis performed in this section, the average cross-sections from Table 4.2 were used to determine the probability of each failure ($P_{SF_x}$ and $P_{MF}$) using equation (4.2). In particular, for $P_{MF}$, that of the PSI has been used.

$$P_{ob_x}(x;\Phi_{ob}) = P_{SF_x}(\Phi_{ob}) \cdot (1 - P_{MF}(\Phi_{ob})) \tag{4.3}$$

where $\Phi_{ob}$ is the Observability Fluence i.e., the fluence to cumulate to observe SFx. This parameter contains information on the minimum time required for the device to complete operations and test flux. It can be defined as follows:

$$\Phi_{ob} = \phi \cdot FWCT \tag{4.4}$$

where $\phi$ is the testing flux. The $P_{ob}(\Phi_{ob})$ evaluated using equation (4.3) for each of the four SF, is depicted in Fig. 4.8. For SF1 the probability of observing such an event using the PSI flux of Table 4.4, is 0.04 % while using the CHARM-R10 flux is 0.69 %, proving the higher observability of the event obtained by reducing the flux. These values also prove the difficulty of observing such an event at PSI if the flux is not properly tuned.

From Fig. 4.8, it is possible to observe the presence of a maximum for each curve, the value of which is reported in Table 4.5. Applying the equation (4.4) to the observability fluence ($\Phi_{ob_{max}}$) for which $P_{ob}$ is maximized, the optimal test flux can be extrapolated for each SFs. In Table 4.5, the optimal test flux for each SF is reported with the difference with respect to SF1 in percentage. For all the SFs this difference is below 10 %. The variation obtained is only due to the different probability of occurrence of the specific SF and highlights how the order of the optimal test flux is mainly a function of the FWCT and MF of the system.

The definition of the probability $P_{ob_x}$ enables the evaluation of another important metric, i.e. the MTBFO, which is defined in equation (4.5). This metric permits the estimation of the time required, on average, for the test to detect the SFs at a particular flux intensity. Consequently, it demonstrates the significant challenge of observing such failures under specific flux conditions.

$$MTBFO_x(x;\Phi_{ob}) = \frac{FWCT}{P_{ob_x}(x;\Phi_{ob})} \tag{4.5}$$

This metric was evaluated for all SFs and is shown in Fig. 4.9. As can be seen from the figure, the MTBFO has a minimum corresponding to the optimal test flux. Table 4.5 shows the minimum MTBFO for each SF. It should be noted that using a flux lower than the optimal one, may give similar PSI results.

To better understand the need for a flux selection methodology for a system characterized by different failure modes with different probabilities and the relationship between

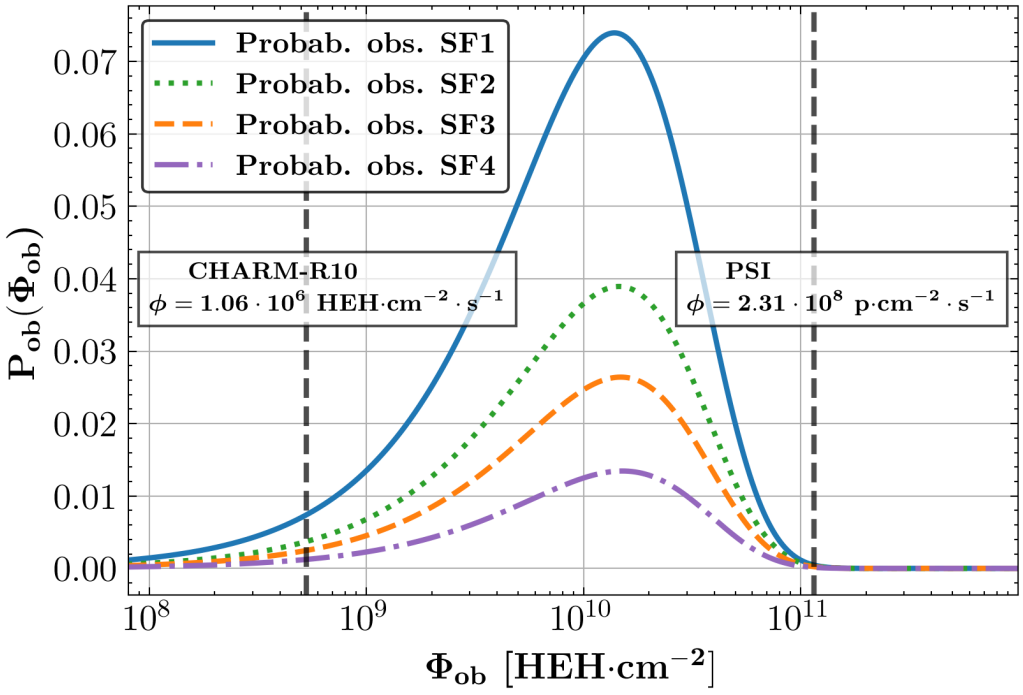


Figure 4.8: The probability of observing an SF is represented for each SF.

failure observability and flux selection, the MTBFO can be evaluated for the typical flux of different test facilities. Considering SF1, the MTBFO would be ~331 $h$ if the maximum flux available at PSI (Table 4.4) is used. Testing for such a time would not be feasible, not only in terms of beam time cost per hour but also in terms of the number of samples that would have to be irradiated to achieve such a test time. At CHARM-R10 flux the MTBFO is reduced to around ~20 $h$, which is a more acceptable time since normally a complete test in CHARM lasts one week. A similar result of CHARM-R10 in terms of MTBFO can be obtained by testing at ChipIr [135], at the Rutherford Appleton Laboratory (U.K.), where a similar CHARM-R10 HEH flux can be used. However, the more interesting result is obtained considering the optimal test flux: the MTBFO corresponding to the usage of such flux would be 1.88 $h$, i.e. ~10 times lower than CHARM-R10. The Minimum MTBFO for each SF is reported in Table 4.5.

Through the usage of these metrics, it was possible to demonstrate several significant insights.

- The $MTBFO_x$ and $P_{ob_x}$ allow us to prove the existence of a link between the chosen flux and the observability of the failure.

- Using a high flux is not always the best choice to get a meaningful result from the test. On the other hand, using a too low flux would not be beneficial either. The optimum

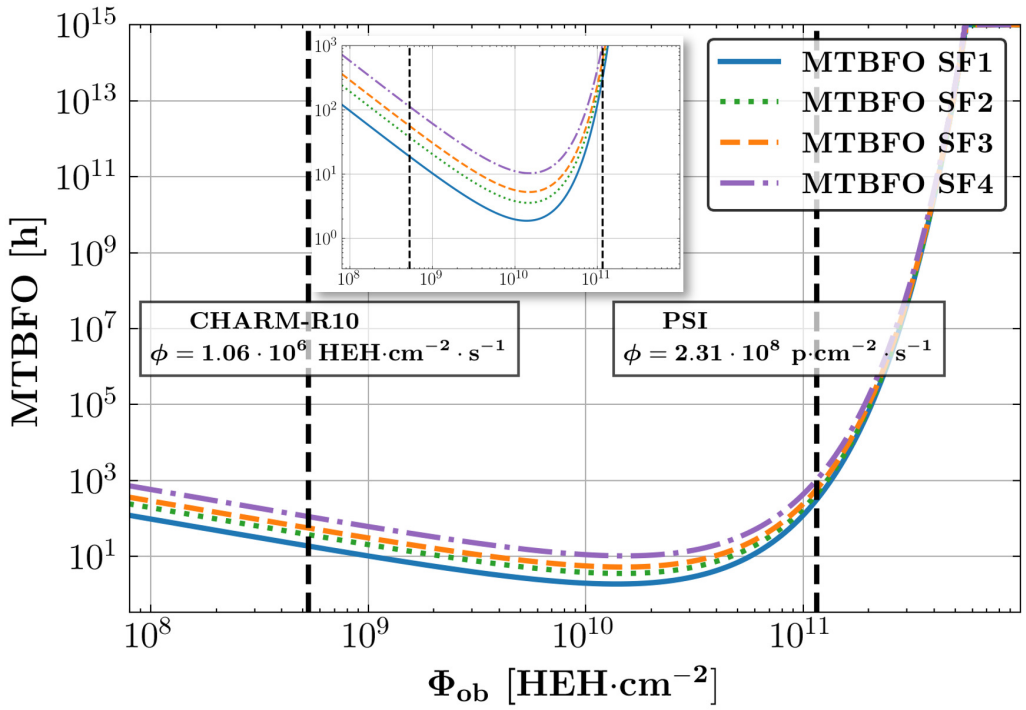


Figure 4.9: The MTBFO for each SF is represented as a function of observability fluence.

Table 4.5: The table lists the different parameters (maximum Probability of observance, minimum MTBFO and optimal test flux) extrapolated from the definition of the $MTBFO_x$ and $P_{ob_x}$ metrics for each SFx.

| Failure Type | Max $P_{ob}$ [%] | Min. MTBFO [Hour] | Optimal Flux [HEH · cm$^{-2}$ · s$^{-1}$] | Optimal Flux difference respect SF1 [%] |
|---|---|---|---|---|
| **SF1** | 7.39 | 1.9 | $2.78 \cdot 10^7$ | - |
| **SF2** | 3.89 | 3.6 | $2.92 \cdot 10^7$ | 5.04 |
| **SF3** | 2.64 | 5.3 | $2.97 \cdot 10^7$ | 6.83 |
| **SF4** | 1.34 | 10.3 | $3.02 \cdot 10^7$ | 8.63 |

flux for the test depends on the MF of the system and the time required to perform all the operations (FWCT).

- Observation of these failures at PSI during the test described in Section 3.5.5 would have been very complex: 331 h for SF1 using the highest possible flux was required to detect it. It would have been worse for the other SFs.

- If a low flux test facility is required, CHARM is a valid option. The methodology presented in the previous chapter can be extended by a test at CHARM using devices at different flux conditions to assess the presence of SFs. By knowing the MF and FWCT (Methodology Chapter 3), a methodology can be established to identify the optimum test flux and improve the test qualification phase at the system-level, avoiding unex-

pected failures during operation.

## 4.5 Radiation Test Flux Selection Methodology to Optimize SEE Observability

As discussed in this chapter and demonstrated in Section 4.4.3, the observability of SFs is strongly affected by flux selection, to the extent that these events may be impossible to observe. Therefore, developing a methodology to determine the optimal test flux and calculate the corresponding mean test time required to observe a failure can significantly improve the quality of system-level qualification. This methodology aims to identify the flux value that maximizes the observability of the SF of interest. This section will demonstrate how starting from a few input information that normally are available for qualified systems, it is possible to extrapolate the $P_{ob}$ and MTBFO for a generic system.

### 4.5.1 Input Parameters for Observability Optimization Methodology

The input parameters required to apply the flux selection methodology are the following:

1. MF cross-section: MF cross-section which can be retrieved with two different approaches:
   (a) System-level testing results: as for the Wireless IoT, the system sensitivity can be obtained by testing under high energy Proton at PSI.
   (b) Component-level testing results: if the system components have been qualified under radiation and their sensitivity is known, the MF cross-section can be estimated by summing the cross-sections of the individual components. However, bear in mind that this cross-section is only an approximation and does not account for system-level combined degradation failures.
2. FWCT: this parameter is intrinsic to the device. In the case of a system based on a duty cycle, the operational FWCT can be extrapolated from the system electrical validation phase as described in Section 3.4.2.
3. Minimum SF cross-section of interest: the cross-section of the fault that has the least chance of appearing in operation for the reference system. If it exists, is the fault with

the least chance of being observed. In order to define this last parameter, some information from Phases 1 and 2 of the CERN RHA can be used.

(a) The expected level of radiation of the environment in which it will be used (RHA - Phase 1).

(b) The expected working life, i.e. how long it is expected to work before it is replaced or dismounted (RHA - Phase 2).

(c) The maximum number of failures that the system requirements can tolerate (RHA - Phase 2).

(d) The number of devices expected to be deployed (RHA - Phase 2).

As an example, it is considered the Wireless IoT whose MF cross-section and FWCT are known. The cross-section of the Minimum SF of interest (MSF) can be evaluated considering the worst case radiation environment in which it will operate which for this application will be the HL-LHC DS region where $5 \cdot 10^{10}\ HEH \cdot cm^{-2}$ are expected per year. If three years of operation are considered, the Total Expected Fluence (TEF) is $1.5 \cdot 10^{11}\ HEH \cdot cm^{-2}$. Finally, one is the number of failures considered critical for the application. Knowing the TEF and the acceptable number of failures, the average cross-section of the MSF event can be obtained. In addition, its uncertainty due to the low number of events considered, can be calculated using Poisson statistics with a 95 % confidence interval. The worst case scenario is represented by the lower limit of the uncertainty obtained. Using a TEF of $1.5 \cdot 10^{11}\ HEH \cdot cm^{-2}$ and one failure, the lower limit obtained is $1.34 \cdot 10^{-13}\ cm^{-2}$. This will be the MSF used for the following analysis.

This cross-section does not take into account the delay between the occurrence of the SEE and the time it is detected. This delay would be a function of the system under test, its FWCT, and the MSF observability over the cycle (i.e. the frequency of test points over the cycle). As the failure is unknown, it may not even exist, its observability over the cycle cannot be predicted and therefore the cross-sections are considered when the SEE is detected.

Once the cross-section of the MSF and therefore its expected probability of occurrence is known, the equations (4.3) and (4.5) the two metrics ($P_{ob}$ and MTBFO) can be implemented. The next section gives an example of their implementation based on the input parameter defined in this paragraph.

### 4.5.2 Optimal Test Flux Evaluation

The input parameters defined in the example in Section 4.5.1, can be used to evaluate the two metrics ($P_{ob}$ and MTBFO) required to identify the optimal flux test.

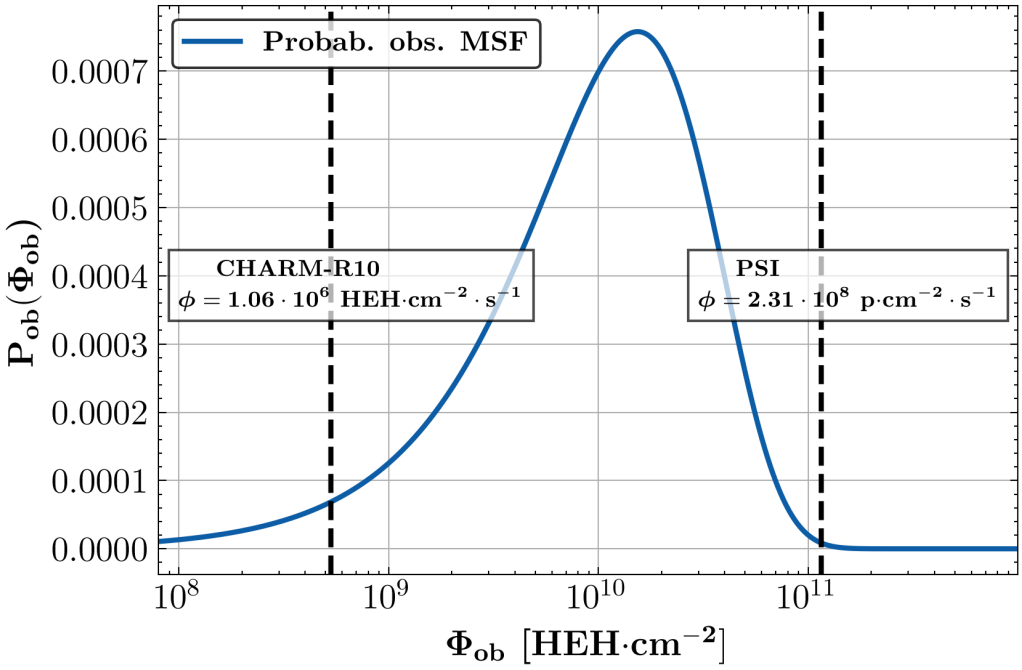


Figure 4.10: The probability of observing the MSF is depicted. A maximum can be observed at a $\Phi_{ob}$ of $1.53 \cdot 10^{10}\ HEH \cdot cm^{-2}$.

In Fig. 4.10, $P_{ob}$ as function of $\Phi_{ob}$ is plotted. A maximum can be identified for $\Phi_{ob}$ of $1.53 \cdot 10^{10}\ HEH \cdot cm^{-2}$. This is where $P_{ob}$ is maximized and is 0.07 %. The optimal test flux can be obtained using the equation (4.4). Considering the FWCT of the Wireless IoT (~500 seconds), the optimal test flux obtained is $3.07 \cdot 10^7\ HEH \cdot cm^{-2} \cdot s^{-1}$.

Performing the inverse procedure reveals a sharp decrease in probability for fluxes other than the optimum. In particular, this is especially true for the highest flux available at PSI, whereby the probability is two orders of magnitude lower (0.0008 %). For a lower flux such as that of CHARM-R10 there is still an order of difference (0.006 %).

Fig. 4.11 also shows the MTBFO obtained from equation (4.5). As highlighted in the figure, the MTBFO is reduced to 183 h where the curve has its minimum. This value appears excessively high for a test, but it must be taken into account that a typical CHARM test lasts around 120 hours.

The results of $P_{ob}$ and MTBFO obtained can be improved by a factor N by testing N systems. Testing ten systems together increases the $P_{ob}$ to 0.7 %, but reduces the MTBFO to 18.3 hours. However, not all testing facilities can accommodate parallel testing of many

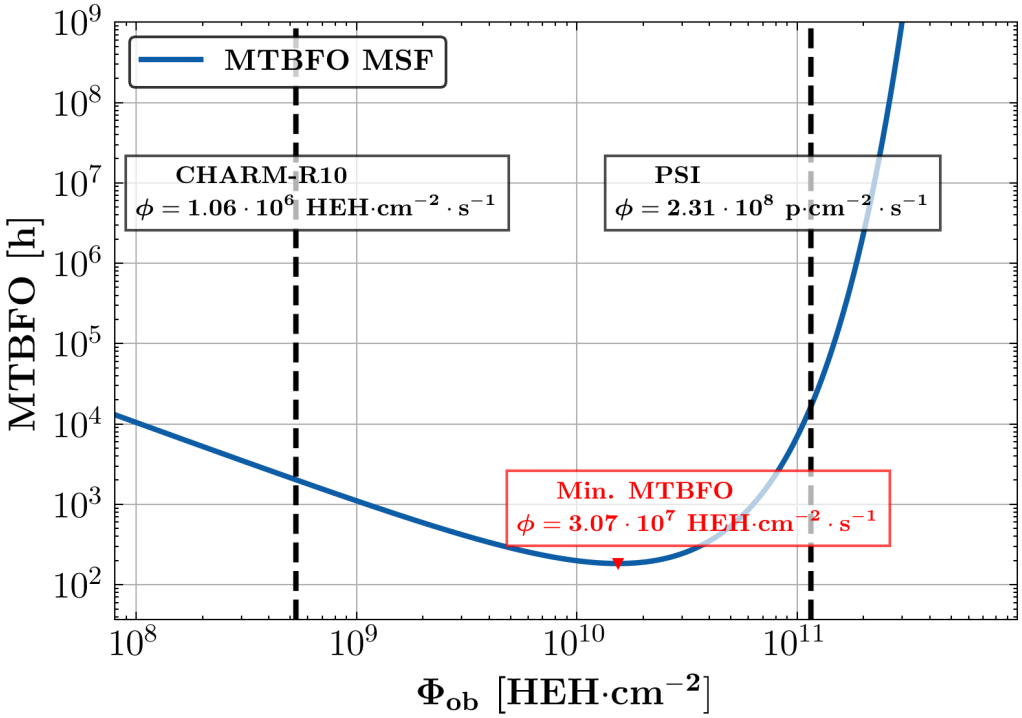


Figure 4.11: The MTBFO of the MSF is represented as a function of observability fluence. In this plot it is possible to see with greater relief, how using the higher flux of PSI the test time required is extremely high and the choice of an optimal flux can strongly reduce it.

systems. CHARM can be a good compromise in terms of flux (not tunable but limited to test positions) and having multiple systems under test to reduce testing time, identify the existence of SF and finally, improve the quality of the test at the system level.

In this example, only one device was considered. If more devices are planned to be installed, the lower limit must be divided by the number of planned systems or equivalent, the TEF multiplied by the number of systems used. In case multiple systems are planned to be installed but in different areas, the expected fluences during their operational time for each system can be cumulated to obtain the TEF.

Based on the input parameters specified at the beginning of the Section (MF, FWCT, and MSF), the flux selection method presented can be applied to any generic system. Using this approach may enhance the observability of SFs if they exist. A similar approach can be extended to Space Applications like CubeSats, which operate on different modes like the Wireless IoT. In this case, the MSF can be obtained considering the expected time of the mission and the expected radiation level using specific simulation software such as OMERE as done in [126].

## 4.6 RHA Implication

In Section 4.4.3 it has been shown, by defining specific metrics (MTBFO and $P_{ob}$), that there is a relationship between the selected flux and the probability of observing failures. In particular, they help quantify the difficulty in observing those events under specific flux conditions and demonstrate that the missing observation of such events during the qualification process presented in Chapter 3 was not because of the method used. Therefore, the SF observed later did not invalidate the methodology presented. On the contrary, they highlighted the importance of conducting tests under different flux conditions and the necessity of selecting an appropriate flux to enhance failure observability.

To provide a method for flux selection and improve the observability of SFs (when existing), an approach has been outlined in Section 4.5. This approach requires some input information to be put in place but it provides the optimal test flux and related minimal MTBFO and maximum $P_{ob}$. It was found that most of them are obtained through system requirements and characteristics, but one must be extrapolated from radiation testing data. The information required means that this method for selecting flux cannot be used alone. However, it can be used as an additional qualification test to carry out after the system has been qualified as done in Chapter 3. Combined with the latter methodology, they will allow the system to know MF sensitivity and lifetime (Chapter 3 methodology) and assert the existence of Flux dependent failure avoiding unexpected behavior during operation (Section 4.5), improving the quality of system-level testing qualification phase. As a drawback, the higher confidence gained, results in a rise in overall qualification costs.

The traditional CERN RHA system-level test method should also involve testing systems at different CHARM positions, i.e. different fluxes, especially when they have different operating modes and may have failure modes with low observability. Since the system-level testing takes place in CHARM-R13, faults can be hidden by the higher flux compared to CHARM-R10 and CHARM-G0 (Table 4.4). An additional method, for such types of systems, could be to run tests on different systems at different test positions, including R13 which is mainly used for lifetime assessment.

## 4.7 Chapter Summary

This Chapter discusses and quantifies the relationship between flux selection and failure observability. The investigation was prompted by the observation of unexpected failures in Wireless IoT operation during the first validation test in CHARM (Section 4.1).

The low level of observability provided by the test did not allow clear identification of failures. However, by comparing the test data obtained from the transmission with the ones stored in the non-volatile flash memory, it was possible to identify four different Potential Failure (PF) modes. To understand why these events were not visible during the qualification performed at PSI (Section 3.5.5), it was necessary to quantify them in terms of probability of occurrence (cross-section).

To achieve this, and to ensure the proper functioning of the system, Software Mitigation Schemes (SMS) have been designed for the platform to detect and mitigate such events and were introduced in Section 4.2. Their implementation does not affect system performance, like the one presented in Section 1.3, and are therefore perfect for IoT applications. Their validation was carried out by another test on CHARM in two different locations, i.e. in different flux environments, and using the USART to obtain a higher level of observability. This test allowed the quantification and identification of different SubFailures (SFs) and the validation of the Software Mitigation Scheme (SMS). These results validated the sensitivity estimations obtained using the methodology described in Chapter 3.

To verify the improvement in terms of system availability, a further test was carried out, always in CHARM, but with two devices: one with all SMSs implemented and the Ext WTD, the other with only the latter and an SMS already available during the tests in Chapter 3 (SMS 6). The result of this test, presented in Section 4.3.2, showed a reduction in downtime during the test by a factor of ~19 in the device with all the SMSs. These results have made it possible to overcome the last remaining challenge, defined in Section 3.2, for the use of IoT in the accelerator, i.e. respecting the LHC availability constraints, as illustrated in Section 4.3.3. These results prove that IoT devices may be a feasible solution for critical high-distribution systems in the future HL-LHC or even in longer accelerator designs such as the FCC. Furthermore, due to its modularity and versatility, Wireless IoT can be used for more critical applications such as wireless remote control of equipment. This topic will be presented in Chapter 5.

Once the different faults had been identified and their probability quantified in terms

of cross-section, the relationship between fault observability and flux selection was investigated. A study of the existing methodology for flux selection was presented in Section 4.4.1. Since existing methods do not allow quantification of the existence of this link, new metrics (probability of observing these failures ($P_{ob}$) and Mean Time Before First Observation (MTBFO)) were introduced in Section 4.4.3. Their application to SF Wireless IoT demonstrated the difficulty of observing such less probabilistic failures at certain flux rates. Analyzing these metrics for SF1, it was quantified the difficulty of observing such an event using the maximum flux available at PSI (MTBFO = ~331 $h$). On the other hand, using the optimal flux extrapolated through this analysis, a drastic reduction in testing time required would have been achieved (MTBFO = 1.88 $h$).

The results obtained led to the definition of a flux selection methodology to detect this type of failure. The method outlined in Section 4.5. can be replicated easily for any system where specific information is available. This information includes the Main Failure (MF) cross-section, which can be evaluated through system-level qualification results or estimated with higher uncertainty from component-level qualification data, the full working cycle time of the system (an intrinsic characteristic of the platform), and the Minimum SF of interest. The latter parameter can be determined by knowing the expected radiation level in the environment in which it will operate (CERN RHA Phase 1), the expected duration of operation, the number of failures considered acceptable for the application, and the number of systems installed, as demonstrated in Section 4.5.

An analysis of the RHA implications of this approach was provided in Section 4.6. As outlined, for systems with different operating modes where fewer probabilistic failures are suspected, the methodology provided in Section 4.5 should be considered alongside that in Chapter 3. However, even when following the traditional CERN RHA procedure for system-level qualification (test in CHARM-R13), it should be considered to conduct parallel tests at the lower flux positions to verify and evaluate the existence of any less probabilistic failures. The proposed methodology would significantly help the qualification process, preventing unexpected failure occurrence during operation and the need for system-level re-qualification. Furthermore, if the latter would be necessary, the application of such an approach will enable the selection of an optimal flux to improve the observability of such failures, optimizing testing time. Finally, as outlined within the section, this approach can be easily extended to the space community, specifically for designs based on work cycles such as CubeSAT.

# CHAPTER 5

# System Sensor Validation and Operational Feedback

This chapter presents the last part of the validation process that the Wireless IoT has gone through. In fact, from a certain point of view, the validation so far has been more about characterizing the reliability and availability aspects of the system under radiation. In this chapter, the validation concerns the operational aspects of the system and can be divided into three parts:

- Radiation Monitoring: in this chapter, the system is validated from a measurement point of view using the RadMon as a reference at different CHARM positions. In addition, the impact of intermediate neutrons (0.1 - 10 MeV) and intra-lot variability of the measurements are discussed.
- Deployment in the accelerator: the usability of the system from the functional point of view in the accelerator and its fast deployment capability are demonstrated and validated by means of some direct installation examples for radiation monitoring
- Multi Application Platform: the possible extension of Wireless IoT to applications other than radiation monitoring is demonstrated through different examples.

These validations conclude this doctoral work and demonstrate the enormous impact this application will have on the operation of the HL-LHC and the huge benefits it will bring in terms of monitoring and diversity applications for the future of the CERN.

Part of the content of this Section refers to the publication [136].

## 5.1 Study of the Impact of Using MCU Internal or External non-volatile Flash

As described in Section 3.3.5, the sensors used by the Wireless IoT are able to cumulate the measurements taken by their operating principle. This property is crucial in the selection of sensors, since during periods of network unavailability or in case of transmission loss (wireless system), if the instantaneous measurements are sent (e.g. bit flips occurred), they would be lost and thus the final reconstructed measurement (e.g. total bit flips) would be underestimated. To exploit the cumulative property and be able to reconstruct the final measurements even in a long period without data, it is necessary to store some information for both the SRAM and the FGDOS detectors.

- SRAM: in Wireless IoT, as in RadMon, the SRAMs are read, the bit flips are cumulated in specific counters, and the original pattern in the sensors is restored, i.e. the bit flips are rewritten with the original value.

- FGDOS: as discussed in Section 3.5.3, recharge counters and in part also the frequency at which the previous recharge was started ($f_{startrecharge}$), can impact the final measurement leading to an error if they are not transmitted and stored.

However, if the measurements are stored in the MCU's SRAM (Volatile Memory), when the Wireless IoT resets, the counters would restart from 0, and if one of the above-mentioned problems (e.g. network unavailability) occurs, the cumulative property would be lost. This storage problem is also critical for a failure mode related to the transceiver itself. During system qualification, it was observed that it could start transmitting corrupted data even though its configuration was still readable and capable of receiving LoRa Confirmed Uplink (CU). When this phenomenon occurs, the data received are unusable and functionality can only be restored by a system reset. There is no way for the MCU to detect the error, as the reception is working correctly. There are two ways to deal with this problem: a) send a custom downlink to perform a reset, or b) delete and insert again the LoRa Identifier (DevEUI) of the malfunctioning system. The latter action will force the faulty system to reset as the NS will discard all its received packets and consequently, no CU will be transmitted. Therefore, non-volatile storage methods must be found to mitigate these problems and provide cumulative measurements over time.

In the Wireless IoT, the usage of External Flash memory (Storage Subsystem already available in the design) seems to be the natural choice to cope with this problem. The measurements are stored there after each transmission, so the last value of the measurement counters (bit flips, recharge counter, and $f_{startrecharge}$) can be retrieved from there. However, there are two main limitations to the use of this component.

1. Lifetime: whenever the lifetime of the system would be increased by replacing the Ext WTD with another one with a longer lifetime compared to the external non-volatile flash memory, the latter would compromise the system's radiation resistance since, if used in this manner, it would become an essential part of the system's operation. In fact, since it stores the measurements, the loss of its functionalities would lead to the partial loss of the whole system's functionalities, especially for the radiation monitoring application, since the system would not be able to transmit cumulative data.

2. Permanent Failure: with the current chip (the 16 MB External Flash Memory used as storage subsystem), a hardware reset is not possible. If a permanent failure of the component occurs, the system cannot mitigate it and external intervention is required.

An alternative can be represented by the Internal Flash memory of the MCU. This memory is already used by the Wireless IoT to store the configuration of the system. This choice is made, to avoid relying on the external component guaranteeing the system to continue to transmit even in case the other component fails. The configuration is written one time in the MCU (before irradiation) and thus is considered a safe operation. Its use could be extended to the storage of measurements. As it is internal to the MCU, its access would be less time and power consuming. However, its reliability is unknown, as it has never been tested for this purpose at the component-level, and at the same time, its capacity is limited to 256 $kB$, part of which is used for firmware storage. For this reason, if it is employed, it can only be used to store the last measurement. The use of an External Flash remains essential to store measurements over time in the event that wireless capability is not available.

As shown in Fig. 5.1, the Internal Flash writing has a critical operation with respect to the reading: the erase. If this operation fails, it can have two critical consequences. If the configuration and the measurements are stored in the same sector, even if the configuration is only read, the failure of the flash write operation would result in the loss of both information (erase of the whole sector). In addition, the system uses two variables to calculate the sector size. These are stored in the MCU's SRAM and if one of them bit flips, the sector size will

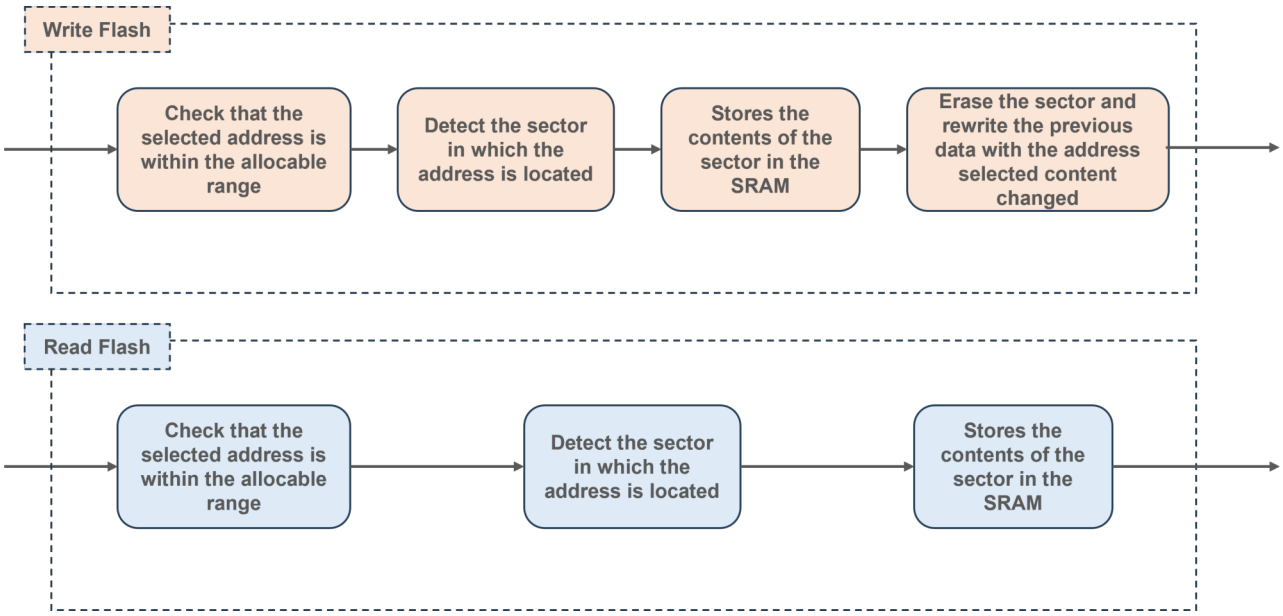


Figure 5.1: The Read and Write operations of the Internal Flash of the MCU are summarized in the block diagram. The main difference is related to the erase operation which does not occur in the Read Flash Operation.

also change. As a result, the erase operation would corrupt a larger partition of the flash (if the resulting size is even) or fail completely (if the resulting size is odd). This would mean that although the configuration and size are in two different sectors, a write failure could also result in the configuration being erased. To avoid this problem, the two variables used to calculate the sector size are compared with the expected value before the erase operation is performed. The expected value, being a constant, is not stored in the MCU SRAM but in the MCU instructions. In this way, if bit flips occur, the operation is aborted and the system identifies the error restoring its functionality via reset. In addition, to avoid the first faulty erase, the configuration and the measurements are in two different sectors. To guarantee the integrity of the measurements, their storage is tripled in three different sectors so that if one write fails (erase), it is possible to recover the correct value from the other two. Another problem is the integrity of the memory if one of its sectors is constantly being written to and consequently erased. If the Internal Flash is used and the measurements are always written to the same address, loss of integrity can affect the cumulative nature of the measurements.

To test which of the two solutions would have been the more reliable in operation, the firmware of the Wireless IoT was modified and a block diagram summarizing it is given in Fig. 5.2. As visible, the App Sleep phase has been replaced by the App Test phase. During this phase, the MCU does not go to sleep, but it continuously stresses both the internal and External Flash every ten seconds. This solution not only affects the battery life of the system,

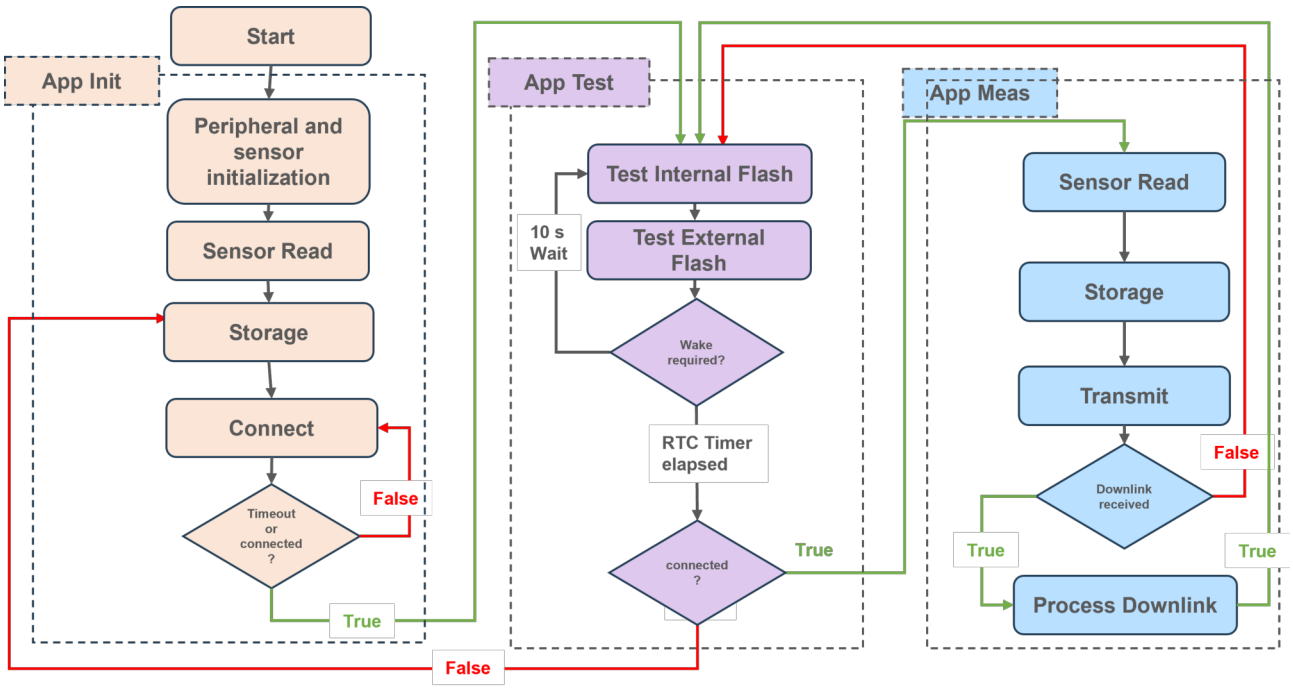


Figure 5.2: Firmware used to test the reliability under radiation of the External and Internal Flashes.

which is not a problem as it is only used for test purposes, but it may also affect the life of the components under radiation as their bias is different to that normally used. This phase is ended by the RTC at the end of the measurement period, as in the App Sleep phase. Fifteen bytes containing a fixed pattern with a counter in the most significant byte are stored in the External Flash. Once stored, the content is read to check for correctness. The WRP is periodically incremented and checked before each operation as described in Section 4.2.4. Similarly, the Internal Flash stores and reads ten bytes at a fixed address. The purpose of always saving to the same address is to verify the integrity of the contents of the Internal Flash after many storage operations. Since it is then only accessible byte by byte and not bit by bit, it is also useful to understand if and when a byte is corrupted. If the byte value is incorrect, an error message is displayed, showing the expected and actual values. The test was performed in CHARM-R10 with a setup similar to the one shown in Fig. 4.4. The main difference was the use of the LoRa CERN network instead of the private network provided by the indoor gateway RAK7258. The integration of the device into the CERN network is described in the next sections. Due to the unavailability of the RadMon, the TID and HEH measurements were evaluated using the facility calibration factors and the measured Proton On Target.

A very interesting behaviour was observed in the MCU's Internal Flash. As shown in

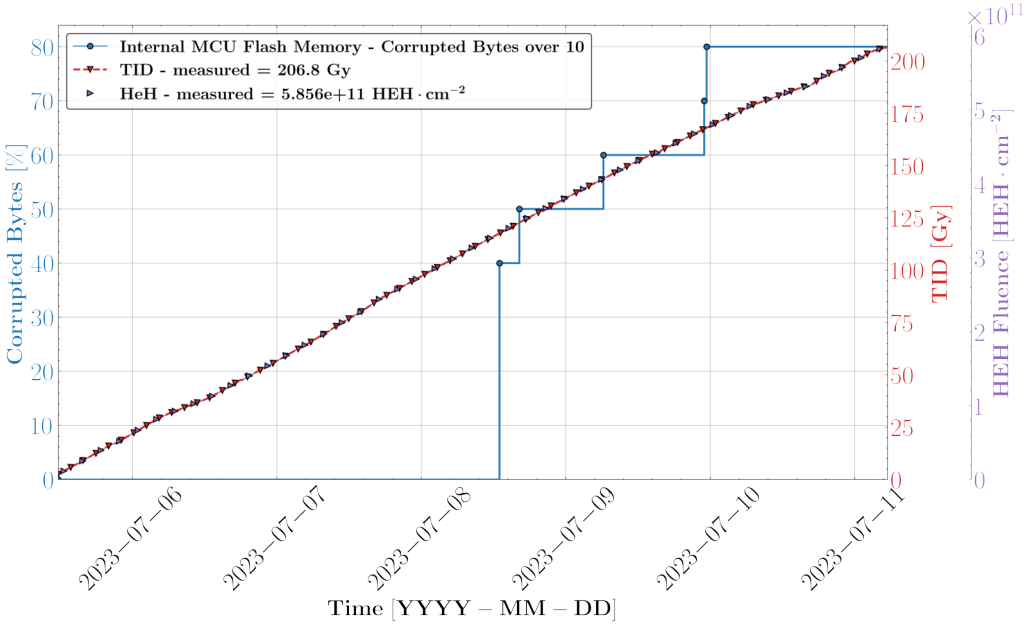


Figure 5.3: The percentage of corrupted bytes observed during the reliability test of the MCU Internal Flash conducted in CHARM-G0, is depicted as a function of time, TID, and HEH measurements.

Fig. 5.3, of the ten bytes stressed during the test with erase, read and write operations. starting at 117.6 *Gy* four were corrupted. The corruption was identified by the fact that the expected value did not match the read value. In particular, some bits of the corrupted bytes could no longer be written to. For example, when the value three was written to the second byte, the read value was two. The LSB of this byte could no longer be written to with the desired value but was fixed at zero. At the end of the test, eight of the ten bytes tested were corrupted. Another important information can be extrapolated from this result. The firmware is also stored in the Internal Flash, and writing new machine code requires erasing and rewriting the relevant sectors. Considering the unreliable behavior of flash above 117 *Gy* and the size of the firmware, which requires a larger number of bytes, we can conclude that reprogramming a device after 100 *Gy* taken, may not be safe. Other tests carried out during this thesis showed that some devices could be reprogrammed even after 200 *Gy* accumulated while others failed the programming process during the verification phase already after 100 *Gy*.

As far as the External Flash is concerned, there were no significant problems with writing or reading. Specifically, 28468 writes were performed and at the end of the test, when the memory was read, all records were present and none were corrupted. The only malfunction observed during the test was due to an incorrect read of the writable size of the flash, which was 4 *kB* at a TID of 124.8 *Gy*. In this case, as a result of the incorrect writable size, SMS 5

detected the fault and reset the functionality of the device. After the reset, the device was found to be correctly readable and no further operations failed. According to the results obtained, the External Flash seems to be the best option to preserve the information of the last measurements and to guarantee the cumulative property of the measurements reliably. However, if the lifetime would be increased by modifying the Ext WTD, another solution may be required to avoid being limited by the storage subsystem. The Internal Flash remains a possible option. The result obtained for the Internal Flash must take into account that the device has not been tested as it would be used in operation. It is expected that if fewer write and read operations are performed on a sector, it will have a longer life. However, to mitigate the problem, it can be considered to use another sector (never erased during the life of the system) when the one used becomes damaged.

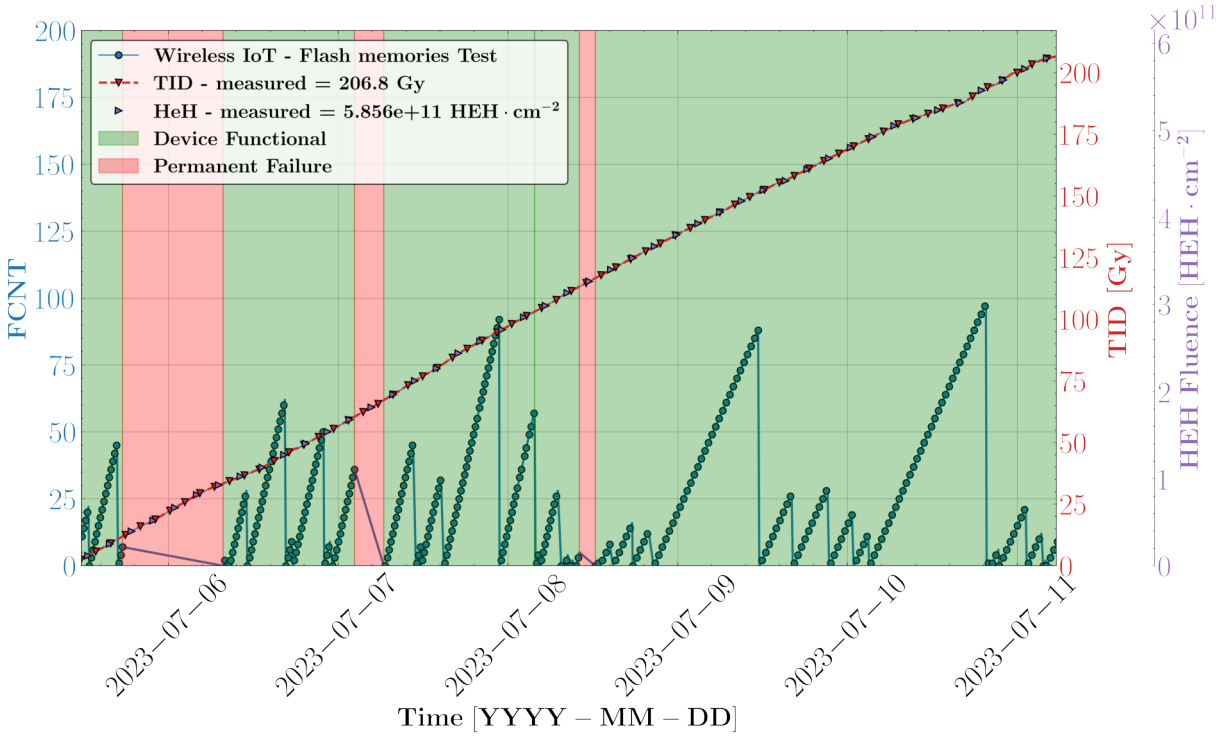


Figure 5.4: The LoRa FCNT is depicted for the Wireless IoT tested in CHARM-R10. As visible the device exhibits three permanent failures during the test.

Another interesting aspect of the general behaviour of the device was also observed. Contrary to previous tests, e.g. in Section 3.5.5, the device operated with a $DC_{Bat}$ of 100 %, as it never entered in power safe mode. During the first part of the test, the device suffered three unrecoverable failures, as shown in Fig. 5.4. In such cases, system functionalities were restored through external power cycles. In particular, the permanent failure cross-section of the device was assessed considering the estimated HEH fluence ($4.96 \cdot 10^{11}$ $HEH \cdot cm^{-2}$) with an error of the order of 10 %. As a result, its average cross-section amounts to $6.05 \cdot$

$10^{-12}\ cm^2 \cdot Device^{-1}$. The results obtained led to an investigation of the relationship between the permanent failure cross-section of the MCU and the $DC_{Bat}$ used.

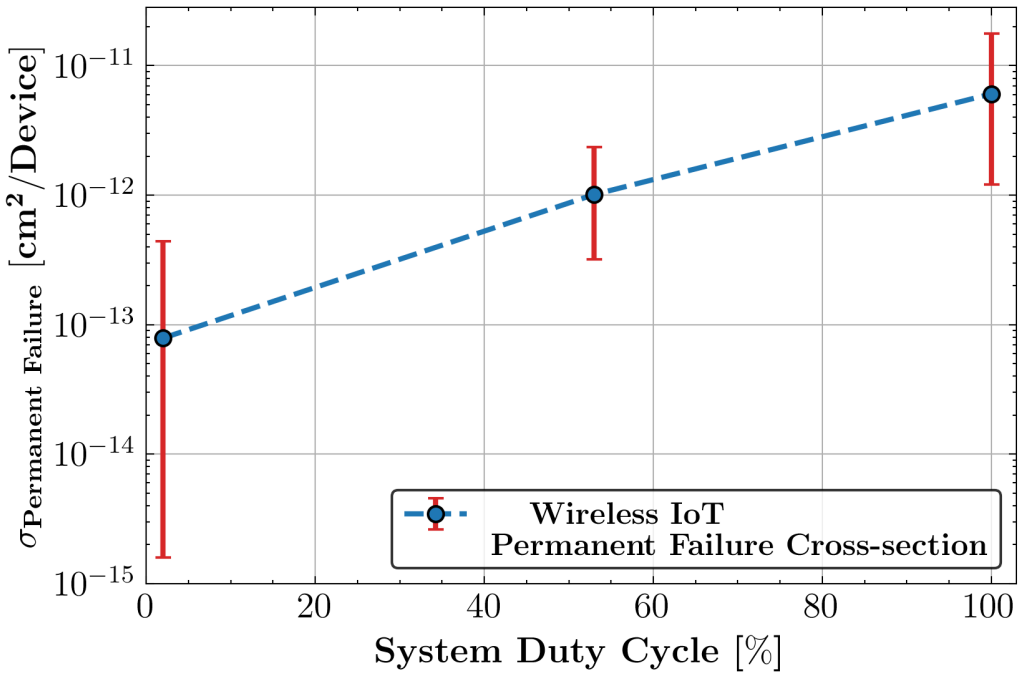


Figure 5.5: The permanent failure cross-sections of the device are depicted as a function of the Duty Cycle of the system (App Meas Period/ Measurement Period (300 $s$)). The Upper and Lower limits depicted have been evaluated considering the uncertainty due to the low number of events' statistics (Poisson process) with a 95 % confidence interval.

In order to study this relationship, data in terms of the permanent fault cross-section obtained through another Wireless IoT (Different Sensor Board) was used. In this application, which will be presented in Section 5.5.2, the App Meas period of the application is only ~6 $s$, and therefore the $DC_{Bat}$ is 2 %. For this application, a total fluence of $1.27 \cdot 10^{13}$ $HEH \cdot cm^{-2}$ was accumulated and only one permanent failure was observed. The average Permanent Failure cross-section is therefore $7.87 \cdot 10^{-14}\ cm^2 \cdot Device^{-1}$. For what is concerned the "normal" $DC_{Bat}$ for the radiation monitoring application (53 %), several permanent failure events were observed during other tests and operations, using a measurement period of 5 minutes and were considered in this analysis in addition to the one observed at PSI and described in Section 3.5.5. Specifically, five events were observed for a total fluence of $4.96 \cdot 10^{12}$ $HEH \cdot cm^{-2}$ ($\sigma_{Permanent\ Failure}$: $1.01 \cdot 10^{-12}\ cm^2 \cdot Device^{-1}$). The cross sections for different duty cycles of the system ($DC_{Bat}$) are shown in Fig. 5.5. As can be seen, the lower the duty cycle used, i.e. the more time the device spends in an idle state during the entire measurement period, the lower the probability of a permanent failure event.

The observed behaviour has several important implications:

- Operational: since the permanent failure cross-section depends on the measurement period used, a higher measurement period, i.e. lower System $DC_{Bat}$) should be used in operation to avoid the occurrence of this dramatic event. This choice would make it possible to reduce the permanent failure cross-section in service. Using a measurement period of one hour, the duty cycle is already reduced to 4 %.

- Design improvement: the most time-consuming operation occurring during App Meas is the reading and rewriting of SRAMs using SPI GPIO expanders. Two alternatives can be used to avoid this component in the design and reduce read and write times:

    1. SPI or I2C SRAM: the use of SPI or I2C SRAMs would not require the use of SPI GPIO expanders. Therefore, the memories could be read faster using a smaller number of pins.

    2. FPGA: using an FPGA to read SRAMs can be a possible solution to avoid the use of SPI GPIO expanders and make memory reading faster. An FPGA is required that is capable of entering a power save mode so as not to affect the battery life of the system and that has sufficient hardware capabilities in terms of resources and GPIOs. The MCU could control the FPGA as an SPI slave and put it into power save mode during App Sleep [137].

- Higher reliability for different IoT applications: normally, in IoT applications, the App Meas period is only a few seconds (for example, the presented case of a 2 % duty cycle is a different IoT application using the Wireless IoT Main-board and firmware). This allows the platform to be used in a safer way for different applications, since its permanent failure cross-section would be much lower compared to that of radiation monitoring, for the same measurement period used (five minutes).

The latter implication drives and justifies the extension of this project to various IoT applications in addition to radiation monitoring.

## 5.2 Measurement Performance Validation

In this Section, the Wireless IoT measurement capability is validated using the RadMon instrument as a reference. The impact of the higher sensitivity to intermediate Neutrons (0.1–10 $MeV$) of the CY62167GE30 and lower intra-lot variation are also discussed and investigated.

### 5.2.1 Assessment of the Neutron Sensitivity in CY62167GE30 for Intermediate Neutrons (0.1–10 MeV)

Before validating the measurement capability of the Wireless IoT, the CY62167GE30 sensitivity to neutrons in the 0.1-10 $MeV$ energy range was investigated. It was shown in [138] that neutrons belonging to this spectrum can play a critical role in the induction of SEUs in $nm$ technologies, with particular criticality at the selected 65 $nm$ (CY62167GE30 technology). To understand the impact of this higher sensitivity to neutrons in this energy spectrum, an irradiation test campaign was performed at the PTB facility to study the response to intermediate neutrons of the production lot (1943) of CY62167GE30, which will be used by Wireless IoT as an HEH sensor.

The measurements were performed using the setup shown in Fig. 5.6a. Eight memories are mounted on a test board (Fig. 5.6b) which is connected to an FPGA board (tester board) via a MicroCoax cable. The tester board is connected to the PC via a serial USB. Several runs were performed to accumulate sufficient statistics and, when possible, three different memories were tested to take into account the intra-lot variability in the final result.

All cross-sections ($\sigma_{SEU}$) were evaluated by the Poisson process with a confidence interval of 95 % and considering a fluence uncertainty due to the PTB facility of 10 %. The measured cross sections are shown in Table 5.1 with the cumulative total fluence on the different chips tested for each energy. For all energies except 0.144 $MeV$, three different memories were tested to account for intra-batch variation in the calculation of the cross-section. For 0.144 $MeV$, two different memories were tested. For 2.5 $MeV$ it was also possible to perform several runs on the same sample to check the repeatability of the measurements, which was confirmed.

In Fig. 5.7, the results obtained for the CY62167GE30 Lot 1943 are compared with those presented in [107] for the memory used in the RadMon (CY62157EV30), where a similar study was carried out in the same facility. As can be seen from Fig. 5.7, the sensitivity of the

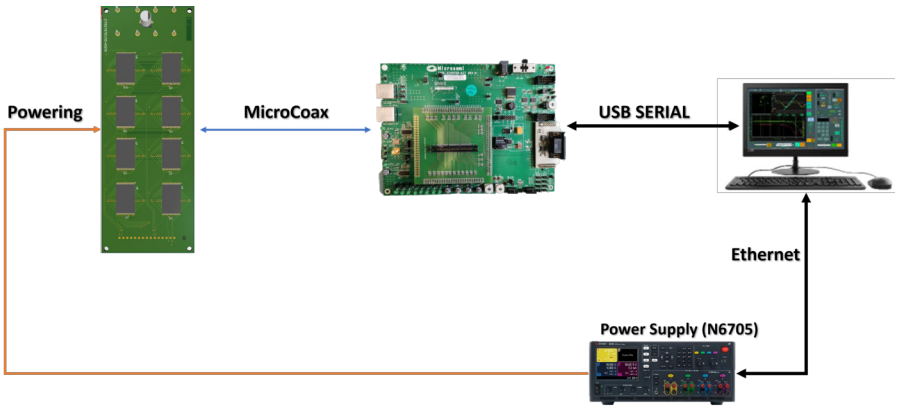


(a) PTB - Test Setup

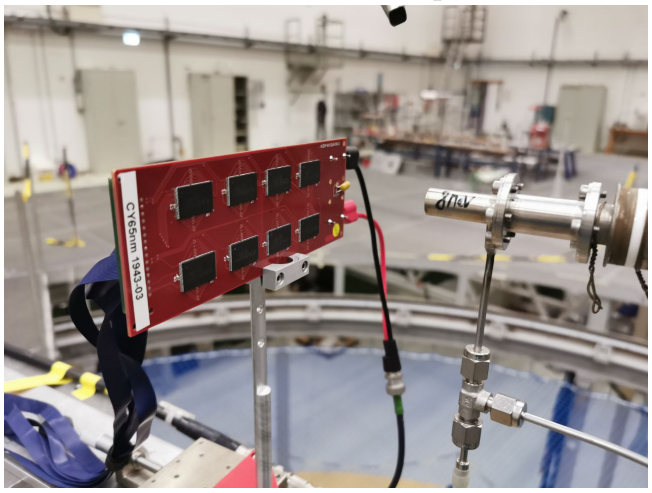

(b) PTB - Test Board

Figure 5.6: In Fig. 5.6, a block diagram summarizing the setup used during the radiation test campaign at PTB. The test board mounting the CY62167GE30 - Lot 1943 and placed in front of the beam is depicted In Fig. 5.6.

CY62167GE30 SRAM is higher compared to the CY62157EV30 at low neutron energies. For example, at 2.5 *MeV* there is a factor of three difference between the two memories. This could affect the measurement provided by the CY62167GE30 SRAM, leading to an overestimation of the HEH fluence due to SEUs produced by intermediate neutrons, to which the CY62157EV30 is less sensitive.

To analyze the impact on the instrument measurements, a validation campaign was carried out on the Wireless IoT, comparing its measurements with those of the RadMon instrument at CHARM test positions representative of the LHC. As already mentioned in Section 2.5.3, the different test positions, shieldings, and target configurations allow the facility to provide different radiation fields and spectra as required. For these tests, it was decided to not use shielding and to use the Copper target (Config CUOOOO). In order to compare and validate the measurements, a progressive approach was taken, moving from environ-

Table 5.1: CY62167GE30 cross-section response for energy from 0.144 to 17 *MeV*.

| Energy [MeV] | Flux [n · cm$^{-2}$ · s$^{-1}$] | Fluence [n · cm$^{-2}$] | Cross-section [cm$^2$ · bit$^{-1}$] Lower Limit | Average | Upper Limit |
|---|---|---|---|---|---|
| **0.144** | 2.39·10$^5$ | 6.9·10$^9$ | $1.40 \cdot 10^{-15}$ | $1.68 \cdot 10^{-15}$ | $1.99 \cdot 10^{-15}$ |
| **1.25** | 8.98·10$^5$ | 9.7·10$^9$ | $9.85 \cdot 10^{-15}$ | $1.11 \cdot 10^{-14}$ | $1.23 \cdot 10^{-14}$ |
| **2.5** | 9.31·10$^5$ | 1.51·10$^{10}$ | $1.01 \cdot 10^{-14}$ | $1.13 \cdot 10^{-14}$ | $1.25 \cdot 10^{-14}$ |
| **5** | 1.01·10$^5$ | 7.29·10$^9$ | $1.15 \cdot 10^{-14}$ | $1.30 \cdot 10^{-14}$ | $1.44 \cdot 10^{-14}$ |
| **6.5** | 1.40·10$^6$ | 1.1·10$^{10}$ | $1.55 \cdot 10^{-14}$ | $1.73 \cdot 10^{-14}$ | $1.91 \cdot 10^{-14}$ |
| **17** | 2.41·10$^5$ | 2.3·10$^9$ | $7.19 \cdot 10^{-14}$ | $8.04 \cdot 10^{-14}$ | $8.88 \cdot 10^{-14}$ |

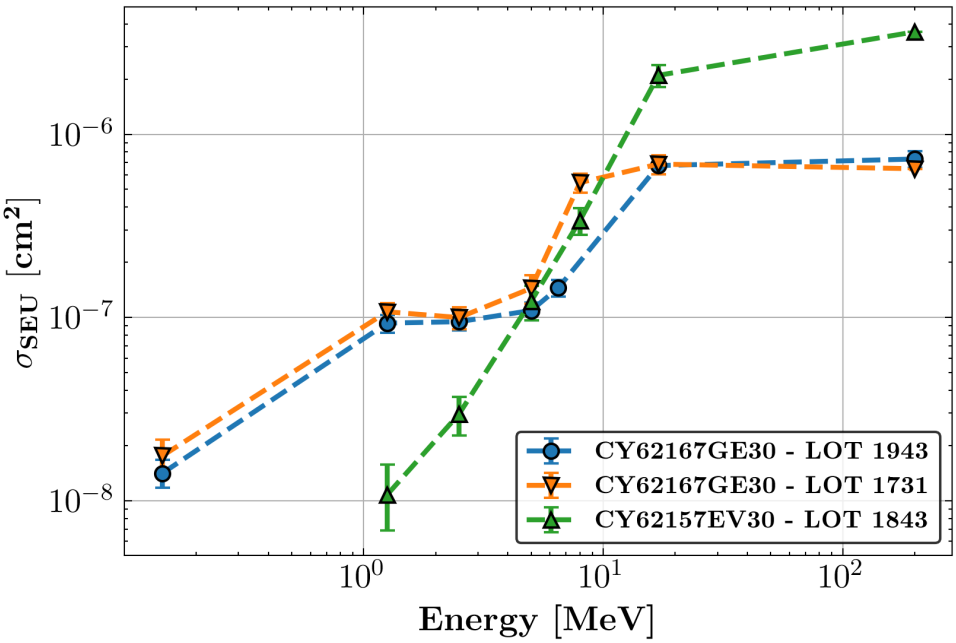


Figure 5.7: The cross-sections of CY62167GE30 SRAM Wireless IoT Production Lot 1943 are compared with those of another Lot of the same memory and with one of CY62157EV30. The latter two cross-section data sets were extracted from [107].

ments dominated by hadrons of different species generated by the interaction of the beam with the target in zones (R10-R5) to positions where, due to the presence of concrete walls surrounding the structure, the spectrum is more dominated by neutrons and there is greater thermalization (G0). The results obtained demonstrated the compatibility of the measurements between the two instruments and justified the use of the CY62167GE30. These measurements are presented in the following sections.

### 5.2.2 Assessment of the Monitoring Performance in CHARM-R10

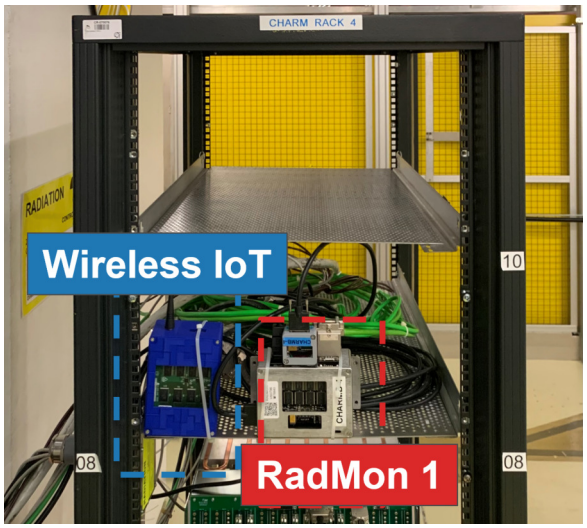


(a) R10 - Test Setup

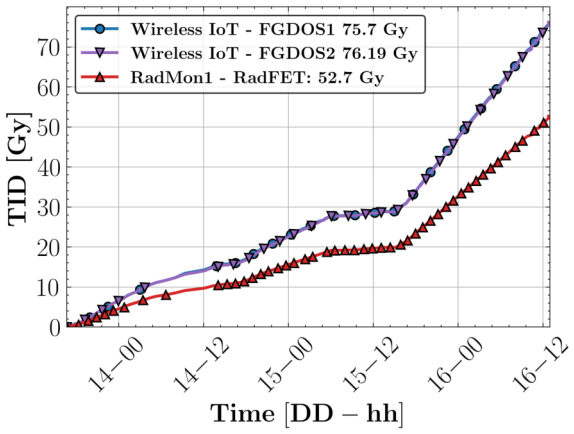


(b) R10 - TID over Time

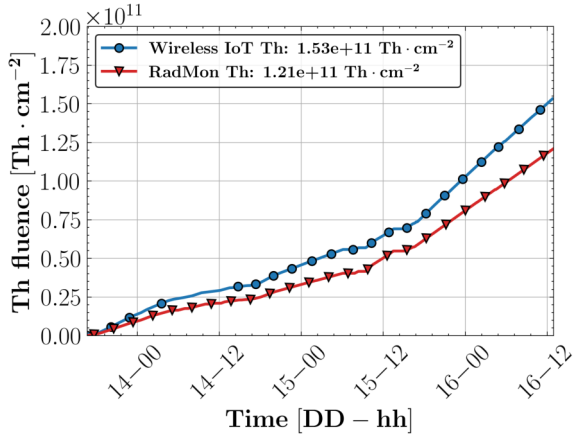


(c) R10 - Th over Time

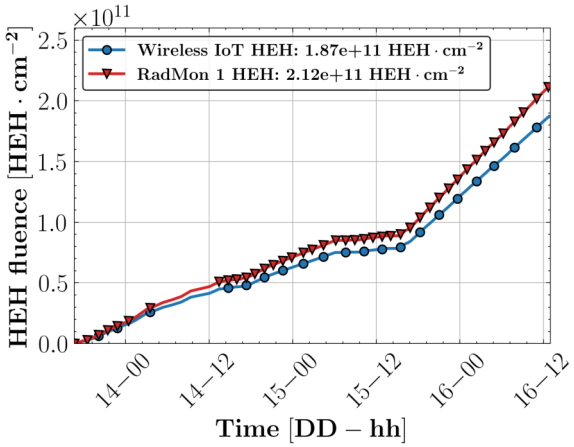


(d) R10 - HEH over Time

Figure 5.8: The Setup used in R10 for Wireless IoT validation and the measurements of TID, Th, and HEH are reported and compared to the one retrieved from the reference RadMon.

The first position selected was R10. In addition to assessing the instrument's ability to measure in a challenging environment, the choice of this position has another purpose: its higher fluence per week allows the system to be stressed as much as possible, and the effect of application resets on the final measurements to be assessed. The Wireless IoT was installed on a rack and a RadMon was placed next to it as shown in Fig. 5.8a.

As can be seen in Fig. 5.8, a good agreement in terms of time behaviour and the final result is obtained for the measurements of TID, HEH, and Th. For the TID, for RadMon 1 the relative difference to the measurement of the Wireless IoT is - 30 %. This value obtained for the TID measurement may be due to the uncertainty introduced by the average sensitivity used for both RadFET and TID. However, since the uncertainty of the RadMon is $\pm$30 %, the

measurements can be considered compatible.

As far as HEH and Th are concerned, the results show a good agreement. For what concerns the Th measured by RadMon 1, the relative difference with respect to the measurement of the Wireless IoT is - 20 %, while for the HEH it is + 13 %. The difference in the final measurements could be due to several factors:

- The two systems use different Toshiba Lot memories, which are also used to calculate the final HEH.
- The Toshiba voltage on the RadMon is unstable and degrades over the TID taken.
- The intra-lot variation is not negligible for Toshiba and CY62157EV30. Even the use of 4 memories per SRAM type affects the uncertainty of the final measurements. It can cause two RadMon's at the same position to measure two fluence values with relative errors of up to 30 %. A comparison of the intra-lot variation for Toshiba, CY62157EV30, and CY62167GE30 is provided in Section 5.2.5.

Thanks to these results and since the uncertainty of the RadMon is estimated to be $\pm$30 %, the measurements can be considered compatible and the system measurements are validated. In particular, in this position, the higher sensitivity to Intermediate neutrons does not affect the final measurements of the CY62167GE30.

### 5.2.3 Assessment of the Monitoring Performance in CHARM-R5

A second test was carried out in R5. This location is less critical than R10. The intermediate neutron and Th contributions are expected to be higher compared to HEH. The Wireless IoT was installed on a pole and the RadMon was placed next to it as shown in Fig. 5.9a. As can be seen in Fig. 5.9, a good agreement in terms of time behaviour and the final result is obtained for the measurements of TID, HEH, and Th.

Based on the TID analysis, for RadMon 1 the relative difference with respect to the Wireless IoT measurement is - 0.9 %. The smaller difference in the measurements can justify the previous hypothesis about the influence of sensitivity on the R10 TID results. In this case, two brand new instruments were used whose sensitivity characteristics may be similar to those of the calibrated instruments. As far as HEH and Th are concerned, these results also show a good agreement. For the Th measured by RadMon 1, the relative difference with respect to the Wireless IoT measurement is + 22 %. The same difference is obtained for HEH.

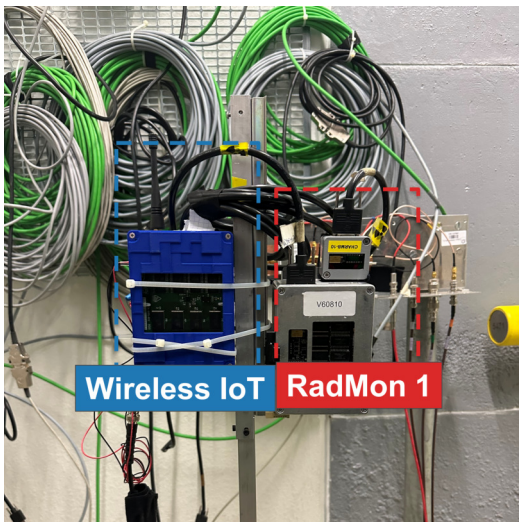


(a) R5 - Test Setup

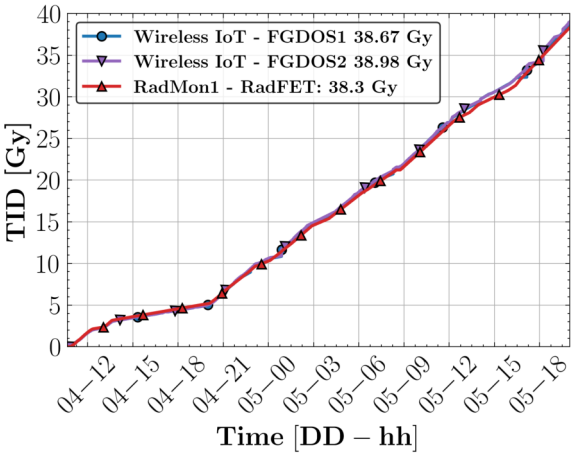


(b) R5 - TID over Time

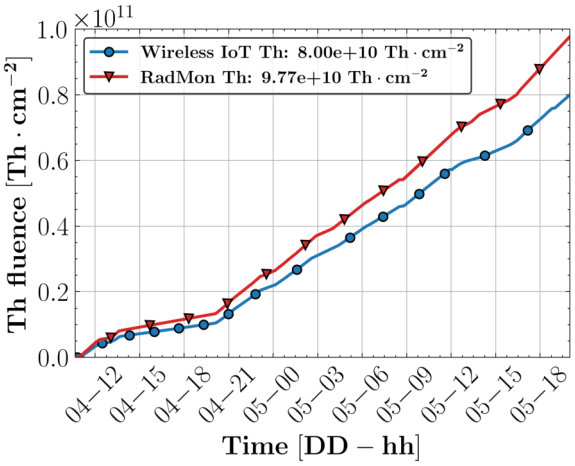


(c) R5 - Th over Time

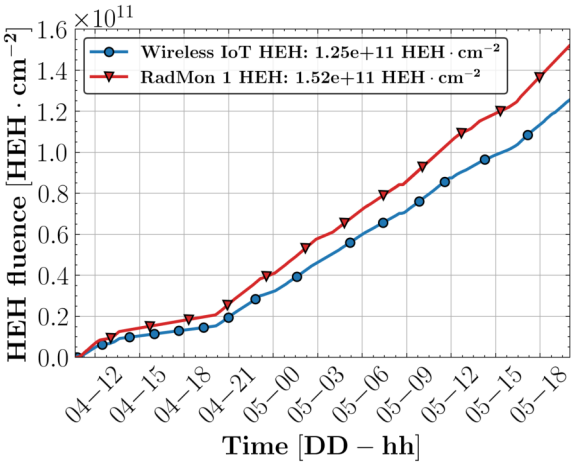


(d) R5 - HEH over Time

Figure 5.9: The Setup used in R5 for Wireless IoT validation and the measurements of TID, Th, and HEH are reported and compared to the one retrieved from the reference RadMon.

The motivations presented in Section 5.2.2, can justify the higher fluences measured by the RadMon. In this case, the higher sensitivity of the CY62167GE30 to intermediate neutrons cannot affect the final measurement, as it should have led to an overestimation of the HEH. Thanks to these results, and since the uncertainty of the RadMon is ±30 %, the measurements can be considered compatible and the system measurements are validated.

### 5.2.4 Assessment of the Monitoring Performance in CHARM-G0

As the measurements were validated in HEH dominated environments, it was decided to move the validation to a more shielded area of CHARM where the spectrum would be more neutron-rich and it would be possible to better analyze the impact of intermediate neutrons on the final measurements. The G0 location is characterized by a grid on which the

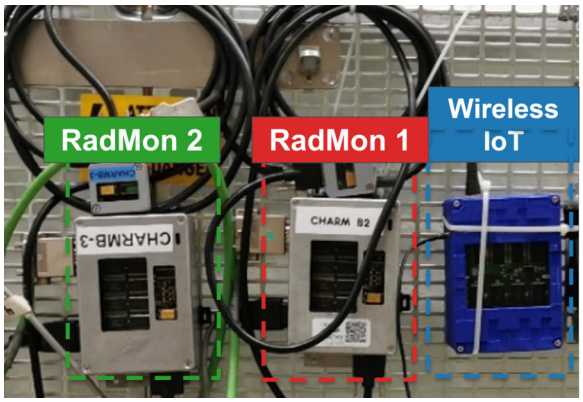


(a) G0 - Test Setup

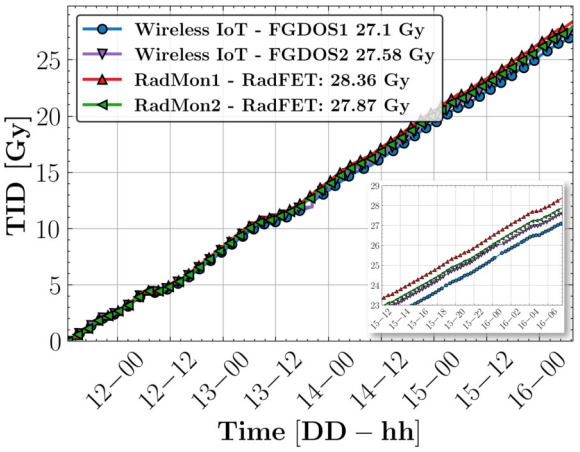


(b) G0 - TID over Time

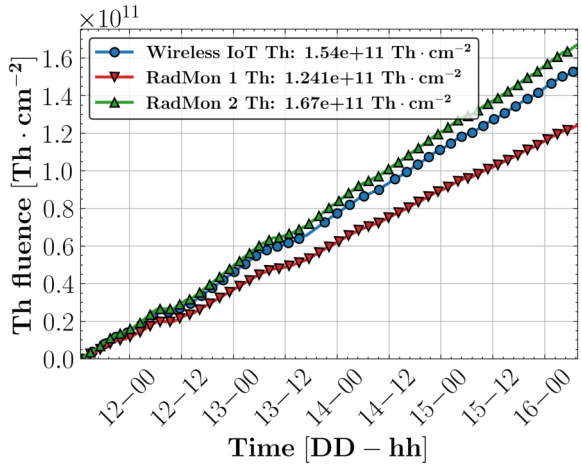


(c) G0 - Th over Time

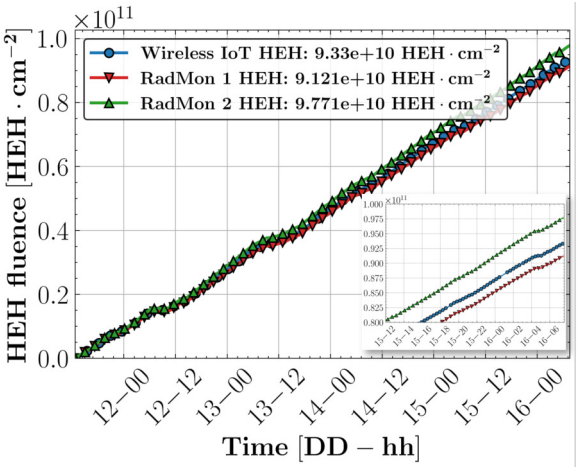


(d) G0 - HEH over Time

Figure 5.10: The Setup used in G0 for Wireless IoT validation and the measurements of TID, Th, and HEH are reported and compared to the one retrieved from the reference RadMon.

equipment can be mounted and is normally used for sensitivity tests. The Wireless IoT and two different RadMon were mounted on this infrastructure as shown in Fig. 5.10a. It was decided to use more RadMon for this test to evaluate the difference between two identical devices in the final measurements.

As can be seen in Fig. 5.10, also in this test position, a good agreement in terms of time behaviour and the final result is obtained for the measurements of TID, HEH, and Th. For the TID a very good agreement is achieved. It can be observed that the relative difference concerning the measurement of the Wireless IoT is + 2.8 % for RadMon 1 and + 1 % for RadMon 2.

For Th and HEH, the situation is more complex. For the first fluence, the relative difference with respect to the Wireless IoT measurement is -19 % for RadMon 1 and + 8.5 % for RadMon 2. In particular, the relative difference of RadMon 2 with respect to RadMon 1 for the Th measurement is + 34 %. Since the two instruments have the same sensors and the flu-

ence on the G0 grid is expected to be uniform, especially when the instruments are so close together, the difference obtained between the two measurements could be caused by the intra-batch sensitivity variation affecting the two sets of memories used.On the other hand, for HEH it is - 2.2 % for RadMon 1 and + 4.7 % for RadMon 2. The higher sensitivity of the CY62167GE30 to intermediate neutrons did not have any effect on the final measurement, does not have any significant effect on the final measurements.

In the study outlined in [83], it was demonstrated that R10 provides a representation of LHC-RRs, whereas R5 and G0 to some extent represent LHC-UJs. Therefore, based on the result presented, it can be reasonably concluded that the relatively higher intermediate neutron sensitivity of CY62167GE30 may not be a significant issue when considering its use in the context of the LHC. Furthermore, as outlined in Section 5.2.5, the reduced intra-lot variation demonstrated by this sensor could potentially decrease measurement uncertainties.

### 5.2.5 Assessment of the Measurement Uncertain Caused by Intra-Lot Sensor Spreading

As shown in the previous sections, the intra-batch variability of the SRAM sensors can have a huge impact on the final measurements, leading to a relative difference of more than 30 % in the measurements of two instruments using the same detectors. To understand if an improvement in terms of uncertainty reduction in the final measurements can be obtained using the CY62167GE30, the bit flips measured at the end of the run by the same sensors on the RadMon and Wireless IoT were extracted and the percentage ratio of their normalized standard deviation to the mean of the counts was evaluated. Data from different batches of the same memory model, obtained from other tests, were included in this analysis to check whether the behaviour was batch specific. The results are shown in Fig. 5.11 and it can be observed that the behaviour appears to be independent of the batch considered but dependent on the type of memory.

Analyses show that TC554001AF are characterized by greater dispersion and are therefore the main source of uncertainty in fluence measurements. This behaviour does not depend on the test positions. Differently, the behaviour of CY62157EV30 seems to deteriorate when moving to more HEH dominated environments and may be caused by type A clusters (Fig. 3.2a) affecting this type of SRAM. Compared to CY62157EV30, CY62167GE30 seems to have less variation within the same batch. This is an important point in favor of using this

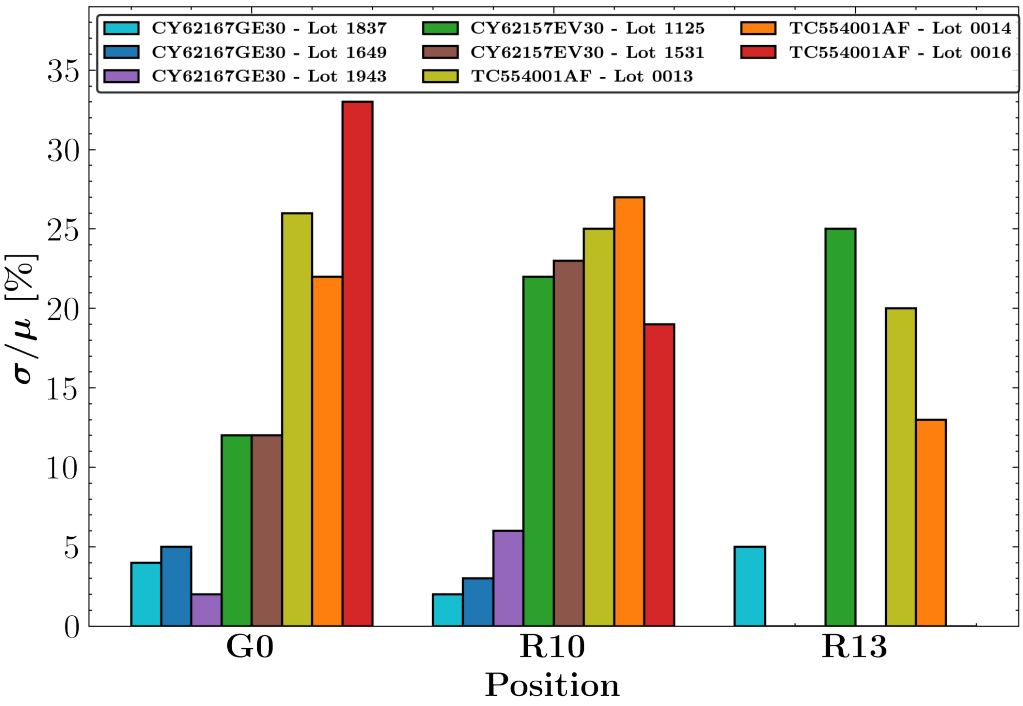


Figure 5.11: The intra-lot variability is provided at different CHARM positions for different lots belonging to the same SRAM model.

memory as it reduces the uncertainty in the final measurements.

This analysis concludes the validation of the Wireless IoT and enables its usage in the LHC. As pointed out in the previous sections, the higher sensitivity to intermediate neutrons would not represent a problem in alcoves such as UJ and RR and HEH dominated environments such as the tunnel. In addition, the lower intra-lot variation can be a major benefit in terms of uncertainty reduction in the final measurements.

## 5.3 Integration of the Wireless IoT in the CERN Network

### 5.3.1 LoRaWAN Network at CERN

Low Power Wide Area Networks (LPWAN) provide low power devices with long-range communication capabilities in a cost-effective manner. The trade-off is that throughput is reduced compared to traditional local or wide-area networks, such as Wi-Fi or cellular networks. To support several use scenarios for battery-powered sensors, CERN has deployed two parallel LPWAN networks covering both the surface of its campus and its underground facilities. The first network, based on LTE-M, is not of interest to this manuscript, which will focus on the second network, a private LoRaWAN one that is fully under the control of

CERN.

The LoraWAN network architecture is based on a star topology. Data sent from a node is typically received by multiple gateways, which forward the messages to a central NS, which holds the brain of the network. It manages the MAC layer, discards non-network belonging frames, authenticates received packets, filters redundant received messages, handles security checks, schedules downlink commands, etc.

The LoRaWAN network designed and deployed by the CERN organization is based on ChirpStack open-source Network Server [139, 140]. To enable CERN to control the network, device provisioning, and data flow, a private instance of ChirpStack is installed on site. To select the location of the gateways, to ensure geographical redundancy on the ground and to comply with the regulatory duty cycle for downlink messages, a capacity and coverage study was carried out:

- To ensure coverage of the campus (60 $km^2$), LoRaWAN gateways have been installed on the roofs of 15 CERN buildings.
- There are 46 additional gateways covering the injector chain, the accelerators, adjacent tunnels, caverns, and experiments, thanks to the existing infrastructure of radiating cables.

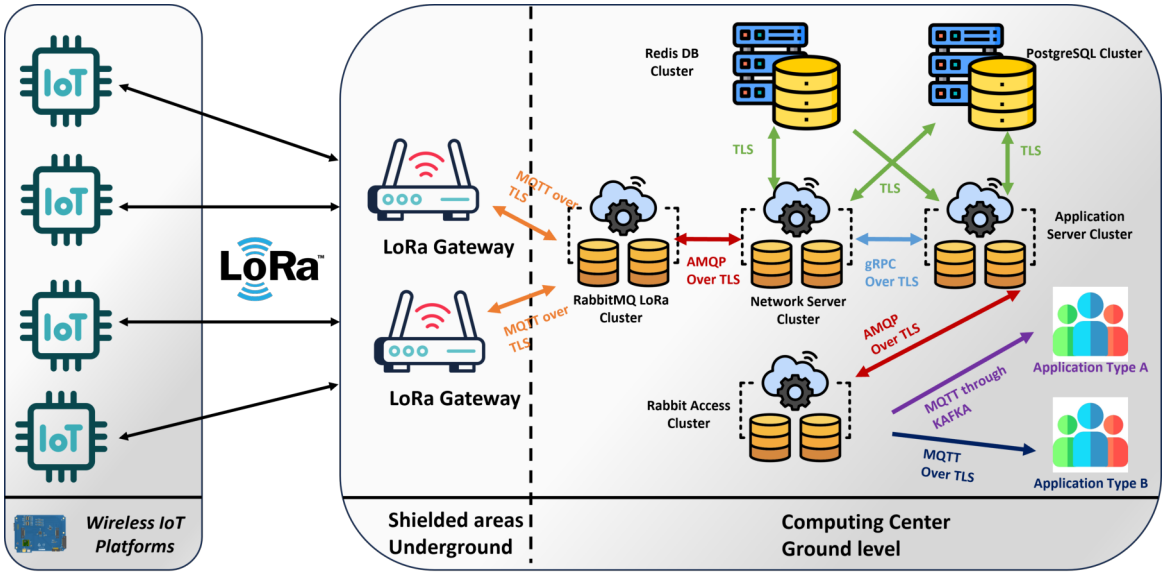


Figure 5.12: CERN LPWAN network architecture.

The LPWAN service, including the gateway software, is provisioned, managed, monitored, and maintained by standard CERN IT services. The architecture is depicted in Fig. 5.12, and detailed below:

- Messaging between the different parts of the service is handled by three different RabbitMQ clusters. To isolate each part of the architecture, they have their own firewall rules and Access Control Lists (ACLs).
- The LoRaWAN service uses two database clusters: one with PostgreSQL and one with Redis to store volatile information.
- A Chirsptack cluster was designed by installing three parallel instances, each running both a network server and an application server and exchanging data with each other. All the instances are connected to the same PostgreSQL and Redis database, which allows for the deduplication of messages and the high availability of the system.

With a dedicated Command Line Interface (CLI), Representational State Transfer Application Programming Interface (REST API), and web tools, LoRaWAN users can deploy and control their devices autonomously. Depending on their integration needs, they can consume the data produced by their sensors in two different ways. They can either interface their customs systems using Message Queuing Telemetry Transport (MQTT) (This is how WinCC OA was integrated into the LPWAN networks of CERN's industrial control systems) or they can connect using Kafka. This latter method is used by the Wireless IoT and is presented in Section 5.3.2.

### 5.3.2 Network Architecture: Data Logging and Configuration at CERN

The LoRaWAN service data flow is captured by a fairly standard data streaming workflow centered on Apache Kafka technologies, as shown in Fig. 5.13. At CERN, this infrastructure has multiple uses and has applications beyond the IoT.

Generic IoT application data is retrieved from the LoRaWAN NS using MQTT and copied to Apache Kafka using Kafka Connect. This data is multiplexed by Kafka Streams into dedicated Kafka topics with different ACLs for permissions. A second pipeline ingests, validates, and decodes device payloads into different decoded Kafka topics using Kafka Streams. After decoding, Kafka Connect moves the data to relational (Oracle, Mysql, PostgreSQL), time-series (InfluxDB), or big data (Apache Hadoop HDFS) storage. Projects may consume data from all parts of the infrastructure, including reading directly from Kafka, decoding from intermediate raw topics or decoded topics, or further enriching this data. Others may decide to link custom applications to the final data repositories, or just use Grafana to create monitoring dashboards that target any of these data stores.

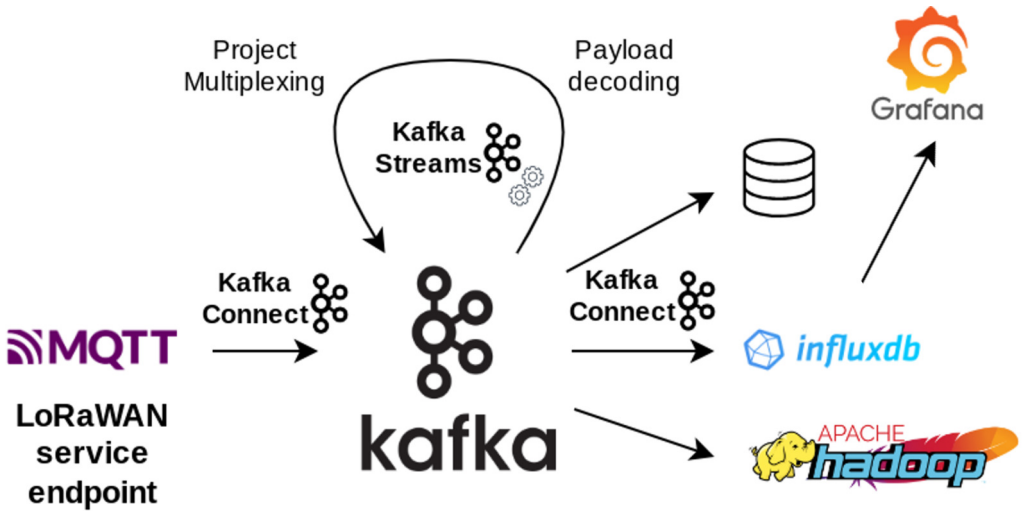


Figure 5.13: Block diagram of the technologies and architecture used for data transformation and streaming.

### 5.3.3 Wireless IoT Integration in CERN Network

Nowadays, the Wireless IoT is fully integrated into the CERN LoRaWAN network. A specific LoRa Topic is defined for each system application and REST APIs can be used to register new devices, remove them, and send customized downlink messages. The frames received by the NS and published via MQTT, are collected and decoded via Kafka and stored in a dedicated InfluxDB database. The process is summarized in Fig. 5.14.

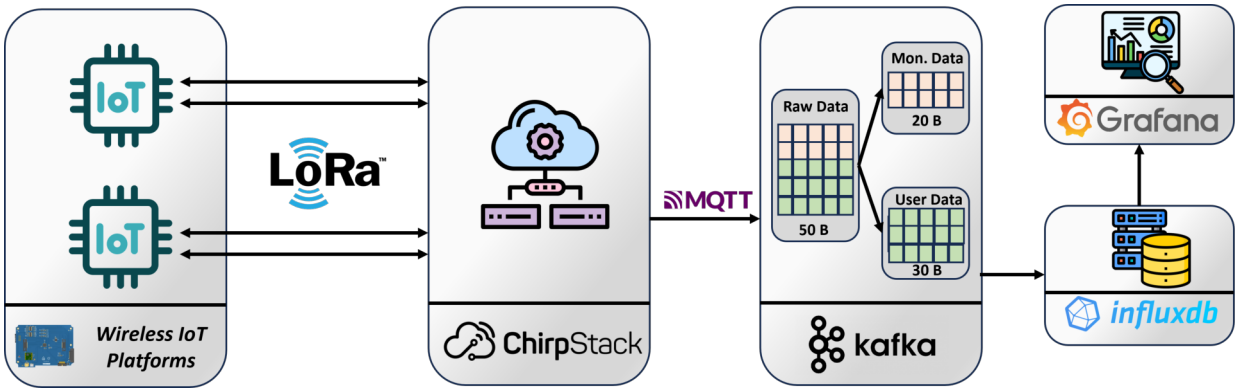


Figure 5.14: Wireless IoT integration in the CERN LoRaWAN Network.

In addition to the payload, the LoRa Transmission Information (i.e. Gateway ID, RSSI, Signal to Noise Ratio (SNR), etc.) provided by the NS and available in the MQTT frames, are decoded and stored in the same topic. The Wireless IoT payload is made of fifty bytes, limited by the constraints of the CERN network. Twenty of these are used by the application to transmit control information and are application-independent (e.g. power rail or functionality monitoring). The others depend on the Wireless IoT application and thus, are

available to the User for custom implementation. These bytes can also be used to store previous measurements to cope with possible packet loss (intra-packet redundancy), depending on the application needs, requirements, and the size of the User payload. This mechanism improves the reliability of the application and has already been implemented in a non-radiation tolerant application based on Wireless IoT [141].


(a) Transmission status monitoring Module


(b) On Board Monitoring Module


(c) SRAM Measurements Module

Figure 5.15: Snapshots of the different Grafana modules provided as examples.

A customized Grafana interface, developed during this doctoral work and depicted in Fig. 5.15, is used to visualize the Wireless IoT measurements and LoRa Transmission Information stored in the dedicated InfluxDB. The Grafana interface is divided into four modules for efficient navigation and information access. The first Module (Fig. 5.15a) provides insights into wireless communication functionalities. The second module (Fig. 5.15b) offers information on the general status of on board peripherals and batteries. The last two modules provide insights into TID and fluence measurements. In Fig. 5.15c, the module dedi-

cated to SRAM Measurements is given as an example. When installed in the accelerator, this interface is used to quickly verify that the system is functioning correctly and to check the system functionalities during their operation.

## 5.4 Operational Insights: Wireless IoT Deployment in the LHC

In 2023, 19 Wireless IoT platforms with LoRa wireless-enabled capabilities were installed in the LHC. Most of the installations were not feasible with RadMon due to limited access time, cable manufacturing costs, and difficulties in integrating new devices into the existing network. In some specific cases, the need for higher resolution and B-field resilience were also requirements not met by RadMon. In particular, the installation specifications ranged from simple analysis of the radiation environment to the evaluation of complex shielding and the detection of beam losses in the LHC. The different locations where the platforms were deployed are shown in Fig. 5.16.

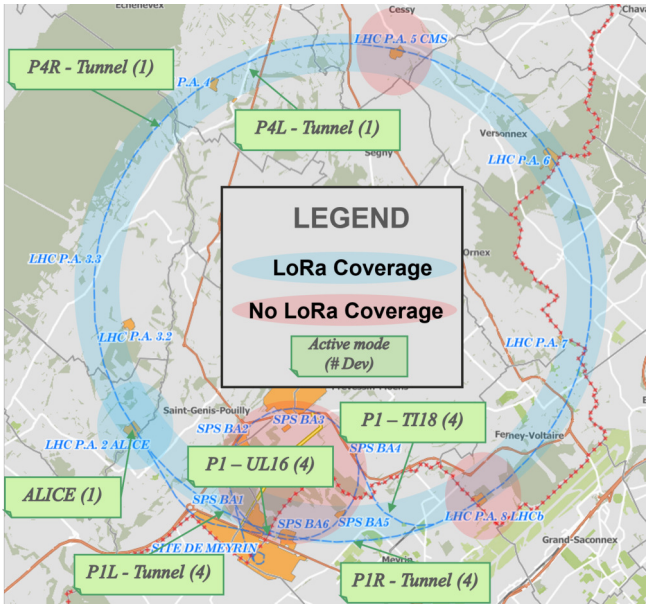


Figure 5.16: The different areas where Wireless IoT has been deployed. In light blue is the area where LoRa coverage was available during 2023 (LHC and ALICE). The other accelerators and experiments will be covered during Year-End Technical Stop (YETS) 2023 when radiating cables will also be deployed there.

### 5.4.1 Scattering and Neutrino Detector at the LHC

The Scattering and Neutrino Detector at the LHC (SND@LHC) [142] is designed to investigate neutrinos and is currently installed in the LHC. Neutrinos are fundamental particles with no electric charge and negligible mass. Although neutrinos are produced in huge numbers in particle colliders, their direct observation in a collider has never been possible because of their weak interaction with matter and no detection by typical collider detectors. Most of the LHC neutrinos are in an energy range where their interactions have not been

investigated. This makes their study all the more fascinating. The SND@LHC consists of a neutrino target and a device for measuring the neutrino energy and detecting muons (produced by the neutrino interaction with the target) in the downstream position. The detector is localized underground in an unused gallery (LHC-P1 TI18) which connects LHC to SPS. Positioned at a small distance from the beam line of the LHC, it will be capable of detecting neutrinos generated in the LHC collisions at small angles with respect to the beam line. Several layers of shielding were added to protect the electronic equipment. The first concrete chicane is positioned between the tunnel entrance and the detector. The latter is contained in a Boron Carbide (B4C) cage. At the back of the detector, a rack with electronic equipment is shielded by another concrete wall.

It was requested to assess the radiation to electronics effects in this area and to evaluate the efficiency of the different shielding to see if more would be required. Using RadMon for this installation would have been complex (short installation time, high cable costs, difficult integration of new devices, higher resolution required). These limitations drove the Wireless IoT installations. In particular, as can be seen in Fig. 5.17 four Wireless IoT platforms were installed, covering the different locations: a) Wireless IoT 1 was installed before the first concrete chicane (Blue), b) Wireless IoT 2 between the first concrete chicane and the B4C Cage (Red), c) Wireless IoT 3 inside the B4C Cage (Green), d) Wireless IoT 4 after the last concrete wall, on the rack with the electronic equipment (Orange).

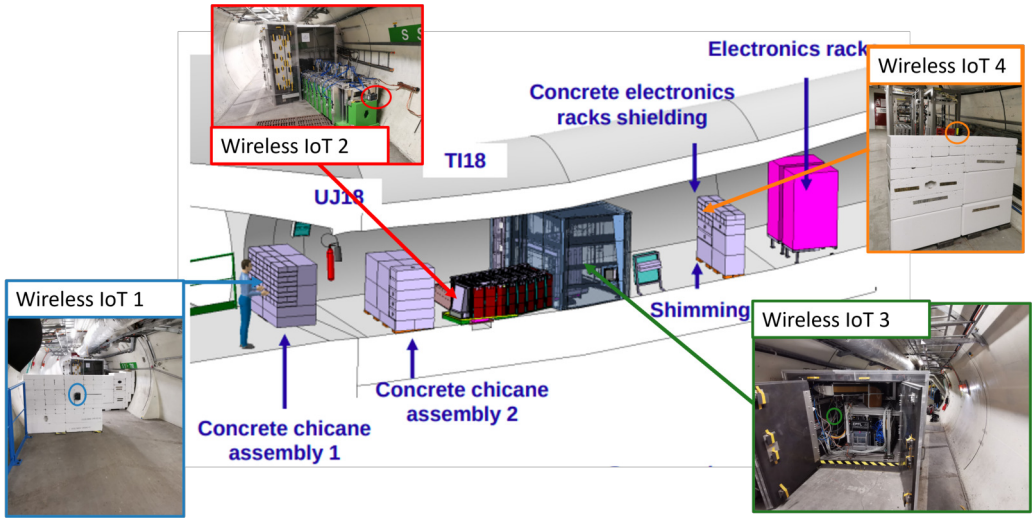


Figure 5.17: The positions of the different Wireless IoT platforms and shieldings installed around the SND@LHC detector are provided in this side view.

During the year of operation in this location (2023), the BatMons did not suffer from any particular problems. Several resets were observed, but these were caused by network un-

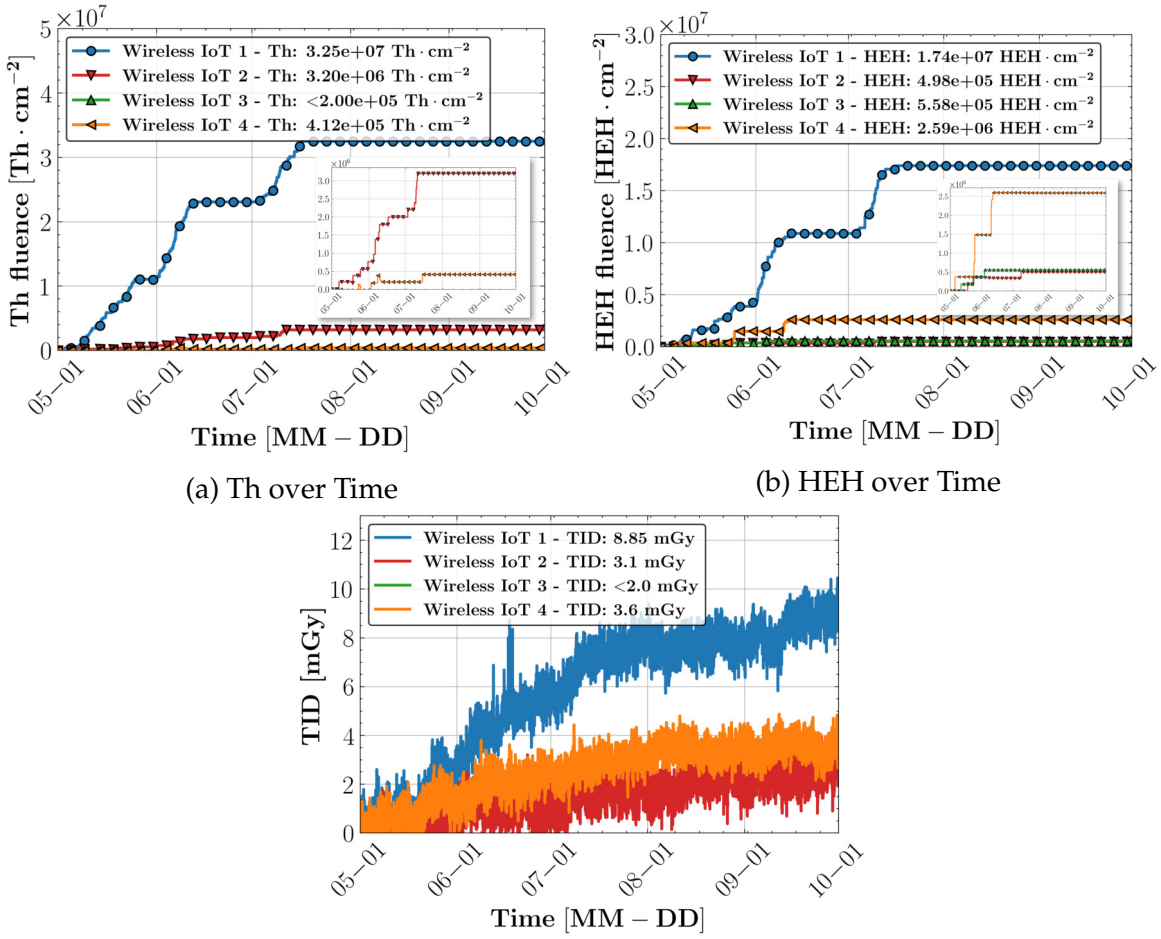


(a) Th over Time

(b) HEH over Time

(c) TID over Time

Figure 5.18: Results in terms of Th (Fig. 5.18a), HEH (Fig. 5.18b) and TID (Fig. 5.18c) are presented. Wireless IoT 3 - TID is not reported because its TID measurement was below the sensor resolution.

availability. The deployment allowed the shielding efficiency for the different positions to be determined. As can be seen in Fig. 5.18, the first shielding greatly reduces the radiation field. In particular, the HEH is reduced by a factor of about ~35. A similar value of HEH is obtained inside the B4C cage, which is an expected result since the B4C can only filter the thermal contribution and convert it into gamma rays. The higher HEH observed with Wireless IoT 4 may be due to the positioning of the platform, which is slightly higher than the concrete wall and therefore only partially shielded. As for the Th fluence, the contribution with respect to that experienced by Wireless IoT 1 is reduced by a factor of ~10 after the first concrete chicane and by a factor of ~78 on the electronic rack. Interesting results are also obtained inside the B4C cage, where no counts were observed on the Th sensor and the fluence is therefore below the resolution of the system ($2 \cdot 10^5\ Th \cdot cm^{-2}$), confirming the correct implementation of the B4C shielding. Finally, due to the higher resolution of the sen-

sor, the contribution of the TID can be assessed. In particular, negligible levels are observed before and after shielding. An interesting confirmation of what was observed for the HEH differences between Wireless IoT 2 and 4, is the slightly higher TID measured by the latter.

### 5.4.2 Experiment: ALICE

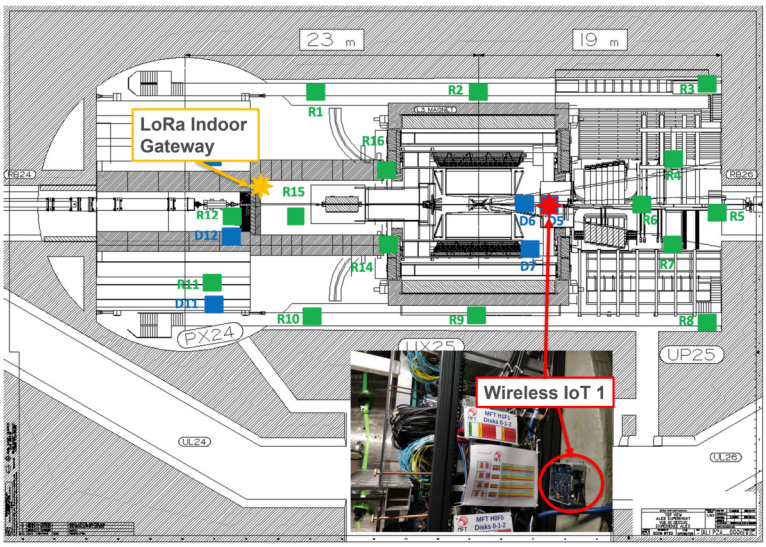


(a) ALICE Experiment Top View

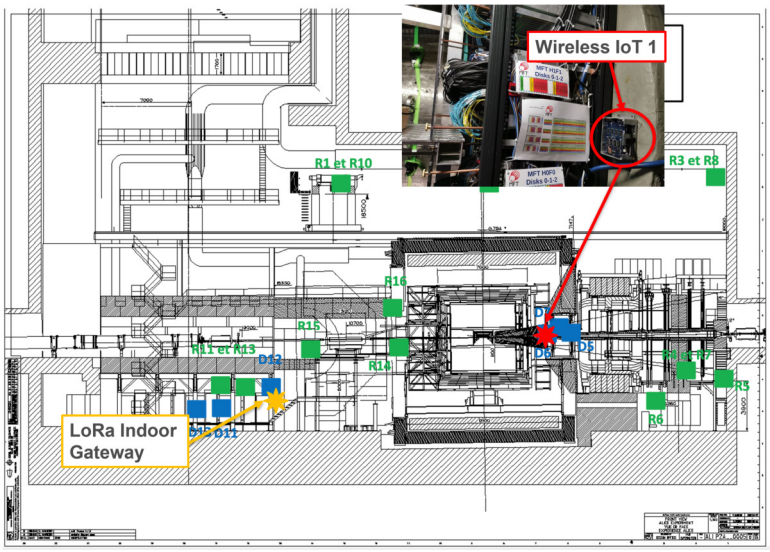


(b) ALICE Experiment Side View

Figure 5.19: The positions of the Wireless IoT platform and the LoRa Indoor Gateway installed in ALICE are depicted in its Side and Top View.

As discussed in Section 3.1.3, the use of RadMon in experimental areas can be rather complex due to the presence of magnetic fields. The requirement to install the RadMon inside the detector, where the B-field is ~300 mT, cannot be fulfilled by the latter instrument. RadMons are installed in the area of the experiment, but they are always placed far away

from the detector. However, it is still possible for this application to deport part of its Sensor Board, consisting of the TID and DD, close to the detector while keeping the rest of the system in a safe area in terms of B-field. As a result, the fluences at these locations cannot be evaluated.

The Wireless IoT platform enables this investigation. However, as the experiments were not yet covered by LoRa connection at the time of installation (no radiating cables), an Indoor LoRa Gateway was installed outside the detector, close to other electronic equipment, in an R2E safe zone. Instead, the wireless platform was installed inside the detector according to the user's requirements. The installation setup is depicted in Fig. 5.19.

During the installation period, the device worked properly without any unexpected failure or malfunction. From 30/06 to 21/07 2023, the LoRa gateway suffered a permanent failure and its functionality was only restored by a power cycle. The cumulative measurements feature allowed to reconstruct the TID and fluences after this period without transmissions. As shown in Fig. 5.20, the device allowed the assessment of fluences in this critical position. The TID measurement would not have been possible also with the deported module of the RadMon due to its insufficient resolution. These results validate and allow the use of the platform in the experimental areas, which from 2024 will be LoRa covered (deployment of radiating cables) and will not require the deployment of a specific gateway.

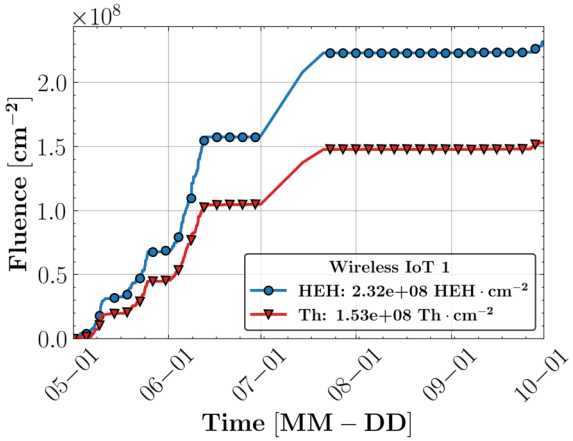


(a) HEH and Th over Time

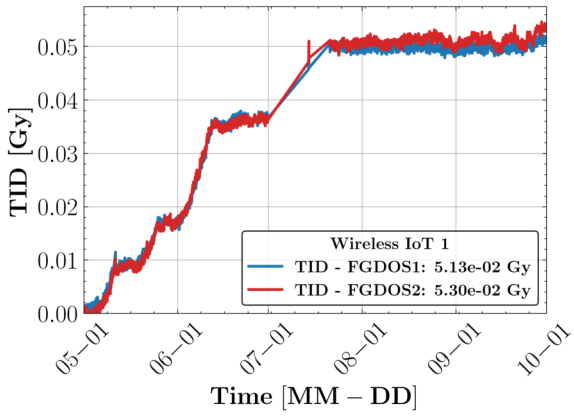


(b) TID over Time

Figure 5.20: The monitoring results in terms of fluences (Fig. 5.20a) and TID (Fig. 5.20b) are presented.

### 5.4.3 Beam Losses Position Detection in the LHC

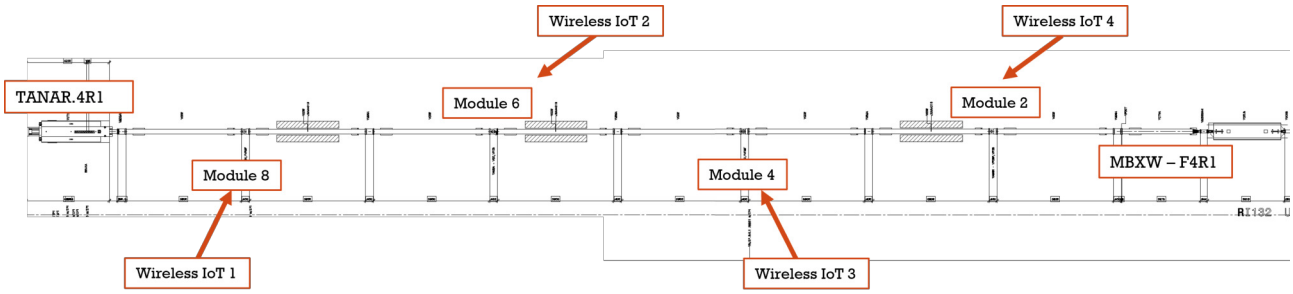


(a) LHC P1 Right Side - From TAN to MBXW: ~86 *m*

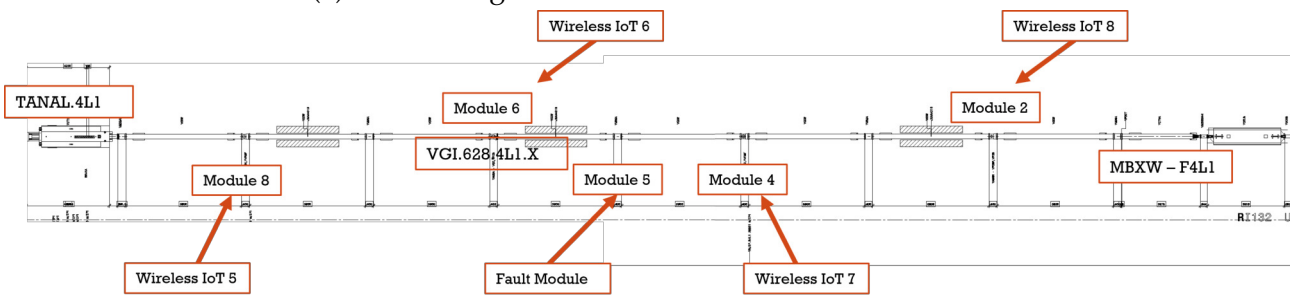


(b) LHC P1 Left Side - From TAN to MBXW: ~86 *m*

Figure 5.21: The positions of the eight Wireless IoT deployed in LHC P1 under different beam line segments or Module.

In May 2023, a beam loss problem was observed at the LHC. Normally, Beam Loss Monitor (BLM) data are used to identify the location of the source of the leak. However, the fault was located in a part of the LHC P1 that was not monitored by such systems at the time. Special intervention was required to identify the source of the problem. The deployment of the BLMs was not possible in a short time due to the unavailability of the cables and the time required for their deployment.

It was decided to take advantage of Wireless IoT platforms, which can be deployed in a few hours thanks to the absence of cables and the simplicity of integrating new devices into the LoRa infrastructure. This is the time that is required for the programming, configuration, and installation of the devices. Eight Wireless IoT platforms were deployed: four on the right-hand side of the Point 1 Tunnel (Fig. 5.21a) and the others on the left-hand side (Fig. 5.21b). The systems were distributed under different beam line segments, also called Modules. Thanks to the improved resolution of the TID platform, it was possible to identify the area where the losses were produced. In particular, the TID measured during the LHC filling phase (Section 2.3.2) was analyzed. As can be seen in Fig. 5.22 (Right Column), on the right side of P1 the TID measured (red and blue lines) during the LHC Fill number 8836 was below the resolution. Therefore, this area was excluded as a possible source of the problem.

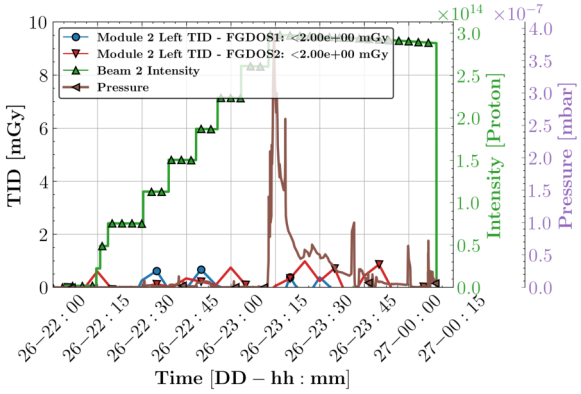


(a) Wireless IoT 8 - Module 2 Left

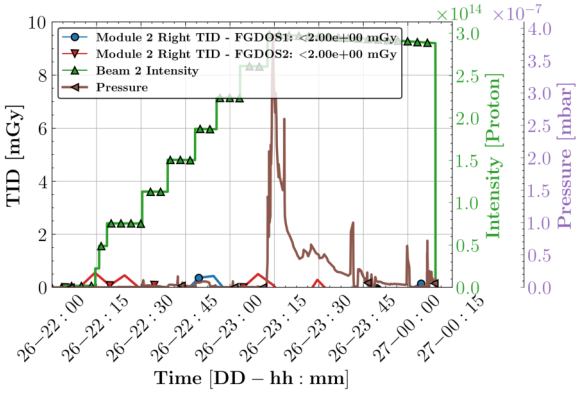


(b) Wireless IoT 4 - Module 2 Right

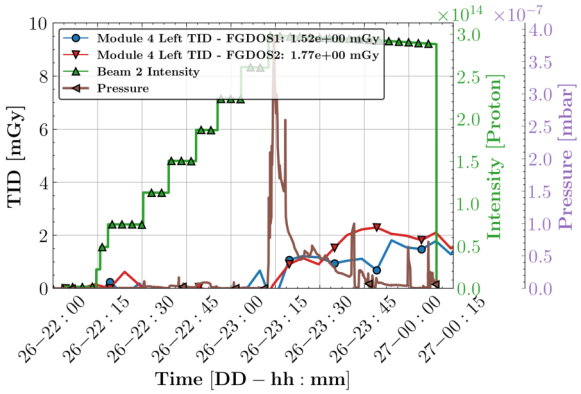


(c) Wireless IoT 7 - Module 4 Left

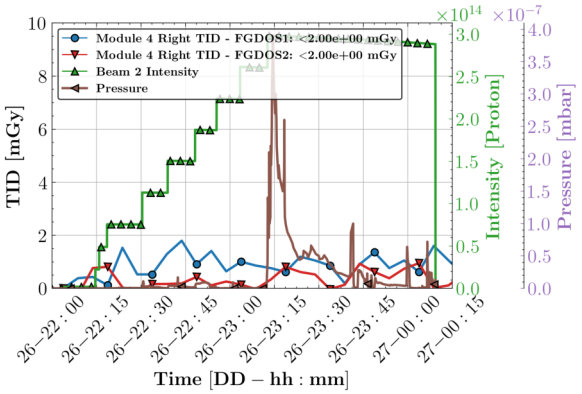


(d) Wireless IoT 3 - Module 4 Right

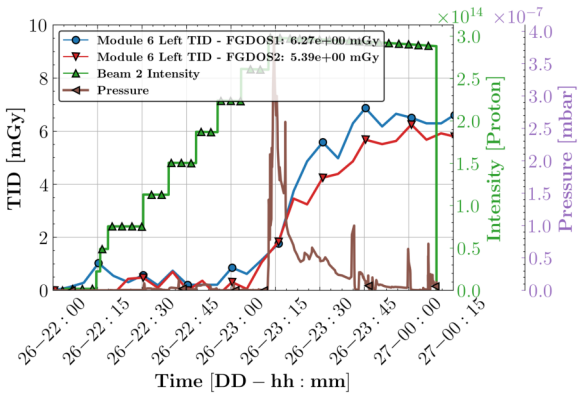


(e) Wireless IoT 6 - Module 6 Left

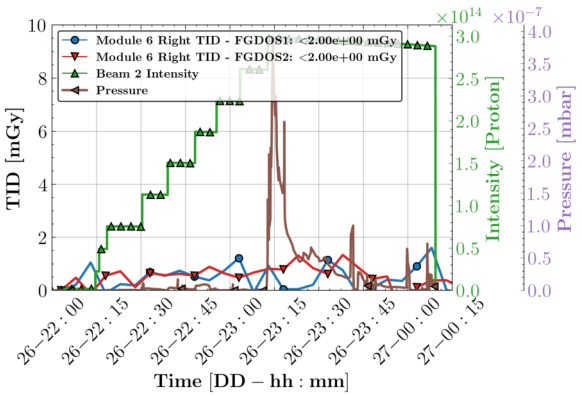


(f) Wireless IoT 2 - Module 6 Right

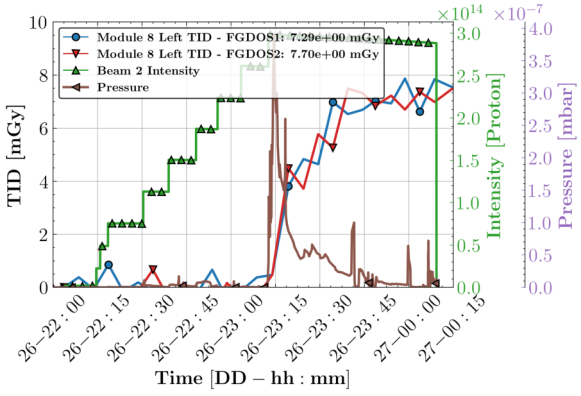


(g) Wireless IoT 5 - Module 8 Left

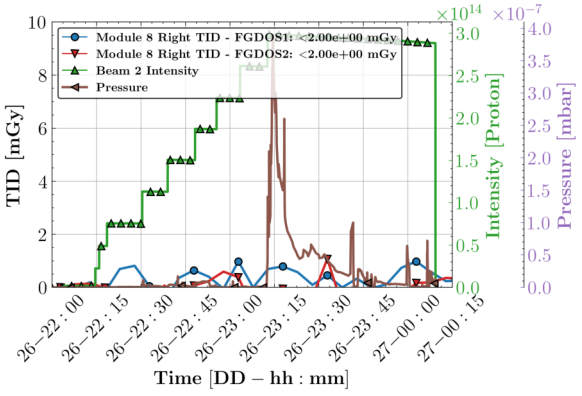


(h) Wireless IoT 1 - Module 8 Right

Figure 5.22: The TID measured by the different Wireless IoT is shown about the Fill 8836. The beam intensity and pressure measured during the degassing process are also shown.

On the other hand, the TID contributions on the left side were not negligible. In particular, it can be seen that below Module 2 (Fig. 5.22a), the TID values were still below the resolution of the sensor, while higher values were recorded below Modules 4 (Fig. 5.22c), 6 (Fig. 5.22e) and 8 (Fig. 5.22g). The area enclosed by these Modules was marked as the source of the fault. Next, an X-ray scan of the Modules belonging to this area allowed identifying the fault segment (Module 5 - Fig. 5.21b), and the damaged part (circular standard RF finger) was replaced.

The application's quick deployment capability and advanced resolution allowed the system to circumscribe the fault area in less than a few hours, significantly reducing accelerator downtime.

### 5.4.4 Wireless Performances of the IoT Platform in the LHC

The different deployments of 2023, allowed the evaluation of Wireless performance in operation under different accelerator scenarios, such as experiments (ALICE's cave), alcoves (ULs and TI), and near the beam line (Tunnel). Table 5.2 reports different LoRa Key Performance Indicators (KPIs) extrapolated from the Wireless IoT platform for the different locations. The LoRa Transmission Information stored in the influxdb allowed the evaluation of several metrics such as lost packets, device unavailability, and average RSSI and SNR. This analysis covers the period from 01/04 to 01/08/2023. In particular, for P1R-Tunnel and P1L-Tunnel the installation lasted twenty days and thus, this shorter period was considered.

Normally, the transmission period for the LHC installation is one hour, but for the higher resolution requirements, the P1-TI18 and P1-Tunnel installations used a shorter period (thirty and five minutes respectively). This motivates the higher number of packets transmitted for these positions. On average, the packet loss rate was 0.4 % of the total number of packets sent.

The device in P4R-Tunnel exhibits the worst behaviour. The reason for the higher packet loss ratio is mainly due to the low RSSI which characterized this position. This is usually the case when a device is far away or shielded from the nearest gateway.

The unavailability reported in Table 5.2 does not take into account periods of network unavailability that are not related to the performance of the equipment. In particular, it cumulates the downtime when a packet is lost and the time required for the device to reconnect after a reset. For the first contribution, the measurement period plays a key role:

the longer the measurement period used, the greater the impact on application downtime. In this first deployment, packet losses were the main cause of downtime. For critical applications, consideration should be given to reducing the measurement period as much as possible to improve this ratio and to increase the LoRa Spreading Factor used when the RSSI is below -110 $dBm$ and the SNR below 3 $dB$.

Table 5.2: KPIs measured from IoT platforms for different LHC areas (Experiment, Alcoves, Tunnel). All the devices were configured to start joining from Spreading Factor 10 and increasing it by one in case of three failed attempts to join. The devices joined most of the time with Spreading Factor 10.

| **Position** | **Packet Transmitted** | **Packet Lost [%]** | **Device Downtime [Minute]** | **Device Unavailability [%]** | **Avg. SNR [dB]** | **Avg. RSSI [dBm]** |
|---|---|---|---|---|---|---|
| ALICE | 2421 | 0.2 | 398 | 0.18 | 9.02 | -89 |
| P1 - TI18 | 5792 | 0.4 | 879 | 0.50 | 6.5 | -100 |
| P1 - UL16 | 2046 | 0 | 13 | 0.01 | 2.93 | -112 |
| P1L - Tunnel | 2276 | 0.6 | 17 | 0.15 | 3.31 | -112 |
| P1R - Tunnel | 2249 | 0.6 | 24 | 0.81 | 5.49 | -107 |
| P4L - Tunnel | 2907 | 0.1 | 207 | 0.12 | 2.65 | -98 |
| P4R - Tunnel | 2907 | 1.3 | 2646 | 1.51 | 2.65 | -117 |

## 5.5 Wireless IoT: Multi-application IoT Platform for Harsh Environments

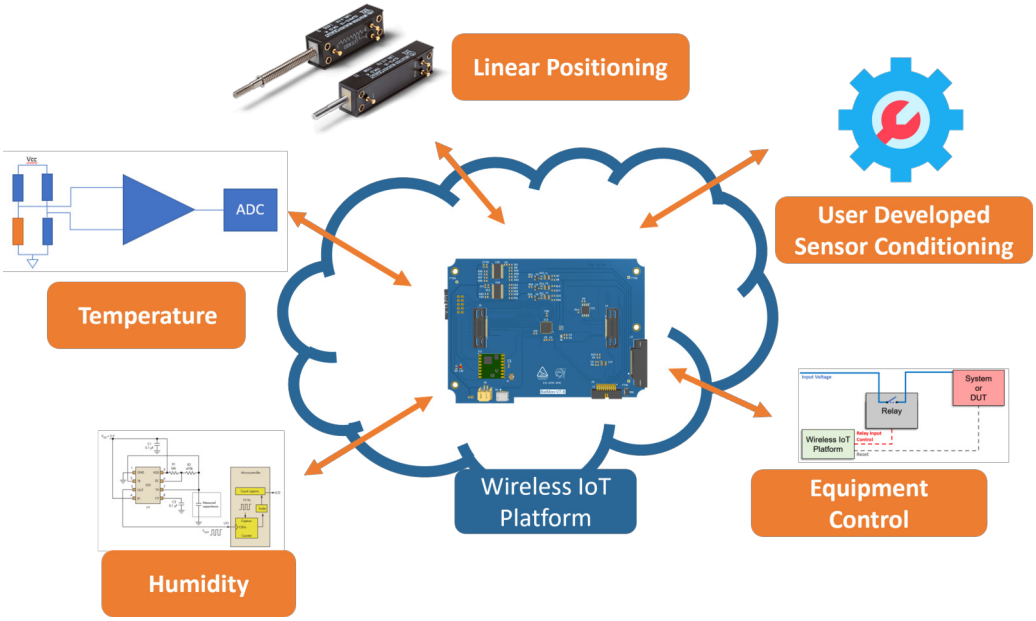


Figure 5.23: A summary of current applications that can be exploited by Wireless IoT is provided. Allowing users to develop their own sensor conditioning board opens up an unlimited number of possible applications and IoT monitoring solutions for the LHC.

As described in Section 3.3, the platform is designed to be modular, so that any general user can take advantage of the Main-Board design and develop their independent application through a different Sensor Board. At the same time, the use of MCUs and modular firmware allows users to easily integrate the control of their sensors into the existing Wireless IoT firmware, using all the mitigation schemes already implemented.

All these features open the way to an unlimited number of possible applications that can be easily implemented with the current design and integrated into the CERN network, as was done for the Wireless IoT - Radiation Monitoring application and after radiation testing, deployed in the accelerator. This section presents and discusses some of the possible applications shown in Fig. 5.23.

### 5.5.1 Position Sensing

Applications requiring accurate position feedback and control often use analog position sensing, particularly using potentiometers. Such boards are capable of processing the variable resistance of potentiometers into a significant amount of data representing the position

or movement of various machine elements. An analog Sensor Board based on a potentiometer as a sensor can provide independent or redundant readings of these positions, assuring that the machine is operating within the desired parameters and providing a backup measurement system in the event of primary sensor failure.

To address these needs, the Wireless IoT platform can be interfaced with an analog Sensor Board based on a potentiometer. This board would be responsible for the measurement of the resistance of a single potentiometer and its translation into wireless uplink messages. The board could be adapted to linear and rotary potentiometers. A wide range of sensor integration would be possible by adjusting the resistor on board and thus, the potentiometer sensing ranges.

### 5.5.2 Temperature and Humidity Sensing


(a) Temperature Readout Circuitry

(b) Humidity Readout Circuitry

Figure 5.24: Block Diagram for the readout circuitry implemented for Temperature (Fig. 5.24a), and Humidity (Fig. 5.24b) monitoring.

In electronics and sensor applications, environmental monitoring, particularly temperature and humidity sensing, is a critical application. These environmental factors can have a distorting effect on sensor readings, necessitating the use of calibration and compensation algorithms. In the particle accelerator context, a wide range of precision sensors, from measuring instruments to beam intercepting, are impacted by these external conditions. In addition, electronic reliability is primarily affected by temperature and humidity. To prevent potential equipment failure, monitoring these parameters ensures that operating conditions are in line with reliability calculations. For instance, tracking temperature and humidity within equipment racks or near specific boards is critical to system performance. In cases where radiation shielding is used, localized temperature measurements are essential to ensure that the shielding doesn't unintentionally raise temperatures outside design specifications.

To address these needs, a Temperature and Humidity (TH) Sensor Board has been designed and integrated within the Wireless IoT platform. This TH board has been designed to ensure radiation resistance by using components that are radiation resistant. Suitable for the above applications thanks to its dimension and flexibility, it can measure temperatures from -23.61 to 75.33 $^{\circ}C$ and relative humidity from 5% to 95 %. The conditioning circuits are depicted in Fig. 5.24. The temperature is measured using a PT100 in a Wheatstone bridge configuration, while a capacitive humidity sensor (proven to be rad-hard) is used for humidity monitoring. The readout circuit consists of a 555 timer in astable mode, which converts the capacitive value to a square wave signal. The advantages of this implementation are low power consumption due to the very short settling time and the ability to turn off the readout circuitry when the device is in sleep mode. The readout circuitry can only be turned on when measurements are being taken. This circuitry can be reused for other analog sensors. The radiation tolerance of the Sensor Board has been tested at CHARM. To evaluate the effects of system lifetime, LDR, and impact of DDEF/TID ratio, the TH Application was tested in CHARM-G0 and CHARM-Conveyer15. The radiation monitoring in the two positions was provided using the RadMon. The two test setups are depicted in Fig. 5.25.

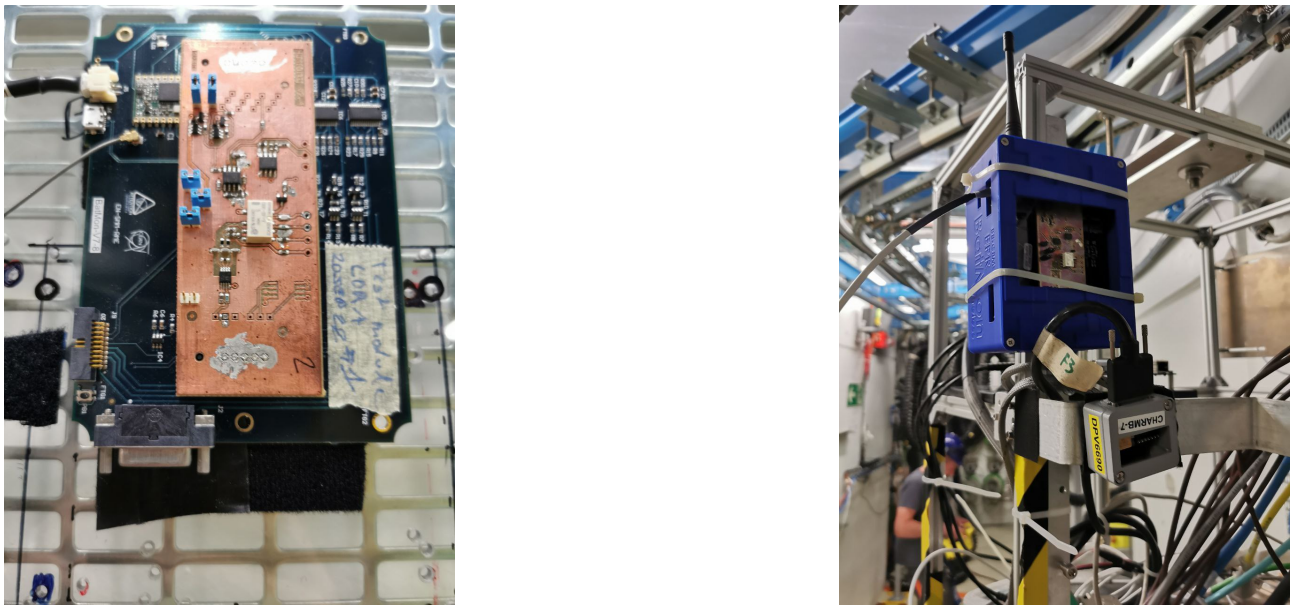

(a) CHARM-G0 (b) CHARM-Conveyer15

Figure 5.25: The Wireless IoT TH application tested at CHARM-G0 (Fig. 5.25a) and CHARM-Conveyer15 (Fig. 5.25b).

The test in the CHARM-Conveyer15 lasted several months and the results are shown in Fig. 5.26. Regarding the temperature monitoring, the readout circuit withstood 1450 $Gy$ with a DDEF/TID ratio of $1.3 \cdot 10^{10}$ 1 $MeV\ neq. \cdot cm^{-2} \cdot Gy^{-1}$ without any failure as

shown in Fig. 5.26a. Since the lifetime of the Wireless IoT Main-board was lower than that of the temperature sensor, different Main-boards need to be used to achieve a TID greater than 1 *kGy* (Application target). In particular, the first Main-board stopped working at 260 *Gy*, the second at 228 *Gy* (but had already accumulated 76 *Gy* in other tests) and the third was functional up to 531 *Gy*. Due to the unavailability of boards, an old board from the Wireless IoT prototype batch was used for Main-board 3. This board may be assembled with components belonging to different batches compared to the one mounted on production boards. The higher lifetime achieved may be due to a lot-to-lot variation in the Ext WTD response.

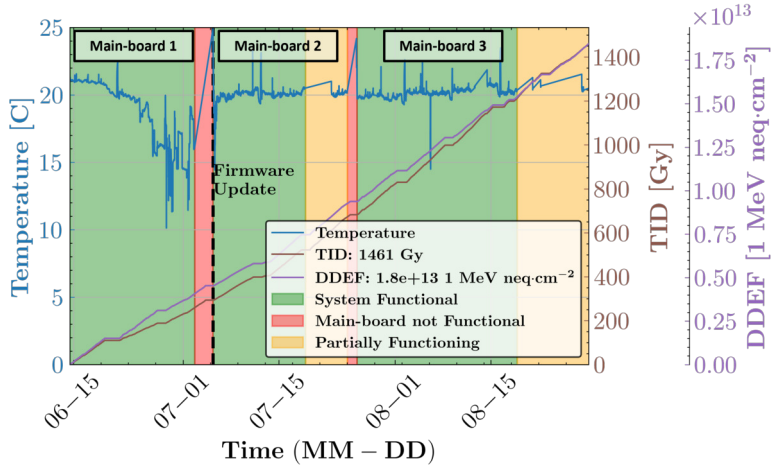


(a) Temperature Over Time

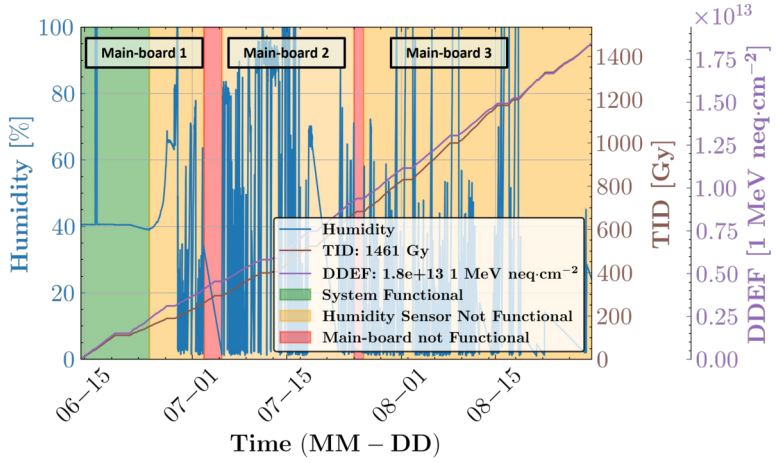


(b) Humidity Over Time

Figure 5.26: The Temperature and Humidity measured through the TH Sensor Board mounted on the Wireless IoT Main-Board during the test in CHARM-Conveyer15.

When the system was considered non-functional (period highlighted in red), the Main-board was replaced, keeping the irradiated Sensor Board. In particular, it can be seen that at the end of the life of the second and third boards, the reliability of the system was reduced.

In these cases, the WTD Ext did not work. After annealing and power cycling, the system recovered but stopped working after a few hours. During these periods of partial functioning (highlighted in orange), it was still possible to evaluate the sensor functionalities.

The temperature was always around 21 $^{\circ}C$ (The temperature in CHARM is stable for testing purposes) during the test, increasing during the weekly CHARM access. As visible in Fig. 5.26a, during the first test period, the temperature reading was not stable (Main-board 1). This was due to a firmware problem, which was resolved when Main-board 2 was used. For the humidity monitoring, the readout circuitry stopped working properly after 151 $Gy$ as depicted in Fig. 5.26b. As can be seen, the reading started to ramp up over time due to a failure of the 555 timer used. This solution is below the lifetime of the system and therefore, a new candidate to improve the lifetime of the sensor will be investigated.

In parallel a test in CHARM-G0 position was also carried out. The results of the test are depicted in Fig. 5.27.

Also in this case no malfunctioning was observed on the Main-board and the temperature sensor part that withstood 386 $Gy$ with a DDEF/TID ratio of $5.8 \cdot 10^{10}$ 1 $MeV\ neq. \cdot cm^{-2} \cdot Gy^{-1}$. On the other hand, the 555 timer used for Humidity monitoring, failed at 151 $Gy$. It is possible to conclude that the lifetime of the Humidity monitoring board does not depend on the DDEF/TID ratio experienced and is not impacted by LDR.

Another interesting observation was that there was no increase in power consumption during either test. As a result, the battery life of the system equipped with this sensor board is independent of the dose rate of the environment in which the system is used. Finally, during the test in G0, one system permanent failure was observed, recovered only through a power cycle. This was the only event observed over an HEH fluence of $1.27 \cdot 10^{13}\ cm^{-2}$. The impact of having a lower permanent failure cross-section when a lower duty cycle is used (in this case 2 %), has been discussed in Section 5.1.

### 5.5.3 Application Control: Increase Reliability with ON-OFF Switching

Digital control is essential in applications where remote system management is required, particularly through Input Output (IO) boards. Such boards allow the control of electronic systems, enabling the switching of power states or the initiation of a system restart. In the particle accelerator context, such digital IO boards can facilitate remote intervention, enabling system resets or power cycling, and mitigating radiation-induced failures.

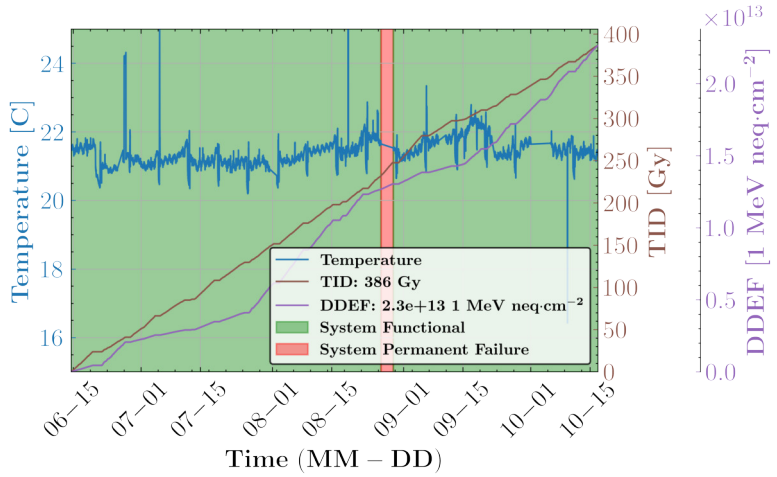


(a) Temperature Over Time

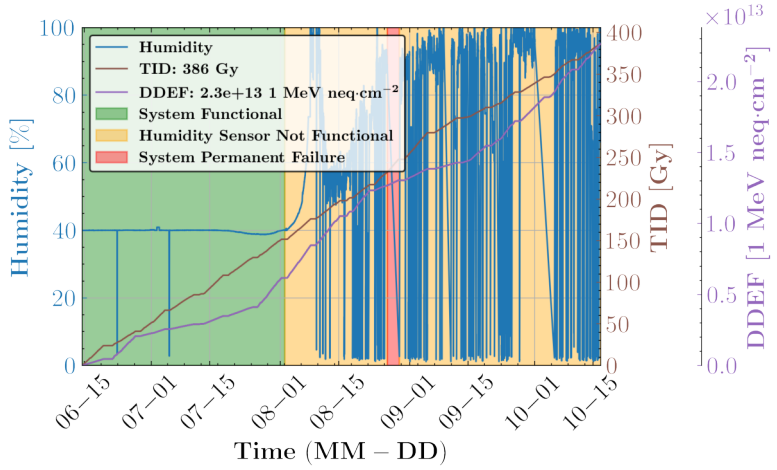


(b) Humidity Over Time

Figure 5.27: The Temperature and Humidity measured through the TH Sensor Board mounted on the Wireless IoT Main-Board during the test in CHARM-G0.

To satisfy these requirements, the Wireless IoT can provide through its deported connector, Digital and Analog IOs that can be used in parallel with the monitoring application. To test this possible application environment, the Wireless IoT platform was used to remotely control a commercial 4G router undergoing radiation testing, resetting the router when a malfunction was detected. In particular, the IO board was connected as input to a high power relay placed in between the router voltage input and the power source as shown in Fig. 5.28a. Being the system a commercial device, the test was carried in the G0 position and the setup is depicted in Fig. 5.28b. Since the commercial router has very limited failure observability, its functionalities were monitored through ping operation. In particular, a ping was sent every 10 $s$. When the system was not able to reply to the first ping request a second check was performed after 20 seconds. When two consecutive pings failed, a downlink message was queued which content was forcing the Wireless IoT to open the switch used

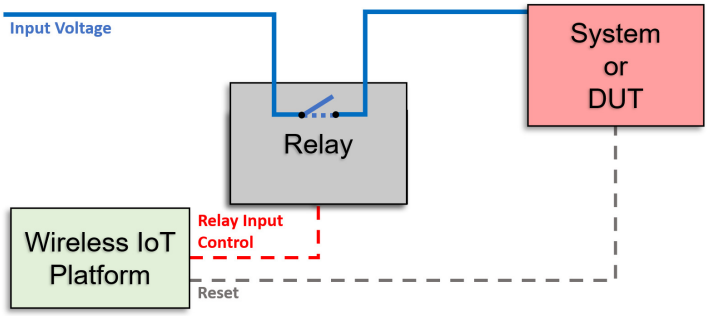


(a) Conceptual Diagram Remote Controlling

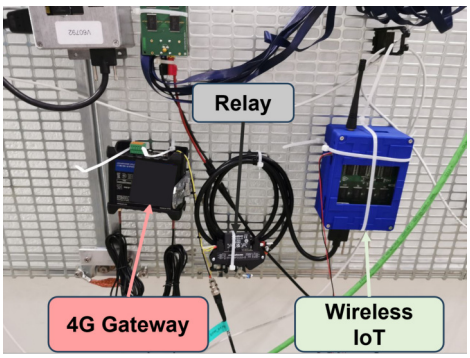


(b) 4G Gateway test setup

Figure 5.28: The conceptual diagram for remote controlling using the Wireless IoT (Fig. 5.28a), and its electrical implementation through testing in CHARM-G0 (Fig. 5.28b).

for the remote controlling of the gateway and in this way power cycling the router.

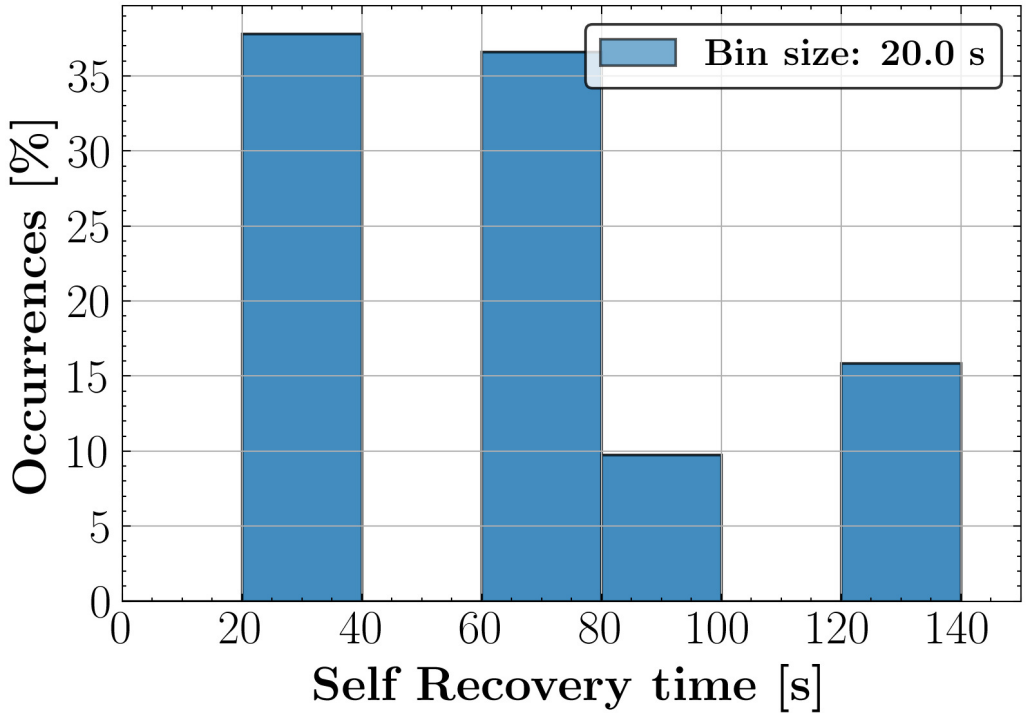


Figure 5.29: Histogram of the 4G router self-recovery time exhibit during CHARM-G0 test.

After the first days of the test, it was observed that the device was able to self-recover its functionalities but the time required for the recovery was not fixed. For this reason, the firmware used to remotely check the status of the gateway was changed on 15/09, so that it had a timeout of 120 $s$ instead of only 20 $s$ after the failure of the first ping interaction. Specifically during this time, the status of the gateway was continuously checked via ping. If the device responded during this time, the device was considered self-recovered and the time spent was saved. On the other hand, if the device was still not functional after this time, the gateway was reset through the use of the Wireless IoT platform by sending a downlink

message. Considering the fluence cumulated in this period when the new control firmware was used ($8.6 \cdot 10^9$ $HEH \cdot cm^{-2}$), the SEFI cross-section of the system is $3.25 \cdot 10^{-9}$ $\pm 1.74 \cdot 10^{-9}$ $cm^2$. In particular, it was possible to observe that most of the time the system was able to self-recover in a time between 20 and 80 $s$ as visible in Fig. 5.29.

On 16/09 the device stopped working and the power cycles attempted were ineffective. As visible in Fig. 5.30, it withstood 5.56 $Gy$ and no SEL were observed showing a cross-section to SEL $< 1.94 \cdot 10^{-10}$ $cm^2$.

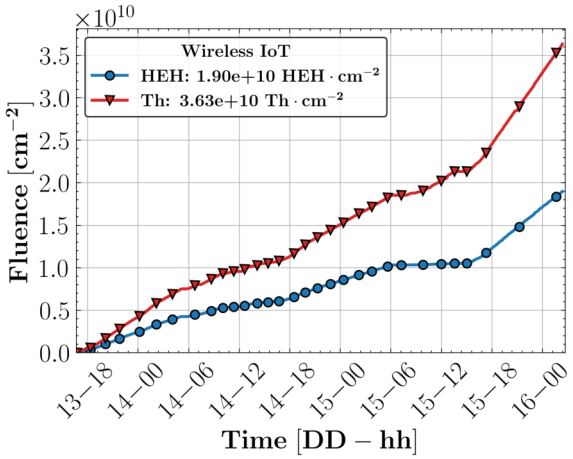


(a) HEH and Th fluence over Time

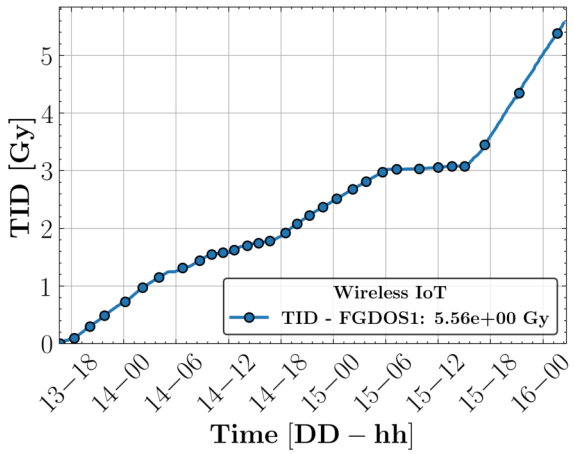


(b) TID over Time

Figure 5.30: The fluences (Fig. 5.30a) and TID (Fig. 5.30b) measured by the Wireless IoT during the 4G router Test in CHARM-G0.

This test showed that the Wireless IoT thanks to its radiation tolerance, can be used for radiation testing of other systems but in particular it can be capable of increasing the reliability and the availability of other systems during operation. Thanks to its downlink capabilities and higher operational availability, the platform can restore gateway functionality in the event of failures lasting more than 140 $s$, thus improving its performance under irradiation. This result opens up a new possibility for the use of commercial systems inside the accelerator. Less reliable devices, such as the commercial router described, can be made more reliable by remote control from an application with a much smaller cross-section. Furthermore, because of the higher reliability achieved, the use of a low data rate communication protocol such as LoRa, when used for remote control, may allow higher data rate but less reliable protocols to be used in the particle accelerator context. This result could be an important breakthrough for FCC accelerator operations, where there is a need to reduce the use of cables and increase the number of commercial systems to save costs.

## 5.6 Chapter Summary

In the presented chapter, the validation process of the Wireless IoT was concluded, through the analysis of its capabilities from an operational point of view (Radiation Monitoring, Deployment in the accelerator, and Multi-Application Platform). While in Chapters 3 and 4, the validation mainly concerned the reliability and availability aspects of the application, this chapter validated its functionality from an operational point of view (e.g. Measurement Quality, fast deployment capability). However, even in this chapter, it was possible to highlight certain considerations regarding the reliability aspects of the application.

The first part of the chapter discussed the choice of the best hardware and software solution that could be implemented to store the measurements cumulatively. This choice has a direct impact on the operability of the system from a radiation monitoring point of view, since, as explained in Section 5.1, in case of network unavailability, if the measurements are not cumulative, the final measurement may be underestimated. The analysis of the best choice between two possible hardware solutions was carried out using a further radiation test in CHARM-R10. This test not only showed that the External Flash memory was the more reliable solution compared to the internal one of the MCU but also revealed a dependency of direct proportionality between the duty cycle used and the permanent failure cross-section of the system. This last discovery provided important insights into the future use of the system for other applications (low duty cycle and therefore low cross-section) and possible hardware modifications to improve this characteristic for the radiation monitoring application.

Once the best solution for storing the measurements had been identified, validation from a measurement point of view came into focus. The problem of the greater sensitivity of the HEH sensor (CY62167GE30) to intermediate neutrons (0.1-10 $MeV$) was introduced and quantified through a calibration campaign at these energies carried out at PTB and presented in Section 5.2.1. The results made it possible to assess the higher sensitivity to the neutron of this energy spectrum compared to a generic lot of CY62157EV30 (HEH sensor used in RadMon), also for the Wireless IoT production Lot (1943).

To quantify the impact of this increased sensitivity, tests were carried out in different CHARM positions using RadMon as a reference. A progressive approach was taken, moving from environments dominated by hadrons of different species generated by the interaction of the beam with the target in zones (R10-R5) to positions where, due to the presence

of concrete walls surrounding the structure, the spectrum is more dominated by neutrons and there is greater thermalization (G0). The analyses, presented in Sections 5.2.2 - 5.2.4, demonstrated the compatibility of the Wireless IoT measurements with those of RadMon, at the positions of greatest interest and representative of the LHC (R10 - RRs, R5 and G0 - UJs). Furthermore, through an analysis of the intra-lot sensor variation presented in Section 5.2.5, it was verified that CY62167GE30 is less affected by this problem compared to CY62157EV30, and its use will allow measurements with lower final uncertainty.

Once the system had been validated from a measurement point of view, its usability in terms of functionality and deployment was validated. In particular, to be used at the LHC, the system was integrated into the CERN network, which is described in detail in Section 5.3.

Operational examples of the system were presented, discussing and demonstrating the benefits of its use. In Section 5.4.1, an example of shielding evaluation was given. This showed how the flexibility and improved resolution of the instrument allowed the effects of different shielding to be characterized at different locations in the area interested by the SND@LHC installation. In Section 5.4.2, an example of installation in the experimental area of ALICE was given. The installation made it possible to monitor an area where the RadMon would not have been able to operate properly, both from a hardware point of view (high B-field compared to RadMon robustness) and from a measurement point of view (TID below RadMon resolution) point of view. Finally, in Section 5.4.3, an example of a fast deployment to detect the source of beam losses along the beam line was provided. In this example, it was possible to show the advantages of the wireless technology and its enhanced resolution, which allowed the deployment of devices and the localization of the leakage zone in a few hours, drastically reducing the unavailability of the accelerator.

Finally, the last part of the chapter was dedicated to a discussion on the possible operational extension of the Wireless IoT Main-board for applications other than radiation monitoring. Several examples were presented. In particular, Section 5.5.2 presented an IoT solution for temperature and humidity monitoring and demonstrated its robustness through radiation tests. The temperature readout circuit was validated by exceeding the *kGy* lifetime, while for humidity only 150 *Gy* was achieved. However, the test identified the cause of the problem and new solutions will improve the lifetime of this sensor in the future. In Section 5.5.3, the application for remote controlling was presented and demonstrated through the application example of remote controlling a 4G router during a radiation test. The test

made it possible to qualify the router in terms of lifetime and sensitivity, but above all to demonstrate that the use of the wireless IoT platform for remote controlling is possible. Furthermore, the test showed that the application could be used to improve the reliability of high-data-rate systems and enable their use in the future FCC, where there is a need to reduce the use of cables and increase the number of commercial systems in order to save costs.

The operational and application examples provided, demonstrate the enormous impact this application will have on the operation of the HL-LHC and the huge benefits it will bring in terms of monitoring and diversity applications for the future of the CERN.

# Conclusions

This doctoral work is devoted to the study and improvement of the current CERN Radiation Hardness Assurance (RHA) procedure applied to the electronic equipment hosted in the accelerator sector. The scheduled Large Hadron Collider (LHC) upgrade in 2029 (High Luminosity LHC (HL-LHC)) will significantly increase radiation levels that the accelerator's systems must withstand. In these circumstances, achieving successful completion of the RHA procedure while maintaining the currently used LHC radiation design margins and using commercial off-the-shelf (COTS) components may prove to be a complex task.

This work reports on the efforts made to improve the reliability of the process by improving two of its procedural steps, namely the 'Radiation Environment Analysis' and 'System-Level Testing' phases. To this end, a new wireless radiation monitoring system for the electronics is being developed to provide faster and more efficient deployment within the accelerator than those currently available. This cutting-edge project aims to decrease the uncertainty of the estimation offered by the 'Radiation Environment Analysis' phase. Its radiation qualification enables the enhancement of the 'System-Level Testing' phase through the development of new system-level testing guidelines and methodologies that enrich the existing process and allow for more reliable results. The newly developed instrument is an Internet of Things (IoT) Wireless radiation monitoring system for electronics. The design choices are based on the desire to overcome the limitations of RadMon. The platform hardware is completely different from its predecessor, enabling a faster and more efficient deployment. Thanks to its low power design, which allows it to be powered by batteries, and the wireless capability provided by the LoRa technology used, the instrument does not

need any cables to operate. This gives the system a high level of mobility compared to its predecessor. With a modular design and the use of a Microcontroller (MCU) instead of an FPGA, new sensor integration is made easier, increasing the system's flexibility. Finally, by replacing RadFET with FGDOS as the TID sensor and the CY62157EV30 Static Random-Access Memory (SRAM) with the CY62167GE30 SRAM as the HEH sensor, the instrument can achieve higher resolution capability and lower uncertainty in the final measurements.

The qualification of this instrument, despite being complicated by the various new features offered by the platform (e.g. wireless, low power components, etc.), allowed the existing RHA procedure to be extended and enriched with different findings.

Traditional CERN RHA does not provide specific guidelines for component-level testing of devices with different operating modes, it was possible to extrapolate several RHA implications concerning low power components and demonstrate the impact of different biases or operating modes on device degradation rates.

Regarding the system-level testing phase, the platform qualification enabled the development of various testing methodologies and approaches.

Firstly, it has been demonstrated that carrying out system-level testing without radiation represents an important test phase to verify the functionality of the system and to extrapolate some important system considerations, such as the expected operating mode. These considerations can support the subsequent system-level testing under radiation by identifying the most realistic conditions for testing.

An alternative methodology for system-level testing under radiation has been developed to allow the 'System-Level Testing' phase to be carried out even if the CHARM facility, defined as the test facility for this phase, is unavailable. This procedure consists of splitting the system-level qualification between different radiation test facilities selected to expose the system to the same radiation to electronic effects that it would experience at CHARM. This approach enables improved observability of system failures and easier identification of causes. During the application of this alternative methodology, practical approaches for system-level testing in facilities that cannot irradiate the entire system have been given as examples.

To obtain higher confidence results from the 'System-Level Testing' phase, a study has been conducted on the link between failure observability and selected flux. The research revealed a significant correlation between the two parameters and the potential difficulty in observing system failure modes within an acceptable time frame when using non optimal

flux. The wireless IoT platform represented the case study around which this investigation was developed. This system exhibits failure modes whose observability depends on the selected flux. The development of software mitigation schemes has enabled the identification and quantification of these failures in terms of cross-section, and improving the system's availability. As these can be extended to any MCU-based system, they will also enhance the availability of other designs if applied. The metrics derived from these characterizations enabled the demonstration and quantification of the relationship between flux and failure observability. Subsequently, this study led to the development of an additional system-level test methodology to determine the optimal test flux for a system. This approach complements existing methodologies and enhances the quality of the 'System-Level Testing' phase. The increased confidence gained will increase the overall cost of qualification, but on the other hand, it will reduce the possibility of unexpected behaviour of the qualified system in operation. Their occurrence will have a greater impact on qualification costs as they would require the system to be retested.

Once qualified, the system was validated from both measurement and operational perspectives. In the former case, the new sensors were validated by direct comparison with RadMon measurements at test positions of CHARM representative of LHC, demonstrating the compatibility of the measurements and the negligible impact on the final measurements of the higher sensitivity to intermediate neutrons of CY62167GE30 SRAM when compared to CY62157EV30 SRAM. The experimental data also confirmed that CY62167GE30 is characterized by lower intra-lot variation, enabling measurements with reduced uncertainties.

From an operational perspective, several operational examples of the Wireless IoT platform were presented, which would not have been possible with the RadMon due to the improved resolution, fast deployment time, and high mobility required by the installation specifications. These examples demonstrate the enormous potential impact of the platform on radiation monitoring operations during the HL-LHC.

The application's modularity and high flexibility demonstrated, through examples of applications other than radiation monitoring, the enormous potential of this platform for the future of CERN in terms of monitoring and different uses.

Finally, as the platform represents the first example of an IoT application at CERN, the experimental results obtained during the qualification of this application allowed to confirm the advantages (infrastructure cost reduction, higher observability with a large number of devices, quick installation time) and demonstrate the feasibility of an IoT network for longer

accelerators such as the Future Circular Collider (FCC).

In the near future, the use of this application will become even more central to the 'Radiation Environment Analysis' phase, as more equipment is deployed. In addition, the coverage of the remaining accelerators and experimental areas will allow more extensive use of this application in these areas as well. Thanks to its modular design, the system's performance can be further enhanced by easily redesigning both the Main-board and Sensor Board.

In terms of the Main-board, as described in this work, it is possible to replace the current External WaTchDog (Ext WTD) with one that performs better under radiation, thereby extending the system's lifespan. However, researching and identifying a suitable alternative is necessary. This investigation and its associated expenses could be avoided by taking advantage of the MCU's excellent performance under radiation and using an additional MCU as a watchdog. This approach would enable an increase in the radiation lifetime of the system without a significant increase in power consumption. Additionally, the second MCU would be in sleep mode most of the time without affecting the power consumption specifications. In this solution, the two MCUs would monitor each other. As the MCU can suffer non-recoverable failures through a simple hardware reset (toggling the reset PIN), an alternative method of resetting the system could be disabling the voltage supplier. In order for this mitigation to be effective, it is crucial to guarantee the complete shutdown of the failed MCU by using separate power lines and during the reset process, avoiding power from SPI slaves with different supply voltages, such as FGDOS that uses a different voltage supply.

In terms of the Sensor Board, several alternatives could enhance the design by reducing the read times of the memories. An FPGA designed as an SPI slave and used to control the SRAM sensors would remove the need for SPI GPIO expanders, reducing the read time of the sensor SRAMs, and if an Ext WTD module would be implemented inside, this could also allow the MCU to be monitored. Researching new SRAM sensors could also reduce uncertainty in system measurements. As demonstrated in this manuscript, Thermal Neutron sensors have non-negligible intra-lot variation, which is not the case for the High Energy Hadrons sensors used. Reducing this variability could lead to an enhanced performance in radiation monitoring on the platform.

From the perspective of the 'System-Level Testing' phase, the new validated methodology will allow the completion of the RHA procedure even during the Long Shutdown period, i.e. when CHARM will be temporarily unavailable (from the end of 2025 to the

beginning of 2029). The existence of an alternative methodology for the 'System-Level Testing' phase, and guidelines for qualifying a system with this methodology, will provide more time to complete the RHA and allow better preparation of the tests. As a result, more reliable systems will be ready for the HL-LHC. In the future, it will be essential to make this phase even more central by increasing the number of samples tested at the system-level in order to obtain the most reliable results and qualify all the new designs. Therefore, enhancing the presented methodology and developing new alternative approaches will be essential for accomplishing these goals and coping with the limited availability of CHARM.

# List of Publications

The work performed at CERN during these three years of Ph.D., concerning the thesis and supporting secondary activities, has led to the publication of several contributions in international journals:

- First Author Publications:

    1. Alessandro Zimmaro, Rudy Ferraro, Jérôme Boch, Frédéric Saigné, Rubén García Alía, Matteo Brucoli, Alessandro Masi, and Salvatore Danzeca. Testing and validation methodology for a radiation monitoring system for electronics in particle accelerators. IEEE Transactions on Nuclear Science, doi: 69(7):1642–1650, 2022.
    2. Alessandro Zimmaro, Rudy Ferraro, Jérôme Boch, Frédéric Saigné, Rubén García Alía, Alessandro Masi, and Salvatore Danzeca. Radiation test flux selection methodology to optimize see observability on systems with different operating modes. In 2022 22nd European Conference on Radiation and Its Effects on Components and Systems (RADECS), pages 1–8, 2022, doi: 10.1109/RADECS55911.2022.10412576.
    3. Alessandro Zimmaro, Rudy Ferraro, Jérôme Boch, Frédéric Saigné, Alessandro Masi, and Salvatore Danzeca. Using software Mitigation Schemes to Improve the Availability of IoT Applications in Harsh Radiation Environments. Journal of Instrumentation, doi: 19(02):C02059, feb 2024.

- Second Author Publications:

1. L. Gallego Manzano, Hamza Boukabache, Salvatore Danzeca, Natalie Heracleous, Fabrizio Murtas, Daniel Perrin, Vasja Pirc, Alejandro Ribagorda Alfaro, Alessandro Zimmaro, and Marco Silari. An iot lorawan network for environmental radiation monitoring. IEEE Transactions on Instrumentation and Measurement, 70:1–12, 2021.

2. Christoph Merscher, Rodrigo Sierra, Alessandro Zimmaro, Marco Giordano, and Salvatore Danzeca. Proximeter cern's detecting device for personnel. In EPJ Web of Conferences, volume 251, page 04025. EDP Sciences, 2021.

3. Salvatore Danzeca, Antony Cass, Alessandro Masi, Rodrigo Sierra, and Alessandro Zimmaro. Wireless IoT in Particle Accelerators: A Proof of Concept with the IoT Radiation Monitor at CERN. JACoW IPAC, pages 772–775, 2022.

4. Ygor Aguiar, Andrea Apollonio, Francesco Cerutti, Salvatore Danzeca, Ruben García Alía, Giuseppe Lerner, Daniel Prelipcean, and Marta Sabaté Gilarte. Radiation to Electronics Impact on CERN LHC Operation: Run 2 Overview and HL-LHC Outlook. JACoW IPAC, pages 80–83, 2022.

5. Rudy Ferraro, Panagiotis Gkountoumis, Gilles Foucard, Antonio Ventura, Antonio Scialdone, Alessandro Zimmaro, Bruno Glecer, Sokratis Koseoglou, Cai Arcos Botias, Alessandro Masi, and Salvatore Danzeca. 2023 compendium of radiation-induced effects for candidate particle accelerator. In 2023 IEEE Radiation Effects Data Workshop (REDW) (in conjunction with 2023 NSREC), pages 1–8, 2023.

6. D. Prelipcean, F. Cerutti, S. Danzeca, R. Garcia Alia, G. Lerner, M. Sabate Gilarte, and A. Zimmaro. Comparison between Run 2 SEU measurements and FLUKA simulations in the CERN LHC tunnel and shielded alcoves around IP1/5. JACoW IPAC, pages 4633-4636, 2023.

7. Auriane Canesse, Alessandro Zimmaro, Daniel Prelipcean, Daniel Ricci, Diego Di Francesca, Giuseppe Lerner, Ruben Garcia Alia, and Salvatore Danzeca. Overview of the radiation levels in the CERN accelerator complex after LS2. JACoW IPAC, pages 4055-4058, 2023.

8. S. Danzeca, J.L.D. Luna Duran, A. Masi, R. Sierra, and A. Zimmaro. Radiation-Tolerant Multi-Application Wireless IoT Platform for Harsh Environments. In

Proc. 19th Int. Conf. Accel. Large Exp. Phys. Control Syst. (ICALEPCS'23), pages 1051–1057. JACoW Publishing, Geneva, Switzerland, 2024.

# Acknowledgements

This activity has received funding from the European Union's 2020 research and innovation program under grant agreement No.101008126, corresponding to the RADNEXT project.

During these years I have had the fortune to meet many people who have helped me to grow as an engineer and researcher. In different ways, they have supported me in achieving my Ph.D. and I would like to dedicate a few lines to them to express my gratitude.

To my supervisor and mentor, Salvatore Danzeca, who has always motivated me and pushed me to improve by always trying to do more. I would like to thank him for believing in me from the first day we met.

I would like to thank my professors, Frédéric Saigné and Jérôme Boch, who have always supported me during these three years, providing me with constant feedback and points of reflection that have helped me to do my best work.

To my supervisor and friend, Rudy Ferraro, who was always willing to discuss ideas and give feedback, even outside of working hours.

I would like to thank Alessandro Masi for allowing me to work in such a stimulating environment. In addition, I would like to thank all my colleagues with whom I have shared these years and the different moments of this Ph.D.

I would also like to thank my family, who, despite being far away, have always supported and encouraged me.

Finally, I would like to thank a special person in my life who, more than anyone else, has shared all the good and bad moments of these three years: Valentina Giovinco. This

achievement is partly thanks to her because, in the failures and dark moments, she has always helped me to get back on my feet and motivated me to try again and again.

# List of Figures

# List of Tables

# Bibliography


[1] Rudy Ferraro. *Development of Test Methods for the Qualification of Electronic Components and Systems Adapted to High-Energy Accelerator Radiation Environments*. PhD thesis, Montpellier, 2019.

[2] Robley Dunglison Evans and RD Evans. *The atomic nucleus*, volume 582. McGraw-Hill New York, 1955.

[3] Rafael Ballabriga. *The Design and Implementation in* 0.13$\mu m$ *CMOS of an Algorithm Permitting Spectroscopic Imaging with High Spatial Resolution for Hybrid Pixel Detectors*. PhD thesis, Barcelona, Universitat Ramon Llull, 2009.

[4] G Barbottin and A Vapaille. Instabilities in silicon devices: New insulators, devices, and radiation effects. instabilities in silicon devices. *Elsevier*, 1:4, 1999.

[5] Donald E Groom, Nikolai V Mokhov, and Sergei I Striganov. Muon stopping power and range tables 10 mev-100 tev. *Atomic Data and Nuclear Data Tables*, 78(2):183–356, 2001.

[6] https://physics.nist.gov/physrefdata/star/text/pstar.html.

[7] https://physics.nist.gov/physrefdata/star/text/estar.html.

[8] https://physics.nist.gov/physrefdata/xraymasscoef/elemtab/z14.html.

[9] Shawn Tornga. A prototype compton imager: simulations, measurements and algorithm development. 2010.

[10] Timothy R Oldham. *Ionizing radiation effects in MOS oxides*, volume 3. World Scientific, 1999.

[11] George A Ausman Jr and Flynn B McLean. Electron- hole pair creation energy in sio2. *Applied Physics Letters*, 26(4):173–175, 1975.

[12] HH Sander and BL Gregory. Unified model of damage annealing in cmos, from freeze-in to transient annealing. *IEEE Transactions on Nuclear Science*, 22(6):2157–2162, 1975.

[13] Joseph M Benedetto and HE Boesch. The relationship between 60co and 10-kev x-ray damage in mos devices. *IEEE Transactions on Nuclear Science*, 33(6):1317–1323, 1986.

[14] Gerard Barbottin and Andre Vapaille. *New Insulators Devices and Radiation Effects*. Elsevier, 1999.

[15] RC Hughes. Hole mobility and transport in thin sio2 films. *Applied Physics Letters*, 26(8):436–438, 1975.

[16] DM Fleetwood, PS Winokur, RA Reber, TL Meisenheimer, JR Schwank, MR Shaneyfelt, and LC Riewe. Effects of oxide traps, interface traps, and "border traps"on metal-oxide-semiconductor devices. *Journal of applied physics*, 73(10):5058–5074, 1993.

[17] R. D. Schrimpf. *Radiation Effects in Microelectronics*, pages 11–29. Springer Netherlands, Dordrecht, 2007.

[18] F Faccio et al. Cots for the lhc radiation environment: the rules of the game. In *LEB 2000 Conference Krakow, Book of Abstracts*, page 50, 2000.

[19] Tomasz Rajkowski. *Méthodologie de qualification des System-In-Package (SiP) soumis au rayonnement ionisant*. PhD thesis, Montpellier, 202.

[20] Ruben Garcia Alia. *Radiation Fields in High Energy Accelerators and their impact on Single Event Effects*. PhD thesis, Montpellier U., 2014.

[21] Salvatore Danzeca. *The new version of the radiation monitor system for the electronics at the CERN: Electronic components radiation hardness assurance and sensors qualication*. PhD thesis, Université Montpellier, 2015.

[22] R.C. Baumann. Radiation-induced soft errors in advanced semiconductor technologies. *IEEE Transactions on Device and Materials Reliability*, 5(3):305–316, 2005.

[23] Andrea Coronetti. *Relevance and Guidelines of Radiation Effect Testing Beyond the Standards for Electronic Devices and Systems Used in Space and at Accelerators*. PhD thesis, 2021. Presented 17 Nov 2021.

[24] M.J. Gadlage, R.D. Schrimpf, J.M. Benedetto, P.H. Eaton, D.G. Mavis, M. Sibley, K. Avery, and T.L. Turflinger. Single event transient pulse widths in digital microcircuits. *IEEE Transactions on Nuclear Science*, 51(6):3285–3290, 2004.

[25] European cooperation for space standardization. ecss-q-st-30-11c: space product assurance - derating eee components. esa-estec. 2011.

[26] Uros Legat, Anton Biasizzo, and Franc Novak. Seu recovery mechanism for sram-based fpgas. *IEEE Transactions on Nuclear Science*, 59(5):2562–2571, 2012.

[27] Melanie Berg, C. Poivey, D. Petrick, D. Espinosa, Austin Lesea, K. A. LaBel, M. Friendlich, H. Kim, and Anthony Phan. Effectiveness of internal versus external seu scrubbing mitigation strategies in a xilinx fpga: Design, test, and analysis. *IEEE Transactions on Nuclear Science*, 55(4):2259–2266, 2008.

[28] Heather Quinn, Zachary Baker, Tom Fairbanks, Justin L. Tripp, and George Duran. Software resilience and the effectiveness of software mitigation in microcontrollers. *IEEE Transactions on Nuclear Science*, 62(6):2532–2538, 2015.

[29] Heather Quinn, Zachary Baker, Tom Fairbanks, Justin L. Tripp, and George Duran. Robust duplication with comparison methods in microcontrollers. *IEEE Transactions on Nuclear Science*, 64(1):338–345, 2017.

[30] Matthew Bohman, Benjamin James, Michael J Wirthlin, Heather Quinn, and Jeffrey Goeders. Microcontroller compiler-assisted software fault tolerance. *IEEE Transactions on Nuclear Science*, 66(1):223–232, 2018.

[31] C. Leroy and P.-G. Rancoita. Principles of radiation interaction in matter and detection. *Matter and Detection, 2nd ed. WORLD SCIENTIFIC*, 2009.

[32] Susan Wood, Natalie Jeanne Doyle, John A. Spitznagel, Wolfgang J. Choyke, Richard M. More, J. N. McGruer, and R. B. Irwin. Simulation of radiation damage in solids. *IEEE Transactions on Nuclear Science*, 28:4107–4112, 1981.

[33] https://rd50.web.cern.ch/niel/.

[34] ECSS-Q-ST-60-15C Radiation Hardness Assurance-EEE Components. ECSS-Q-ST-60-15C, ECSS, ESA, 2012.

[35] Christian Poivey and John H Day. Radiation hardness assurance for space systems. In *IEEE NSREC 2002 short course*, 2002.

[36] Lyndon Evans and Philip Bryant. Lhc machine. *Journal of Instrumentation*, 3(08):S08001, aug 2008.

[37] Anton Lechner, Bernhard Auchmann, Francesco Cerutti, Pier Paolo Granieri, Roderik Bruce, Arjan Verweij, Stefano Redaelli, Nikhil Vittal Shetty, Aurelien Marsili, Eleftherios Skordis, et al. Power deposition in lhc magnets with and without dispersion suppressor collimators downstream of the betatron cleaning insertion. 2014.

[38] Rubén García Alía, Markus Brugger, Francesco Cerutti, Salvatore Danzeca, Alfredo Ferrari, Simone Gilardoni, Yacine Kadi, Maria Kastriotou, Anton Lechner, Corinna Martinella, Oliver Stein, Yves Thurel, Andrea Tsinganis, and Slawosz Uznanski. Lhc and hl-lhc: Present and future radiation environment in the high-luminosity collision points and rha implications. *IEEE Transactions on Nuclear Science*, 65(1):448–456, 2018.

[39] L. Coull, D. Hagedorn, V. Remondino, and F. Rodriguez-Mateos. Lhc magnet quench protection system. *IEEE Transactions on Magnetics*, 30(4):1742–1745, 1994.

[40] Reiner Denz, Knud Dahlerup-Petersen, Andrzej Siemko, and Jens Steckert. Upgrade of the protection system for the superconducting elements of the lhc during ls1. *IEEE Transactions on Applied Superconductivity*, 24(3):1–4, 2014.

[41] Andrea Apollonio, Odei Rey Orozko, Ruediger Schmidt, Matthieu Valette, Daniel Wollmann, and Markus Zerlauth. Lessons Learnt from the 2016 LHC Run and Prospects for HL-LHC Availability. page TUPVA006, 2017.

[42] R2e mitigation project: www.cern.ch/r2e.

[43] Ygor Aguiar, Andrea Apollonio, Giuseppe Lerner, Matteo Cecchetto, Jean-Baptiste Potoine, Matteo Brucoli, Salvatore Danzeca, Ruben García Alía, Kacper Biłko, Alessandro Zimmaro, et al. Implications and mitigation of radiation effects on the cern sps operation during 2021. *JACoW IPAC*, 2022:740–743, 2022.

[44] M Brugger. R2e and availability. *CERN Yellow Reports*, 2:149–149, 2015.

[45] Ygor Aguiar, Andrea Apollonio, Francesco Cerutti, Salvatore Danzeca, Ruben García Alía, Giuseppe Lerner, Daniel Prelipcean, and Marta Sabaté-Gilarte. Radiation to Electronics Impact on CERN LHC Operation: Run 2 Overview and HL-LHC Outlook. pages 80–83, 2021.

[46] Slawosz Uznanski, Benjamin Todd, Arend Dinius, Quentin King, and Markus Brugger. Radiation hardness assurance methodology of radiation tolerant power converter controls for large hadron collider. In *2013 IEEE Nuclear Science Symposium and Medical Imaging Conference (2013 NSS/MIC)*, pages 1–6, 2013.

[47] S Danzeca, M Brugger, A Masi, and S Gilardoni. R2E – is it still an issue? pages 39–42, 2016.

[48] L.R. Greenwood. Neutron interactions and atomic recoil spectra. *Journal of Nuclear Materials*, 216:29–44, 1994.

[49] Rudy Ferraro, Gilles Foucard, Angelo Infantino, Luigi Dilillo, Markus Brugger, Alessandro Masi, Rubén García Alía, and Salvatore Danzeca. Cots optocoupler radiation qualification process for lhc applications based on mixed-field irradiations. *IEEE Transactions on Nuclear Science*, 67(7):1395–1403, 2020.

[50] Ketil Roed, Vittorio Boccone, Markus Brugger, Alfredo Ferrari, Daniel Kramer, Elias Lebbos, Roberto Losito, Alessio Mereghetti, Giovanni Spiezia, and Roberto Versaci. Fluka simulations for see studies of critical lhc underground areas. *IEEE Transactions on Nuclear Science*, 58(3):932–938, 2011.

[51] Ketil Roeed, Markus Brugger, Daniel Kramer, Paul Peronnard, Christian Pignard, Giovani Spiezia, and Adam Thornton. Method for measuring mixed field radiation levels relevant for sees at the lhc. *IEEE Transactions on Nuclear Science*, 59(4):1040–1047, 2012.

[52] Rubén García Alía, Markus Brugger, Salvatore Danzeca, Francesco Cerutti, Joao Pedro de Carvalho Saraiva, Reiner Denz, Alfredo Ferrari, Lionel L Foro, Paul Peronnard, Ketil Røed, Raffaello Secondo, Jens Steckert, Yves Thurel, Iacocpo Toccafondo, and Slawosz Uznanski. Single event effects in high-energy accelerators. *Semiconductor Science and Technology*, 32(3):034003, feb 2017.

[53] J. L. Autran, S. Serre, S. Semikh, D. Munteanu, G. Gasiot, and P. Roche. Soft-error rate induced by thermal and low energy neutrons in 40 nm srams. *IEEE Transactions on Nuclear Science*, 59(6):2658–2665, 2012.

[54] Alex Hands, Paul Morris, Keith Ryden, Clive Dyer, Pete Truscott, Andrew Chugg, and Sarah Parker. Single event effects in power mosfets due to atmospheric and thermal neutrons. *IEEE Transactions on Nuclear Science*, 58(6):2687–2694, 2011.

[55] D. Kramer, M. Brugger, V. Klupak, C. Pignard, K. Roeed, G. Spiezia, L. Viererbl, and T. Wijnands. Lhc radmon sram detectors used at different voltages to determine the thermal neutron to high energy hadron fluence ratio. *IEEE Transactions on Nuclear Science*, 58(3):1117–1122, 2011.

[56] T.T. Böhlen, F. Cerutti, M.P.W. Chin, A. Fassò, A. Ferrari, P.G. Ortega, A. Mairani, P.R. Sala, G. Smirnov, and V. Vlachoudis. The fluka code: Developments and challenges for high energy and medical applications. *Nuclear Data Sheets*, 120:211–214, 2014.

[57] Giuseppe Battistoni, Till Boehlen, Francesco Cerutti, Pik Wai Chin, Luigi Salvatore Esposito, Alberto Fassò, Alfredo Ferrari, Anton Lechner, Anton Empl, Andrea Mairani, Alessio Mereghetti, Pablo Garcia Ortega, Johannes Ranft, Stefan Roesler, Paola R. Sala, Vasilis Vlachoudis, and George Smirnov. Overview of the fluka code. *Annals of Nuclear Energy*, 82:10–18, 2015. Joint International Conference on Supercomputing in Nuclear Applications and Monte Carlo 2013, SNA + MC 2013. Pluri- and Trans-disciplinarity, Towards New Modeling and Numerical Simulation Paradigms.

[58] G. Lerner. Radiation level specifications for hl-lhc. Technical report, CERN EDMS document, https://edms.cern.ch/document/2302154/1.0, Geneva, CH, 2020.

[59] Kacper Biłko, Rubén García Alía, Diego Di Francesca, Ygor Aguiar, Salvatore Danzeca, Simone Gilardoni, Sylvain Girard, Luigi Salvatore Esposito, Matthew Alexander Fraser, Giuseppe Mazzola, Daniel Ricci, Marc Sebban, and Francesco Maria Velotti.

Cern super proton synchrotron radiation environment and related radiation hardness assurance implications. *IEEE Transactions on Nuclear Science*, pages 1–1, 2023.

[60] E. B. Holzer, Bernd Dehning, Ewald Effinger, Jonathan Emery, G. Ferioli, Jose Gonzalez, Edda Gschwendtner, G. Guaglio, Michael Hodgson, Daniel Kramer, Roman Leitner, Luis Ponce, V. Prieto, Markus Stockner, and C. Zamantzas. Beam loss monitoring system for the lhc. *IEEE Nuclear Science Symposium*, 2:1052 – 1056, November 2005.

[61] M. Kalliokoski, Bernhard Auchmann, Bernd Dehning, Fernando Domingues Sousa, Ewald Effinger, Jonathan Emery, Viatcheslav Grishin, Eva Barbara Holzer, Stephen Jackson, Blazej Kolad, Eduardo Nebot Del Busto, Ondrej Picha, Chris Roderick, Mariusz Sapinski, Marcin Sobieszek, and Christos Zamantzas. Beam Loss Monitoring for Run 2 of the LHC. 2015.

[62] Kacper Biłko and Oliver Stein. Report on the prompt dose distribution along the lhc based on blm data for proton-proton operation in run 2. Technical report, 2019.

[63] L. Sarchiapone, M. Brugger, B. Dehning, D. Kramer, M. Stockner, and V. Vlachoudis. Fluka monte carlo simulations and benchmark measurements for the lhc beam loss monitors. *Nuclear Instruments and Methods in Physics Research Section A: Accelerators, Spectrometers, Detectors and Associated Equipment*, 581(1):511–516, 2007. VCI 2007.

[64] Diego Di Francesca, Iacopo Toccafondo, G Li Vecchi, S Calderini, Sylvain Girard, Antonino Alessi, Rudy Ferraro, Salvatore Danzeca, Yacine Kadi, and Markus Brugger. Distributed optical fiber radiation sensing in the proton synchrotron booster at cern. *IEEE Transactions on Nuclear Science*, 65(8):1639–1644, 2018.

[65] Diego Di Francesca, Angelo Infantino, Gaetano Li Vecchi, Sylvain Girard, Antonino Alessi, Yacine Kadi, and Markus Brugger. Dosimetry mapping of mixed-field radiation environment through combined distributed optical fiber sensing and fluka simulation. *IEEE Transactions on Nuclear Science*, 66(1):299–305, 2019.

[66] Helmut Vincke, Isabell Brunner, I Floret, D Forkel-Wirth, M Fuerstner, S Mayer, and C Theis. Response of alanine and radio-photo-luminescence dosemeters to mixed high-energy radiation fields. *Radiation protection dosimetry*, 125(1-4):340–344, 2007.

[67] Dejan Pramberger, Ygor Q. Aguiar, Julia Trummer, and Helmut Vincke. Characterization of radio-photo-luminescence (rpl) dosimeters as radiation monitors in the cern accelerator complex. *IEEE Transactions on Nuclear Science*, 69(7):1618–1624, 2022.

[68] G. Spiezia, P. Peronnard, A. Masi, M. Brugger, M. Brucoli, S. Danzeca, R. Garcia Alia, R. Losito, J. Mekki, P. Oser, R. Gaillard, and L. Dusseau. A new radmon version for the lhc and its injection lines. *IEEE Transactions on Nuclear Science*, 61(6):3424–3431, 2014.

[69] J. Mekki, M. Brugger, S. Danzeca, L. Dusseau, K. Røed, and G. Spiezia. Mixed particle field influence on radfet responses using co-60 calibration. *IEEE Transactions on Nuclear Science*, 60(4):2435–2443, 2013.

[70] Giovanni Spiezia, Julien Mekki, Sergio Batuca, Markus Brugger, Marco Calviani, Alfredo Ferrari, Daniel Kramer, Roberto Losito, Alessandro Masi, Anna Nyul, et al. The lhc radiation monitoring system—radmon. *Proc. Sci*, 143:1–12, 2011.

[71] Esa/escc 25100 basic specification, single event effects test methods and guidelines, 2005.

[72] Rudy Ferraro, Panagiotis Gkountoumis, Gilles Foucard, Antonio Ventura, Antonio Scialdone, Alessandro Zimmaro, Bruno Glecer, Sokratis Koseoglou, Cai Arcos Botias, Alessandro Masi, and Salvatore Danzeca. 2023 compendium of radiation-induced effects for candidate particle accelerator. In *2023 IEEE Radiation Effects Data Workshop (REDW) (in conjunction with 2023 NSREC)*, pages 1–8, 2023.

[73] Rudy Ferraro, Rubén García Alía, Salvatore Danzeca, and Alessandro Masi. Analysis of bipolar integrated circuit degradation mechanisms against combined tid–dd effects. *IEEE Transactions on Nuclear Science*, 68(8):1585–1593, 2021.

[74] Robert Reed. Guideline for ground radiation testing and using optocouplers in the space radiation environment. *Nasa Nepp Program Erc Project Report*, 2002.

[75] C.J. Dale, P.W. Marshall, E.A. Burke, G.P. Summers, and E.A. Wolicki. High energy electron induced displacement damage in silicon. *IEEE Transactions on Nuclear Science*, 35(6):1208–1214, 1988.

[76] R.A. Reed, P.W. Marshall, C.J. Marshall, R.L. Ladbury, H.S. Kim, Loc Xuan Nguyen, J.L. Barth, and K.A. LaBel. Energy dependence of proton damage in algaas light-emitting diodes. *IEEE Transactions on Nuclear Science*, 47(6):2492–2499, 2000.

[77] P.F. Hinrichsen, A.J. Houdayer, A.L. Barry, and J. Vincent. Proton induced damage in sic light emitting diodes. *IEEE Transactions on Nuclear Science*, 45(6):2808–2812, 1998.

[78] Conference record of the twenty-eighth ieee photovoltaic specialists conference - 2000 (cat. no.00ch37036). In *Conference Record of the Twenty-Eighth IEEE Photovoltaic Specialists Conference - 2000 (Cat. No.00CH37036)*, 2000.

[79] Rudy Ferraro, Salvatore Danzeca, Chiara Cangialosi, Rubén García Alía, Francesco Cerutti, Andrea Tsinganis, Luigi Dilillo, Markus Brugger, and Alessandro Masi. Study of the impact of the lhc radiation environments on the synergistic displacement damage and ionizing dose effect on electronic components. *IEEE Transactions on Nuclear Science*, 66(7):1548–1556, 2019.

[80] P. Oser, J. Mekki, G. Spiezia, E. Fadakis, G. Foucard, P. Peronnard, A. Masi, and R. Gaillard. Effectiveness analysis of a non-destructive single event burnout test methodology. In *2013 14th European Conference on Radiation and Its Effects on Components and Systems (RADECS)*, pages 1–8, 2013.

[81] IEC Electropedia. Electropedia, 2020.

[82] Andrea Coronetti, Rubén García Alía, Jan Budroweit, Tomasz Rajkowski, Israel Da Costa Lopes, Kimmo Niskanen, Daniel Söderström, Carlo Cazzaniga, Rudy Ferraro, Salvatore Danzeca, Julien Mekki, Florent Manni, David Dangla, Cedric Virmontois, Nourdine Kerboub, Alexander Koelpin, Frédéric Saigné, Pierre Wang, Vincent Pouget, Antoine Touboul, Arto Javanainen, Heikki Kettunen, and Rosine Coq Germanicus. Radiation hardness assurance through system-level testing: Risk acceptance, facility requirements, test methodology, and data exploitation. *IEEE Transactions on Nuclear Science*, 68(5):958–969, 2021.

[83] J. Mekki, M. Brugger, R. G. Alia, A. Thornton, N. C. Dos Santos Mota, and S. Danzeca. Charm: A mixed field facility at cern for radiation tests in ground, atmospheric, space and accelerator representative environments. *IEEE Transactions on Nuclear Science*, 63(4):2106–2114, 2016.

[84] M. Rousselet, P. C. Adell, D. J. Sheldon, J. Boch, H. Schone, and F. Saigné. Use and benefits of cots board level testing for radiation hardness assurance. In *2016 16th Euro-*

*pean Conference on Radiation and Its Effects on Components and Systems (RADECS)*, pages 1–5, 2016.

[85] Tomasz Rajkowski, Frédéric Saigné, Kimmo Niskanen, Jérôme Boch, Tadec Maraine, Pierre Kohler, Patrick Dubus, Antoine Touboul, and Pierre-Xiao Wang. Comparison of the total ionizing dose sensitivity of a system in package point of load converter using both component-and system-level test approaches. *Electronics*, 10(11):1235, 2021.

[86] Israel C. Lopes, Vincent Pouget, Frederic Wrobel, Frederic Saigne, Antoine Touboul, and Ketil Røed. Development and evaluation of a flexible instrumentation layer for system-level testing of radiation effects. In *2020 IEEE Latin-American Test Symposium (LATS)*, pages 1–6, 2020.

[87] Gonzalo Fernández, Javier Bárcena, and Eugenio Muñoz. Tid test on iter interlock discharge loop interface box (dlib) system, an example of radiation test at equipment level. In *2017 17th European Conference on Radiation and Its Effects on Components and Systems (RADECS)*, pages 1–8, 2017.

[88] G. Tsiligiannis, S. Danzeca, R. García Alía, A. Infantino, A. Lesea, M. Brugger, A. Masi, S. Gilardoni, and F. Saigné. Radiation effects on deep submicrometer sram-based fpgas under the cern mixed-field radiation environment. *IEEE Transactions on Nuclear Science*, 65(8):1511–1518, 2018.

[89] Shay Gal-On and Markus Levy. Exploring coremark a benchmark maximizing simplicity and efficacy. *The Embedded Microprocessor Benchmark Consortium*, 2012.

[90] Douglas A. Santos, Lucas M. Luza, Maria Kastriotou, Carlo Cazzaniga, Cesar A. Zeferino, Douglas R. Melo, and Luigi Dilillo. Characterization of a risc-v system-on-chip under neutron radiation. In *2021 16th International Conference on Design and Technology of Integrated Systems in Nanoscale Era (DTIS)*, pages 1–6, 2021.

[91] G Gnemmi, G Tsiligiannis, A Masi, and S Danzeca. Reliability Analysis of Ethernet-Based Solutions for Data Transmission in the CERN Radiation Environment. *IEEE Trans. Nucl. Sci.*, 67(7):1614–1622, 2020.

[92] Heather Quinn. Challenges in testing complex systems. *IEEE Transactions on Nuclear Science*, 61(2):766–786, 2014.

[93] Philippe Adell, Gregory Allen, Gary Swift, and Steve McClure. Assessing and mitigating radiation effects in xilinx sram fpgas. In *2008 European Conference on Radiation and Its Effects on Components and Systems*, pages 418–424. IEEE, 2008.

[94] Gregory Allen, Larry D. Edmonds, Gary Swift, Carl Carmichael, Chen Wei Tseng, Kevin Heldt, Scott Arlo Anderson, and Michael Coe. Single event test methodologies and system error rate analysis for triple modular redundant field programmable gate arrays. *IEEE Transactions on Nuclear Science*, 58(3):1040–1046, 2011.

[95] J. A. Zoutendyk, H. R. Schwartz, R. K. Watson, Z. Hasnain, and L. R. Nevill. Single-event upset (seu) in a dram with on-chip error correction. *IEEE Transactions on Nuclear Science*, 34(6):1310–1315, 1987.

[96] Gregory R. Allen, Larry Edmonds, Chen Wei Tseng, Gary Swift, and Carl Carmichael. Single-event upset (seu) results of embedded error detect and correct enabled block random access memory (block ram) within the xilinx xqr5vfx130. *IEEE Transactions on Nuclear Science*, 57(6):3426–3431, 2010.

[97] W Hajdas, F Burri, Ch Eggel, R Harboe-Sorensen, and R De Marino. Radiation effects testing facilities in psi during implementation of the proscan project. In *IEEE Radiation Effects Data Workshop*, pages 160–164. IEEE, 2002.

[98] Alessandro Zimmaro, Rudy Ferraro, Jérôme Boch, Frédéric Saigné, Rubén García Alía, Matteo Brucoli, Alessandro Masi, and Salvatore Danzeca. Testing and validation methodology for a radiation monitoring system for electronics in particle accelerators. *IEEE Transactions on Nuclear Science*, 69(7):1642–1650, 2022.

[99] J. Mekki, M. Brugger, R. G. Alia, A. Thornton, N. C. Dos Santos Mota, and S. Danzeca. Charm: A mixed field facility at cern for radiation tests in ground, atmospheric, space and accelerator representative environments. *IEEE Transactions on Nuclear Science*, 63(4):2106–2114, 2016.

[100] Adam Thornton. Charm facility test area radiation field description. Technical report, 2016.

[101] Fabio Pozzi, Ruben Garcia Alia, Markus Brugger, Pierre Carbonez, Salvatore Danzeca, Blerina Gkotse, Martin Richard Jaekel, Federico Ravotti, Marco Silari, and Maris Tali. Cern irradiation facilities. *Radiation protection dosimetry*, 180(1-4):120–124, 2018.

[102] Ralf Nolte and David J Thomas. Monoenergetic fast neutron reference fields: I. neutron production. *Metrologia*, 48(6):S263, 2011.

[103] Ralf Nolte and David J Thomas. Monoenergetic fast neutron reference fields: Ii. field characterization. *Metrologia*, 48(6):S274, 2011.

[104] HJ Brede, M Cosack, G Dietze, H Gumpert, S Guldbakke, R Jahr, M Kutscha, D Schlegel-Bickmann, and H Schölermann. The braunschweig accelerator facility for fast neutron research: 1: Building design and accelerators. *Nuclear Instruments and Methods*, 169(3):349–358, 1980.

[105] Ralf Nolte and Stefan Röttger. Ptb contribution to the key comparison ccri (iii)-k11. comparison of neutron fluence measurements for neutron energies of 27 kev, 565 kev, 2.5 mev and 17 mev. 2018.

[106] Matteo Cecchetto, Rubén García Alía, Frédéric Wrobel, Andrea Coronetti, Kacper Bilko, David Lucsanyi, Salvatore Fiore, Giulia Bazzano, Elisa Pirovano, and Ralf Nolte. 0.1–10 mev neutron soft error rate in accelerator and atmospheric environments. *IEEE Transactions on Nuclear Science*, 68(5):873–883, 2021.

[107] Matteo Cecchetto. Experimental and Simulation Study of Neutron-Induced Single Event Effects in Accelerator Environment and Implications on Qualification Approach, 2021. Presented 13 Apr 2021.

[108] K Ambrožič, G Žerovnik, and L Snoj. Computational analysis of the dose rates at jsi triga reactor irradiation facilities. *Applied Radiation and Isotopes*, 130:140–152, 2017.

[109] Loïc Barbot, Christophe Domergue, Stephane Breaud, Christophe Destouches, Jean-Francois Villard, Luka Snoj, Žiga Štancar, Vladimir Radulović, and Andrej Trkov. Neutron field characterization of irradiation locations applied to the slovenian triga reactor. In *2013 3rd International Conference on Advancements in Nuclear Instrumentation, Measurement Methods and their Applications (ANIMMA)*, pages 1–5. IEEE, 2013.

[110] Salvatore Danzeca, Antony Cass, Alessandro Masi, Rodrigo Sierra, and Alessandro Zimmaro. Wireless IoT in Particle Accelerators: A Proof of Concept with the IoT Radiation Monitor at CERN. *JACoW IPAC*, 2022:772–775, 2022.

[111] Alessandro Masi, Giovanni Spiezia, Paul Peronnard, Mathieu Donze, Markus Brugger, and Roberto Losito. The new generation of lhc accelerator radiation monitoring system. In *2012 18th IEEE-NPSS Real Time Conference*, pages 1–7, 2012.

[112] Raffaello Secondo. *Upgrades of the RadMon V6 and its Integration on a Nanosatellite for the Analysis and the Comparative Study of the CHARM and Low Earth Orbit Environments*. PhD thesis, 2017. Presented 24 Apr 2017.

[113] G. Tsiligiannis, L. Dilillo, A. Bosio, P. Girard, S. Pravossoudovitch, A. Todri, A. Virazel, H. Puchner, C. Frost, F. Wrobel, and F. Saigné. Multiple cell upset classification in commercial srams. *IEEE Transactions on Nuclear Science*, 61(4):1747–1754, 2014.

[114] Stephane Deghaye and Eve Fortescue-Beck. Introduction to the BE-CO Control System. 2020.

[115] John-Paul Jones, Simon C. Jones, Keith J. Billings, Jasmina Pasalic, Ratnakumar V. Bugga, Frederick C. Krause, Marshall C. Smart, and Erik J. Brandon. Radiation effects on lithium cfx batteries for future spacecraft and landers. *Journal of Power Sources*, 471:228464, 2020.

[116] C. Rivetta, B. Allongue, G. Berger, F. Faccio, and W. Hajdas. Single event burnout in dc-dc converters for the lhc experiments. In *RADECS 2001. 2001 6th European Conference on Radiation and Its Effects on Components and Systems (Cat. No.01TH8605)*, pages 315–322, 2001.

[117] Stefano Agosta, Rodrigo Sierra, and Frederic Chapron. High-Speed Mobile Communications in Hostile Environments. Technical Report 5, CERN, Geneva, 2015.

[118] Rodrigo Sierra and Hubert Odziemczyk. Readying cern for connected device era. In *EPJ Web of Conferences*, volume 245, page 07015. EDP Sciences, 2020.

[119] Kais Mekki, Eddy Bajic, Frederic Chaxel, and Fernand Meyer. A comparative study of lpwan technologies for large-scale iot deployment. *ICT Express*, 5(1):1–7, 2019.

[120] LoRa Alliance. Lora alliance technical spec., https://resources.lora-alliance.org/technical-specifications.

[121] Antonio Scialdone, Rudy Ferraro, Rubén García Alía, Luca Sterpone, Salvatore Danzeca, and Alessandro Masi. Fpga qualification and failure rate estimation methodology for lhc environments using benchmarks test circuits. *IEEE Transactions on Nuclear Science*, 69(7):1633–1641, 2022.

[122] M. Brucoli, J. Cesari, S. Danzeca, M. Brugger, A. Masi, A. Pineda, L. Dusseau, and F. Wrobel. Investigation on passive and autonomous mode operation of floating gate dosimeters. *IEEE Transactions on Nuclear Science*, 66(7):1620–1627, 2019.

[123] F Faccio et al. Cots for the lhc radiation environment: the rules of the game. In *LEB 2000 Conference Krakow, Book of Abstracts*, page 50, 2000.

[124] Martin Cejp. Wireless radiation monitoring system for particle accelerators, 2020.

[125] https://physics.nist.gov/physrefdata/xraymasscoef/comtab/air.htm.

[126] R. Secondo, R. García Alía, P. Peronnard, M. Brugger, A. Masi, S. Danzeca, A. Merlenghi, E. Chesta, J. R. Vaillè, M. Bernard, and L. Dusseau. System level radiation characterization of a 1u cubesat based on cern radiation monitoring technology. *IEEE Transactions on Nuclear Science*, 65(8):1694–1699, 2018.

[127] Stephen Buchner, Paul Marshall, Scott Kniffin, and Ken LaBel. Proton test guideline development-lessons learned. *NASA/Goddard Space Flight Center, NEPP*, 2002.

[128] Alessandro Zimmaro, Rudy Ferraro, Jérôme Boch, Frédéric Saigné, Rubén García Alía, Alessandro Masi, and Salvatore Danzeca. Radiation test flux selection methodology to optimize see observability on systems with different operating modes. In *2022 22nd European Conference on Radiation and Its Effects on Components and Systems (RADECS)*, pages 1–8, 2022.

[129] A. Zimmaro, R. Ferraro, J. Boch, F. Saigne, A. Masi, and S. Danzeca. Using software mitigation schemes to improve the availability of iot applications in harsh radiation environment. *Journal of Instrumentation*, 19(02):C02059, feb 2024.

[130] Thomas Cartier-Michaud, Andrea Apollonio, Gennaro Blarasin, Benjamin Todd, and Jan Uythoven. Data-Driven Risk Matrices for CERN's Accelerators. DATA-DRIVEN RISK MATRICES FOR CERN'S ACCELERATORS. *JACoW IPAC*, 2021:2260–2263, 2021.

[131] Michael Benedikt, Alain Blondel, Patrick Janot, Michelangelo Mangano, and Frank Zimmermann. Future circular colliders succeeding the lhc. *Nature Physics*, 16(4):402–407, 2020.

[132] A Gregory, S Gary, and C Carl. Virtex-4qv static seu characterization summary. *NASA Electronic Parts and Packaging; National Aeronautics and Space Administration: Washington, DC, USA*, 2008.

[133] JESD89A JEDEC. Measurement and reporting of alpha particles and terrestrial cosmic ray-induced soft errors in semiconductor devices: Jesd89a. *JEDEC STANDARD, JEDEC Sold State Technology Association*, 89:1–85, 2006.

[134] Melanie D. Berg, Kenneth A. LaBel, Hak Kim, Mark Friendlich, Anthony Phan, and Christopher Perez. A comprehensive methodology for complex field programmable gate array single event effects test and evaluation. *IEEE Transactions on Nuclear Science*, 56(2):366–374, 2009.

[135] Carlo Cazzaniga, Marta Bagatin, Simone Gerardin, Alessandra Constantino, and Christopher D. Frost. First tests of a new facility for device-level, board-level and system-level neutron irradiation of microelectronics. *IEEE Transactions on Emerging Topics in Computing*, 9(1):104–108, 2021.

[136] S. Danzeca, J.L.D. Luna Duran, A. Masi, R. Sierra, and A. Zimmaro. Radiation-Tolerant Multi-Application Wireless IoT Platform for Harsh Environments. In *Proc. 19th Int. Conf. Accel. Large Exp. Phys. Control Syst. (ICALEPCS'23)*, number 19 in International Conference on Accelerator and Large Experimental Physics Control Systems, pages 1051–1057. JACoW Publishing, Geneva, Switzerland, 02 2024.

[137] Alessandro Zimmaro. FPGA - MCU design for the performance improvement of a space payload for radiation monitoring, 2020. Presented 25 Jan 2020.

[138] Matteo Cecchetto, Rubén García Alía, Frédéric Wrobel, Andrea Coronetti, Kacper Bilko, David Lucsanyi, Salvatore Fiore, Giulia Bazzano, Elisa Pirovano, and Ralf Nolte. 0.1–10 mev neutron soft error rate in accelerator and atmospheric environments. *IEEE Transactions on Nuclear Science*, 68(5):873–883, 2021.

[139] Rodrigo Sierra and Hubert Odziemczy. Readying CERN for connected device era. 2019.

[140] Christoph Merscher, Rodrigo Sierra, Alessandro Zimmaro, Marco Giordano, and Salvatore Danzeca. Proximeter cern's detecting device for personnel. In *EPJ Web of Conferences*, volume 251, page 04025. EDP Sciences, 2021.

[141] L. Gallego Manzano, Hamza Boukabache, Salvatore Danzeca, Natalie Heracleous, Fabrizio Murtas, Daniel Perrin, Vasja Pirc, Alejandro Ribagorda Alfaro, Alessandro Zimmaro, and Marco Silari. An iot lorawan network for environmental radiation monitoring. *IEEE Transactions on Instrumentation and Measurement*, 70:1–12, 2021.

[142] Simona Ilieva. Measurement of the muon flux at the SND@LHC experiment. Technical report, CERN, Geneva, 2023.